DEFORMATION AND RECRYSTALLISATION IN LOW CARBON STEELS

A thesis submitted to The University of Manchester for the degree of
Doctor of Philosophy
in the Faculty of Engineering and Physical Sciences

2010

Marwan A. Almojil

Manchester Materials Science Centre

Contents

Final word Count: 42,800

List of Figures

List of Tables

Abstract

The annealing behaviour, including studies of recrystallisation kinetics and development of crystallographic texture, of two low carbon steels after different cold rolling reductions have been investigated using Optical Microscopy (OM), Electron Back-Scatter Diffraction (EBSD) and Transmission Electron Microscopy (TEM). The primary recrystallisation behaviour of 20, 50, 70 and 90% cold rolled Interstitial Free (IF) and High Strength Low Alloy (HSLA) steels was studied. The HSLA was initially processed to give a volume fraction of about 0.2 of fine pearlite colonies, which acted as mechanically hard particles. The presence of such particles on the HSLA steel significantly reduced the temperature needed for recrystallisation by enhancing the recrystallisation and acting as nucleation sites by the Particle Stimulated Nucleation (PSN) mechanism. The inhomogeneous deformation and the local orientation changes introduced in the neighbourhood of the carbide particles (i.e. the particle deformation zone) were observed using TEM and selected area electron diffraction. The JMAK model was used to analyse the recrystallisation kinetics of the two steels. The experimental data plotted according to the JMAK model could be represented by straight lines with a JMAK exponent *n* falling in the range from 1.4 to 2.0.

The development of crystallographic textures after cold rolling reductions and subsequent recrystallisation has been investigated. The texture development is shown to be largely dependent on the rolling reduction. With increasing rolling reduction, the annealing texture show gradual intensification of α- and γ-fibre components. However, the intensity of both fibres is weaker in the HSLA steel. Despite the dominance of PSN in HSLA steel, the recrystallisation textures were similar to that of the rolling textures with weaker intensity of both fibres. To help clarify the reasons for that, *in-situ* EBSD experiments of recrystallising HSLA steel deformed to 50% and 70% have been carried out. It shows that the formation of the nucleus seems to occur within the deformation zones in regions away from the particle surface leading to recrystallisation textures similar to that of the rolling textures (i.e. both α- and γ-fibre exist).

The validity of this assumption has been confirmed by the use of Monte Carlo modelling. This model was used to simulate, in general way, and study the phenomenon of PSN during the recrystallisation process. The simulation shows the discontinuous evolution of the subgrains in the deformation zone to form recrystallisation nuclei around the particle. It shows also the subsequent growth of these nuclei to consume the matrix region around the particle. The simulation results are shown to match with the experimentally observed features of the recrystallisation phenomena in low carbon steel containing coarse cementite particles.

Declaration

No portion of the work referred to in the thesis has been submitted in support of an application for another degree or qualification of this or any other university or other institute of learning.

Copyright Statement

i. The author of this thesis (including any appendices and/or schedules to this thesis) owns certain copyright or related rights in it (the "Copyright") and he has given The University of Manchester certain rights to use such Copyright, including for administrative purposes.

ii. Copies of this thesis, either in full or in extracts and whether in hard or electronic copy, may be made **only** in accordance with the Copyright, Designs and Patents Act 1988 (as amended) and regulations issued under it or, where appropriate, in accordance with licensing agreements which the University has from time to time. This page must form part of any such copies made.

iii. The ownership of certain Copyright, patents, designs, trade marks and other intellectual property (the "Intellectual Property") and any reproductions of copyright works in the thesis, for example graphs and tables ("Reproductions"), which may be described in this thesis, may not be owned by the author and may be owned by third parties. Such Intellectual Property and Reproductions cannot and must not be made available for use without the prior written permission of the owner(s) of the relevant Intellectual Property and/or Reproductions.

iv. Further information on the conditions under which disclosure, publication and commercialisation of this thesis, the Copyright and any Intellectual Property and/or Reproductions described in it may take place is available in the University IP Policy (see http://www.campus.manchester.ac.uk/medialibrary/policies/intellectual-property.pdf), in any relevant Thesis restriction declarations deposited in the University Library, The university Library's regulations (see http://www.manchester.ac.uk/library/aboutus/regulations) and in The University's policy on presentations of Theses.

Acknowledgements

I humbly thank Allah, the Almighty, for having made everything possible by giving me health, thoughts and co-operative people to enable me complete this work.

I greatly appreciate the efforts of my supervisor Pete Bate for his endless support, guidance and encouragement throughout the period of this work. I do strongly appreciate the time and effort he spent reviewing this report and giving me the feedback.

I would sincerely like to thank John Humphreys and Ian Brough for their assistance with the *in-situ* experiments. I also appreciate their valuable comments on my work.

I would like to express my sincere thanks to all my LAP colleagues for their support and encouragement. Thanks are also due to the staff and faculty members of the Materials Science Centre for their constant support.

Gratitude is expressed to my employer, Saudi Basic Industries Corporation (SABIC), for providing me this opportunity to carry out this work.

I would like to thank my parents, brothers and sisters for their never ending moral support and prayers.

And last but certainly not least, I owe my deepest gratitude to my dear wife Sarah and my son Abdulrahman. I will never forget their love and “patience” during the period of this work.

Chapter 1

INTRODUCTION

Low Carbon (LC) steels are described as steels that contain less than 0.25% C, with one of the most important products being thin-gauge strip and sheet. The production of these steels with very low carbon and nitrogen contents constitutes the most recent step in the evolution of formable, cold rolled and annealed steels. Low carbon content and additions of elements that have a strong affinity for carbon, such as niobium or titanium, have long been known to promote recrystallisation textures favourable for severe forming operations with a high degree of tolerance to processing variables (Krauss *et al.* 1991).

One of the major industrial applications of LC sheet steels has been for deep drawing. The understanding of the recrystallisation texture is important for an improved prediction of the resulting drawability. Considerable work has been done on the recrystallisation behaviour and texture formation during the annealing process after cold rolling. However, few studies have dealt with the effect of coarse particles on the recrystallisation texture of LC steels. In addition, these previous studies were carried out using Transmission Electron Microscopy (TEM) techniques in which detailed measurements, with sufficient data production for statistical use, of the highly misoriented regions near the particles were not allowed. This study describes this phenomenon with the aid of Electron Back-Scatter Diffraction (EBSD) on Scanning Electron Microscopy (SEM) technique. This technique has many advantages over TEM techniques. It offers faster data collection, over larger areas of the specimen, and simpler methods of data analysis.

Generally, the idea of this study is that the LC steel has a very good drawability when it is processed to have a recrystallisation texture with {111} parallel to the

sheet plane (Hutchinson and Ushiode 1984; Satoh *et al.* 1986). The formation of this texture is strongly affected by second phase particles. Depending on their size, it is believed that a dense dispersion of fine particles does not impair the recovery and nucleation of recrystallised grains. However, the growth of these grains is retarded by the pinning force exerted by these particles on the grain boundary. On the other hand, large particles can act as nucleation sites for recrystallisation through the Particle Stimulated Nucleation (PSN) mechanism (Humphreys and Hatherly 2004). One important aspect of this mechanism is that the nucleation sites are well defined regions of the microstructure. So, the recrystallised grain size may be controlled by altering the alloy or processing.

The orientations of the recrystallisation nuclei produced by PSN and the types of the crystallographic texture formed is a major focus of this project. The understanding of this will allow the potential for optimizing the drawability of LC steel sheet. Generally, four goals were identified for this work.

1. To study the recrystallisation behaviour of low carbon steels, undertaking in detail the study of the effect of different parameters including composition, reduction and temperature.

2. To provide a detailed study of the development of crystallographic texture during various cold rolling reductions and recrystallisation of low carbon steels having different microstructural features.

3. To give a detailed investigation of the features of the particle deformation zone around large particles in low carbon steels including its influence on the rolling and recrystallisation textures.

4. To simulate the PSN mechanism, and the recrystallisation process in general, allowing a better understanding of this phenomenon.

This thesis is divided into several chapters. In chapter two, a review of the literature that is important for the understanding of the problem being investigated in this study is given. It starts by giving an introduction to low carbon steel; its microstructure, classification and properties. Special attention is drawn to the deep drawing properties. This part also describes the process of annealing and consequent microstructural changes, particularly in the presence of large particles. It gives a

broad overview of the PSN mechanism and a summary of the previous work done on this subject. A general background of the Monte Carlo model for recrystallisation and grain growth simulation is also given.

The third chapter details the materials examined (i.e. IF and HSLA steels) in this study as well as the experimental techniques used to investigate the microstructures and textures following deformation and subsequent heat treatment. It also explains the methods used for data analysis. More attention was given to the EBSD technique, specifically the procedure used for the *in-situ* EBSD study of the annealing process.

The fourth chapter describes the observations made and findings obtained from the experiments during this study. It proceeds by giving detailed microstructural investigation, using SEM and TEM, along with the texture development of the two low carbon steels, presented by ODFs and pole figures, during deformation and subsequent annealing. In addition, the result of the *in-situ* EBSD experiments and the model used to simulate the recrystallisation process are also given in this chapter.

The fifth chapter is a discussion of all the results presented in the previous chapter, taking into account the recent related studies. This chapter aims to discuss all the various effects that the different cold rolling reductions, compositions and annealing temperatures can bring about in the annealing behavior and the texture evolution of the low carbon steels investigated.

Finally, several conclusions, explicitly or implicitly inferred from this study, are summarised in the last chapter.

Chapter 2

LITERATURE REVIEW

2.1 Low Carbon Steels: Microstructure, Classification and Properties

2.1.1 Iron Carbon Equilibrium Phase Diagram

A study of the constitution and structure of all steels and irons must first start with the iron-carbon equilibrium phase diagram (Figure 2.1). It is the foundation on which all heat treatment of steel is based and the basic features of this system influence even the most complex alloy steels.

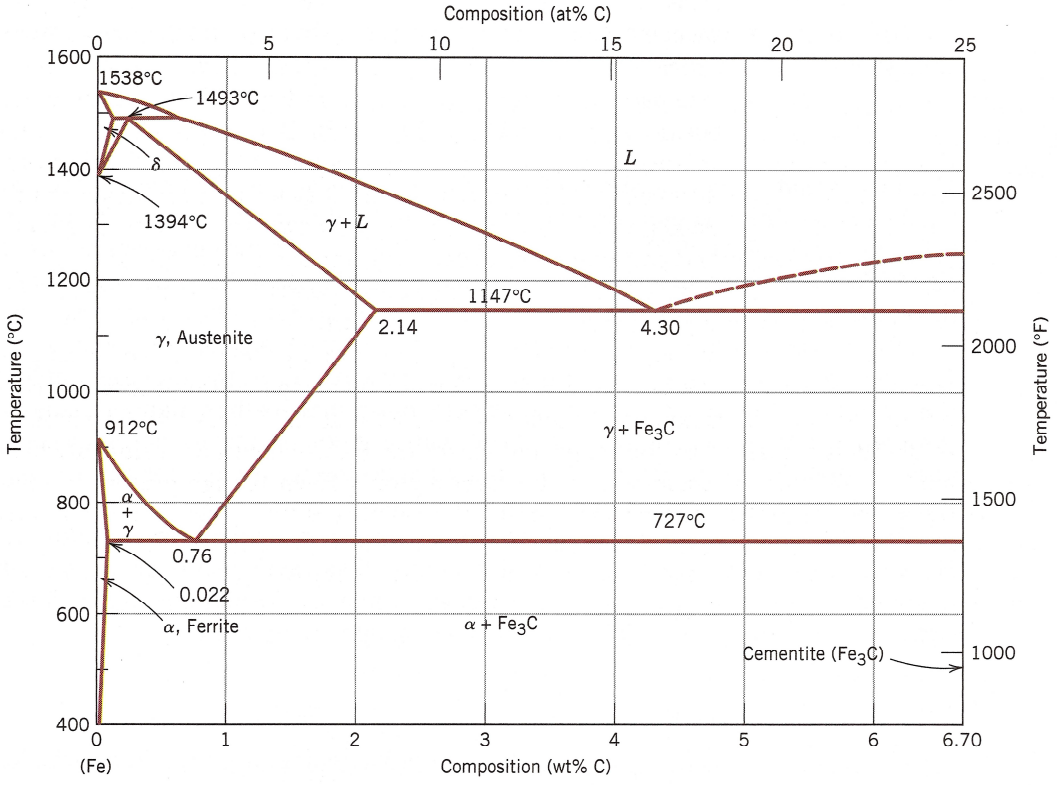

Figure 2.1: Iron carbon phase diagram (Callister 2001).

According to this diagram, all binary Fe-C alloys containing less than about 2.11 wt % carbon are classified as steels while all those containing higher carbon content are termed cast iron. In addition, it can be noticed that pure iron, at atmospheric pressure, exists in more than one crystal form depending on the temperature. Alpha iron (ferrite) which has the Body Centred Cubic (BCC) structure exists up to 912^{o}C, gamma iron (austenite) which has the Face Centred Cubic (FCC) structure exists between 912 and 1394^{o}C and delta iron (delta ferrite) which has the BCC structure exists from 1394^{o}C to the melting point of pure iron, 1538^{o}C (Bhadeshia and Honeycombe 2006).

There are three critical temperatures which are important in the heat treatment of steel. Firstly, the A_1 temperature (723^{o}C) at which the eutectoid reaction occurs. Secondly, the A_3 temperature which corresponds to the boundary between the ferrite-austenite and austenite fields. This occurs at 910^{o}C for pure iron and it is lowered with the addition of carbon. Finally, the A_{cm} temperature which corresponds to the boundary between cementite-austenite and austenite fields. This temperature increases as the carbon content increases.

It is important to notice the great difference in carbon solubility between gamma and alpha iron. During slow cooling of steel containing less than 0.8 wt% C, ferrite is formed in the range 910-723^{o}C with the rest of austenite becoming enriched in carbon until at 723^{o}C where the remaining austenite, which contains 0.8 wt% carbon, transforms to pearlite through the eutectoid reaction. Pearlite is a lamellar mixture of ferrite and iron carbide (cementite) formed via that eutectoid reaction.

In the case of high cooling rate, the formation of ferrite and pearlite is suppressed since atomic diffusion is necessary for nucleation and growth of these products. As a result, austenite will decompose to non-equilibrium microstructures (i.e. Bainite and Martensite) (Krauss 2005).

2.1.1.1 Effect of Alloying Elements in Low Carbon Steels

Alloying elements are added to low carbon steels to modify and improve their properties. They have a strong influence on the stable temperature range of the alpha and gamma fields. Elements like Ni, Mn, C and N expand the gamma field and encourage the formation of austenite (austenite stabilisers) while elements such as Si,

Al, Cr, Nb, Ti and S contract the gamma field and encourage the formation of ferrite (ferrite stabilisers) (Bain 1939).

In addition, alloying elements can be divided into two categories according to their interaction of carbon; the carbide-forming elements, such as Mn, Cr, V, Nb and Ti and the noncarbide-forming elements such as Ni, Si, P and Al (Totten 2007).

The effects of micro-alloying elements (e.g. V, Nb and Ti) on low carbon steels are of particular interest since low levels of these microalloying elements yield a significant improvement in mechanical properties through grain refinement and precipitation strengthening.

All of the microalloying elements (i.e. V, Nb and Ti) are very strong carbide formers, and help provide grain refinement after a normalising heat treatment. However, other roles are more characteristic of certain microalloying elements. For example, a vanadium addition is able to give precipitation strengthening in high carbon steels, niobium has a particularly strong influence in reducing recrystallisation during hot rolling thus aiding grain refinement, and a small titanium addition is very effective in refining grain size at high temperatures in the austenite range (Gladman 1997). Figure 2.2 shows the effects of various microalloying elements on austenitic grain growth during heating. It shows clearly that vanadium has the highest solubility while titanium has the lowest solubility in austenite (Repas 1988). However, it should be noted that the effects of a single alloying element is modified by the influence of other elements and the interaction of them must be considered. For example, the solubility temperature of niobium (i.e. temperature at which Nb starts dissolution) increases from about 1170^{o}C in a typical niobium steel to about 1250^{o}C in a Nb-Ti steel (Fernandez *et al.* 2003).

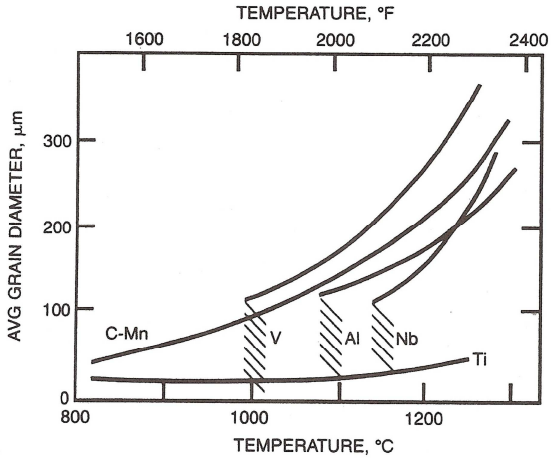

Figure 2.2: Austenite grain coarsening in various microalloyed steels (Repas 1988).

The choice of microalloying element to use in steel is strongly influenced by the solubility of the microalloy carbide or nitride. The solubility products of the individual carbides and nitrides are shown in Figure 2.3 as a function of temperature (Gladman 1997). This figure shows that the solubilities for carbides and nitrides in ferrite are lower than in austenite at temperatures in the ferrite range. It shows also that nitrides of the various microalloys are less soluble than their respective carbides.

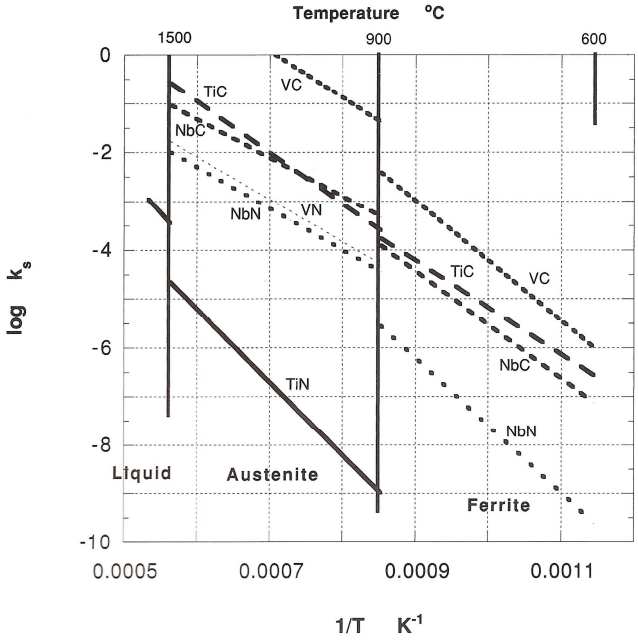

Figure 2.3: Solubility products versus temperature for various compounds in austenite and ferrite (Gladman 1997).

The precipitation behaviour of microalloy carbo-nitrides in steels, on the other hand, has a strong influence on the choice of microalloying elements and can occur in the austenite, during the γ-α transformation or in the ferrite, depending upon the composition and the thermomechanical treatments applied to the steel.

Precipitation in austenite is a very slow process and can be accelerated by applying hot deformation which increases the dislocation density and, hence, increases the number of nucleation sites (Hoogendorn and Spanraft 1977). On the other hand, precipitation is found to occur at the interface between the growing ferrite and the austenite matrix during the γ-α transformation (interphase precipitation) (Honeycombe 1976). However, rapid cooling rates can suppress this interphase reaction. So, in reheating within the ferrite temperature range, low carbon steels will generally show a precipitation hardening reaction with carbo-nitride particles forming either on dislocations or as matrix precipitates (Gladman 1997).

2.1.1.2 Spheroidisation Treatment

The cementite phase present in most low carbon steels is in the form of fine plates in pearlite. However, it is possible to heat-treat such steels and change the shape of the cementite into a spherical form which gives the most ductile and softest condition (Figure 2.4).

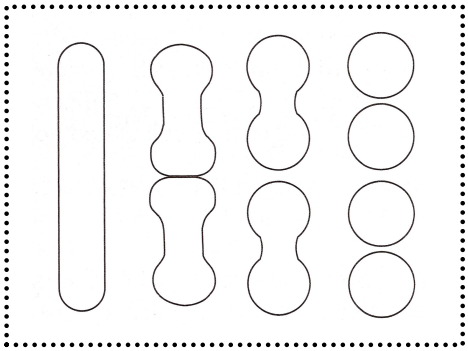

Figure 2.4: Schematic diagram of the process of transforming cementite lamella to spheroids during soft annealing (Thelning 1984).

Spheroidised microstructures are the most stable microstructures found in steels (Bhadeshia and Honeycombe 2006). The thermodynamic driving force for spheroidisation is the reduction of ferrite/carbide interfacial energy associated with spherical carbide particle formation. Spherical particles have minimum surface to volume ratios relative to other particle shapes, and the coarser and the fewer the particles, the lower will be the interfacial energy associated with a spheroidised microstructure (Krauss 2005).

The physical mechanism of spheroidisation is based on the coagulation of cementite particles within the ferrite matrix, for which the diffusion of carbon is decisive. The carbon diffusion depends on temperature, time and the kind and amount of alloying elements in the steels. The solubility of carbon in ferrite, which is very low at room temperature, increases considerably up to the Ac_1 temperature where the diffusion of carbon, iron and alloying atoms is so great that it is possible to change the structure in the direction of minimising its energy content (Totten 2007).

The degree of coagulation, as well as the size of carbides, after a spheroidising treatment is dependent on the starting structure before annealing (i.e. pearlitic, bainitic or martensitic microstructures).

Spheroidisation is more rapid than in pearlitic microstructure if carbides are initially in the form of discrete particles, as in Bainite, and especially if the particles are formed by tempering of martensite. Many other approaches to spherodising are used to accelerate the process (Krauss 2005). Heat treating to accomplish either complete or partial austenitisation, and then holding just below Ac_1, cooling quickly through the Ac_1, or cycling above and below Ac_1 are all techniques used to reduce the time for spheroidisation. Figure 2.5 shows possible temperature-time regimes for spheroidisation treatment.

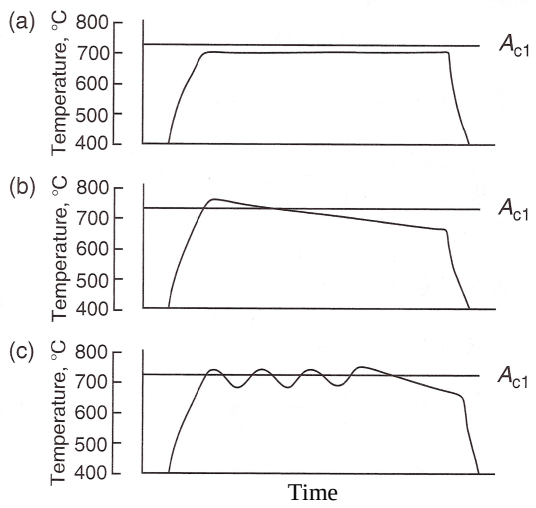

Figure 2.5: Temperature-time regimes at soft annealing. (a) Annealing at 20°C below Ac_1, for unalloyed and alloyed steels with Bainatic or Martensitic starting structures; (b) annealing at 10°C above Ac_1 (start) and decreasing temperature to 30°C below Ac_1 for alloyed steels; (c) cyclic annealing ±5°C around Ac_1 for hypereutectoid steels (Spur and Stöferle 1987).

Transformation of austenite directly into a spheroidised cementite + ferrite structure rather than into the plate shaped pearlite structure is sometimes called Divorced Eutectoid Transformation (DET) (Taleff *et al.* 1996; Verhoeven and Gibson 1998). Figure 2.6 compares schematically the transformation of austenite to the lamellar ferrite/cementite microstructure of pearlite and to the dispersed cementite/ferrite microstructure produced by the DET.

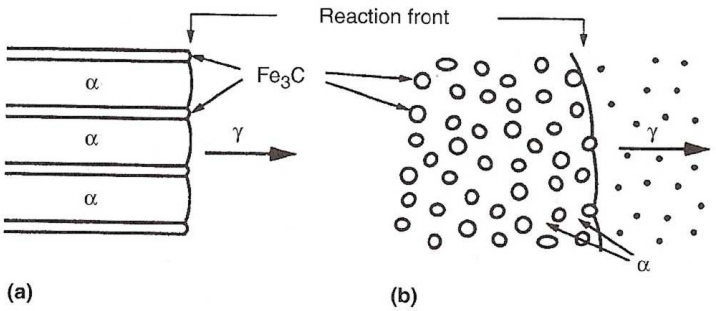

Figure 2.6: Schematics of interface growth fronts associated with the transformation of austenite to (a) pearlite and (b) dispersed cementite particles in ferrite (Verhoeven and Gibson 1998).

2.1.2 Ferritic Microstructures

2.1.2.1 Classification of Ferritic Microstructures

Ferritic microstructures that form in low carbon steels during continuous cooling or during isothermal holding at intermediate transformation temperatures have recently received considerable attention (Reynolds *et al.* 1988; Krauss 2005; Bhadeshia and Honeycombe 2006). Figure 2.7 shows the continuous cooling transformation (CCT) diagram for a low carbon High Strength Low Alloy (HSLA) steel where classifications of various morphologies of ferrite are shown.

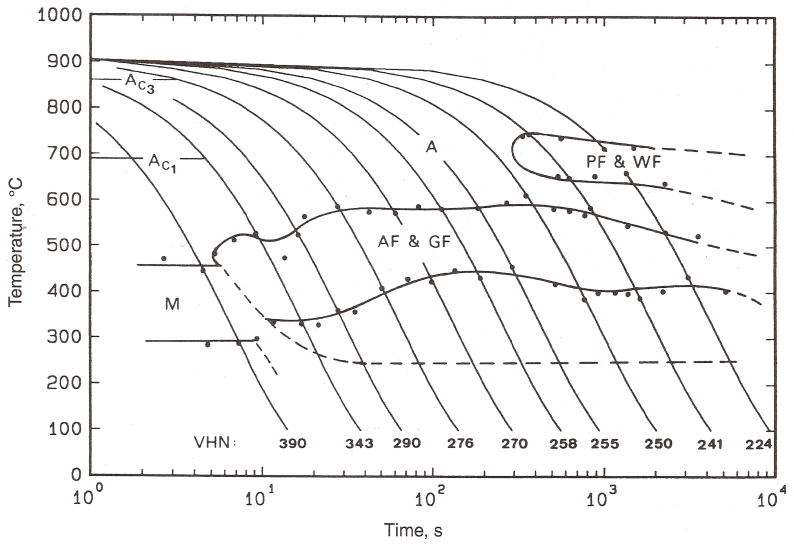

Figure 2.7: Continuous cooling transformation diagram for an HSLA steel containing 0.06%C, 1.45% Mn, 1.25% Cu, 0.97% Ni, 0.72% Cr and 0.42% Mo. PF, polygonal ferrite; WF, Widmanstätten ferrite; AF, acicular ferrite; GF, granular ferrite (Thompson *et al.* 1990).

Dubé *et al.* (1958) proposed a classification of the ferrite morphologies which occur as the austenite-ferrite transformation temperature is lowered (Figure 2.8). At a very low cooling rate, the grain boundary allotriomorphic crystals nucleate at the austenite grain boundaries and grow preferentially along them (Figure 2.8a). Some of these adjacent polygonal ferrite grains with similar orientations coalesce into one grain. As the cooling rate increases, Widmanstätten side plates start to appear. These plates advance into the interior of the austenite grain from the vicinity of its grain boundary. When the plates grow directly from the grain boundary, the ferrite is called primary Widmanstätten (Figure 2.8(b1)). However, it is called secondary Widmanstätten when the plates grow from grain boundary allotriomorphs (Figure 2.8(b2)). In addition, Widmanstätten "saw teeth" have a more triangular appearance and can also be nucleated either directly on the grain boundaries or on grain boundary allotriomorphs (Figure 2.8c). As the cooling rate is further increased, intragranular idiomorphs of equiaxed crystals, in addition to intragranular Widmanstätten plates (Figure 2.8e), could be nucleated within austenite grains (Figure 2.8d). When the supercooling is sufficiently large, acicular ferrite would be formed in addition to the Widmanstätten structure (Farrar and Harrison 1987; Barbaro *et al.* 1989).

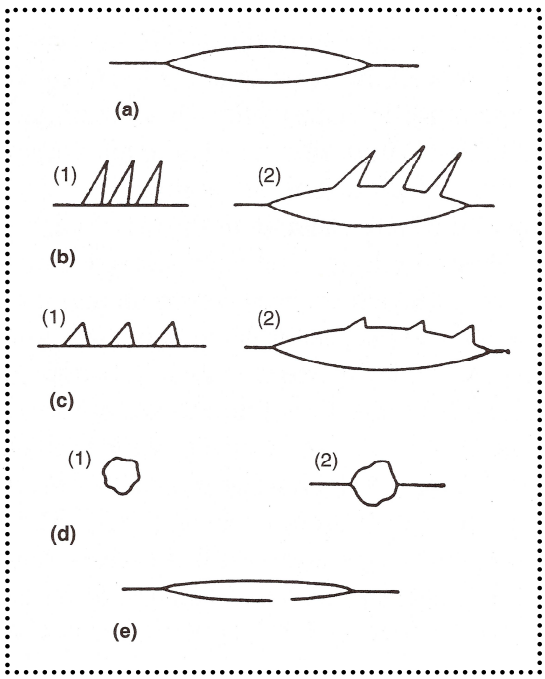

Figure 2.8: Schematic diagrams of ferrite morphologies according to the Dubé classification systems. The text describes the terms used for each morphology. (Dubé 1948; Aaronson 1962).

During nucleation, the allotriomorphic ferrite, which is the first morphology to appear over the whole range of composition and temperature (Bhadeshia and Honeycombe 2006), exhibit a preferred orientation relationship of the Young-Kurdjumov-Sachs (YKS) type (Young 1926; Kurdjumov and Sachs 1930) with one of the austenite grains, which is given as:

$$\{111\}_{\gamma} // \{110\}_{\alpha} \text{ and } <1\bar{1}0>_{\gamma} // <1\bar{1}1>_{\alpha}$$

When the ferrite is nucleated at the austenite grain boundary, it satisfies one of the available 24 variants of the YKS orientation relationship with one of the adjacent austenite grains. The other incoherent α-γ interface with a random orientation relationship grows faster than the boundary with the YKS relationship.

The formation and morphology of polygonal ferrite (PF), Widmanstätten ferrite (WF), massive ferrite (MF), and acicular ferrite (AF) are briefly described below.

2.1.2.1.1 Polygonal Ferrite

This ferritic microstructure, shown in Figure 2.9, forms at the highest austenite transformation temperature and slowest cooling rates in low carbon steels. The nucleation sites for polygonal ferrite are austenite grain boundaries and they grow to form equiaxed grains or shapes that minimise the surface energy. Growth of PF may be more anisotropic since growth may occur in preferred directions, such as along grain boundaries or into bands of high defect concentration. However, significant reduction in growth rates may be caused by planar arrays of particles at interfaces of polygonal ferrite (Aaronson and Domian 1966; Aaronson *et al.* 2004). The size of polygonal ferrite decreases with decreasing transformation temperature and increasing cooling rate (Llewellyn and Hudd 1998).

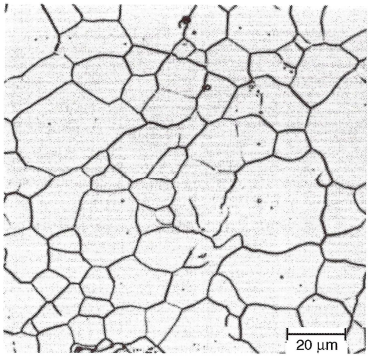

Figure 2.9: Polygonal ferrite microstructure formed in ultra low carbon steel (Totten 2007).

2.1.2.1.2 Widmanstätten Ferrite

Widmanstätten ferrite has a coarse, elongated morphology and occurs in the form of side plates or laths. WF forms at faster cooling rates and at temperatures just below those at which polygonal ferrite forms. The elongated shape and surface relief associated with WF formation are explained by the movement of semi-coherent interfaces by small steps in the interface (ledge mechanism of growth) (Aaronson *et al.* 1970; Spanos *et al.* 1991; Aaronson 1993) or by a displacive transformation mechanism (Bhadeshia 1981). The lath ferrite, which grows directly from the austenite grain boundaries, is referred to as primary Widmanstätten while the secondary Widmanstätten nucleates on the pre-existing allotriomorphic ferrite present in the microstructure (as discussed in Section 2.1.2.1). This ferrite morphology is not common in relatively fine grained (i.e. < 30µm) low carbon steels. A typical microstructure of secondary WF is shown in Figure 2.10a with Figure 2.10b showing a schematic illustration of such a microstructure evolution where the growth of the plates occurs on only one side of the original allotriomorphic ferrite.

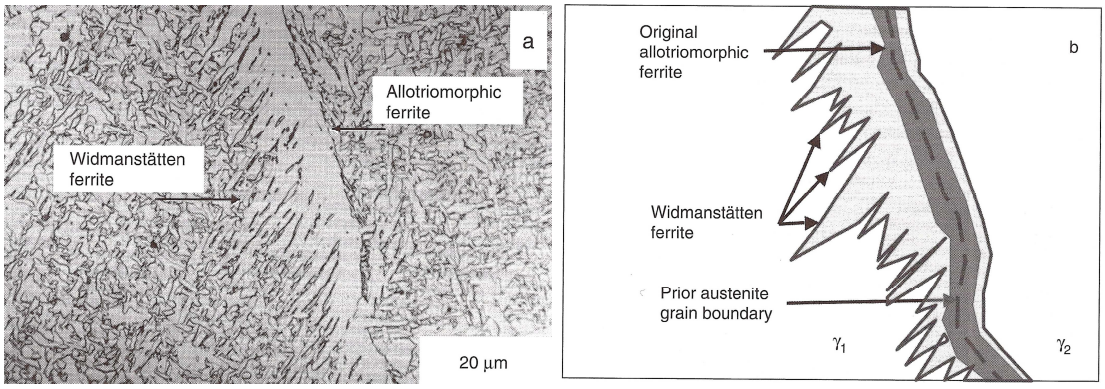

Figure 2.10: (a) Optical micrograph showing secondary Widmanstätten ferrite microstructure in an Fe-C-Mn steel weld obtained through continuous cooling, (b) Schematic illustration showing possible mechanism for the formation of Widmanstätten ferrite microstructure (Totten 2007).

2.1.2.1.3 Massive Ferrite

With rapid cooling of very low carbon steels from an austenitic microstructure to a ferritic microstructure, coarse ferrite grains are produced which are referred to as massive ferrite (Massalski 1970; Wilson 1994). The cooling rate must be high enough to prevent the partitioning of carbon between the austenite and ferrite. In this

transformation, there is no composition change, just the crystal structure changes from FCC to BCC, with short-range atom transfer across austenite/ferrite interfaces.

Massive ferrite, shown in Figure 2.11, differs from polygonal ferrite in that the grain boundaries are irregular and the grains show evidence of a substructure. This type of ferrite contains high dislocation densities and it has excellent combinations of strength and ductility in continuously cooled low carbon steels.

Figure 2.11: Massive ferrite formed in ultra low carbon steel containing 0.003% C and 3.00% Mn cooled at 50^{o}C/s (Krauss 2005).

2.1.2.1.4 Acicular Ferrite

This type of ferrite forms at high cooling rates in the intermediate temperature transformation range. It has a lath or plate structure with length, width and thickness normally less than about 36, 6 and 3 μm, respectively (Wu 2006). Figure 2.12a shows the formation of AF in a weld deposit of low carbon steel, with Figure 2.12b illustrating the three dimensional lath structure (Wu *et al.* 2004).

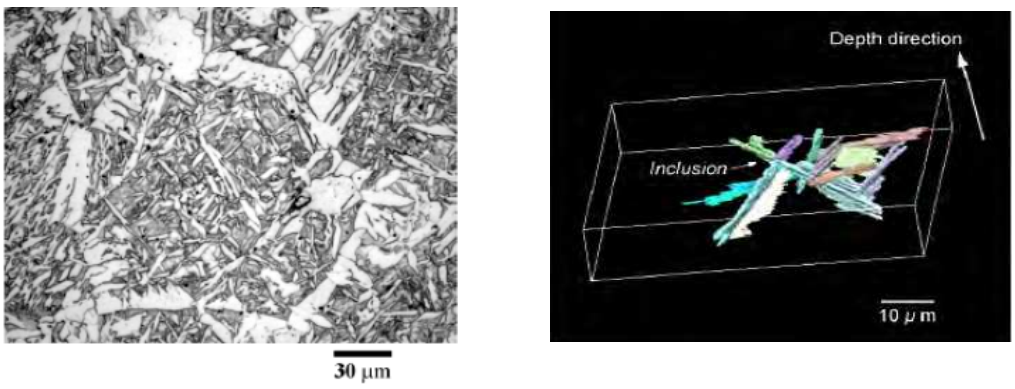

Figure 2.12: (a) Two dimensional and (b) three dimensional structure of AF in a weld metal zone of steel, showing the AF with a lath-type structure (Wu *et al.* 2004).

The single plates of AF are nucleated heterogeneously on non metallic inclusions which in turn stimulates other plates by an autocatalytic nucleation process, thus causing plates to radiate in different directions from the point of nucleation, as illustrated in Figure 2.13 (Ricks *et al.* 1982) . In addition, crystallographic analysis of AF plates show that highly misoriented plates may nucleate on a single inclusion (Gourgues *et al.* 2000). These inclusions show good lattice matching with AF and promote its nucleation (Bhadeshia and Honeycombe 2006). A coarse austenite grain size promotes the decomposition of austenite to AF as shown in Figure 2.13.

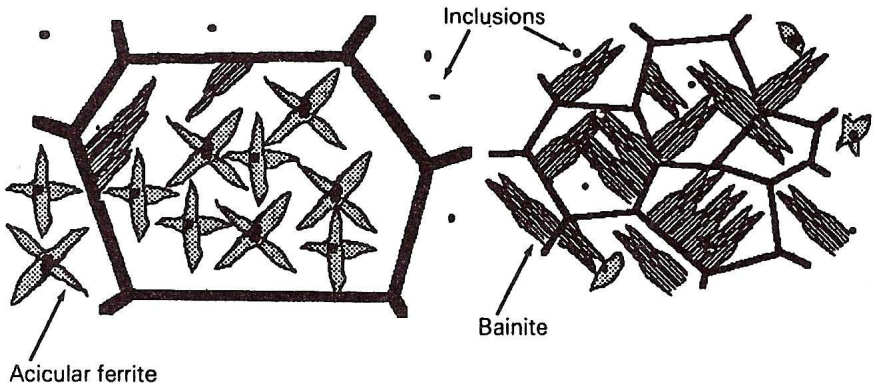

Figure 2.13: Illustration showing the effect of austenite grain size on the final transformed structure (Bhadeshia and Honeycombe 2006).

There are similarities of the transformation mechanisms of both AF and bainite. While the AF nucleates at point sites and grows in several directions in the form of plates, bainite nucleates at austenite grain boundary and grows in the form of parallel plates. As a result of this difference in nucleation mechanism, the lath morphology in AF differs from that of bainite. The heating rate and the chemical composition of the steel also have a significant effect on the formation of both AF and bainite.

2.1.2.2 Strengthening Mechanisms in Ferritic Microstructures

Strength is one of the fundamental properties of steels, and there is a significant commercial benefit in producing high strength steel by reducing the cost per unit strength as a result of material saving.

Strengthening of a metal, which represents the increase in the resistance to yielding or plastic deformation, can be obtained by changes in microstructure that impede the motion of dislocations (Cottrell 1964; Courtney 1990; Ashby 1970). Based on the type of obstacles that hinder the motion of dislocation and hence increase the

strength, the yield strength (σ_y) of steels is usually expressed in the form of generalised equation where the contribution of all the strengthening mechanisms are added as follows (Pickering 1978):

$$\sigma_y = \sigma_o + \sigma_{SS} + \sigma_P + \sigma_{GB} + \sigma_D + \sigma_T \qquad (2.1)$$

where σ_o is the lattice friction, σ_{SS} is the solid solution strengthening, σ_P is the precipitation strengthening, σ_{GB} is the grain boundary strengthening, σ_D is the dislocation strengthening and σ_T is the texture strengthening. The mechanisms involved in each of them are briefly discussed in the following sections with particular attention being focused upon their effect on the ferritic microstructure.

2.1.2.2.1 Lattice Friction Stress

Lattice friction stress is also termed Peierls-Nabarro stress as it was first described by Peierls (1940) and Nabarro (1947). It represents the stress required to move free dislocations (i.e. with no obstacles) along the slip planes through a crystal. It can be regarded as the yield stress of a pure single crystal. This stress is particularly sensitive to temperature. It is generally recognised that the temperature-dependence of this stress will arise from the thermal broadening of dislocations and from the thermally activated jump of sections of the dislocations from one energy minimum to the next (Heslop and Petch 1956).

2.1.2.2.2 Solid Solution Strengthening

The introduction of substitutional and interstitial solutes increase the yield strength as shown in Figure 2.14. The substitutional solute atoms, typically P, Mn, Si, Ti and Nb in low carbon steels, replace the Fe atoms in the Fe crystal structure causing a symmetrical distortion in the lattice (Fletcher 1979). This leads to the appearance of elastic deformation fields which retard the movement of dislocations in slip planes under the action of applied stresses and, hence, the strengthening effect. The strengthening achieved by substitutional solute atoms depends mainly on the size difference between the solute and solvent atoms, being high when the difference is large.

Interstitial solutes such as C and N, on the other hand, introduce an asymmetric or tetragonal lattice distortion which produces strengthening effects that are 10 – 100 times that of substitutional elements (Leslie 1972; Pickering 1978; Ginzburg 1989).

In the case of IF steel, the contribution to strength due to the presence of C and N in solid solution is non-existent since they are almost completely stabilised as precipitates (i.e. TiN, TiC, NbC...etc).

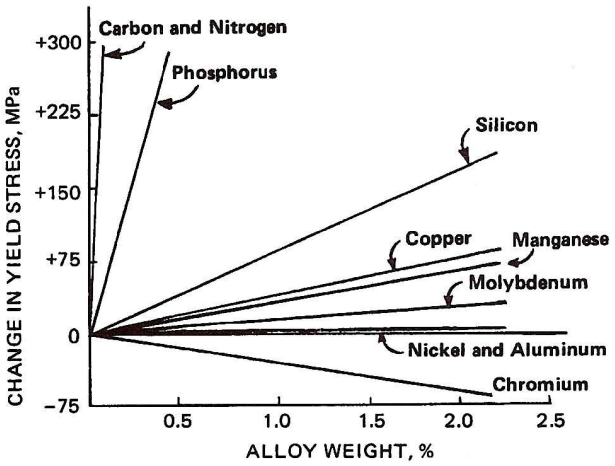

Figure 2.14: Solid solution strengthening of ferrite as a function of alloying element in low carbon steels (Pickering 1977).

In addition to the size effect, the difference in the elastic modulus and the electro-negativity of the solvent and solute are other mechanisms of solid solution strengthening (Leslie 1972; Dieter 1986; Courtney 1990). However, the contribution of these strengthening mechanisms is very limited (Leslie 1972).

2.1.2.2.3 Precipitation (Dispersion) Strengthening

Precipitation within a crystalline lattice can promote strengthening by impeding the motion of dislocations. This resistance is primarily dependant on the shape, size, distribution and volume fraction of the precipitate particles, and their coherency or misfit with the matrix. Based on these factors, dislocations may shear precipitates (Friedel mechanism) or avoid precipitates by looping/extruding and bypassing them (Orowan mechanism). Figure 2.15a shows the obstacles that particles present to dislocation motion as first described by Orowan (1948) where this mechanism is predominant for incoherent, semi-coherent and hard particles (Gladman *et al.* 1977; Meyers and Chawla 1984). On the other hand, Figure 2.15b shows a dislocation intersecting second phase particles (particle cutting) where the interfacial area of the particle/matrix is increased (Gladman 1997). The stress required for plastic deformation increases with decreasing spacing of particles. The strong carbide, nitride and carbonitride forming elements such as Ti, Nb, V and Mo can have a remarkable effect on strength.

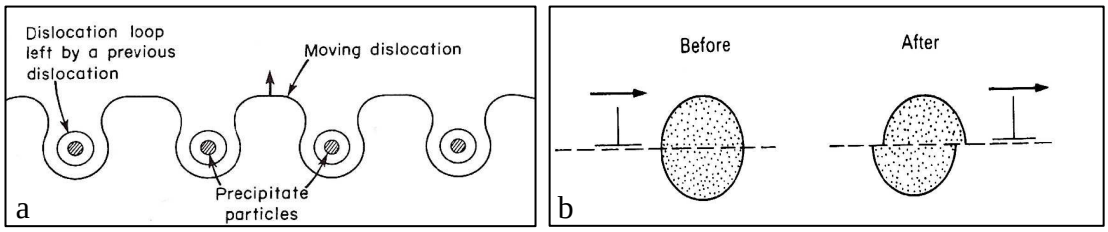

Figure 2.15: Interaction between dislocations and precipitate particles. (a) Dislocations loop around the particles (Orowan) or may climb around them (not shown) (Reed-Hill and Abbaschian 1994). (b) Dislocations glide through the slip plane and shear the particles (Friedel) (Gladman 1997)

2.1.2.2.4 Grain Boundary Strengthening

The refinement of the grain size of ferrite provides one of the most important strengthening routes in the heat treatment of steel. The first scientific analysis of the relationship between grain size and strength was described by the equation developed by Hall (1951), based on experimental observations, and greatly extended by Petch (1953), based on both experimental and theoretical approaches. The Hall-Petch equation for the dependence of stress on grain size, d, is:

$$\sigma_y = \sigma_o + k\, d^{-½} \qquad (2.2)$$

where σ_o is the lattice friction and k is a constant which represents the difficulty required to unlock or generate dislocations in neighbouring grains. Figure 2.16 shows Hall-Petch plots of lower yield strength, flow stresses at various strains, and ductile fracture stress as a function of ferrite grain size in low carbon steels. This figure shows that the slope is steepest for the lower yield strength compared with higher strains where grain boundaries decrease in importance as the dislocation cell structure develops within ferrite grains and contribute to strengthening. Fine grain sizes also significantly increase ductile fracture stresses since grain boundaries increase the resistance to crack propagation.

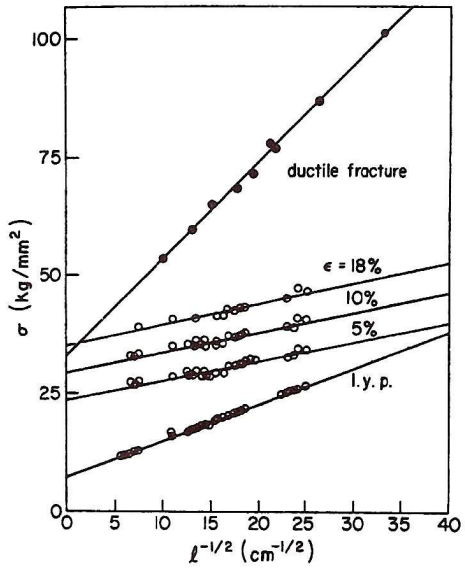

Figure 2.16: Lower yield strength, flow stresses at various strains, and fracture stress as a function of grain size in low carbon steels (Armstrong 1983).

In addition to their role in precipitation strengthening, microalloying elements (MAE) such as Ti, V and Nb are found to be very effective grain refiners (Pickering 1978; Cohen and Hansen 1986). It is important to note that grain refinement is the desirable strengthening mechanism since it is the mechanism that increases both strength and toughness as shown in Figure 2.17. This figure compares the effects of various strengthening mechanisms of low carbon steels on the impact transition temperatures. It can be seen that while dislocation strengthening, precipitation and pearlite content of ferritic microstructure increase strength, they also raise the transition temperature except for grain refinement, where the strength increases with a decrease in the transition temperature.

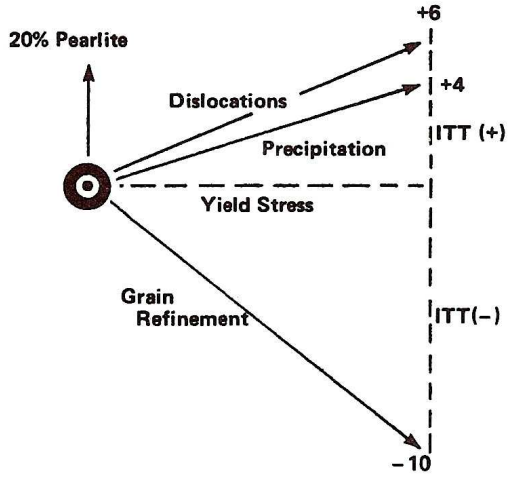

Figure 2.17: Change in impact-transition-temperature (ITT) produced by 15 MPa increases in strength by various strengthening mechanisms (Pickering 1977).

2.1.2.2.5 Dislocation Strengthening

Dislocation strengthening, or work hardening, is an important process in steel and can be introduced by cold working, quenching strain, differences in thermal expansion between particles and the matrix, volume changes accompanying precipitation and strains produced during low temperature transformations (Pickering 1978). It is determined mainly by the interaction of dislocations and is associated with the structural changes that impede the movement of dislocations.

The presence of dislocations generates internal stress fields. Extra work needs to be done to move a dislocation through such internal stress fields of other dislocations. Michalak (1965) and Kuhlmann-Wilsdorf (1984) have theoretically evaluated work (strain) hardening and have presented the following equation to characterise it:

$$\tau_i = \alpha G \boldsymbol{b} \rho^{½} \qquad (2.3)$$

where τ_i is the internal stress, α is a constant depending upon crystal structure, G is the shear modulus, $\boldsymbol{b}$ is the dislocation Burgers vector and ρ is the dislocation density.

Whereas work hardening or dislocation strengthening can result in very high levels of strength in steels, these are achieved at the expense of toughness and ductility. For this reason, little use is made of this method of strengthening (Smallman and Bishop 1999; Bhadeshia and Honeycombe 2006).

2.1.2.2.6 Texture Strengthening

The flow stress of a single crystal varies with orientation and, hence, materials with a preferred orientation will show plastic anisotropy, depending on the strength of the texture. In fact, the presence of texture is known to strongly influence the deep drawability and introduces anisotropy in the yield strength of the sheet steels.

Specific reference to this important aspect of texture effects will be made in Section 2.1.4.1 when considering the use of textures in relation to through-thickness strength and plastic anisotropy in formable sheet steels.

2.1.3 Low Carbon Cold Rolled and Annealed Sheet Steel

Many applications for steel require thin sheet or strip with thicknesses in the range 0.3 - 2 mm. Such material cannot be produced by hot rolling due to heat loss, scaling (oxidation) and dimensional control. Many applications for thin strip, such as car body applications, require that the steel has a very good formability, sufficient strength, good weldability, corrosion resistance, good surface quality, etc. Within the family of low carbon steels, which have been developed for applications requiring these properties, interstitial free steels and high-strength low-alloy steels will be discussed in the following Sections.

2.1.3.1 Interstitial Free (IF) Steels

Interstitial free steels are described as steels with an extra-low carbon and nitrogen content making it virtually free of interstitial atoms. Residual carbon and nitrogen in IF steel are combined with elements that have a strong affinity for them, such as niobium or titanium which lead to the formation of relatively coarse nitrides (TiN), carbonitrides (NbCN/TiCN), carbosulfides $(Ti,Nb)_4C_2S_2$ and carbides (TiC/NbC) (Gladman 1997; Raabe and Hantcherli 2005). This process of stabilisation of the interstitial solutes imparts excellent formability to IF steels, enabling them to be extensively used in automotive applications (Krauss *et al.* 1991; Tsunoyama 1998).

Table 2.1 shows typical composition ranges of the elements in IF steels. Based upon the chemistry, IF steels are typically classified into single stabilized (Ti-IF) and (Nb-IF) or as dual stabilized (Ti-Nb IF).

Table 2.1: Composition ranges (in wt %) of IF steels (Krauss 2005).

C	Si	Mn	P	Al	N	Nb	Ti	S
0.002-0.008	0.01-0.03	0.10-0.34	0.01-0.02	0.03-0.07	0.001-0.005	0.005-0.040	0.01-0.11	0.004-0.01

The Fe-rich side of the Fe-C diagram is shown in Figure 2.18. The low carbon contents of IF steels are well below those of steels which form pearlite after hot rolling. Figure 2.18 also shows that A_1 and A_3 temperatures of IF steels are higher than those of higher carbon steels where the addition of microalloying elements in solid solution (i.e. Ti, Nb or V) will further increase these temperatures as ferrite stabilisers. This increased range of ferrite stability affects temperatures used for

finish hot rolling and for annealing after cold rolling. It can also be seen that with decreasing temperature the solubility of carbon in ferrite decreases and it is negligible at room temperature.

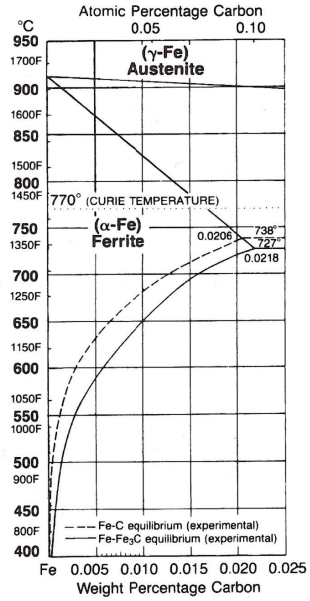

Figure 2.18: Fe-rich side of Fe-C diagram, showing the extent of the ferrite phase field and the decrease of carbon solubility with decreasing temperature (Krauss 2005).

It is important to point out that the cold rolled and annealed IF steels have very strong <111>//ND recrystallisation textures and high r_m (defined in Section 2.1.4.1) when titanium and niobium levels are near or just in excess of that required for the stoichiometric combination with carbon and nitrogen to form the carbo-nitrides (Hudd 1987). Figure 2.19 shows the increase in r_m value when the Ti and Nb content reach the stoichiometric value.

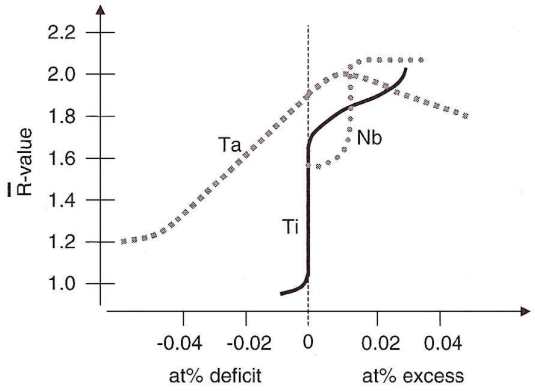

Figure 2.19: Influence of Ti, Ta and Nb content on the r_m value. The graph shows the deficit/excess in at % of the alloying elements relative to C+N content. (Hutchinson 1994)

The main problem with IF steel is the low strength, though this can be raised by generating a fine grain size. However, controlling the grain size is very difficult especially after hot rolling. The rolling schedule must be designed in such a way that during hot rolling some carbo-nitrites can precipitate and hinder an excessive austenite grain growth. Also, the last hot rolling passes should typically be carried out with large reductions at relatively low rolling temperature since this will lead to a refinement of ferrite grain size (Verlinden *et al.* 2007). In addition to the grain refinement, this type of steel is sometimes re-phosphorised to increase the strength level, and may be re-siliconised to further increase the strength (Gladman 1997).

2.1.3.2 High Strength Low Alloy (HSLA) Steels

High Strength Low Alloy steels are described as controlled-rolled microalloyed steels and derive their name from their higher strengths, relative to plain carbon steels with ferrite-pearlite microstructures, and the extremely small amount of alloying elements compared to the main commercial alloyed engineering steels designed to be hardened by martensite. HSLA steels usually contain low carbon contents (0.03-0.25%), and give improved strength to weight ratios with high toughness and good weldability.

HSLA steels are precipitation strengthened/ grain refined steel where the small amount of microalloying elements (i.e. V, Nb and Ti) combined with controlled rolling, controlled cooling, and with an optimum utilisation of microalloying additions produce a fine ferritic structure in the final product (Kozasu 1992; Gladman 1997). It has been noted (see Section 2.1.2.2.4) that only grain refinement can increase both strength and toughness and decrease the ductile-brittle transition temperature. Figure 2.20 shows the variation of the yield strength as a function of grain size for both mild steel and HSLA. It shows also that HSLA steels gain extra strength, ΔY, as a function of the precipitation strengthening associated with microalloying elements (Cohen and Hansen 1979). HSLA steels are used in many applications including car body components, structural sections and welded beams.

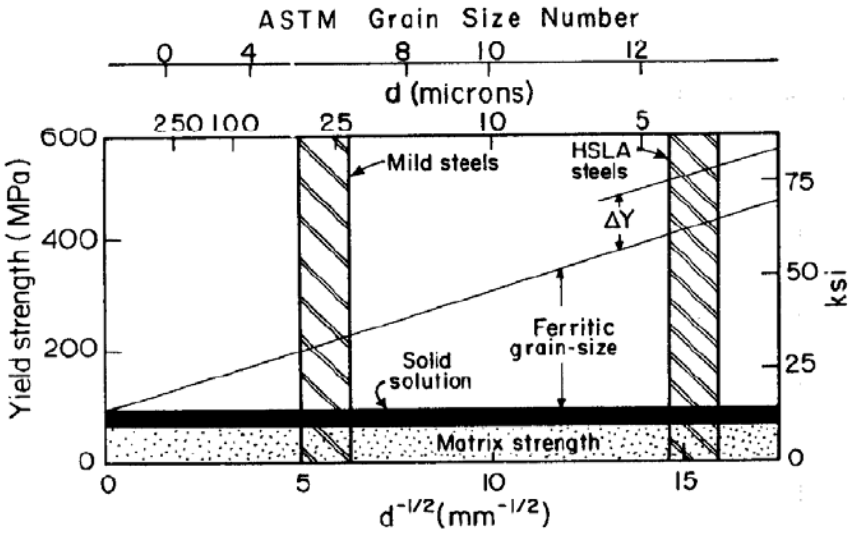

Figure 2.20: The effect of the grain size and other strengthening mechanisms on the yield strength in low-carbon steels (Cohen and Hansen 1979)

2.1.4 Properties of Low Carbon Steel

2.1.4.1 Formability

Low carbon steel sheets used for car body applications, for example, are subjected to a variety of forming operations, including deep drawing. This requires that the material should flow easily in all directions in the plane of the sheet and resist local thinning in the side walls during elongation. The anisotropy of a material has a marked influence on the distribution of strains that can be obtained during deep drawing.

The criterion for plastic anisotropy in the context of drawability is usually given by the ratio of the true strains in the width (ε_w) and thickness (ε_t) directions of a tensile test (the Lankford value, r) (Lankford *et al.* 1950) as follow:

$$r = \frac{\varepsilon_w}{\varepsilon_t} \tag{2.4}$$

It is clear that deep-drawing steels require a high r-value (r > 1) to minimise the local reduction of the strip thickness during the forming operation. However, the r-value is conventionally not constant over the various directions within the strip plane, leading to planar anisotropy, Δr. This planar anisotropy is responsible for the unfavourable formation of ears during deep-drawing (Humphreys and Hatherly 2004). The planar anisotropy can be described by:

$$\Delta r = \frac{r_0 + r_{90} - 2r_{45}}{2} \qquad (2.5)$$

where subscripts stand for the angle between the tensile specimen axis and the rolling direction of the sheet. A planar anisotropy of $\Delta r > 0$ leads to the formation of ears in the rolling direction and transverse to the rolling direction, whereas $\Delta r < 0$ leads to ears at 45^o to the rolling direction. A low planar anisotropy, $\Delta r \approx 0$, together with a high mean r-value, r_m, defined in Equation 2.6, yields an optimal deep-drawing performance (Llewellyn and Hudd 1998).

$$r_m = \frac{r_0 + 2r_{45} + r_{90}}{4} \qquad (2.6)$$

To meet the above-mentioned requirements a suitable chemical composition is crucial. The chemical composition of such steels is characterised by a low carbon and overall low alloying content (Hutchinson *et al.* 1990). Figure 2.21 shows the strong effect of very low carbon content on increasing r_m values. Severe cold work prior to annealing also promotes favourable textures and high r_m values, as shown in Figure 2.22. Both of these curves demonstrate the very positive effect of low C on r_m.

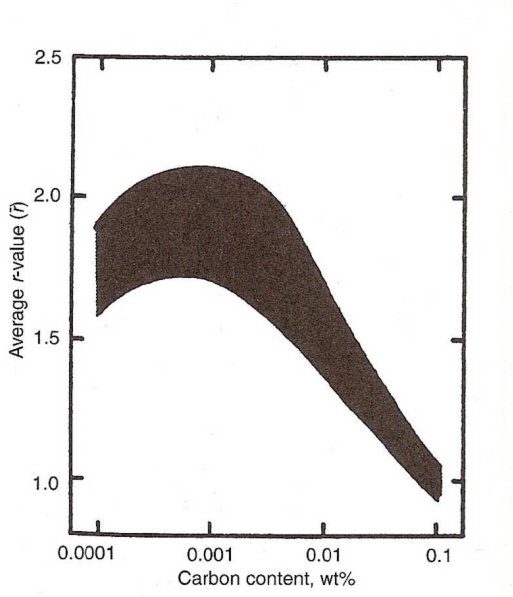

Figure 2.21: Effect of steel carbon content on r_m values (Hutchinson *et al.* 1990).

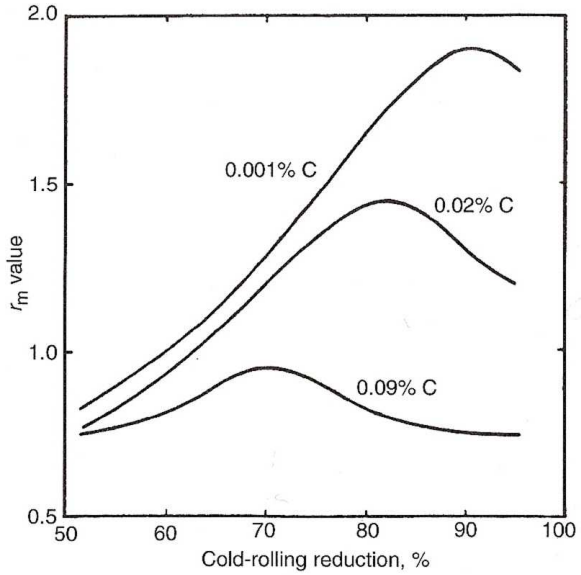

Figure 2.22: Effect of steel carbon content and cold reduction on r_m values (Fukuda 1967).

In fact, the high r_m values and, hence, the improved drawability are associated with the formation of γ-fibre (ND // <111>) recrystallisation texture which is produced after hot deformation, cold rolling and annealing (Hutchinson and Ushioda 1984; Hutchinson 1984; Satoh *et al.* 1986). Figure 2.23 shows that the higher the volume fraction of {111} oriented grains, the higher is the r-value. Moreover, the increase of carbon atoms in interstitial solid solution degrade the beneficial {111} recrystallisation texture and increase unfavourable {110} and {100} components (Krauss *et al.* 1991).

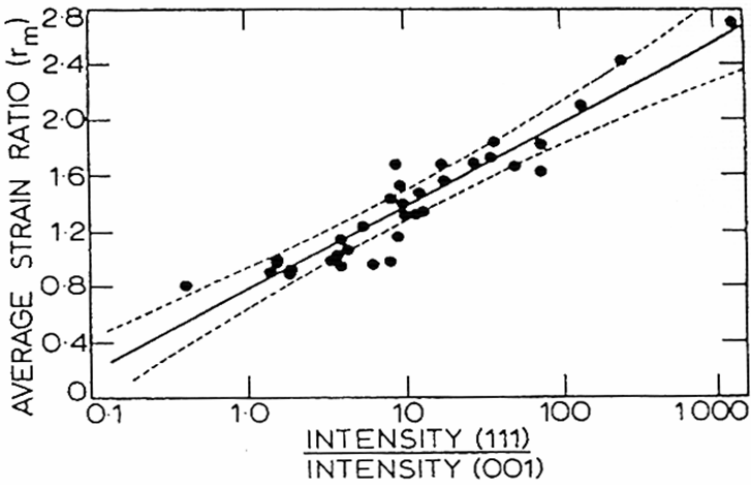

Figure 2.23: Influence of Crystallographic Texture on r_m Values (Held 1965).

2.1.4.2 Ductility and Strength

Changing the processing and chemistry of low carbon steels produces different mechanical properties. In addition, the different microstructural morphologies of these types of steels (i. e. different ferrite morphologies) have an important influence on the mechanical properties due to the difference in the nature of the internal microstructure in terms of dislocation density, supersaturation of solute atoms and lattice distortion. For example, polygonal ferrite exhibits a high ductility, low strength and low hardness since this ferrite morphology has a low dislocation density and a low supersaturation of solute atoms.

Depending on their application, steels have been developed with different values of strength and ductility as shown in Figure 2.24. IF steels, for example, usually have high ductility values of more than 45% total tensile elongation. However, they show considerably lower values of yield strength compared to HSLA, dual phase and TRIP steels. Yield strengths for IF steels typically range between 140 and 180 MPa and tensile strengths range between 290 and 340 MPa whereas the tensile strength for HSLA steels can reach up to 700 MPa (Krauss 2005).

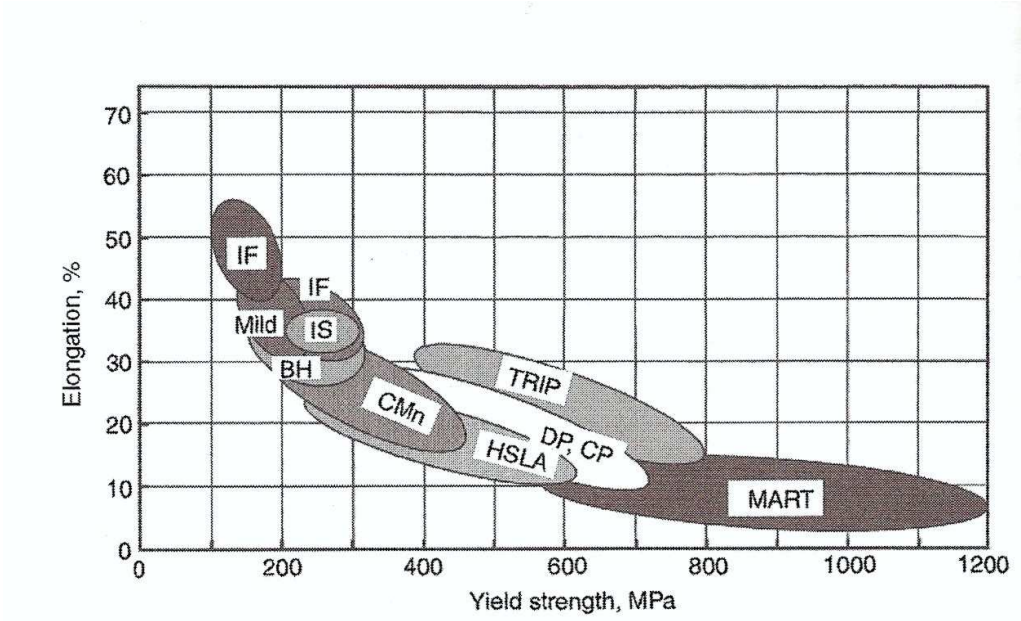

Figure 2.24: Ranges of elongation and yield strength combination for various types of low-carbon steels (Krauss 2005). BH, bake-hardening; CMn, carbon-manganese; CP, complex phase; DP, dual-phase; HSLA, high-strength low-alloy steel; IS, isotropic steels; MART, martensitic; TRIP, transformation-induced plasticity.

2.2 The Deformed State

Many metals need to undergo plastic deformation (i.e. rolling, drawing, forging, etc.) to generate useful final products. In this study, attention will be given to the cold rolling process where the metal is passed between counter-rotating rolls. Cold rolling is carried out below ~0.3 T_m, where T_m is the absolute melting point of the metal. This process is widely used to make sheets and strips with superior surface finish and dimensional tolerance (Llewellyn and Hudd 1998)

During deformation, the internal structure of a metal changes in several ways; the grains change their shape, total grain boundary area increases, an internal substructure forms within each grain and point defects are generated. These structural changes are associated with the formation and accumulation of dislocations (Humphreys and Hatherly 2004).

Most of the energy expended in cold deformation appears in the form of heat, with only a very small amount stored in the metal as strain energy associated with various lattice defects created by the deformation (Dieter 1986). The amount of energy retained depends on the deformation process and a number of other variables, for examples, composition of the metal as well as the rate and temperature of deformation (Reed-Hill and Abbaschian 1994).

In cubic metals, there are two principle modes of deformation: slip and twinning. If the stacking fault energy is relatively high as in the case of low carbon steels, plastic deformation at normal conditions is only due to crystallographic slip (i.e. slip on planes and along directions fixed with respect to the crystal axis). Typical slip systems for BCC materials are on the {110}, {112} or {123} planes in the close packed <111> directions (Taylor and Elam 1926; Hosford 2005).

During deformation, each grain tends to change its orientation with respect to the direction of the applied deformation which leads to a preferred orientation or texture as deformation proceeds. However, these changes in grains' orientation are not uniformly distributed since each grain of an aggregate is subjected to the constraints exercised by neighbour grains, each of which is deforming in a unique manner, thereby generating microstructural heterogeneities in the form of deformation bands, transition bands and shear bands (Humphreys and Hatherly 2004). Figure 2.25 shows the hierarchy of microstructure in polycrystalline metal deformed by slip. At the

smaller scale, dislocation cells, which comprise the smallest volume elements, are surrounded by single walled Dense Dislocation Walls (DDW) at low strain or double walled Micro Bands (MB) at medium strain (Figure 2.26a). At high strain, the cell blocks become elongated and surrounded by lamellar dislocation boundaries (LB) which replaces the DDW and MB structure as shown in Figure 2.26b (Doherty *et al.* 1997).

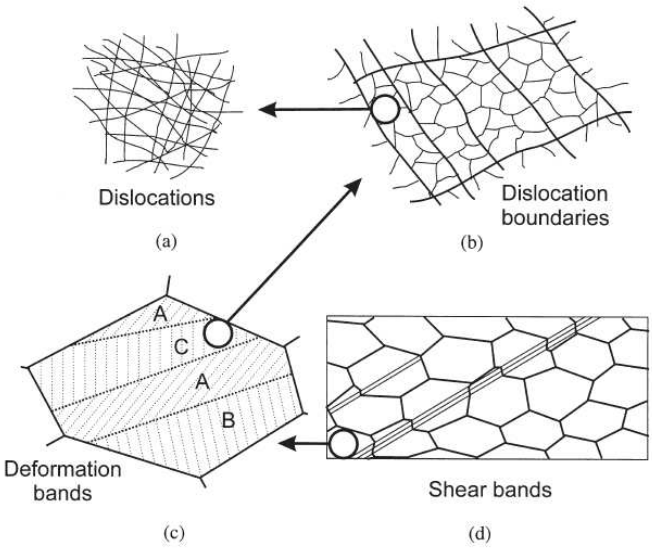

Figure 2.25: The hierarchy of microstructure in a polycrystalline metal deforming by slip (Humphreys and Hatherly 2004). The various features are shown at increasing scale: (a) Dislocations, (b) Dislocation boundaries, (c) Deformation and transition bands within a grain, (d) Specimen and grain-scale shear bands.

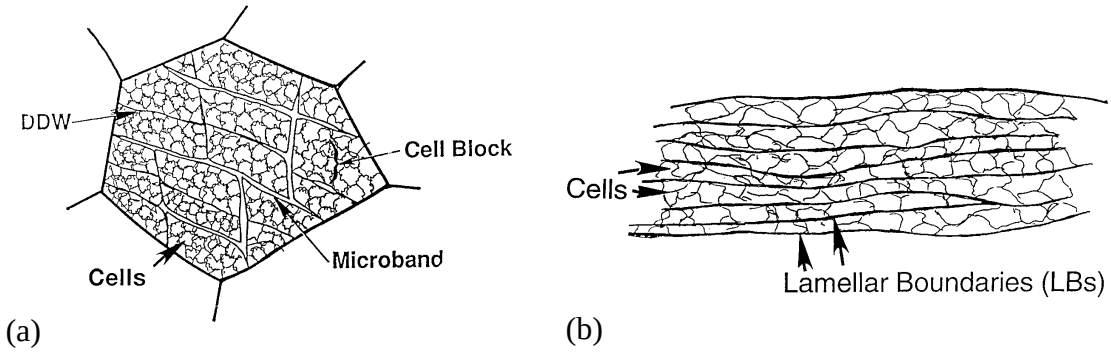

Figure 2.26: Schematic of grain subdivision at (a) small and (b) large strains (Doherty *et al.* 1997).

During the deformation of low carbon steels, an inhomogeneous distribution of the dislocations occurs (i.e. formation of cell and subgrain structures) as a result of dynamic recovery. The size of these cells/subgrains decreases with increasing strain, independently of the mode of deformation, as shown in Figure 2.27 for low carbon steel and iron (Langford and Cohen 1969; Gil Sevillano 1980). However, the cell/subgrain misorientations increase with strain (Humphreys and Hatherly 2004). In addition, it is important to mention that both the size and misorientation of the cell/subgrain structure is dependent on the grain orientation and, therefore, the stored energy will vary with different texture components. Dillamore *et al.* (1972) found that the stored energy of the α-fibre components (discussed in Section 2.4) of the rolling texture in deformed iron is of the following order: $E_{110} > E_{111} > E_{112} > E_{100}$ as can be deduced from Figure 2.28.

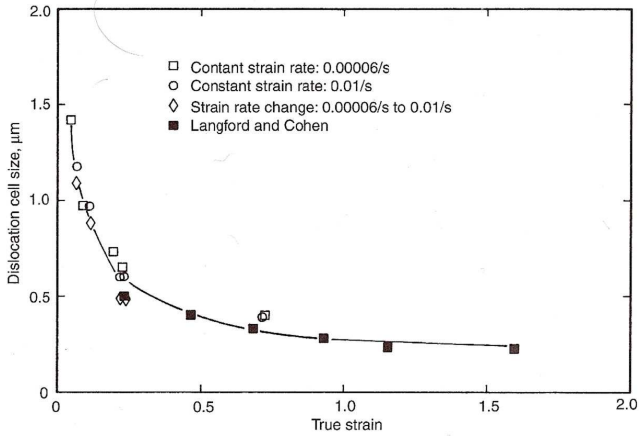

Figure 2.27: Dislocation cell size as a function of true strain in a low carbon steel and highly deformed iron (Langford and Cohen 1969; Gil Sevillano 1980).

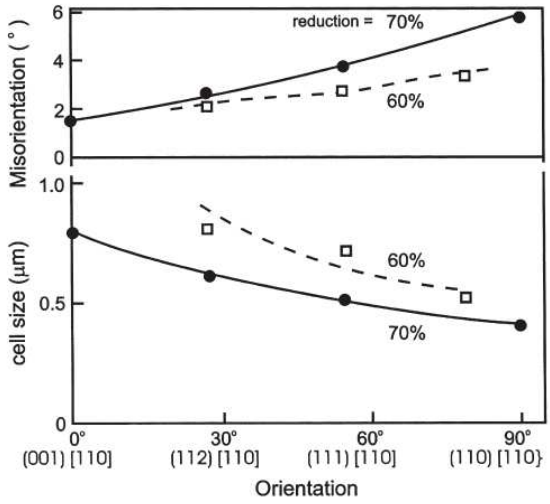

Figure 2.28: Variation of cell size and cell boundary misorientation in rolled iron as a function of local orientation (Dillamore *et al.* 1972).

During deformation in the presence of large second phase particles, large strain inhomogeneities are formed. The large particles hinder dislocation slip and, hence, accumulate dislocations in their surroundings where local lattice rotations, generally about <112> orientation axis, may occur creating a relatively high dislocation density zone with a large orientation gradient. Such zones are termed Particle Deformation Zones (PDZ) (Figure 2.29) and are affected by strain, particle size, particle shape, interface strength and the plastic properties of the matrix (Humphreys 1985). These zones are known to extend to a distance of about a particle diameter from the surface of the particle (Doherty *et al.* 1997).

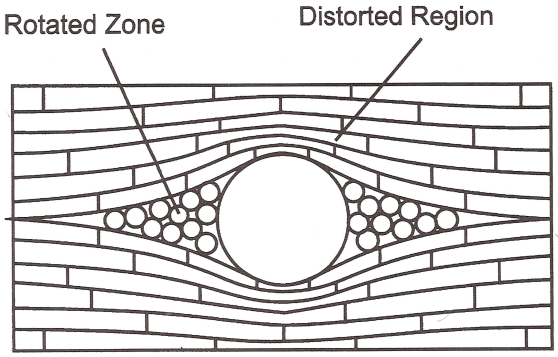

Figure 2.29: A deformation zone in a rolled polycrystal (Porter and Humphreys 1979)

2.3 The Annealing Process

When a metal is cold rolled, almost all of its physical and mechanical properties are changed (Reed-Hill and Abbaschian 1994). Cold rolling increases strength and hardness and it decreases ductility. So, most cold rolled sheet products are usually annealed in order to increase the ductility.

During annealing, the deformation microstructure may experience up to three stages of structural alteration: recovery, recrystallisation and grain growth (Doherty *et al.* 1997). Recovery includes all processes releasing stored energy that do not require the movement of high angle grain boundaries. Typically, it involves the annihilation and rearrangement of dislocations to lower the energy stored, for example by the formation of low-angle cell boundaries. On the other hand, recrystallisation is the migration of high angle grain boundaries driven by the stored energy (Doherty *et al.* 1988). Two types of recrystallisation can be identified (Doherty 1996):

- **Continuous recrystallisation**, where the recovered dislocation substructure keeps on coarsening. It is a homogeneous type–II Gibbs process.

- **Discontinuous recrystallisation** (the most common, and the case of interest in this study), where a new set of strain–free grains nucleate and grow, and thereby consume the deformed/recovered microstructure. It is a heterogeneous type–I Gibbs process.

The last stage of the annealing process is grain coarsening. It is the growth of the mean grain size driven by the reduction in grain boundary area (Novikov 1996; Martin *et al.* 1997). All of these three stages will be discussed in detail in this report.

2.3.1 Recovery

The recovery stage of annealing involves only partial restoration of properties characteristic of undeformed material prior to recrystallisation. Dislocations are annihilated and rearranged during this process to reduce the stored energy of the matrix as shown in Figure 2.30. In this process, significant subgrain growth can occur to lower the stored energy. However, the original grain boundaries will not be affected. By the end of this stage, a small amount of ductility will be regained without a significant reduction in strength.

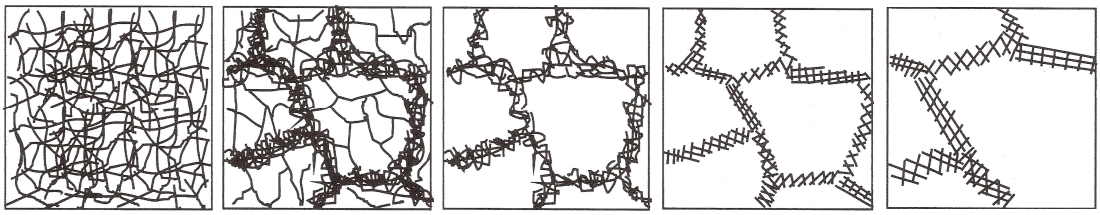

Figure 2.30: Various stages in recovery of plastically deformed materials: (a) dislocation tangles; (b) cell formation; (c) annihilation of dislocation within cells; (d) sub-grain formation, and (e) sub-grain growth. (Humphreys and Hatherly 2004)

The driving force for recovery is the reduction in stored energy due to a decrease in both point (vacancies) and line (dislocation) defects (Doherty *et al.* 1997). Both recovery and recrystallisation are competing processes as they have the same driving forces. If sufficient recovery is allowed to occur, there will be a lower driving force for recrystallisation which may result in a slower rate of recrystallisation (Beck 1954).

The rate of recovery is influenced by any feature in the microstructure that inhibits dislocation motion such as solute content or fine particles (Leslie *et al.* 1963). Also, Stacking Fault Energy (SFE) influences the rate of recovery since it influences the rate at which dislocation climb and cross slip occur. In addition, the rate of recovery is affected by the annealing temperature with high temperatures resulting in a higher rate of recovery (Humphreys and Hatherly 2004).

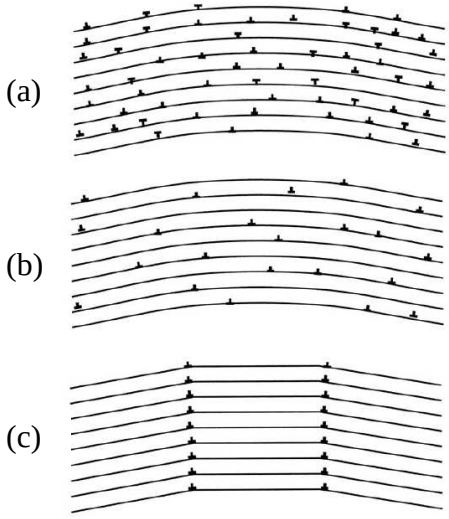

Figure 2.31: Realignment of edge dislocation during polygonisation (Humphreys and Hatherly 2004). (a) As deformed, (b) After dislocation annihilation, (c) Formation of tilt boundary.

One of the most important recovery processes which lead to a rearrangement of the dislocations, with a resultant lowering of the lattice strain energy, is polygonisation (Cahn 1949). This is the mechanism, illustrated schematically in Figure 2.31, whereby dislocations all of one sign align themselves into walls to form small-angle, polygonised, or sub-grain boundaries. The dislocation walls shown in Figure 2.31c are known as tilt boundaries. These are a particularly simple type of low angle grain boundary. The energy of a tilt boundary increases with increasing misorientation and the energy per dislocation decreases with increasing misorientation (Figure 2.32). Therefore there is a driving force to form fewer, more highly misoriented boundaries as recovery proceeds (Read 1953; Humphreys and Hatherly 2004).

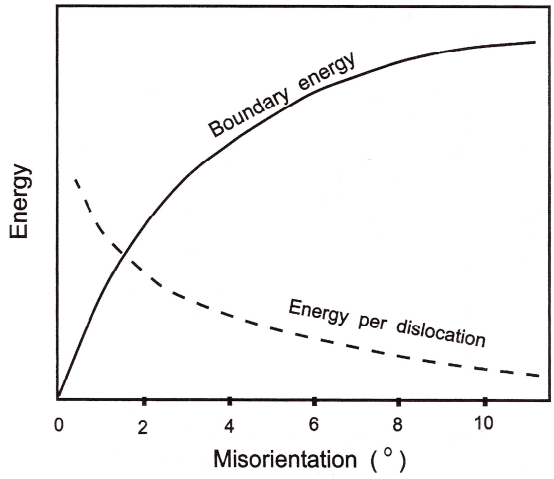

Figure 2.32: Effect of misorientation angle on the boundary energy and energy per dislocation in low-angle boundaries (Humphreys and Hatherly 2004).

2.3.2 Recrystallisation

In this stage, the deformed lattice is completely replaced by a new unstrained one by means of a nucleation and growth process (discontinuous recrystallisation) (Humphreys 2004), in which strain-free grains grow from nuclei formed in the deformed matrix. Recrystallisation after deformation is the only method for producing a completely new grain structure with a modified grain size, shape, and, in particular, orientation or texture. Compared to recovery, recrystallisation results in a more significant increase in ductility and decrease in strength.

2.3.2.1 The Laws of Recrystallisation

There are five rules which are generally obeyed when recrystallisation is considered and they summarise the behaviour during recrystallisation (Mehl 1948; Burke and Turnbull 1952). These rules are:

1. A minimum amount of deformation is necessary to initiate recrystallisation at high temperature.
2. The smaller the degree of deformation, the higher the temperature necessary to cause recrystallisation.
3. Increasing the annealing time decreases the temperature required for recrystallisation.
4. The recrystallised grain size depends mainly on the degree of deformation, being smaller for large amounts of deformation.
5. For a given amount of deformation the recrystallisation temperature will be increased by:

   - a large starting grain size.

   - a higher deformation temperature.

2.3.2.2 Factors Affecting Recrystallisation

Some of the main factors influencing the rate at which recrystallisation occur in materials are described briefly in the following (Humphreys and Hatherly 2004):

1. **The Level of Strain:** an increase in the degree of cold work increases the dislocation density which means an increase in the stored energy of the system.

Moreover, a high level of strain increases the differences in stored energy which provides favourable sites for recrystallisation and, hence, increases the rate of recrystallisation.

2. **Initial Texture:** recrystallisation of different texture components will occur at different rates since the stored energy distributes heterogeneously according to the different orientations of the texture components.

3. **Initial Grain Size:** this factor affects the rate of recrystallisation in several ways as follows:

   - A finer grain size provides a higher stored energy after low degrees of deformation.

   - An increase in grain size increases the formation of inhomogeneities such as shear bands which are sites for nucleation.

   - Grain boundaries are preferred sites for nucleation, and these sites are greater in number for a fine grained material.

   - Grain size affects the formation of deformation textures and hence the recrystallisation texture.

4. **Solutes:** the effect of solutes is to hinder recrystallisation. An increase in the solute in solid solution slows the recrystallisation rate.

5. **The Deformation Temperature and Strain Rate:** with high deformation temperature and low strain rate, the stored energy is reduced by dynamic recovery processes and hence the recrystallisation rate will be less.

6. **The Annealing Temperature:** The recrystallisation rate will be increased if the annealing temperature increases because it is a thermally activated process. To some extent, the Arrhenius plot determines the relationship between time and temperature in the recrystallisation process (Humphreys and Hatherly 2004). If the time for 50% recrystallisation ($t_{0.5}$) is considered to be a measure of the rate of recrystallisation, then the relationship will be as follows:

$$Rate = 1/t_{0.5} = C\exp\left(-\frac{Q}{RT}\right) \qquad (2.7)$$

Where C is a constant, Q is the activation energy (in J/mol), R is the gas constant and T is the temperature (in Kelvin). A plot of $\ln(t_{0.5})$ against $1/T$

gives a straight line with a slope which allows the activation energy to be determined.

7. **The Heating Rate:** if the heating rate is increased, the recovery will consume less stored energy which leads to an increase in the recrystallisation rate.

2.3.2.3 The Nucleation of Recrystallisation

The conventionally used term "nucleation" to describe the origin of recrystallisation is not appropriate because nucleation in the classic thermodynamic sense does not occur (Humphreys and Hatherly 2004). What happens is that these new grains grow from small regions, recovered subgrains or cells, that are already present in the deformed microstructure. One of the many important consequences of this idea is that the orientation of each new grain arises from the same orientation present in the deformed state (Doherty *et al.* 1997). However, the term "nucleation" will be used in this report as it is widely accepted.

Typical "nucleation" sites, all of which have high local misorientations, include (Doherty *et al.* 1997):

1. **Pre-existing high angle grain boundaries or triple junctions:** it has been reported that grain boundaries give rise to inhomogeneity of slip (Ashby 1970; Leffers 1981) which may lead to the operation of different slip systems, hence, increase local misorientation where recrystallisation is likely to originate in, with new grains of orientations which are not close to those of the parent grains (Beck and Sperry 1950). Some evidence of this mechanism has been reported by Hutchinson (1989) in iron bicrystals in which the orientations of the new grains were rotated by 30^{o} from the parent grains. Recrystallised grains of gamma-fibre orientations in low carbon steels seem to originate from prior grain boundaries of similar orientation grains (Akbari *et al.* 1997).

2. **Transition bands:** these bands are inside and between different parts of the grain that have undergone different lattice rotations due to different slip systems being activated. Therefore, they are regions of large orientation gradient which are ideal sites for recrystallisation (Inokuti and Doherty 1978). Recrystallisation at transition bands in iron was first reported by Hu (1963) and Walter and Koch (1963). This nucleation site is important in determining the recrystallisation texture as the recrystallised grains nucleated from these bands tend to have a

preferred orientation. However, transition band nucleation is not significant in low carbon steels (Humphreys and Hatherly 2004).

3. **Highly misoriented deformation zones around large particles:** large particles of diameter greater than approximately 1 μm (Hansen 1975; Humphreys 1977) can act as nucleation sites for recrystallisation through the Particle Stimulated Nucleation (PSN) mechanism. It has been found that large particles hinder dislocation slip and therefore accumulate dislocations in their surrounding where local lattice rotations of the matrix adjacent to the particle may occur to reduce the deformation incompatibilities. One important aspect of this mechanism is that the nucleation sites are well defined regions of the microstructure. So, the recrystallised grain size may be controlled by altering the alloy or process (Humphreys and Hatherly 2004). (discussed in details in Section 2.3.2.5).

4. **Shear bands:** they are highly misoriented regions characterised by an angle of about 35^{o} with respect to the rolling plane and parallel to the transverse direction. They can initiate at the grain scale and then develop to cross several grains. The occurrence of shear bands is influenced by the deformation condition, composition, texture and microstructure of the material (Dillamore *et al.* 1979; Liu *et al.* 1989; Humphreys and Hatherly 2004). Shear bands preferentially form in {111}<112> regions and can result in the creation of Goss oriented nuclei (Haratani *et al.* 1984).

The mechanisms of recrystallisation nucleation occurring in low carbon steels can be classified into three main mechanisms, which are described in the following Sections.

2.3.2.3.1 Strain Induced Boundary Migration (SIBM)

This mechanism takes into account the migration of a pre-existing high angle grain boundary, or the one generated during deformation, toward the interior of a more highly strained grain, as shown in Figure 2.33. The condition for the process to occur is the favourable energy-balance between the decrease of stored energy due to the elimination of defects caused by the passage of the boundary and the increase in total grain boundary surface due to bulging (Beck and Sperry 1950; Bailey 1960).

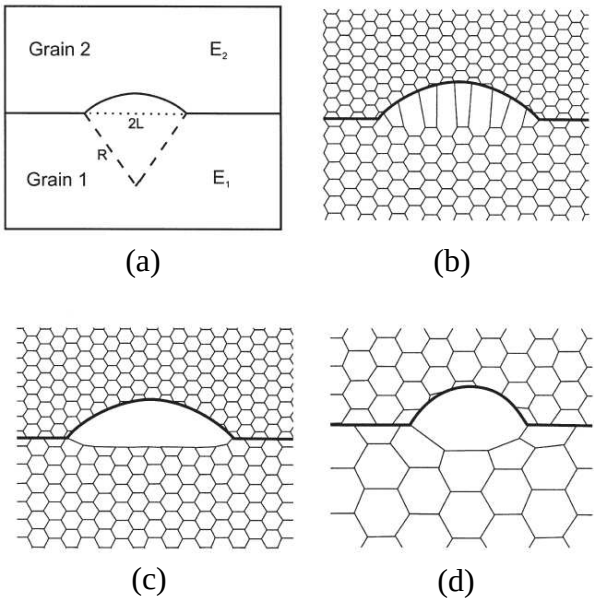

Figure 2.33: (a) SIBM of a boundary separating a grain of low stored energy (E1) from one of higher energy (E2), (b) dragging of the dislocation structure behind the migrating boundary, (c) the migrating boundary is free from the dislocation structure, (d) SIBM originating at a single large subgrain (Humphreys and Hatherly 2004).

The boundary of the bulge moves with an irregular curved shape (Reed-Hill and Abbaschian 1994), as can be seen from Figure 2.34. This can be explained by assuming that the rate of motion is a function of the substructure density in the metal. The boundary should move faster into those regions where the distortion has been greatest.

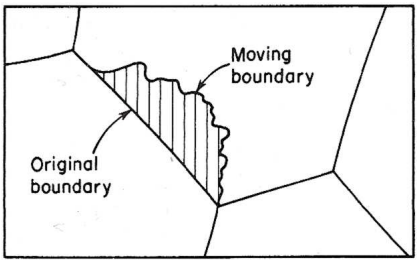

Figure 2.34: The irregular form of the moving boundary (Beck and Sperry 1950).

One of the interesting aspects of SIBM is that instead of the boundary of the moving grain lowering its surface energy through the movement, it may actually increase it by increasing its area. SIBM is particularly important after low strains and a characteristic feature of this mechanism is that the new grains have similar orientations to the old grains from which they have grown.

2.3.2.3.2 Nucleation by Subgrain Coalescence

Coalescence is an alternative mechanism, proposed by Hu (1962), by which neighbouring subgrains may merge into a critical embryo, leading to disappearance of sub-boundaries (decreasing the stored energy) and changing the orientation differences between a group that went through coalescence and its neighbouring subgrains. The increase in the orientation difference leads to the appearance of a high angle boundary capable of high-speed migration, forming the nucleus of recrystallisation. Moreover, the disappearance of sub-boundaries is favourable since it leads to a decrease in total free energy (Li 1962). Figure 2.35 illustrates schematically the formation of a nucleus by subgrain coalescence.

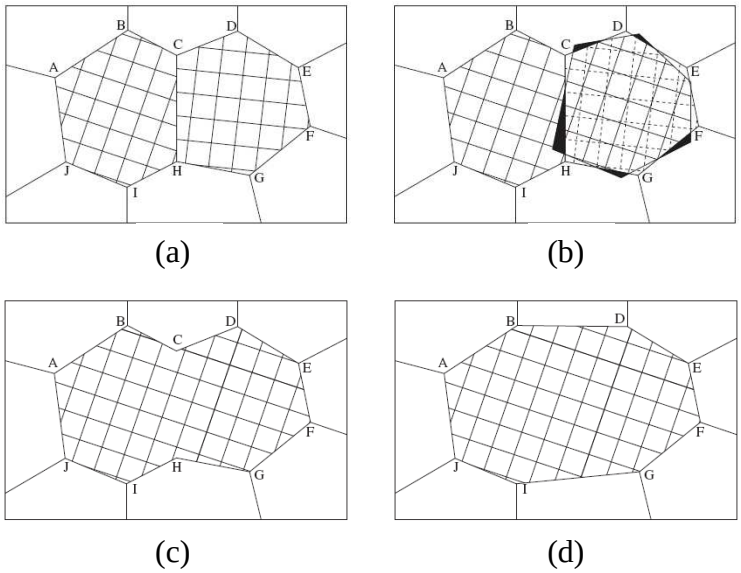

Figure 2.35: Coalescence of two subgrains by "rotation" of one of them: (a) original structure prior to coalescence; (b) rotation of the CDEFGH grain; (c) subgrain structure subsequent to coalescence; and (d) final structure after sub-boundaries migration (Li 1962).

This mechanism has been associated with transition bands, a large spread in the distribution of subgrain angles, moderate and high strains, regions next to grain boundaries, relatively low annealing temperatures and metals with high SFE (Ray *et al.* 1975; Kreisler and Doherty 1978). However, it is important to mention that the experimental evidence for this mechanism is limited and inconclusive (Humphreys 2004).

2.3.2.3.3 Nucleation by Subgrain Coarsening

This mechanism is based upon the polygonisation phenomena (discussed in Section 2.3.1) where regions of low dislocation densities are surrounded by low angle grain boundaries (LAGB) (Beck 1949; Cahn 1950; Cottrell 1953). Once a subgrain is formed, it will be capable of growing at the expense of its neighbours by thermally assisted LAGB migration. In this way, a decrease in stored energy will occur during annealing due to the removal and rearrangement of microstructural defects. The moving LAGB (sub-boundary) absorbs dislocations, increasing its orientation difference, its energy and mobility until it is transformed into a high angle boundary, hence characterizing nucleation.

Experimental evidence suggests that this process occurs primarily within regions with large orientation gradients. In such regions statistical studies show an increase in the mean misorientation across boundaries, and an increase in the mean subgrain size with annealing time (Humphreys and Hatherly 2004).

The subgrain coarsening mechanism (illustrated schematically in Figure 2.36) seems to be associated with high strains, a large spread in the subgrain size distribution, relatively high annealing temperatures, and occurs preferentially in low-SFE metals (Walter and Koch 1963; McQueen and Jonas 1975).

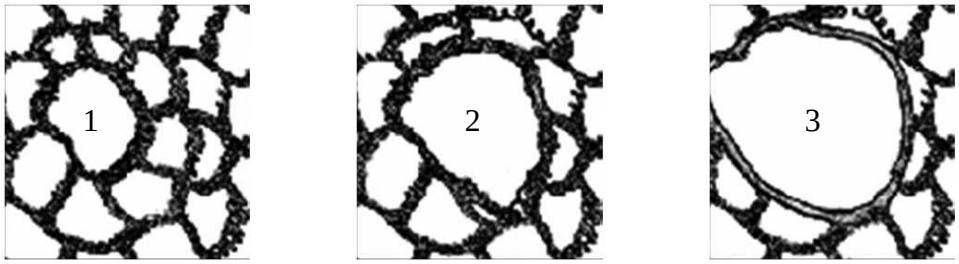

Figure 2.36: The sequence shows the nucleation of a recrystallised grain starting from a subgrain by the subgrain coarsening mechanism (Rangel *et al.* 2005).

2.3.2.4 Growth of Nuclei

Migration of high angle boundaries is the fundamental mechanism acting during recrystallisation and grain growth, the main difference between them being the driving force related to both phenomena. The driving force for grain growth (discussed in Section 2.3.3) is the energy of the high angle boundaries. However, the main driving force for recrystallisation to occur is the stored energy developed during straining in the form of crystalline defects. Another important difference between recrystallisation and grain growth is the sense of curvature of the migrating high angle boundary relative to its direction of movement (Rangel *et al.* 2005). However, this fact can only be recognised at a certain scale of measurement.

It important to mention that the nucleus is subjected to two pressures during recrystallisation. The retarding pressure (P_C) due to its radius of curvature as given by:

$$P_C = 2\gamma_b/r \qquad (2.8)$$

Where γ_b is the specific energy of the high angle boundary and r is the radius of the nucleus. The other pressure is the driving pressure (P_D) due to the dislocation density (ρ) of the material into which the nucleus is growing and is given approximately as:

$$P_D=\alpha\rho G\boldsymbol{b}^2 \qquad (2.9)$$

where α is a constant of the order of 0.5, ρ is the dislocation density, G is the shear modulus and $\boldsymbol{b}$ is the Burgers vector. Thus, the nucleus will grow if $P_D > P_C$, i.e.

$$D \geq 4\gamma_b / \alpha\rho G\boldsymbol{b}^2 \qquad (2.10)$$

Under isothermal conditions, primary recrystallisation generally displays an incubation time, associated with the formation of a nucleus. The absence of the incubation time is generally related to nucleation of the type of SIBM, not having in this case the need of time for the formation of a high mobility boundary. Growth of the recrystallised regions due to high angle boundaries continues until mutual impingement of recrystallised grains, i.e. primary recrystallisation finishes when all recrystallised grain boundaries meet. The distribution of the recrystallised regions is heterogeneous and grain impingement already occurs even for low volumetric recrystallised fractions (Rangel *et al.* 2005).

2.3.2.5 Effect of Second Phase Particle on Recrystallisation

Second phase particles within the microstructure can have one of two effects on the recrystallisation behaviour (Humphreys and Hatherly 2004). If the particles have large diameter (i.e. d >1 μm), they can give rise to high local concentrations of stored energy and large misorientations in the surrounding microstructure when the particle–containing material is deformed, and can thus act as favourable nucleation sites (Hansen 1975; Humphreys 1977). These zones of high stored energy tend to extend to a distance of about a particle diameter from the surface of the particle, which means that the size of the zone is determined by the size of the particle. Thus if the strained region, which depends on the particle size, is larger than the critical nucleus size, nuclei can form in these strained regions and immediately start growing due to the misorientation to the surrounding microstructure.

If however, the particles are present as a dispersion of fine particles (d<0.1 μm), they will actually retard the nucleation process (Zener drag), as the fine particles act as inhibitors to the movement of both dislocations and grain boundaries (Smith 1948; Nes *et al.* 1985). Both effects of particles on the recrystallisation behaviour will be discussed below.

1. Large (d > 1 μm) Particles

The presence of large particles on the matrix tends to promote recrystallisation through the Particle Stimulated Nucleation (PSN) mechanism due to the large orientation gradient around the particle. This mechanism is of particular interest since it is significantly different to other nucleation mechanisms. It occurs in well-defined regions of the microstructure which can be altered by alloying or processing. Thus, the recrystallised grain size may be controlled (Figure 2.37). The nuclei's orientation produced by PSN differs, in general, from those produced by other mechanisms and, hence, the recrystallisation texture may be controlled by changing the amount of PSN (Humphreys and Hatherly 2004).

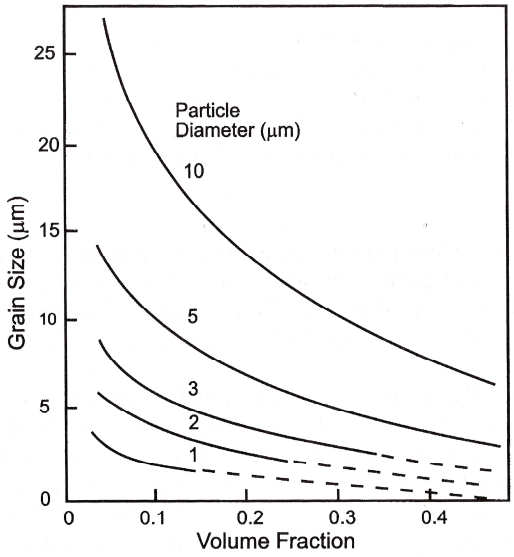

Figure 2.37: The predicted grain size for a PSN efficiency of unity (i.e. all particles give a recrystallisation nucleus). The dashed lines show conditions under which Zener pinning effects may prevent discontinuous recrystallisation (Humphreys *et al.* 1990).

Since the deformation zone has a gradient of both orientation and dislocation density, the nucleation of the subgrain may occur in any part of the deformation zone starting from the particle surface up to the periphery. Work using aluminium alloys (Humphreys 1980) has shown a drop in the maximum misorientation within a deformation zone during annealing, as shown in Figure 2.38. This indicates that PSN may not occur at the regions of highest misorintation close to the particle interface.

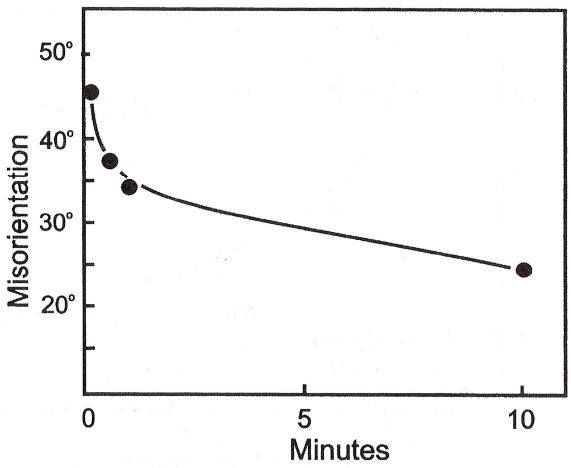

Figure 2.38: Changes in the maximum misorientation within the deformation zone of Si particles in Al as determined by *in-situ* HVEM annealing at 250^{o}C (Humphreys 1980).

The formation of this nucleus within the deformation zone depends mainly on the particle size and the strain (Figure 2.39) and can be considered as a subgrain growth mechanism due to the high orientation gradient where the subgrain increases its misorientation with neighbouring subgrains until it becomes a high angle grain boundary (e.g. 10-15^{o}). After that, the driving force for the growth of this nucleus within the deformation zone is provided by the high dislocation density of the deformation zone.

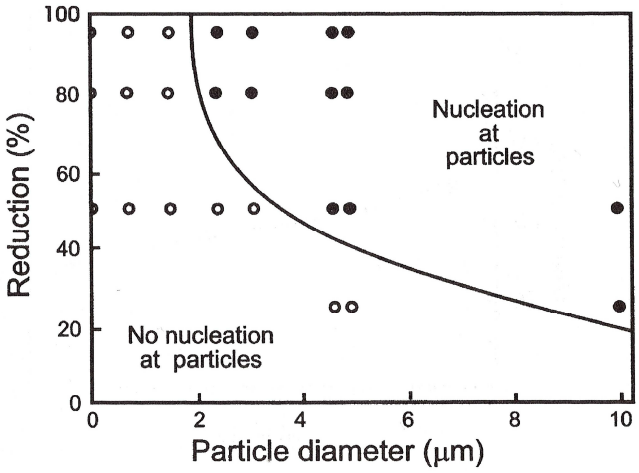

Figure 2.39: The effect of rolling reduction and particle size on the occurrence of PSN (Humphreys 1977).

In the case of low carbon steels, the most common second phase particles, with d>1μm, are cementite particles which usually precipitated on the ferrite grain boundaries. These particles have complex form since they are neither spherical nor isolated from grain boundaries. Stress concentration on these particles can occur which leads to fracture of the particle, forming pieces of various sizes and morphologies. In addition, these fragmented particles are rotated during deformation and align themselves to best accommodate the deformation incompatibilities. Based on these situations, deformation zones around these particles may not have any systematic orientation change (Inagaki 1987b).

In addition, since cementite particles are fragmented into strings located on grain boundaries of the deformed grains during rolling, recrystallised grains nucleated at these particles also form elongated bands running parallel to the rolling direction situated, also, on these grain boundaries (Inagaki 1991).

It is also important to mention that during annealing, some of the carbon atoms of the cementite particles will dissolve into the ferrite matrix which leads to a competition between the dissolving carbides and the nucleation of the recrystallised grains (Figure 2.40a). However, the activation energy for recrystallisation is greater than for carbon diffusion in ferrite. So, high temperature (i.e. fast heating rate) will accelerate recrystallisation more than cementite dissolution where the inter-particle spacing has an important role in this issue (Hutchinson 1994). Figure 2.40b shows how the average dissolved carbon content at the start of recrystallisation varies as a function of heating rate for three different particle dispersions. It shows that for high heating rates, the average carbon content in the ferrite depends critically on the inter-particle spacing, being high with a fine carbide structure (Hutchinson 1984). The dissolved carbon has a significant effect on the recrystallisation texture which will be discussed in Section 2.4.3.

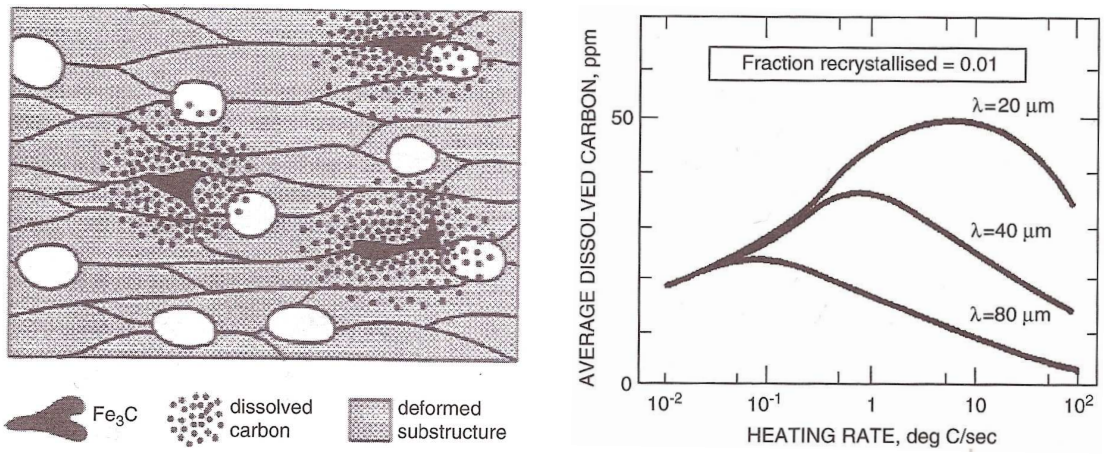

(a) (b)

Figure 2.40: (a) Illustration of the competition between recrystallisation and the distribution of re-dissolved carbon atoms into the ferrite matrix (Hutchinson 1994) (b) Calculated average dissolved carbon contents in ferrite as a function of the heating rate for three different inter-particle spacing (λ) (Hutchinson 1984).

2. Small or Closely Spaced Particles

A dispersion of closely spaced second phase particles has been known to prevent or delay recrystallisation (Zener drag) (Smith 1948). This arises from the fact that a small area of grain boundary disappears when the grain boundary intersects a particle, as shown in Figure 2.41A. Therefore, to move away from the particle requires the creation of new surface. The net drag force on a boundary of energy σ per unit area due to a particle of radius r is given by (Figure 2.41B):

$$F = 2 \pi r \sigma \sin\theta \cos\theta \qquad (2.11)$$

It is a maximum when $\theta = 45^{o}$. Substituting this value gives for the maximum force:

$$F = \pi r \sigma \qquad (2.12)$$

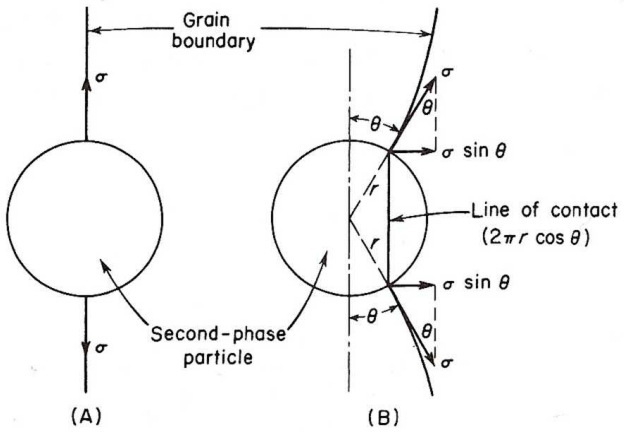

Figure 2.41: Interaction between a grain boundary and a second phase particle (Reed-Hill and Abbaschian 1994).

In the case of recrystallisation by Strain Induced Boundary Migration (SIBM), a dispersion of pinning particles will have its effect on the critical bulge sizes for SIBM. As the pinning pressure increases, the critical bulge sizes for nucleation will increase. Moreover, it is frequently found that preferential growth of certain texture components will result when SIBM occurs under particle pinning conditions (Higginson *et al.* 1997).

2.3.2.6 Quantifying the Recrystallisation Kinetics

The kinetics of the recrystallisation process is often quantified using the Johnson-Mehl-Avrami-Kolmogorov (JMAK) model (Kolmorgorov 1937; Johnson and Mehl 1939; Avrami 1939). This model is based on the nucleation and the growth processes. In this model, the fraction recrystallised, X_v, is related to the annealing time, t, by the following equation:

$$X_v = 1 - \exp(-B\, t^n) \qquad (2.13)$$

where n is the JMAK exponent and B is a constant which depends on the nucleation rate, $\dot{N}$,and the growth rate, $\dot{G}$. If it is assumed that

- $\dot{N}$ and $\dot{G}$ are constant,
- the nucleation sites are randomly distributed, and
- the new grains are spherical,

then the original JMAK equation will be generated with n=4 and B= $\frac{f\dot{N}\dot{G}^3}{4}$ where f is a shape factor ($4\pi/3$ for spheres).

This model assumes that the grains, prior to impingement, grow isotropically in three-dimensions. However, if there are constraints like sample geometry or any other internal microstructural constraints which makes the grains grow only in one or two-dimensions, then the JMAK exponent is lowered.

Experimental recrystallisation kinetics measurements are usually compared with the JMAK model by plotting $\ln[\ln\{1/(1-X_v)\}]$ against $\ln(t)$. According to Equation 2.13, a straight line is usually produced with n as the slope.

2.3.2.7 The Role of Grain Boundaries in Recrystallisation

A grain boundary is a defective region that separates two grains or crystals having different crystallographic orientations in polycrystalline materials, where various degrees of crystallographic misalignment between adjacent grains are possible. Focusing on the misorientation angle, grain boundaries are classified in terms of low

and high angle boundaries, where the angles of misorientation are less or more than 15^{o}, respectively.

There are two important properties characterising a grain boundary and controlling the migration of the new grain boundaries into the deformed matrix during recrystallisation; they are the grain boundary energy and grain boundary mobility. Both of them are not independent variables but related to the nature of the boundary. In general, they depend on the relative misorientation between the two crystals and on the boundary plane with respect to one or the other crystal. It is well-known that small angle grain boundaries have low energies and mobilities relative to high angle grain boundaries.

For low angle grain boundaries, Read and Shockley (1950) derived an expression relating the boundary energy, γ, to the misorientation, θ, as follows

$$\gamma = \gamma_m \frac{\theta}{\theta_m}\left(1 - \ln\frac{\theta}{\theta_m}\right) \qquad (2.14)$$

where γ_m and θ_m are the boundary energy and misorientation when the grain boundary becomes a high angle boundary. Grain boundary energies for high angle boundaries are relatively independent of misorientation and considered to have uniform high angle energy.

Grain boundary mobility, on the other hand, is an intrinsic property of the grain boundary characterising grain boundary response to a driving pressure. It increases with misorientation and assumed to take a sigmoidal form such as (Humphreys 1997):

$$M = M_m\left[1 - e^{-B\left(\frac{\theta}{\theta_m}\right)^n}\right] \qquad (2.15)$$

where M_m is the mobility of a high angle grain boundary, n and B are constants. The variation of boundary energy and mobility with misorientation can be seen in Figure 2.42.

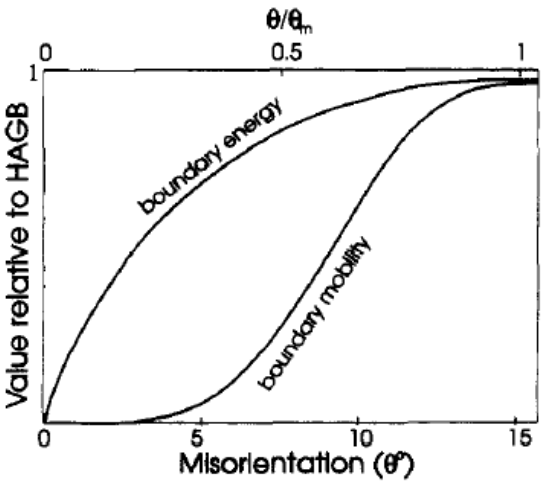

Figure 2.42: Relative boundary energy and mobility as a function of misorientation angle (Humphreys 1997).

2.3.3 Grain Growth

In a completely recrystallised metal, the driving force for grain growth lies in the surface energy of the grain boundaries. As the grains grow in size and their number decreases, the grain boundary area diminishes and the total surface energy is lowered accordingly (Hillert 1965).

The grain growth is a function of time, temperature and composition. In addition, when a preferred orientation is present, it has been observed that grain growth rates are reduced (Reed-Hill and Abbaschian 1994).

Grain growth can be divided into two types, normal grain growth and abnormal grain growth. During normal grain growth, sometimes called "continuous grain growth", the distribution of grain sizes remains approximately constant and the grains increase their diameter continuously and gradually. During abnormal grain growth or secondary recrystallisation (sometimes called "discontinuous grain growth"), particular grains grow faster. The mean size of the others remains constant and the grain size distribution becomes very inhomogeneous. Three main factors affect the occurrence of abnormal grain growth: the influence of second phase particles, the effect of orientation on boundary mobility, and the interaction of boundaries with specimen surfaces (Dunn and Walter 1966).

2.4 Textures

Low carbon steel sheets are subjected to a variety of forming operations. The formability characteristics of low carbon steel, as measured by Lankford r-value from a tensile test (as discussed in Section 2.1.4.1), is critically dependent on the texture of the sheet (Hutchinson and Ushioda 1984; Hutchinson 1984; Satoh *et al.* 1986).

The texture of the material can be defined as the sum of the crystallographic orientations of the crystallites within a polycrystalline aggregate (Humphreys and Hatherly 2004). The development of a texture can be driven by a variety of processes such as solidification, phase transformation, deformation and/or recrystallisation. The particular type and strength of the texture is governed both by the material (i.e. crystal structure, purity, etc.) as well as the processing route.

The crystallographic texture is described either as a macrotexture or microtexture (Randle and Engler 2000). In describing the macrotexture, the grains in a polycrystal are regarded as constituting a single statistical population without regard to the spatial location of any particular grain or its relation to its neighbours. The microtexture, on the other hand, involves determining the orientation of each grain of the population and determining the nature and degree of its misorientation with respect to its immediate neighbours.

Textures in rolled sheet metals are frequently represented as {hkl}<uvw> where {hkl} are the Miller indices of planes of these grains which are parallel to the plane of the sheet while <uvw> are the Miller indices of their directions which are parallel to the rolling direction (RD) (Ray *et al.* 1994). A crystal orientation can also be represented by three consecutive rotations relative to the sample (i.e φ_1,Φ, and φ_2) which are called Euler angles. There are several different conventions for expressing the Euler angles. The most common ones are those used by Bunge (1965). Detailed information on texture representation and the relationship between Euler angles and Miller indices for cubic materials can be found in Appendix A.

2.4.1 Typical Textures in Low Carbon Steels

The textures discussed in this report are produced by cold rolling and annealing (CRA) processes. The most useful representation of these types of textures (e.g. cold

rolling texture and annealing texture) in low carbon steels are via the (200) pole figure (Figure 2.43a) or the φ_2=45^o section in Euler space (Figure 2.43b). In addition, they are usually described in terms of certain orientation fibres in Euler space. Figure 2.43b shows the following two important fibres:

1. α-fibre or RD fibre, runs from {001}<110> to {111}<110> along <110> // RD, and also described as {hkl}<110>.

2. γ-fibre or ND fibre, runs from {111}<110> to {111}<231> and {111}<112> along <111> // ND, and is also described as {111}<uvw>.

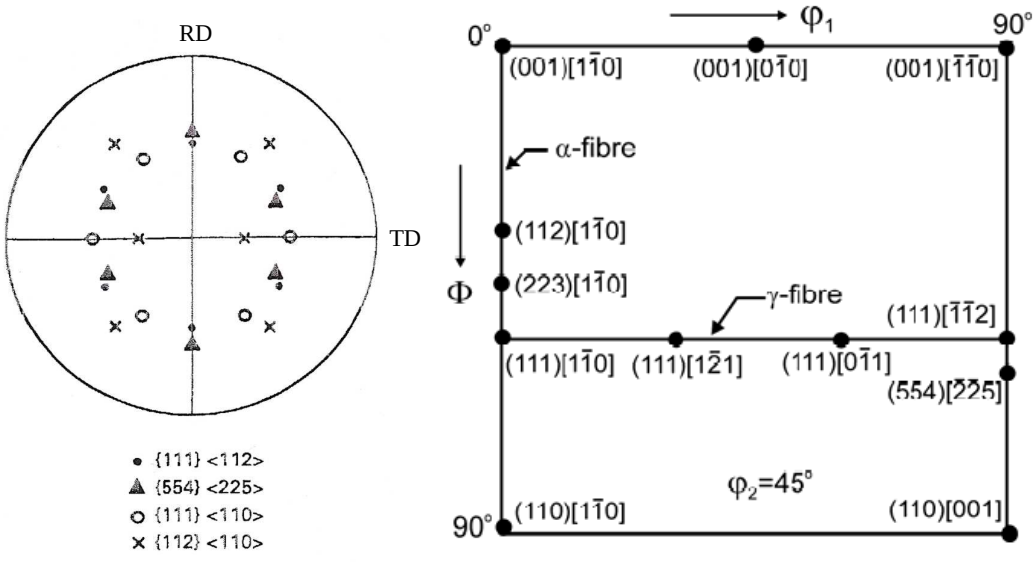

(a) (b)

Figure 2.43: (a) Some important orientations in low carbon steels represented by (200) pole figure (Ray and Jonas 1990). (b) Two dimensional view of φ_2=45^o section of Euler space showing the most important orientations and fibres in low carbon steels (Ray *et al.* 1994).

As discussed in Section 2.1.4.1, the γ-fibre orientation is most ideally suited for good deep drawability of the sheet steels, whereas the presence of α-fibre components imparts poor deep drawability. This comes from the fact that the greatest strength lies in the direction of the cube diagonal or <111> direction and it is weaker in the direction of the face diagonal <110> and weakest along the cube edge <100> as indicated in Figure 2.44a. A cube-on-corner texture (i.e. {111}) with the strongest crystal direction oriented normal to the sheet is favourable to the development of a high strain ratio (Figure 2.44b).

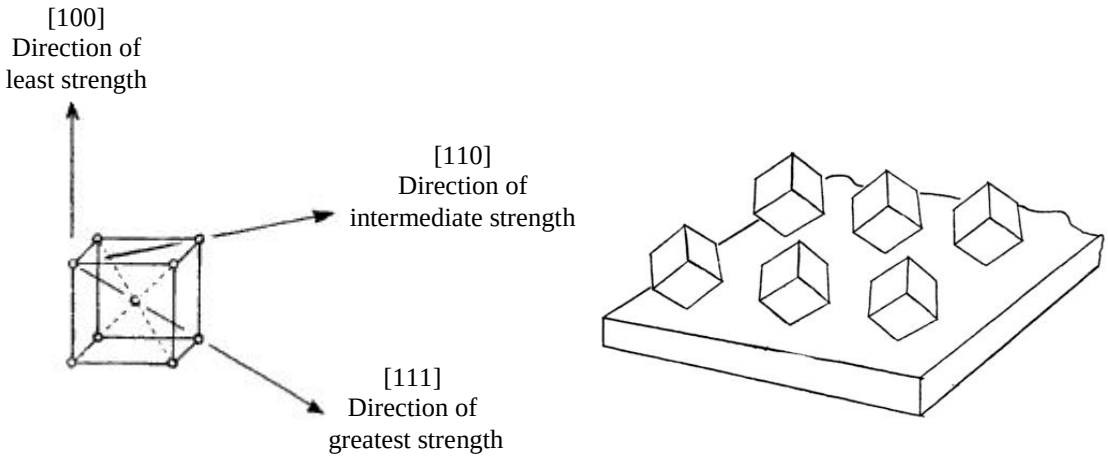

(a) (b)

Figure 2.44: (a) Effect of orientation on the strength of crystal, (b) Cube-on-corner orientation where the cube diagonal is normal to the plane of the strip surface (Roberts 1978).

2.4.2 Cold Rolling Textures

In low carbon steels and BCC metals in general, the cold rolling textures are rather insensitive to material and process parameters. The most significant factor is the degree of deformation (rolling reduction) and to some extent the presence of a starting texture (Hutchinson 1999). Almost all the important components in rolled steels are shown in Figure 2.45. This figure shows the textures after 50%, 74% and 95% reductions of low carbon steel. In all cases, the textures are concentrated into the main two fibres, the α- and γ-fibres discussed above. It can also be seen that the α-fibre becomes stronger as the rolling reduction increases.

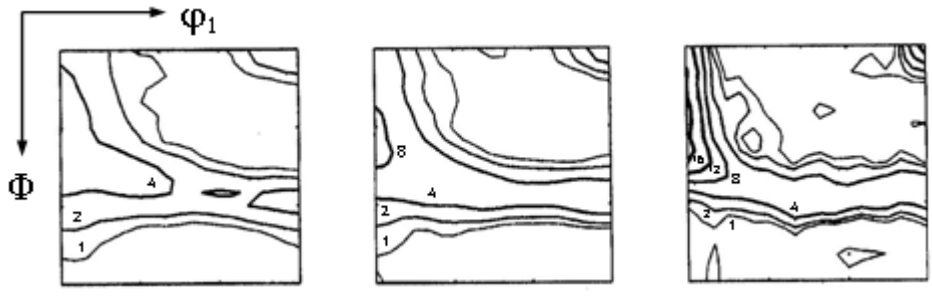

(a) (b) (c)

Figure 2.45: Textures of low-carbon steel (φ_2=45^o sections) cold rolled (a) 50%, (b) 74% and (c) 95% (Schläfer and Bunge 1974).

Moreover, Figure 2.46 shows how the volume fraction for various important components increases with strain during cold rolling. This figure shows the continuous strengthening of α-fibre components as the strain increases while all the γ-fibre components increase up to 70% reduction and then remain constant. This implies that 70% cold reduction is the optimum reduction for the formation of a strong γ-fibre during the recrystallisation process.

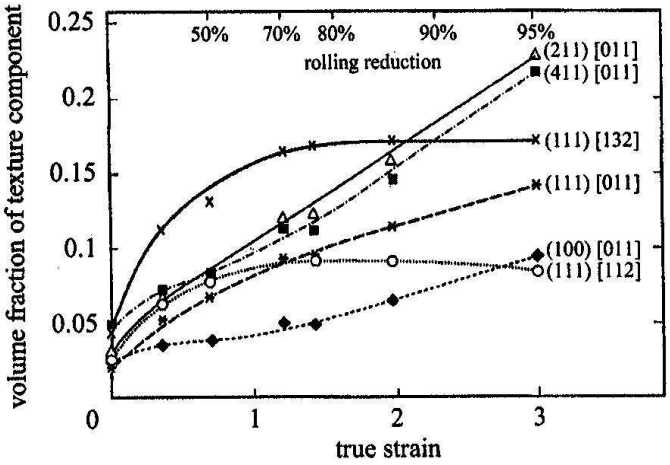

Figure 2.46: Volume fraction of various important components during cold rolling in low-carbon steels (Schläfer and Bunge 1974).

The presence of cementite particles in the matrix also plays a role in controlling the rolling texture. These particles suppress the rotation toward the stable end orientations creating more randomly-oriented zones around these particles which in turn randomises, to some extent, the rolling texture. Figure 2.47 shows the effect of these particles, where the effect is more pronounced if these particles are coarse (Inagaki 1994)

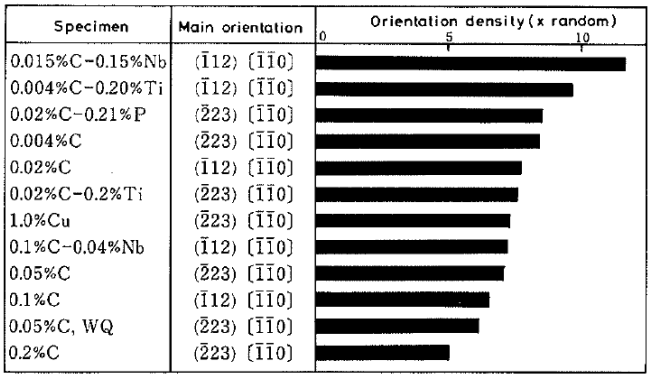

Figure 2.47: Orientation density of the {112}<110> {223}<110> stable end orientation observed in various Fe alloys cold rolled 70% (Inagaki 1994).

2.4.3 Development of Recrystallisation Textures

Recrystallisation, as discussed in Section 2.3.2, is characterised by nucleation and growth and both of them determine the recrystallisation texture. If there is a direct correlation between the orientation of the nuclei and the recrystallisation texture, this is termed oriented nucleation. In contrast, the oriented growth theory proposes that the resulting texture is only influenced by different growth rates of the randomly oriented nuclei into the deformed matrix. Humphreys and Hatherly (2004) concluded that oriented growth does not occur independently of oriented nucleation.

Recrystallisation texture is strongly influenced by the stored energy since it determines which of the nucleation mechanisms for recrystallisation will dominate. In the case of low stored energy grains, the SIBM nucleation mechanism dominates (Humphreys and Hatherly 2004) and it allows subgrains with low stored energy, i.e. {001}<110> or {112}<110> subgrains, to grow into areas of high stored energy. Therefore, the SIBM mechanism favours the formation of α-fibre texture components which are usually considered undesirable for good deep drawability.

On the other hand, nucleation may take place by the subgrain growth mechanism if the stored energy of the grains is high. This mechanism generally favours the formation of {111}<110> and {110}<110> orientations (Dillamore *et al.* 1967).

Figure 2.48 shows the cold rolling and annealing textures (φ_2=45^o sections) for 75% cold rolled IF steel. A typical cold rolling texture is shown in Figure 2.48a and comprises well-formed α- and γ-fibres. During recrystallisation, the α-fibre is almost eliminated whereas a new γ-fibre is created, becoming in many cases the sole feature of the texture as in Figure 2.48b.

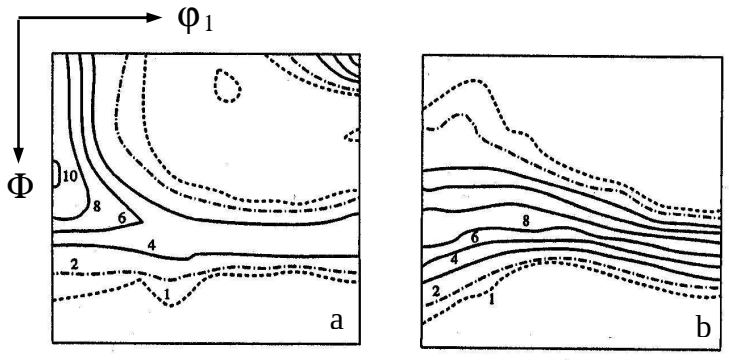

Figure 2.48: Textures of IF steel (φ_2=45^o sections) for 75% cold rolled steel, (a) as rolled, (b) recrystallised (Hutchinson and Artymowicz 2001).

Another factor which has an important effect on the recrystallisation texture is the initial grain size prior to cold rolling. Figure 2.49 shows that as the initial grain size increases the intensity of the γ-fibre decreases and there is an increase in the intensity of Goss component. Moreover, the recrystallisation texture ratio (222)/(200) and r-value both depend on grain size, and are plotted against the inverse initial grain size in Figure 2.50.

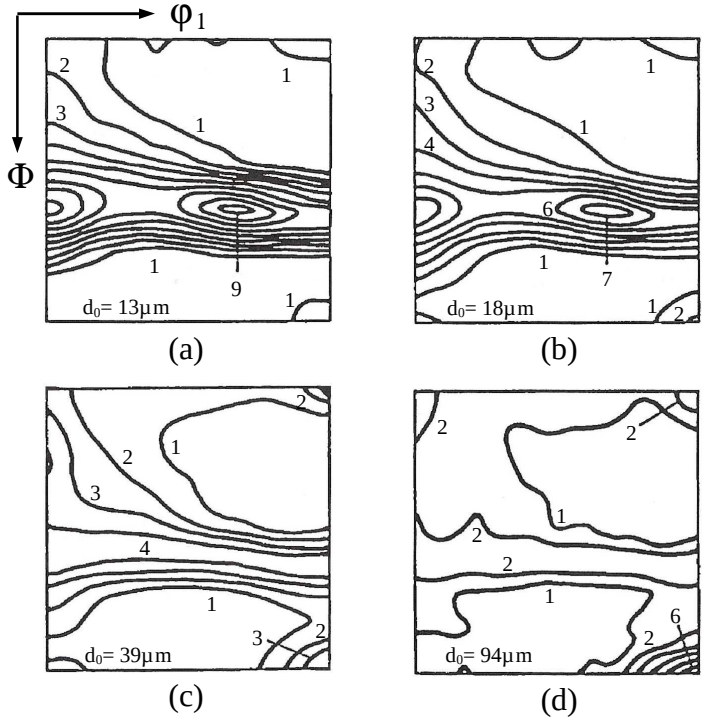

Figure 2.49: The effect of initial grain size of 70% cold rolled and annealed IF steel on the recrystallisation textures (φ_2=45° sections) (Hutchinson *et al.* 1990).

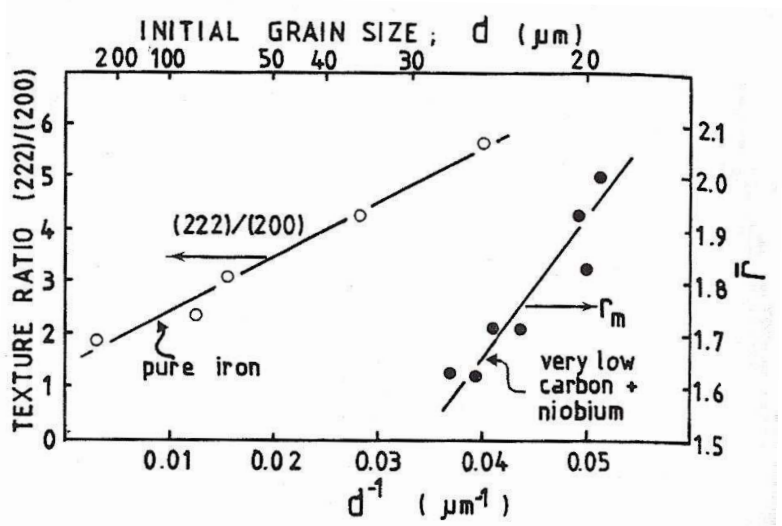

Figure 2.50: Effect of initial grain size on texture ratio and r-value after annealing for pure iron and low carbon/niobium steel (Hutchinson and Ushioda 1984).

In both figures, a fine grain size will result in a weaker Goss component and an increased intensity of γ-fibre, and hence a higher r-value. It has been suggested that this behaviour is due to the existence of (111) oriented subgrain structures adjacent to the original grain boundaries which are preferential sites for the nucleation of recrystallisation. Another explanation is that inhomogeneous deformation in the form of shear banding tends to become more prominent in the case of coarse grained metals and it leads to nucleation with orientations towards the Goss component (Hutchinson and Ushioda 1984).

The most important factor in controlling the recrystallisation texture is the pinning effect of second phase particle (Satoh *et al.* 1986). It provides a resistance to both nucleation and growth of new grains. It has been found that a dense dispersion of fine second phase particles suppresses the growth of recrystallised grains with {111} texture, thereby impairing the deep drawing property of the steel. Moreover, the removal of interstitials to give a sparse dispersion of coarse second phase particles (as in IF steels) is a key factor for promoting high r-value (Subramanian *et al.* 1994). However, coarse particles tend to promote recrystallisation through the Particle Stimulated Nucleation (PSN) mechanism creating new grains highly misoriented from the matrix which leads to a weakened texture, although Humphreys and Hatherly (2004) state that the PSN nuclei are not randomly oriented even if the orientation spread of the nuclei is high.

In the case of low carbon steels with cementite particles, the heating rate has an important role in determining the recrystallisation texture (Figure 2.51). In respect to γ-fibre texture formation, a few coarse cementite particles are less harmful than several small ones generated with a low heating rate as a result of carbon dissolution, as illustrated in Figure 2.52 (Abe 1992; Hutchinson 1984). Also, this figure shows clearly that the addition of carbon, either in solid solution or as carbides, will result in a reduction of γ-fibre strength.

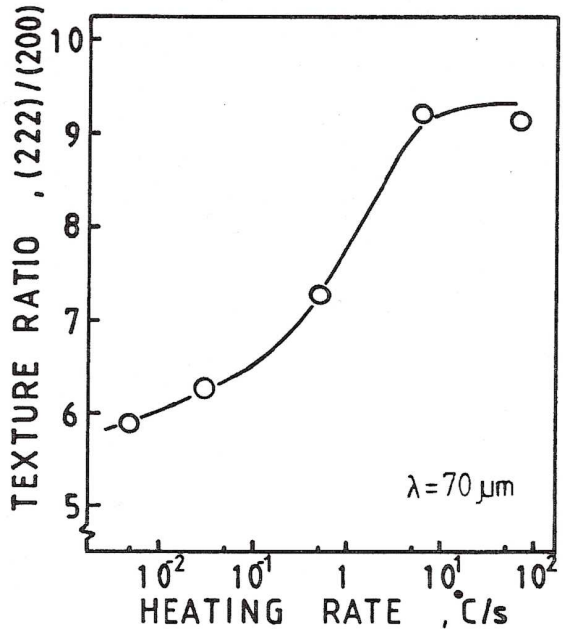

Figure 2.51: Effect of heating rate on the texture intensity ratio I_{222}/I_{200} for cold rolled and annealed low carbon steel (Hutchinson 1984).

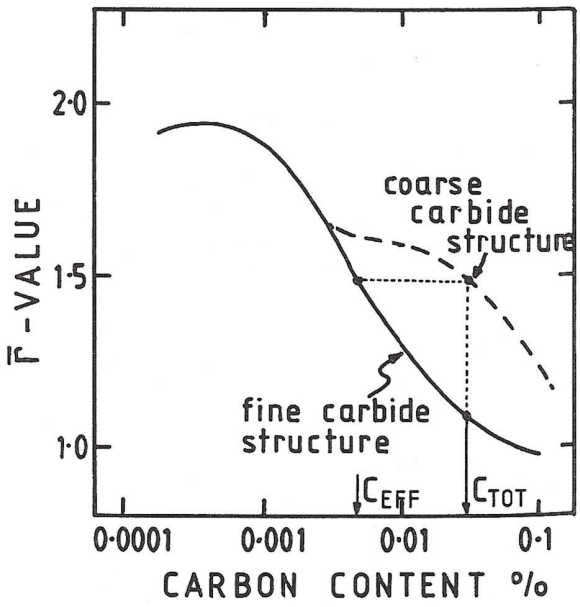

Figure 2.52: Effects of carbon content and carbide morphology on $\bar{r}$ -values of steel (Hutchinson 1984).

2.5 Monte-Carlo Modelling

The need for computer simulation of recrystallisation and grain growth is driven by two different considerations (Doherty *et al.* 1997). First, it is of fundamental interest for improved understanding of the highly complex phenomenon of recrystallisation and grain growth from a microstructural point of view. Second, from an engineering perspective, quantitative predictions of the microstructure and properties of materials as affected by annealing can be made, where the average texture and grain size can be predicted.

The application of computer simulation to recrystallisation and grain growth was strongly stimulated in the early 1980s by Anderson *et al.* (1984). They realised that Monte Carlo models could be applied to problems of grain structure evolution by the extension of the Ising lattice model, used to model magnetic domain evolution, to the Potts model. It was then possible to represent discretely grains (domains) by regions of similarly oriented (lattice) points.

A wide range of "mesoscale" simulation techniques have been developed to model evolution of microstructure, including: Vertex models, Monte-Carlo Potts models, Phase-Field model, Cellular automata, etc. (Weaire and Kermode 1983; Anderson *et al.* 1984; Chen and Yang 1996; Raabe 1998). Of these, the Monte-Carlo Potts model, the principles of which are discussed in Appendix C, is well-known and particularly amenable to the incorporation of a wide range of metallurgical phenomenon including recrystallisation and grain growth. It simulates boundary motion via an energy minimisation procedure (Rollett 1997).

The applicability of the models is hindered by the lack of the experimental data on boundary mobility and the absence of methods to input real 3D experimentally measured microstructures into the models (Miodownik 2002). In addition, there is a conflict of length scale in modelling the annealing processes arising from the fact that recrystallisation, for instance, is driven by thermal energy and internal energy which are controlled by factors at very different length scales. Humphreys (2000) concluded that the development of the modelling of annealing requires further development in computing power, modelling methods and the scientific understanding of the physical metallurgy of annealing processes.

2.5.1 Application to Recrystallisation

The use of Monte Carlo modelling for simulating the recrystallisation process is more difficult than for the grain growth process. This is due to the size of the model relative to the scale of the structure which is of importance in determining the recrystallisation of real materials. In addition, realistic simulations of recrystallisation using an abnormal subgrain growth approach, as in the case of Monte Carlo model, require proper handling of the energy and mobility of grain boundaries. Many observations have been made which suggest that individual subgrains acquire a growth rate advantage over their neighbours and become identifiable as new grains. This growth advantage can result from a difference in mobility between the boundary of the new grain and the boundaries in the surrounding material. By altering the rate at which sites are sampled for reorientation, the mobility of specific grain boundaries can be varied and, hence, lead to marked abnormal grain growth behaviour which may correspond to the early growth of new grains in recrystallisation.

In order to investigate the annealing of materials containing large particles - the focus of this study - the particle must be dealt with in a different manner. It is important to mention that little work has been done on modelling the effect of large particles on recrystallisation. The particle, as stated by Humphreys (1992) using his network model, may introduce microstructural and orientation gradients, with small subgrains and large orientation gradients close to the particles (Humphreys 1992). In this case, he found that nucleation of recrystallisation from the deformation zone close to the particle occurs.

Radhakrishnan and Sarma (2004) described the application of a coupled crystal-plasticity-based finite-element with a Monte Carlo technique to study the phenomenon of PSN during hot deformation and recrystallisation of aluminium and the subsequent growth and orientation of the nuclei. They started by simulating the plastic deformation using a crystal-plasticity-based finite element technique. The simulation domain in the form of a single crystal, bicrystal or a tricrystal was discretised such that a large number of elements in each grain or crystal. The hard particle in the form of sphere, a cube or a rotated cube was also discretised in similar fashion. After that, the evolution of the deformation substructure, which was extracted from the output of the finite element simulations, was carried out using a

Monte Carlo technique applied to subgrain growth. Their simulation results compared well to experimental observations.

2.5.2 Application to Grain Growth

Normal grain growth has been defined as the uniform increase in grain size which occurs upon annealing a polycrystalline aggregate after primary recrystallisation is complete. The kinetics of normal grain growth can be characterised by proportionality between the mean grain radius and t^n, where t is time and n is the grain growth exponent which is equal to 0.5 as theoretically predicted. The basic Potts algorithm (Anderson *et al*. 1984 and 1989; Srolovitz *et al*. 1984) shows a smaller value than the expected one of n equal to 0.5. In fact, the basic algorithm shows some disadvantages that are inherent to the technique, e.g. unrealistic nucleation events, and it was very time consuming. Recently, changes in the algorithm have been suggested improving the accuracy of the simulation results and reducing the run-time of the simulations.

There is no evidence for great differences between two and three-dimensional grain growth, providing that no pinning particles exist (Miodownik 2002). However, two-dimensional Monte Carlo simulations of grain growth in particle-containing materials (Zener pinning) found a limiting grain size which differed from that which was expected. It was later found that the pinning behaviour of real three-dimentional materials cannot be predicted from two-dimensional computer simulations (Hillert 1988; Miodownik *et al*. 1999).

Chapter 3

EXPERIMENTAL METHODS

This chapter details the materials examined throughout this study as well as the experimental techniques used to investigate the microstructures and textures following deformation and subsequent heat treatment.

3.1 Materials

The types of steels used in this study are Interstitial Free (IF) steel and High Strength Low Alloy (HSLA) steel. The chemical compositions are given in Table 3.1. Both steels have low carbon content, with no free interstitial atoms in solution in the IF steel. The steels were obtained in the form of hot rolled plate with a thickness of ~ 4.2 mm for the IF steel and ~12 mm for the HSLA steel.

Table 3.1: Chemical composition (in wt %) of the steels investigated.

Material	C	N	Mn	Al	Ti	Nb
IF	0.003	0.003	0.15	0.05	0.08	-
HSLA	0.068	0.006	1.39	0.05	0.003	0.059

3.2 Initial Heat Treatment

In the case of HSLA steel, initial heat treatment was carried out to produce a structure with fine, spheroidal, pearlite colonies. A schematic illustration showing the heat treatment cycle applied to the HSLA steel is shown in Figure 3.1. The sample was heated to 1250^{o}C for one hour in order to dissolve the (Nb, Ti)(C, N) carbonitrides and then water quenched. After that it was reheated to 945^{o}C for 30 minutes followed by water quenching. This step was done to give Nb(C,N) precipitation. Finally, the sample was aged at 712^{o}C for 24 hours to change the shape of pearlite colonies into a spherical form (fine pearlitic particles). These particles are

coarse enough to act as nucleation sites for recrystallisation. The particles' volume fraction were measured to be about 20 ~ 24% with an average diameter of 3 μm.

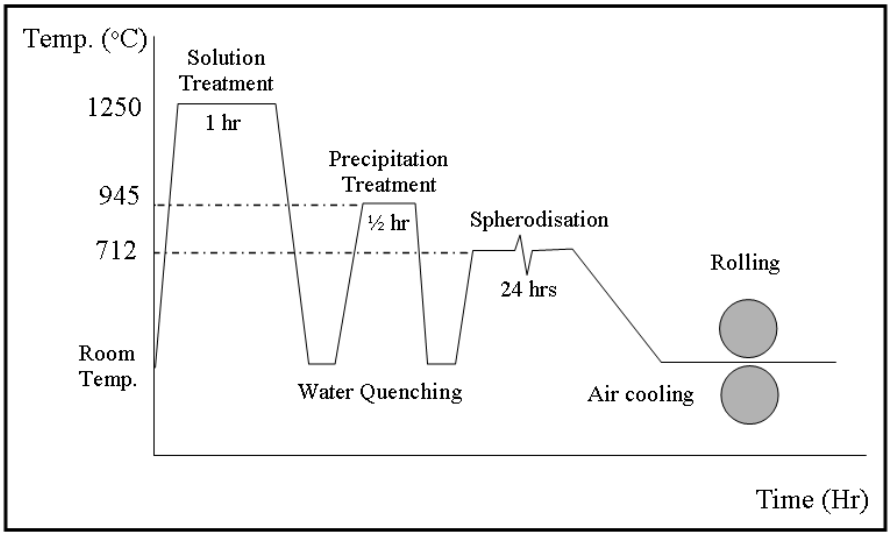

Figure 3.1: Initial heat treatment for HSLA steel prior to rolling.

3.3 Cold Rolling

The steels were cold rolled to four different reductions; 20%, 50%, 70% and 90%. After each reduction a sample was removed, giving a total of four samples collected for each steel. A small amount of error in thickness was allowed for due to the difficulties of obtaining the exact desired amount of reduction. The comparison between the actual thicknesses and the ideal ones are shown in Table 3.2. Cold rolling was performed using a two-high rolling mill with 250mm diameter rolls operating with a roll surface speed of 150 mm/s and with light paraffin lubrication.

Table 3.2: Comparison between the ideal and actual thicknesses.

Material	Ideal		Actual	
	Reduction (%)	Thickness (mm)	Reduction (%)	Thickness (mm)
IF	20	3.36	22	3.28
	50	2.1	50	2.1
	70	1.26	72	1.17
	90	0.42	89.3	0.45
HSLA	20	9.6	20.4	9.55
	50	6.0	50.5	5.94
	70	3.6	70	3.6
	90	1.2	89.5	1.26

3.4 Annealing

In order to study the recrystallisation kinetics, static annealing was carried out for samples from all the different reductions for different times and temperatures. This process was done using a LMF Carbolite high temperature furnace. Prior to heat treatment, the samples were cut to a length of about 15 mm and a width of about 7 mm, with the scale on the surface removed by grinding each face of the sample on silicon carbide (SiC) paper.

Regarding the accuracy for each annealing temperature examined, a copper rig housing the sample with an attached thermocouple was used. This overcomes the problem with the accuracy of the furnace temperature reading. The annealing temperatures used range from 620^{o}C to 690^{o}C for IF steel and from 500^{o}C to 560^{o}C for HSLA steel depending on the four degrees of reductions to give full recrystallisation within one day.

3.5 Hardness Testing

A classical way of studying recrystallisation is by hardness indents, which gives a direct measure of the recrystallisation–induced softening in the material. A hardness test measures the resistance of a material to penetration by a harder test body. Many different hardness tests exist, but they mainly differ in the shape of the object which is pressed into the sample. For this study, the Vickers macrohardness indentation test with a load of 20 kg was used. Each as-polished sample was tested three times to obtain a reliable set of results.

3.6 Metallographic Preparation and Microscopy

In order to measure the grain size, calculate the recrystallisation fraction and analyse the texture evolution, metallographic examination was conducted on specimens, in the as-received condition, cold rolled conditions and following isothermal annealing. In this study, most of the microstructural characterisation and analysis was done on the transverse cross section except for the texture analysis measured by XRD in which the normal cross section was used (Figure 3.2). It is important to mention that about 2mm of the surface was removed prior to the texture measurement by XRD.

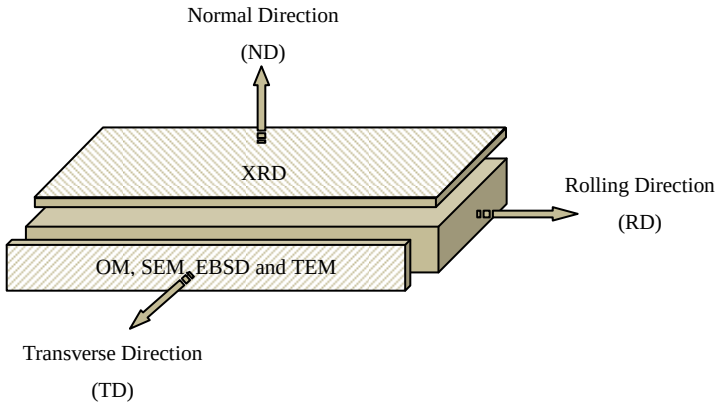

Figure 3.2: Schematic diagram showing the cross section planes used for the examination of various techniques. (OM: Optical Microscopy, SEM: Scanning Electron Microscopy, EBSD: Electron Back-Scatter Diffraction, TEM: Transmission Electron Microscopy and XRD: X-ray Diffraction)

3.6.1 Optical Microscopy (OM)

Despite the limitations in resolution, optical microscopy, also referred to as light microscopy, allows a simple, rapid and relatively accurate assessment of grain size and microstructure, including grain misorientation and the presence of second phase particles. In this study, an Olympus BH2 optical microscope equipped with a digital camera was used for microstructural characterization, grain size measurements and recrystallisation fraction determination.

All samples for optical microstructural examination were initially hot mounted in Bakelite and identified to prevent mixing. Then, the samples were ground through a series of successively finer grades of silicon carbide (SiC) paper: 240, 480, 600, 800

and 1200, using water as lubricant and coolant. After that, the samples were mechanically polished through successive 6 μm, 1 μm and ¼ μm diamond pads.

The structure for both steels samples was revealed using a 2% Nital etch at room temperature for around 50 seconds. In general, it was necessary to repeat the 1μm polishing and etching several times to obtain a satisfactory microstructure.

3.6.1.1 Grain Size Measurement

The grain size of the etched sample was measured using the mean linear intercepts method because of its accuracy and high speed. A line of known length was placed on the micrograph. The number of times grain boundaries intercept this line was counted. Then, this number was divided by the scaled length of the line which gives the average mean linear intercept grain size.

3.6.1.2 Recrystallisation Fraction Determination

The recrystallisation fraction in a sample was measured using three random images on transverse cross sections. A grid of 30 X 30 (900) squares printed on a transparency was placed over the micrographs and the number of crossings that contain a recrystallised grain was counted. This number was divided by 900 which gave the point fraction of recrystallised grains.

3.6.1.3 Measurement of Pearlitic Particle size and Volume Fraction

An in-house image analysis program was used to measure the fine pearlitic particle size and its volume fraction. It is important to mention that the pearlitic particles present in this steel have complex form since they are neither spherical nor isolated from grain boundaries. Stress concentration on these particles can occur during deformation which leads to fracture of the particle, forming pieces of various sizes and morphologies which make the measurement of particle's size difficult.

The program used determines the area fraction of the particles. Optical images were used. They were inverted into monochrome bitmaps by adjusting the contrast and changing threshold colour limits as can be seen in Figure 3.3. These steps have to be done accurately as they can significantly affect the precision of the measurement. Several areas of the specimen were viewed to calculate the total area of the particles per total viewed area of the specimen.

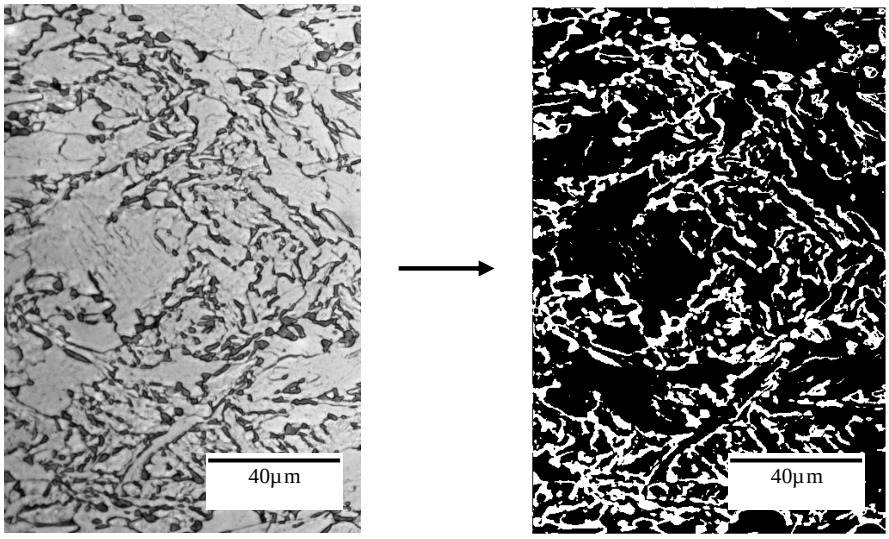

Figure 3.3: An example of the transformation of optical image into a monochrome bitmap for the particle's size and volume fraction measurement.

3.6.2 Scanning Electron Microscopy

The Scanning Electron Microscope (SEM) provides an image of surfaces and is capable of both high magnification and good depth of field. Unlike a light microscope, the SEM uses electrons instead of white light to view the specimen.

In SEM, the electron beam scans across the specimen surface point by point. The signal collected from each point is used to construct an image on the display, with the cathode ray tube beam and the column beam following a synchronised scanning pattern. This means the displayed image is the variation in detected signal intensity as the column beam is scanned across the sample.

The sample preparation for SEM examination was as for optical microscopy (described in Section 3.5.1). Samples were examined using a Philips XL30 FEG-SEM operating at a voltage of 20 KeV and spot size 3-4.

3.6.2.1 Electron Back-Scatter Diffraction on SEM

Electron back-scatter diffraction (EBSD) is based on a phenomena that was first observed in 1928 by Kikuchi. It is widely used for many applications including the studying of individual grain orientations, local texture, point-to-point orientation correlations and phase identification. Figure 3.4 shows the schematic diagram of the main components of an EBSD system.

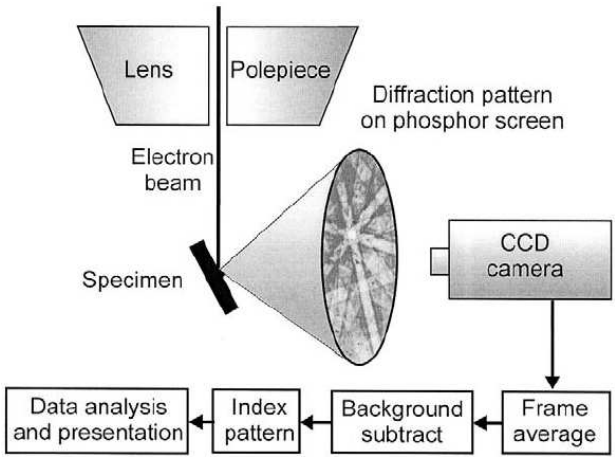

Figure 3.4: Schematic diagram showing the typical EBSD components (Humphreys and Hatherly 2004).

Briefly, the technique is based on acquisition of diffraction patterns from the flat surface of a specimen. To obtain an EBSD diffraction pattern, a stationary beam of electrons is sited on the specimen in an SEM. Backscattered electrons diffract at crystal lattice planes within the probe volume, according to Bragg's law. Since diffraction of the elastically scattered electrons through the Bragg angle is occurring in all directions, the result is a cone which appears as almost straight line when intersecting the phosphor screen where the Kikuchi lines are formed (Figure 3.5). The whole EBSD Kikuchi pattern consists of pairs of parallel lines where each pair is known as a Kikuchi band. These bands, which are collected on a phosphor screen, are viewed with a low-light video camera. Each Kikuchi band is effectively the trace of the plane from which it is formed. The fraction of diffracted backscatter electrons which are able to escape from the specimen surface is maximised by tilting the specimen so that it makes a small angle with the incoming electron beam (typically 20^{o}).

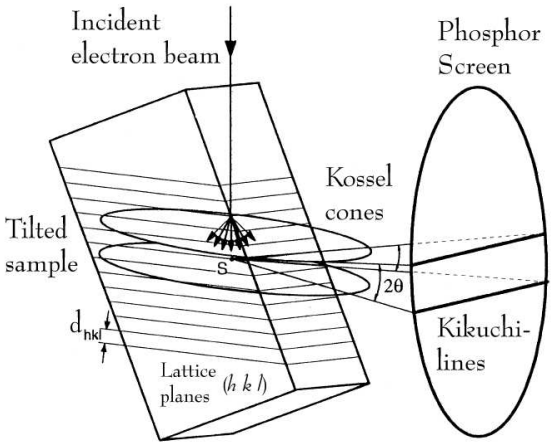

Figure 3.5: Origin of Kikuchi lines (Schwartz *et al*. 2000).

The EBSD technique was conducted on the as-rolled, partially recrystallised and fully recrystallised specimens using the CamScan MaXim, FEI-Sirion and Philips XL-30 FEGSEM microscopes equipped with Channel 5 EBSD acquisition software by HKL. In this study, this technique was used for orientation and texture analysis and, to some extent, quantifying the volume fraction of recrystallisation. The working distance ranged from 13 to 27 mm depending on the microscope used while the accelerating voltage and the sample tilt with respect to the electron beam were always 20 KeV and 70^{o}, respectively. The Philips XL-30 was mainly used for high magnification microtexture analysis (i.e. 6000x) while the others were used for macrotexture analysis with low magnification.

3.6.2.1.1 Sample Preparation for EBSD

Sample preparation is one of the most important steps for optimum EBSD analysis. The sample surface must be very flat, free from debris and deposits and have as little surface deformation as possible. The steps for grinding and polishing followed the same sequence as the preparation for optical microscopy. Then, the samples were etched lightly with 2% Nital to remove any residual surface deformation. After that, the samples were repolished on a ¼ μm diamond pad to remove the etched layer. The final polishing procedure was carried out using an oxide suspension for around 3 minutes. In some cases (specially with the HSLA steel), the samples were electro-polished using a solution of 8% perchloric acid and 92% acetic acid at around 50 volts for 50 seconds at room temperature.

3.6.2.1.2 EBSD Data Analysis

The EBSD data processing was mainly carried out using VMAP V.8, an in-house software developed by Humphreys (1999). This software is able to produce orientation maps using the three Euler angle colouring scheme. It has several features for the quantitative analysis of microstructures including misorientation statistics, boundary statistics and orientation representation by pole figures. The local texture determination from the EBSD technique was obtained using a coarser step size and covering a larger area compared to the EBSD measurement for microstructure investigation. The texture measurement was done using Textan III software, an in-house software developed by Bate (1990). This software is able to calculate and generate pole figures and orientation distribution functions (ODFs) from the EBSD

data. For the texture analysis of certain group of grains (e.g. recrystallised grains), HKL Channel 5 software (HKL Technology 2001) was used.

3.6.2.2 *In-Situ* EBSD

In order to more clearly identify the nucleation sites and, particularly, the location of the nucleation events within the deformation zones around the particles and to characterise the misorientation associated with moving boundaries, *in-situ* annealing treatments have been performed within the scanning electron microscope, during which the orientation of the growing grains and of their environment have been recorded. Generally, *in-situ* observations have the advantage of evaluating sequential microstructural changes and directly relating the deformed and recrystallised states. Figure 3.6 shows the hot stage used in this experiments in which the main components are identified. The heating element was of Kanthal wire having a resistance of about ~15Ω. It was wound onto an alumina tube. A cylindrical heat shield, made of stainless steel, surrounded the heater and covered the top of the stage except a small area which allowed the electron beam to hit the sample and the EBSD pattern to be emitted. The stage was mounted on an aluminium base with three 2.5mm diameter titanium alloy legs. The sample was fixed by graphite cement to a carbon disk of diameter 8mm and 1mm thickness which was close to the heating element. A chromel-alumel (K type) thermocouple was located at the centre of the carbon disk to allow an accurate measure of the temperature. The hot stage was then inserted in the CamScan MaXim FEG-SEM where the *in-situ* experiment was carried out. A series of EBSD maps were taken during annealing to allow a study of the texture development, specially the PSN effect on texture.

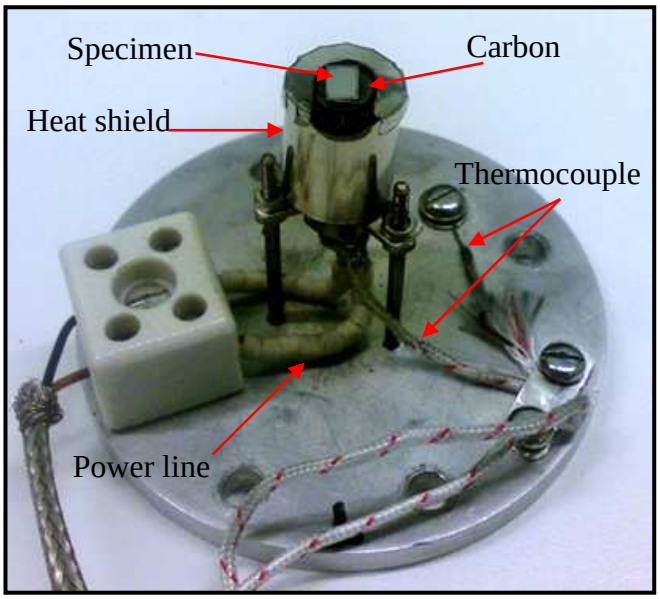

Figure 3.6: Photo of the hot stage used for the *in-situ* SEM/EBSD experiment and the main components are labled.

Three HSLA steel samples with different reductions (i.e. two 50% and one 70% reduction) were used in this *in-situ* experiment. Small samples of about 5x4 mm^2 with a thickness of 2mm were cut from the transverse cross section of the rolled material. Then, they were ground and polished following the same sequence as for the preparation for optical microscopy until a thickness of less than 1mm for all the samples was achieved. The samples were than electro-polished using a solution of 8% perchloric acid and 92% acetic acid at around 50 volts for 50 seconds at room temperature. The sample description and the operational conditions are explained in Table 3.3. The experimental conditions were, to some extent, similar to the static EBSD except for the reduction of time required for data collection which has a subsequent effect on the data produced.

Table 3.3: Operational conditions for the different samples used for the *in-situ* SEM/EBSD.

Material	**Mapping area (μm^2)**	**Step size (µm)**	**Acquisition time (min)**	**Heating temp. (^oC)**
HSLA 70%	40 x 30	0.2	~10	500-575
HSLA 50%	35 x 30	0.15	~15	500-580
HSLA 50%	30 x 25	0.1	~25	500-530

3.6.2.3 Energy Dispersive X-ray Spectrometry Analysis (EDX) on SEM

Energy Dispersive X-ray (EDX) analysis was carried out using the X-ray detector in the SEM in order to characterise the composition of the second phase particles present in the steels. The EDX system works by analysing the energy of X-rays emitted from the sample, which are characteristic of the element from which they have been produced. To stimulate the emission of characteristic X-rays from a specimen, a high energy beam of charged particles, such as electrons, is focused onto the sample. At rest, an atom within the sample contains ground state (or unexcited) electrons in discrete energy levels or electron shells bound to the nucleus. The incident beam may excite an electron in an inner shell, ejecting it from the shell while creating an electron hole where the electron was. An electron from an outer, higher-energy shell then fills the hole, and the difference in energy between the higher-energy shell and the lower energy shell may be released in the form of an X-ray. The number and energy of the X-rays emitted from a specimen can be measured by an energy dispersive spectrometer. As the energy of the X-rays is characteristic of the difference in energy between the two shells, and of the atomic structure of the element from which they were emitted, this allows the elemental composition of the specimen to be measured.

The sample preparation for EDX examination was as for optical microscopy (described in Section 2.4.1.1). EDX analysis was carried out on an XL30 FEG-SEM operating at a voltage of 20 KeV and spot size 3-4. Quantax software was used to analyze the data acquired from the second phase particles.

3.6.3 Transmission Electron Microscopy (TEM)

Transmission Electron Microscopy (TEM) uses a high energy electron beam to image and analyse the microstructure with atomic scale resolution. Unlike the SEM, the TEM electrons are transmitted through the sample instead of capturing the secondary and backscattered electrons near the surface. The main factor causing the high spatial resolution in the TEM is the small wavelength of the electrons used.

The bright field / dark field imaging modes of the microscope, which operate at intermediate magnification, combined with electron diffraction are invaluable and can be used to show structural, crystallographic and compositional information relating to very specific areas of the sample.

Sample preparation for TEM generally requires more time and experience than for most other characterization techniques. A piece of parent material, approximately 30 mm x 15 mm and 10 mm thick, was cut where the two large faces are parallel and flat. Discs with 3 mm diameter were cut from the block using electrical discharge machining. Each of these was mechanically ground to a thickness of 100 µm prior to electropolishing.

The as-ground discs were thinned until electron-transparent using a twin-jet Tenupol electropolishing machine containing 5% perchloric acid in ethanol. The temperature for the solution was maintained at about -30^{o}C using liquid nitrogen. After electropolishing, all foils were washed thoroughly in methanol and stored to prevent oxidation. All the TEM investigation was performed using an FEI Tecnai F30 FEG TEM at an accelerating voltage of 300 kV.

3.6.4 Texture Analysis by X-ray Diffraction (XRD)

The texture, in X-ray diffraction analysis, is determined from a set of pole figures. These pole figures are measured by the Schulz back-reflection technique (Schulz 1949) where the intensity distribution of a single *(hkl)* reflection is recorded by tilting and rotating the sample over the orientation sphere. In this way, the orientation distribution of a single reflection, and thus for a single lattice plane type, is determined. When a set of pole figures for independent crystal orientations has been measured, the orientation distribution function (ODF) of the crystallites can be calculated.

In this study, the texture of the cold rolled and fully annealed samples was determined by XRD from the central region of RD-TD sections using a Philips X-pert system. Specimens examined were sectioned to 20x20 mm slices. The steps for grinding and polishing followed the same sequence as the preparation for optical microscopy. The samples were then lightly etched in 2% Nital.

Samples were examined with Co Kα radiation and 110, 200 and 211 incomplete pole figures were generated using a step size 5^{o} for intensity measurement. The intensity values of the measured pole figures were connected for background level and defocusing.

Chapter 4

RESULTS

4.1 Microstructural Characterisation

Figure 4.1a shows the microstructure of the as-received IF steel sample taken from the central region of the sample thickness. This figure reveals a typically recrystallised structure with an average grain size of about 45µm. The microstructure of the as-received HSLA can be seen in Figure 4.1b which shows a mixture of equiaxed and acicular ferrite with a bimodal grain size distribution where smaller equiaxed grains surround the larger acicular grains. The average prior austenite grain size for the HSLA steel is about 113µm. The microstructures of both steels were uniform throughout the sample thickness.

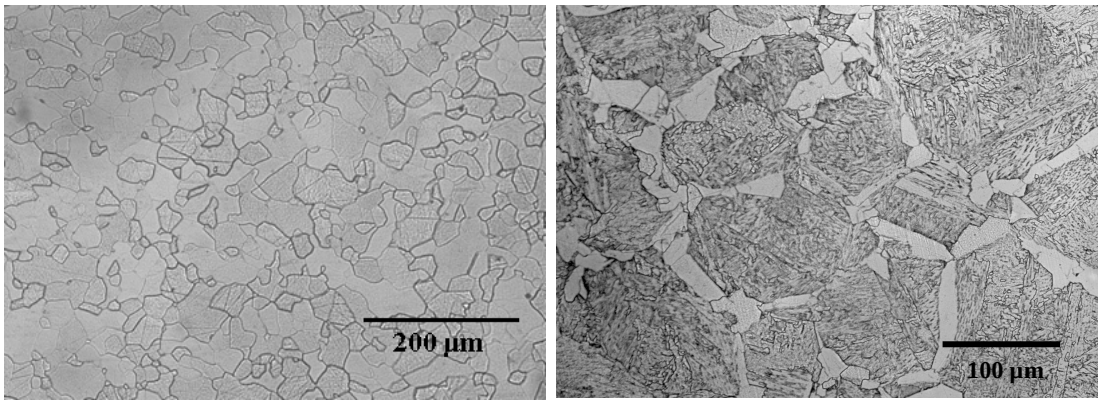

(a) (b)

Figure 4.1: Microstructure of the as-received samples of (a) IF steel and (b) HSLA steel.

In the case of HSLA steel, initial heat treatment was carried out to produce a spheroidised cementite structure. The heat treatment cycle applied is schematically illustrated in Figure 3.1 and discussed in Section 3.3. Figure 4.2a and b show the microstructures after different heat treatment steps while Figure 4.3 shows the final microstructure used in this study after completing the necessary heat treatment. Pearlite colonies or particles are formed, usually on the ferrite grain boundaries. The particles' volume fraction were measured to be about 20 ~ 24% with an average diameter of 3 μm.

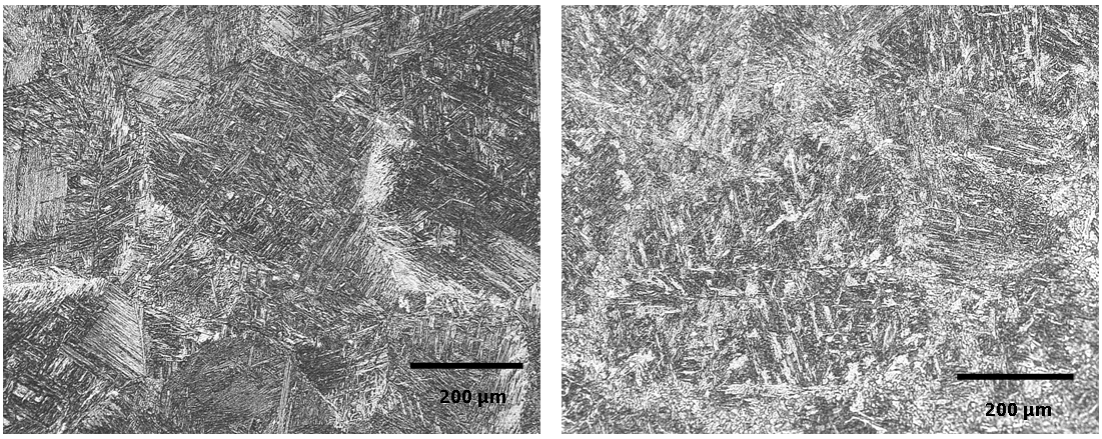

(a) (b)

Figure 4.2: Microstructure of the as-received HSLA samples after (a) heating at 1250^{o}C then water quenched (b) Reheating at 945^{o}C then water quenched.

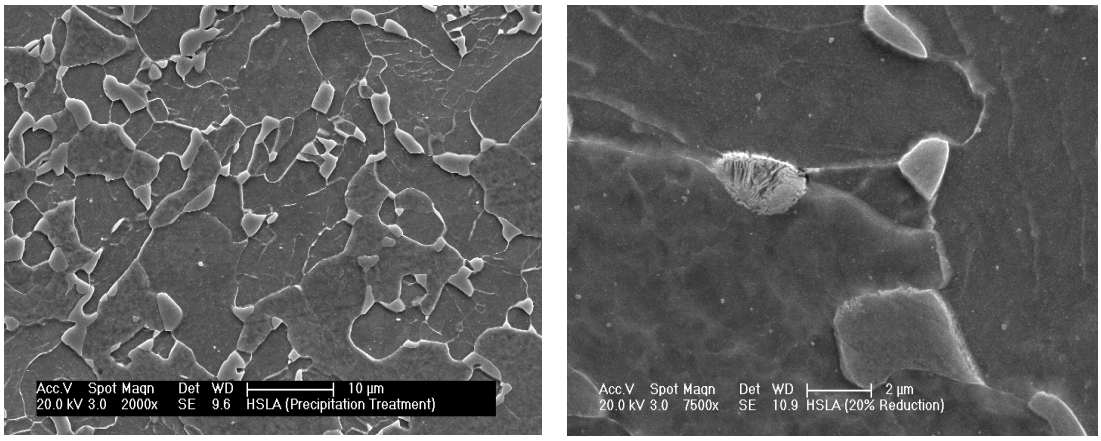

(a) (b)

Figure 4.3: Microstructures of the as-received HSLA sample after completing the heat treatment; (a) SEM image showing the size and distribution of the particles, and (b) at higher magnification showing the pearlitic nature of the particles.

In addition, EDX analysis of the inclusions present in the HSLA steel was done. The main type of inclusion was found to be the MnS. Some small NbC particles were also found. The EDX spectrum and the SEM images of the inclusions in the HSLA steel are shown in Figure 4.4.

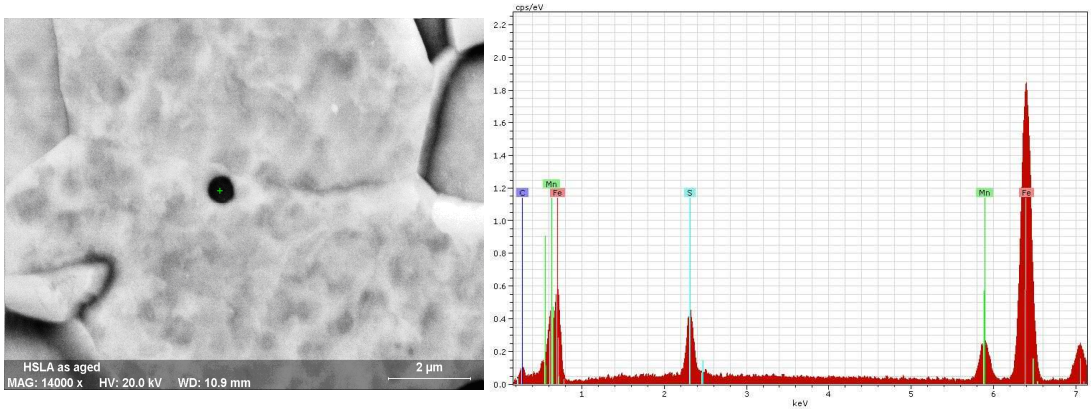

(a)

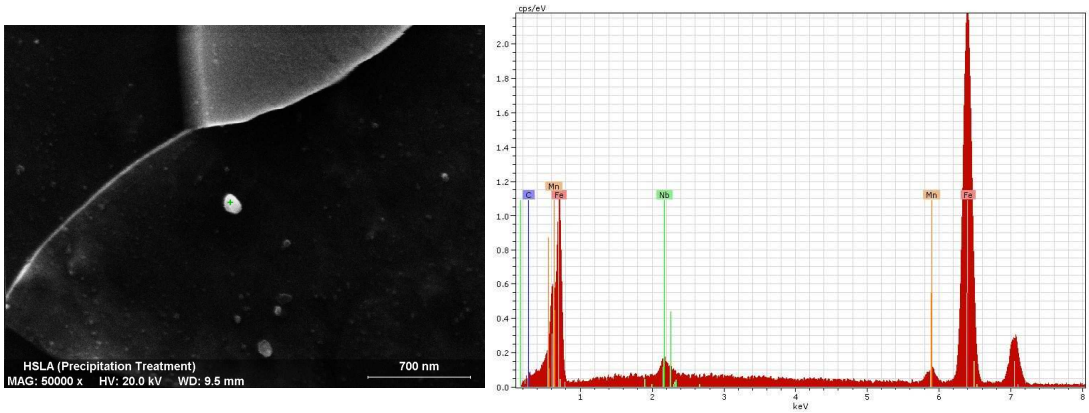

(b)

Figure 4.4: SEM-EDX analysis of the HSLA steel inclusions after heat treatment. (a) MnS and (b) NbC.

4.2 Microstructures of As-Rolled Material

In this study, both steels were cold rolled to reductions of 20%, 50%, 70% and 90%. The effect of different reductions on the microstructure can be seen in Figure 4.5 and Figure 4.6 for the IF and HSLA steel, respectively. These figures show that the grains became more elongated along the rolling direction as the reduction level increases. Also, evidence of deformation features such as deformation bands and shear bands (especially at 20% reduction) are clearly seen in Figure 4.7 for the IF steel. This figure shows the presence of in-grain shear bands in some grains inclined at an angle of ~ 35^{o} to rolling direction. Fracture of the particles on the HSLA steel occurred due to stress concentration during rolling, which led to the formation of fragments of various sizes and morphologies.

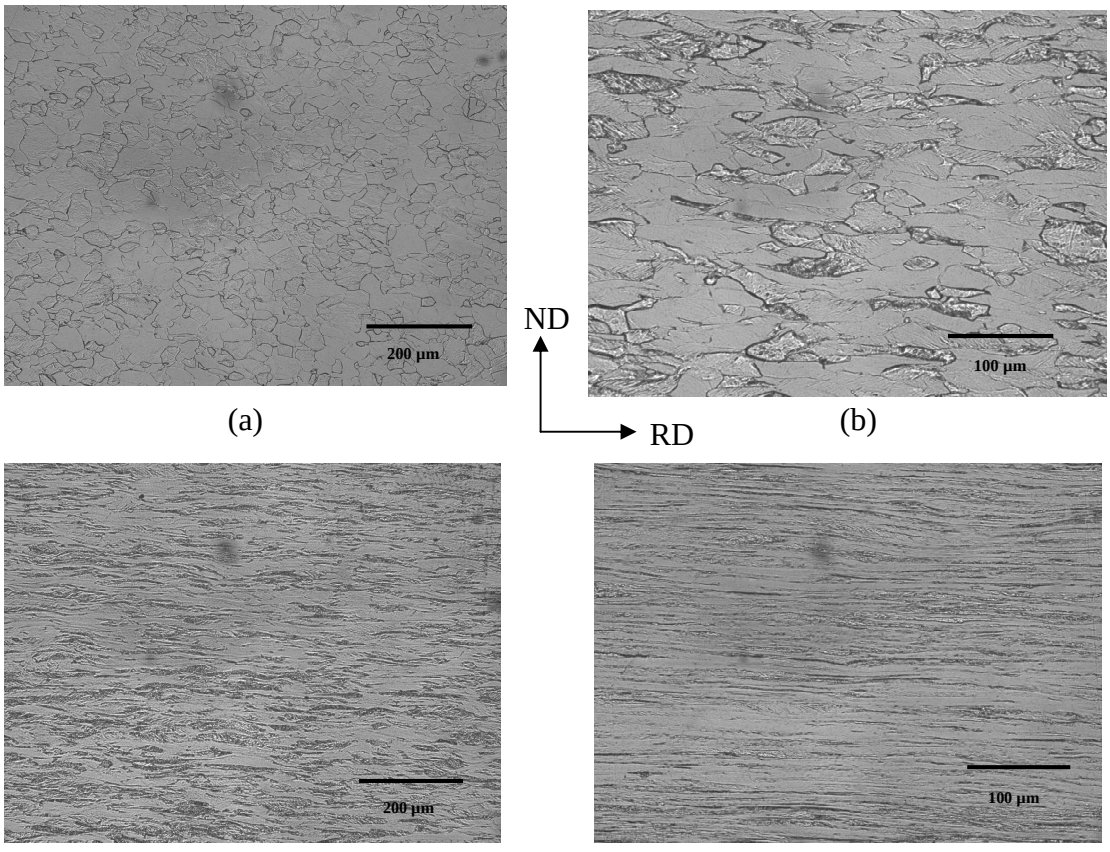

Figure 4.5: Transverse cross section microstructures of as-received IF steel sample rolled to (a) 20%, (b) 50%, (c) 70% and (d) 90%.

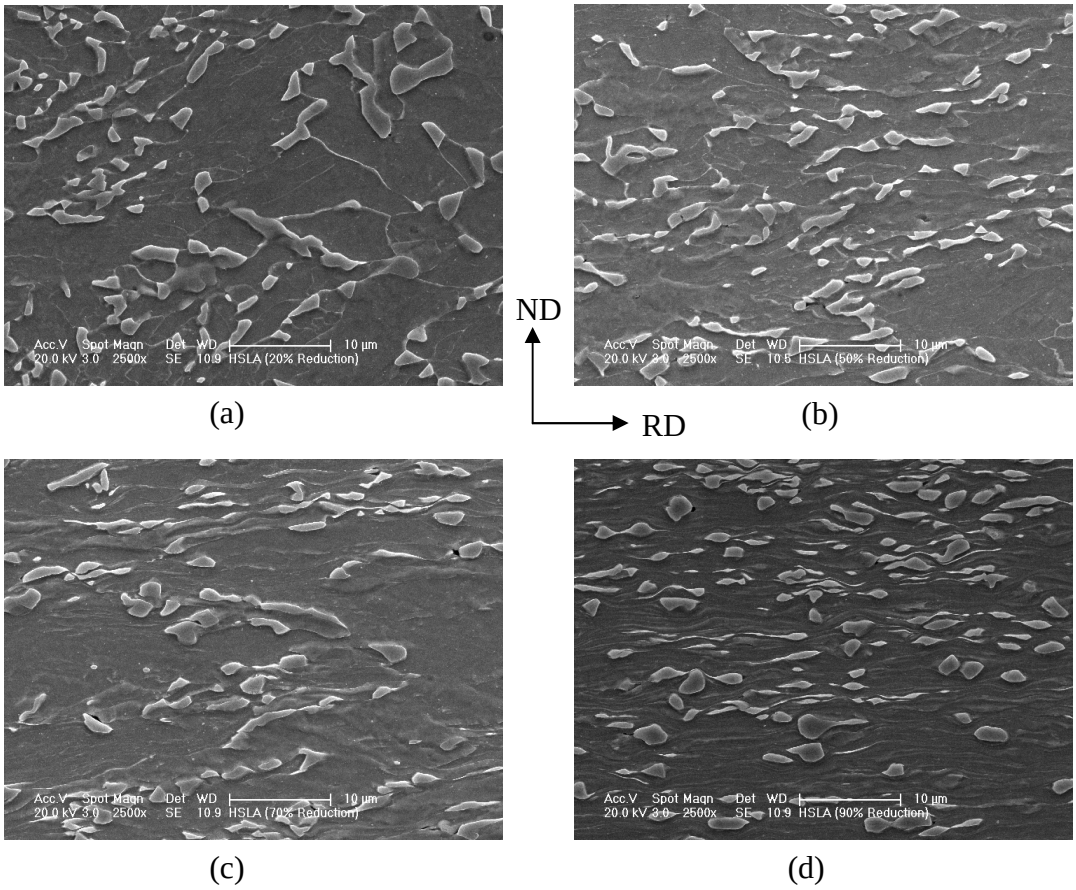

Figure 4.6: SEM images showing transverse cross section microstructures of HSLA steel sample rolled to (a) 20%, (b) 50%, (c) 70% and (d) 90%.

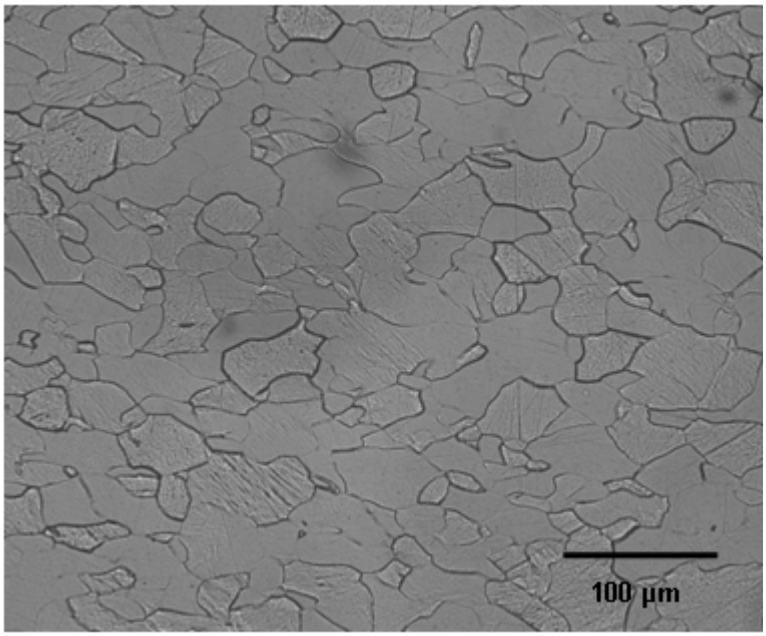

Figure 4.7: 20% cold rolled IF steel sample showing the presence of in-grain shear bands in some grains.

In order to determine the cell morphology and the misorientation between the cells of the deformed samples with higher accuracy and especially to take a closer look at the continuous orientation gradients, TEM investigations were carried out. Figure 4.8a shows the formation of cell and subgrain structures of a 50% cold rolled HSLA sample. This inhomogeneous distribution of the dislocations is a result of dynamic recovery. The size and misorientation of the cell/subgrain structure are dependent on the grain orientation as can be seen in Figure 4.8b. This figure shows two different grains where the size of the subgrains is different. The elongated subgrains (grain A) are separated by much sharper boundaries than the other grain (grain B) which indicate higher misorientations between neighbouring subgrains and, hence, higher stored energy.

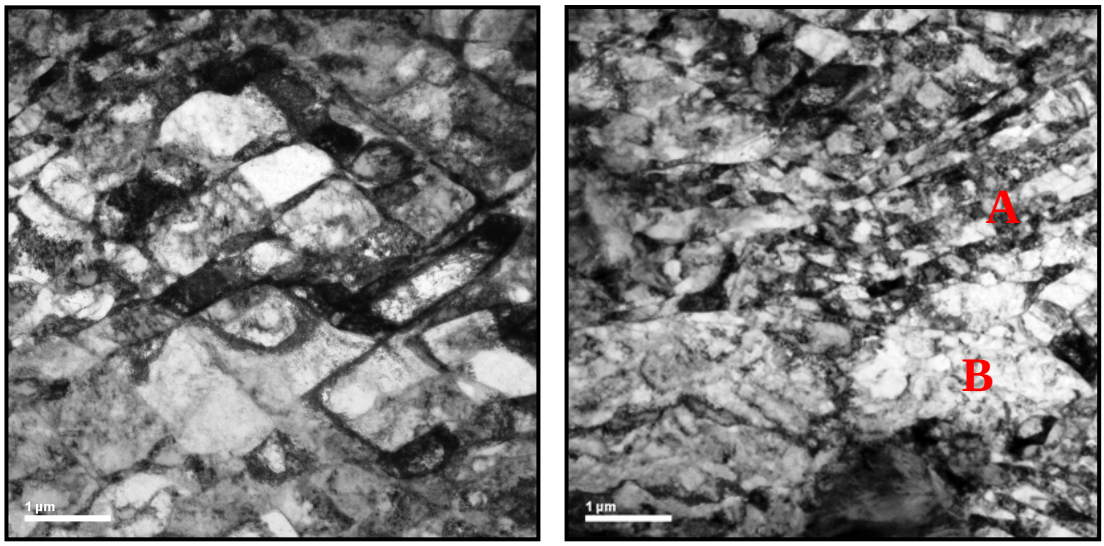

(a) (b)

Figure 4.8: Bright field TEM image of the HSLA steel rolled to 50% showing (a) the formation of cell/subgrain structure and (b) the effect of grain orientation on the size and misorientation of the cell/subgrain structure.

The presence of pearlitic particles in HSLA steel caused large strain inhomogeneities during deformation. These particles create high density dislocation zones (i.e. particle deformation zone) around them as can be seen in Figure 4.9. This figure shows clearly the effect of the particle on the dislocation structure where the dislocation cell size close to the particle-matrix interface is found to be very small. These zones are expected to act as recrystallisation nucleation sites and to accelerate the recrystallisation process.

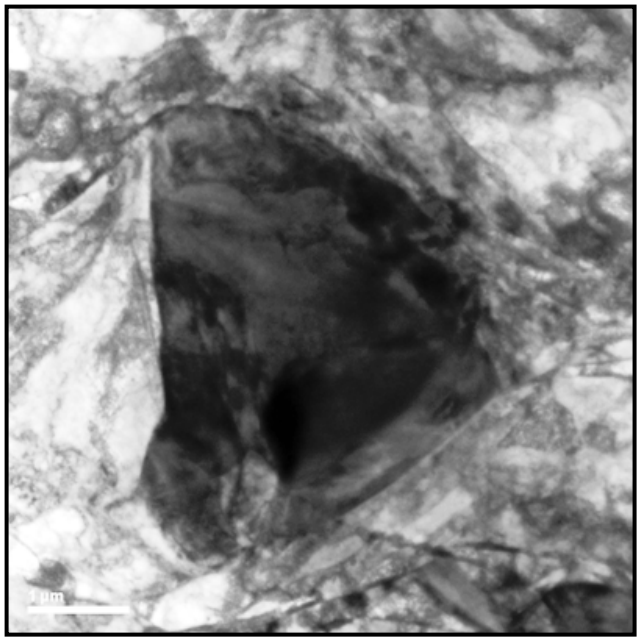

Figure 4.9: Bright field TEM image showing the effect of the particle on the dislocation structure on 50% cold rolled HSLA steel.

4.3 Hardness Measurements

The hardness of the samples after various stages of cold rolling and subsequent heat treatment were measured, except for the 90% reduction IF steel sample where the macrohardness measurements were difficult to obtain due to the small sample thickness.

Figure 4.10a shows the hardness of both HSLA and IF steel samples after various stages of cold rolling. From this figure it can be seen that as the level of reduction increases the hardness increases due to the increase in the dislocation density. Moreover, the interactions between the particles and the dislocations involved in the deformation of HSLA steel are responsible for the greater increase in hardness compared with the IF steel.

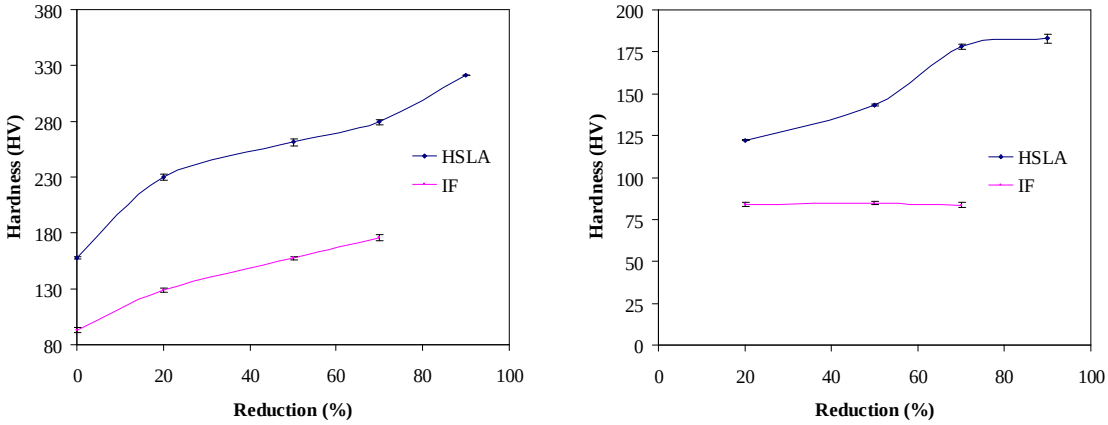

Figure 4.10: Macrohardness measurements of the (a) as rolled and (b) material fully annealed after rolling.

In addition, the hardness of the fully annealed samples for every stage of reduction is given in Figure 4.10b. This was measured prior to any significant grain growth occurred in the material and is shown, particularly in IF steel, to be not affected by the degree of reduction. However, the increase in hardness observed in the fully annealed samples of HSLA steel with increasing reduction is associated with the dissolution of the pearlitic particles during annealing.

4.4 Recrystallisation Kinetics

4.4.1 Recrystallisation Kinetics using Optical Microscopy

The effect of cold rolling degree and annealing time and temperature on recrystallisation kinetics were investigated in this study mainly using optical metallography. A full list of figures related to the annealing process for all different reductions of both steels has been included in Appendix B. Figure 4.11 shows the microstructural evolution of the 70% cold rolled IF steel sample annealed at 620^{o}C for different time intervals. These are partially recrystallised microstructures where the recrystallisation fraction increases with increasing annealing time. The preferred nucleation sites for this steel were the grain boundaries, due to the small original grain size. "Strain-free" grains formed at shear bands were rarely found and they mainly in the low reduction (i.e. 20%) material.

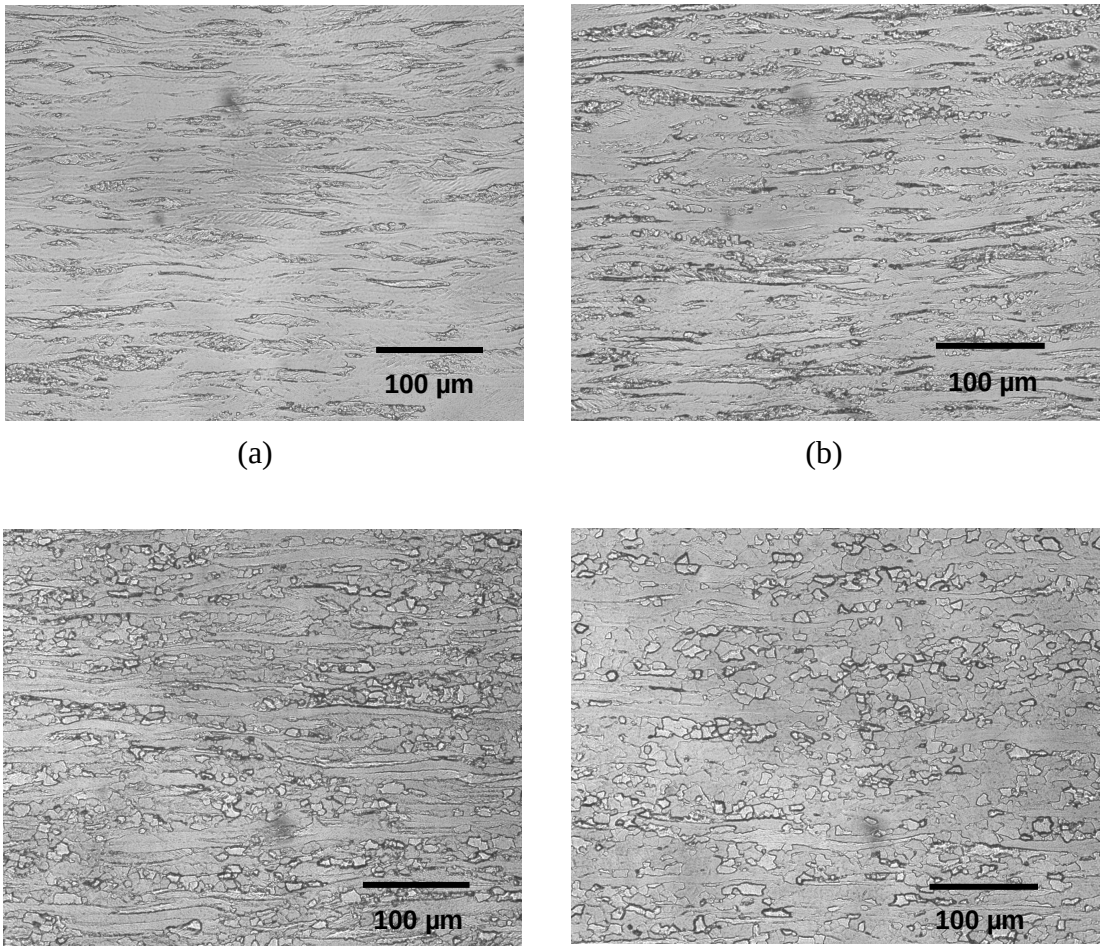

(a) (b)

(c) (d)

Figure 4.11: IF steel sample cold rolled to 70% and annealed at 620^{o}C for (a) 2 hrs, (b) 7hrs, (c) 10 hrs and (d) 15 hrs.

Figure 4.12 shows the microstructural evolution of the 70% cold rolled HSLA steel sample annealed at 500^{o}C for different time intervals. The preferred nucleation sites were the pearlitic particles. There was no evidence of any other nucleation sites as can be seen in Figure 4.13a-b. The reasons behind that are the low recrystallisation temperature and the high volume fraction of the particles.

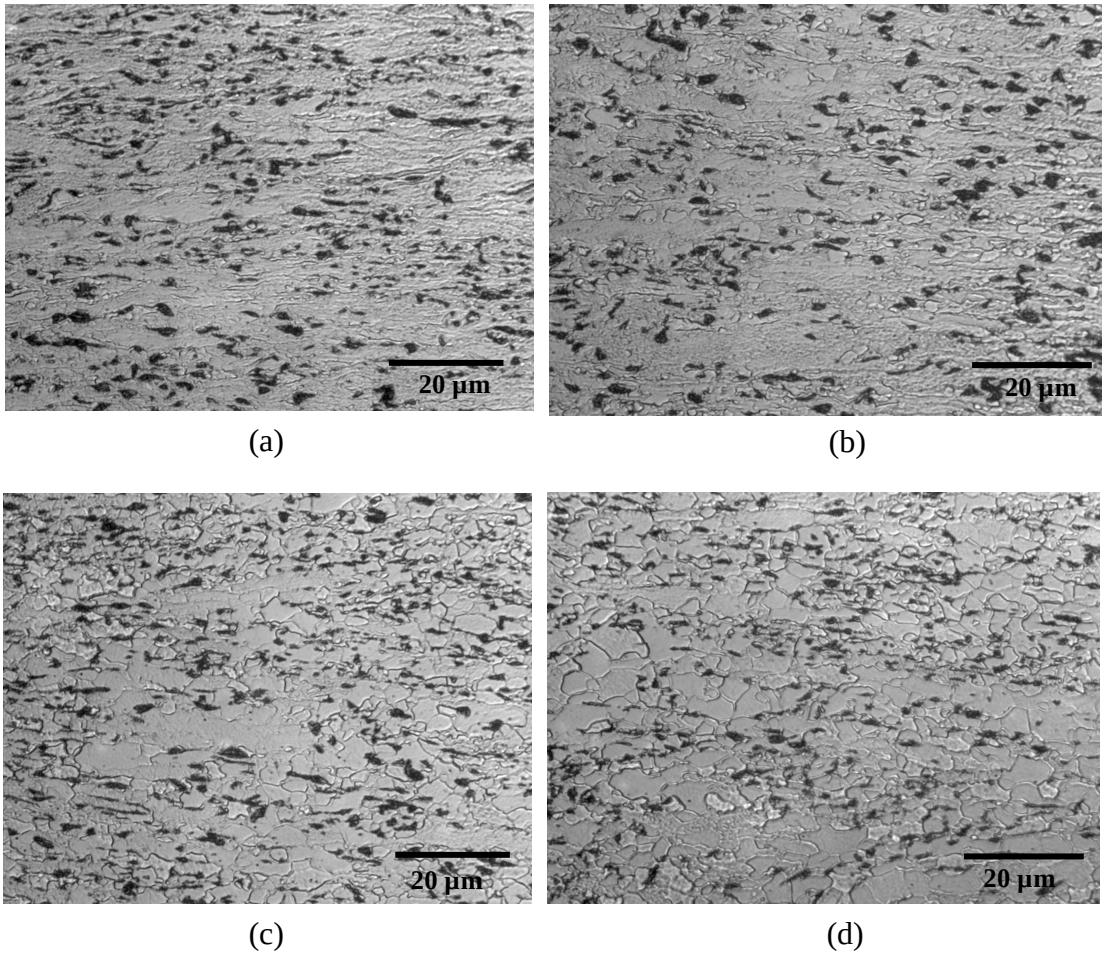

Figure 4.12: HSLA steel sample cold rolled to 70% and annealed at 500^{o}C for (a) 2 hrs, (b) 7hrs, (c) 16 hrs and (d) 24 hrs.

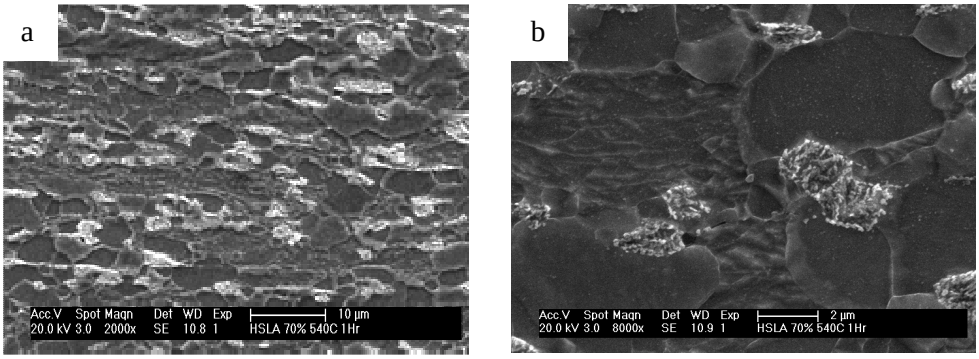

Figure 4.13: HSLA steel sample cold rolled to 70% and annealed to 60% recrystallisation showing the locations of the nuclei (a) at low magnification and (b) at higher magnification.

The recrystallisation kinetics for different annealing temperatures and cold rolling reductions are shown in Figure 4.14a-d for IF steel and Figure 4.15a-d for HSLA steel. The aim was to have full recrystallisation for all four degrees of reductions within one day. This means decreasing the annealing temperature as the level of reduction increases. The same figures (Figure 4.14a-d and Figure 4.15a-d) also show the influence of annealing process on the hardness. It was observed that the hardness of the materials decreases with increasing the recrystallisation fraction.

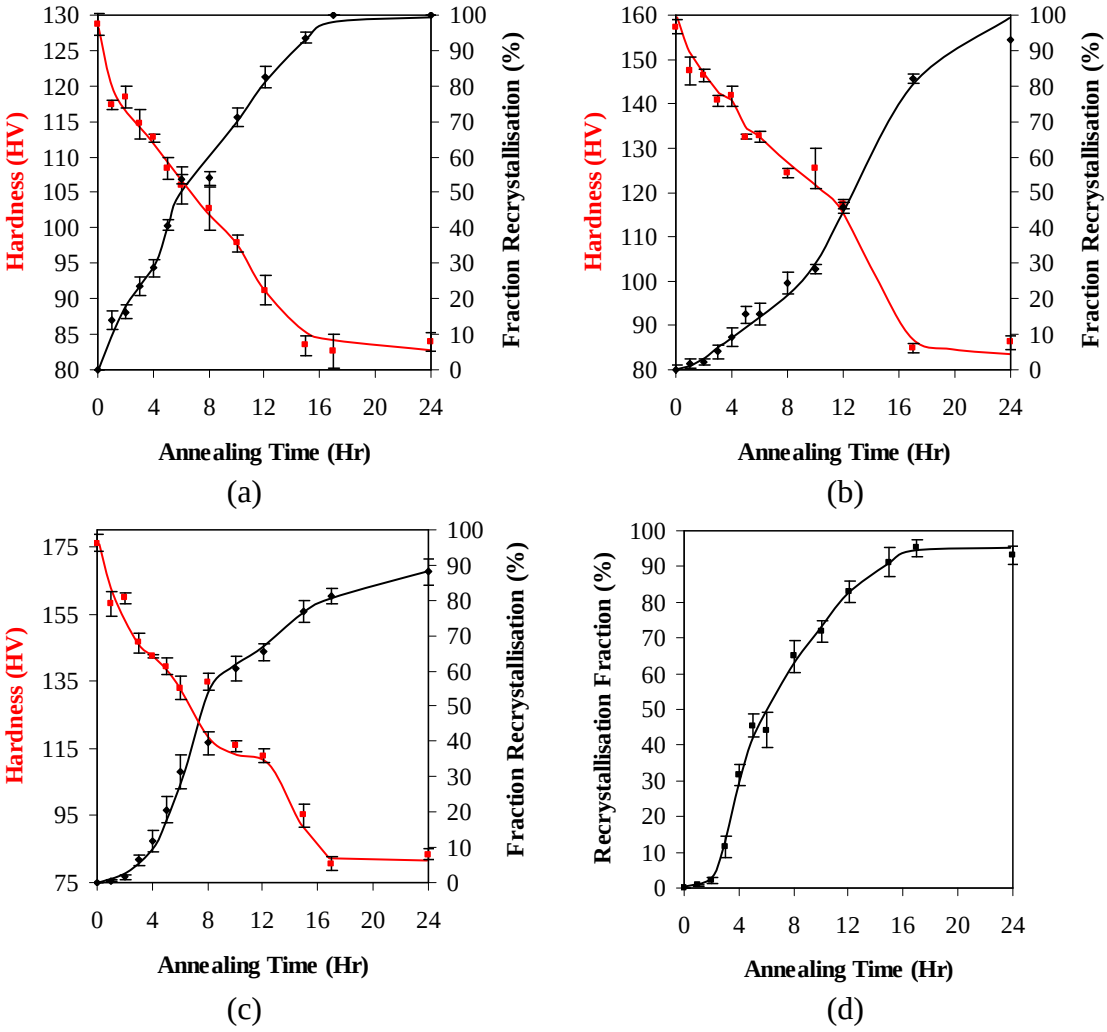

Figure 4.14: Effect of annealing temperature and rolling reduction on the kinetics of recrystallisation in IF steel. (a) 20% reduction annealed at 690^{o}C, (b) 50% reduction annealed at 640 ^{o}C, (c) 70% reduction annealed at 620^{o}C and (d) 90% reduction annealed at 620^{o}C.

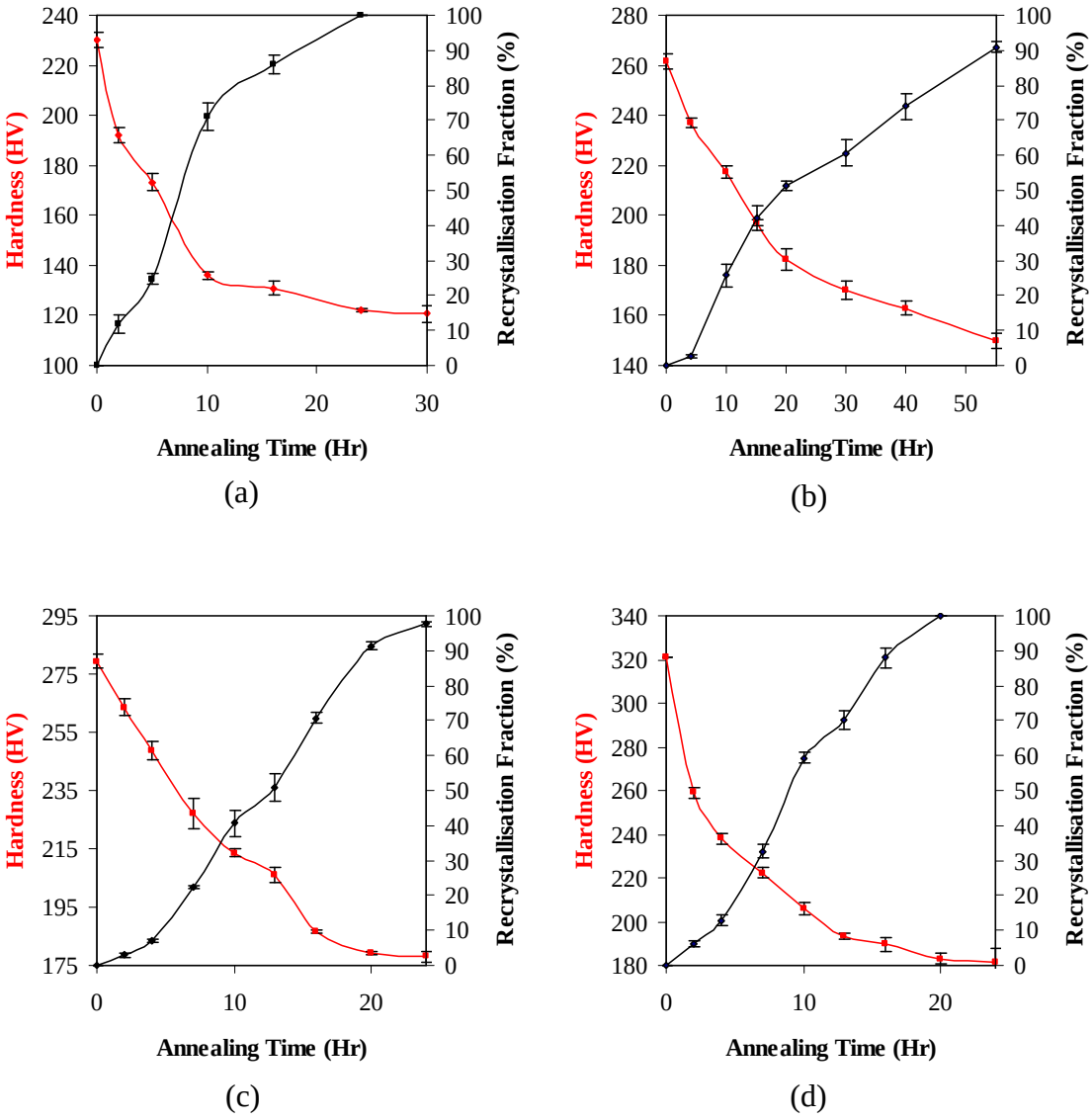

Figure 4.15: Effect of annealing temperature and rolling reduction on the kinetics of recrystallisation in HSLA steel. (a) 20% reduction annealed at 560^{o}C, (b) 50% reduction annealed at 500 ^{o}C, (c) 70% reduction annealed at 500^{o}C and (d) 90% reduction annealed at 500^{o}C.

An example of the effect of annealing temperature on recrystallisation is given in Figure 4.16a for 50% cold rolled IF steel and in Figure 4.16b for 20% cold rolled HSLA steel. Both figures show that a higher annealing temperature results in a higher rate of recrystallisation. In addition to the effect of annealing temperature, Figure 4.17a-b show the effect of the degree of cold rolling on recrystallisation during annealing at 620°C and 500°C for IF and HSLA steel, respectively. All of these figures show that the rate of recrystallisation increases with increasing annealing temperature and cold rolling reduction.

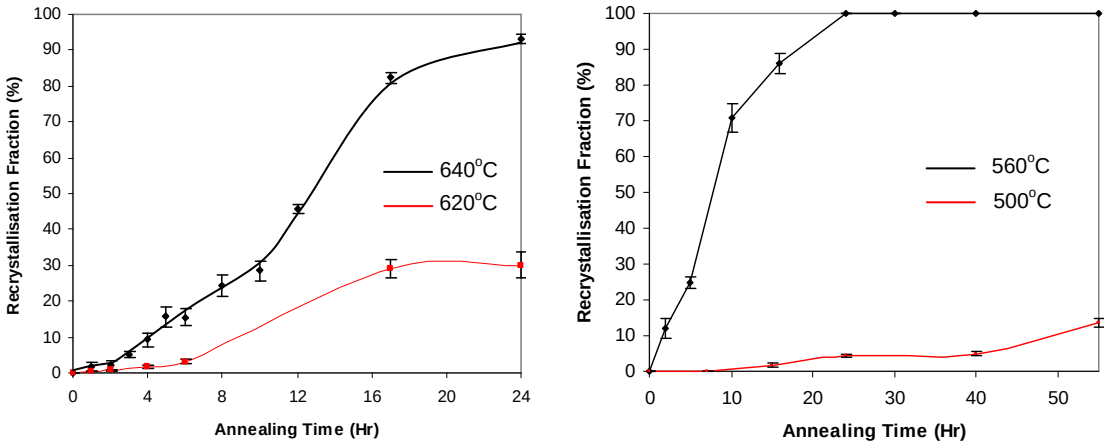

(a) (b)

Figure 4.16: Effect of annealing temperature on the kinetics of recrystallisation in (a) 50% cold rolled IF steel and (b) 20% cold rolled HSLA steel.

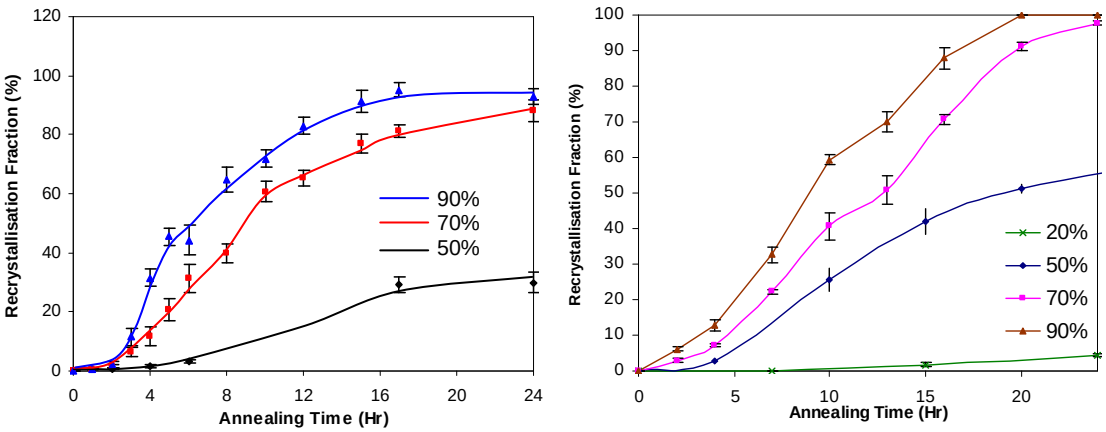

(a) (b)

Figure 4.17: Effect of cold rolling reduction on the kinetics of recrystallisation during annealing at (a) 620°C for IF steel and (b) 500°C for HSLA steel.

4.4.2 JMAK Modelling

The kinetics of recrystallisation, obtained in this study by using mainly optical microscopy, can be used to obtain a JMAK-type relationship between fraction recrystallised (X_v) and time for annealing (t). A linear plot between ln[ln{1/(1-X_v)}] and ln(t) can be used to obtain the values for JMAK exponent n and the parameter B. Figure 4.18a-c and Figure 4.19a-b show this type of plot (known as JMAK plot) for the four different cold reductions, each with its own annealing temperature for the IF and HSLA steels, respectively. In addition, the corresponding JMAK exponent n and the parameter B are given in Table 4.1 for all four different levels of reduction for both steels.

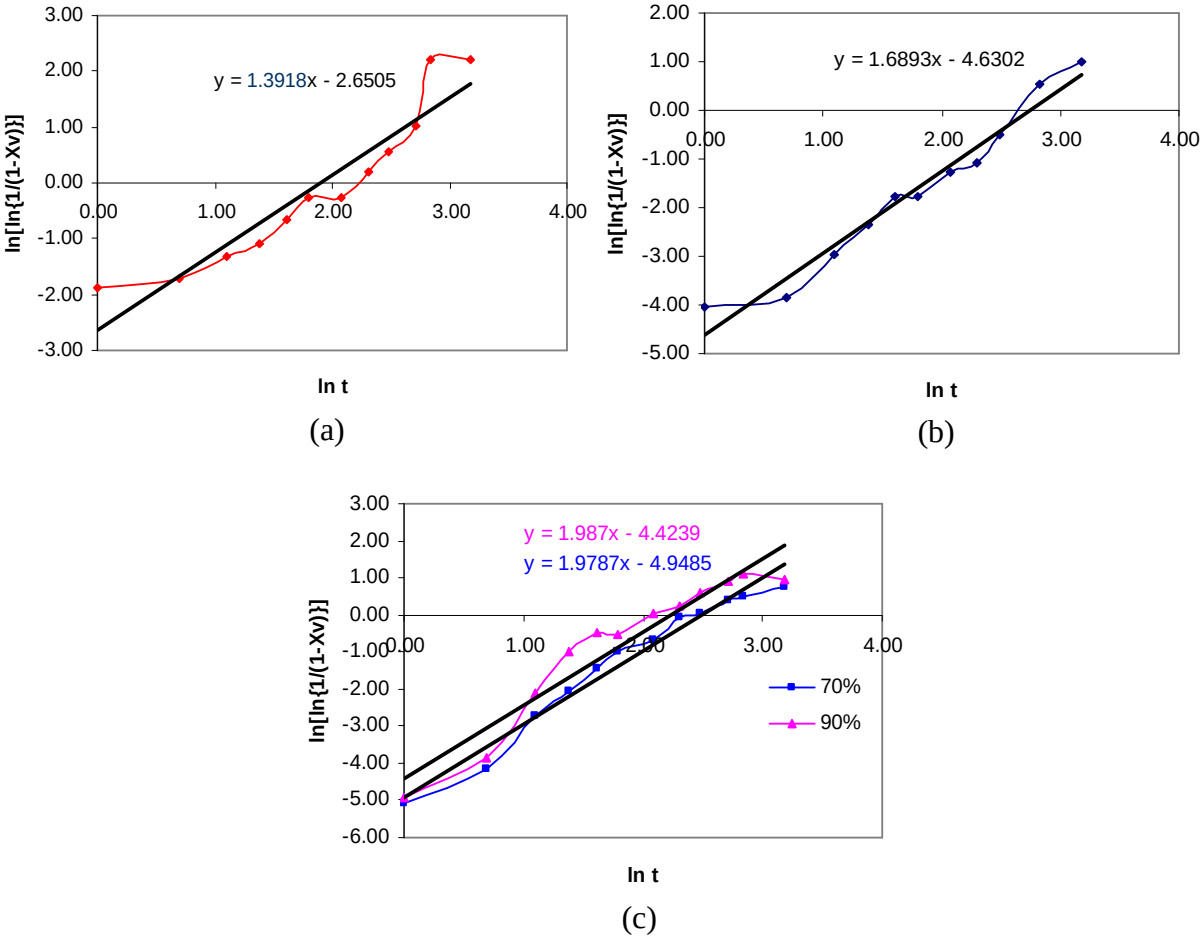

Figure 4.18: JMAK plots of recrystallisation kinetics (showing the trend line with its formula) for IF steel for (a) 20% reduction annealed at 690^{o}C, (b) 50% reduction annealed at 640 ^{o}C, (c) 70% and 90% reductions annealed at 620^{o}C.

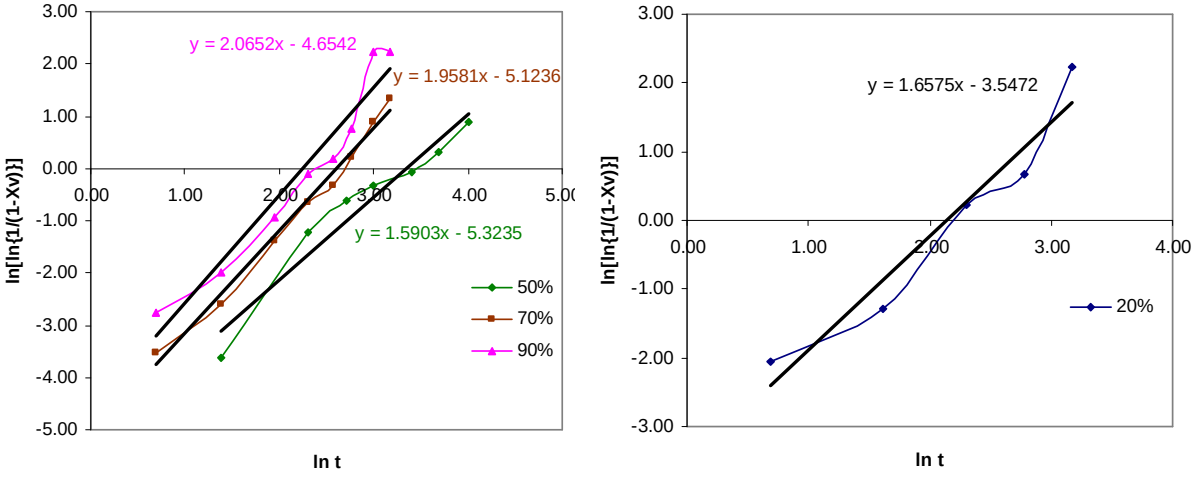

(a) (b)

Figure 4.19: JMAK plots of recrystallisation kinetics (showing the trend line with its formula) for HSLA steel for (a) 50%, 70% and 90% reductions annealed at 500^{o}C, (b) 20% reduction annealed at 560^{o}C.

Table 4.1: JMAK exponent n, the parameter B and the data deviation from a straight line (R^2-value) determined for the various levels of reduction with different annealing temperature for both steels.

Material	Reduction % @ Anneal. Temp	*n*	B	R^2
IF	20% @ 690^{o}C	1.3918	0.07062	0.89
	50% @ 640^{o}C	1.6893	0.009753	0.96
	70% @ 620^{o}C	1.9787	0.007094	0.97
	90% @ 620^{o}C	1.987	0.01199	0.92
HSLA	20% @ 560^{o}C	1.6575	0.02881	0.94
	50% @ 500^{o}C	1.5903	0.004876	0.94
	70% @ 500^{o}C	1.9581	0.005955	0.99
	90% @ 500^{o}C	2.0652	0.009522	0.94

Plots for comparison of recrystallisation kinetics as obtained from original optical microscopy data and from JMAK analysis of this data can be seen in Figure 4.20a-d and Figure 4.21a-d for IF and HSLA steels, respectively. Both methods show similar recrystallisation kinetics behaviour for all four reductions.

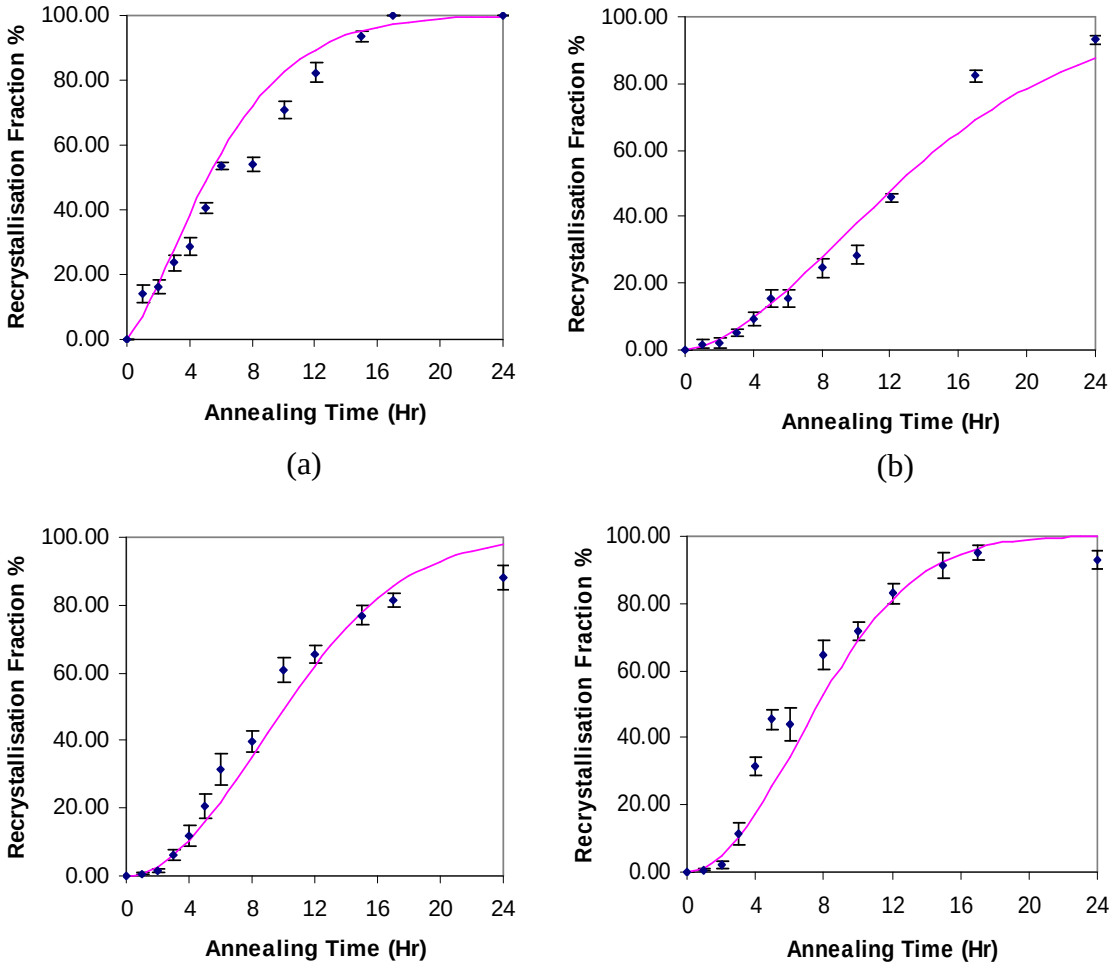

Figure 4.20: Comparison of recrystallisation kinetics obtained from optical microscopy (points) and from JMAK model fitting (line) for IF steel for (a) 20% reduction annealed at 690^{o}C, (b) 50% reduction annealed at 640 ^{o}C, (c) 70% reduction annealed at 620^{o}C and (d) 90% reduction annealed at 620^{o}C.

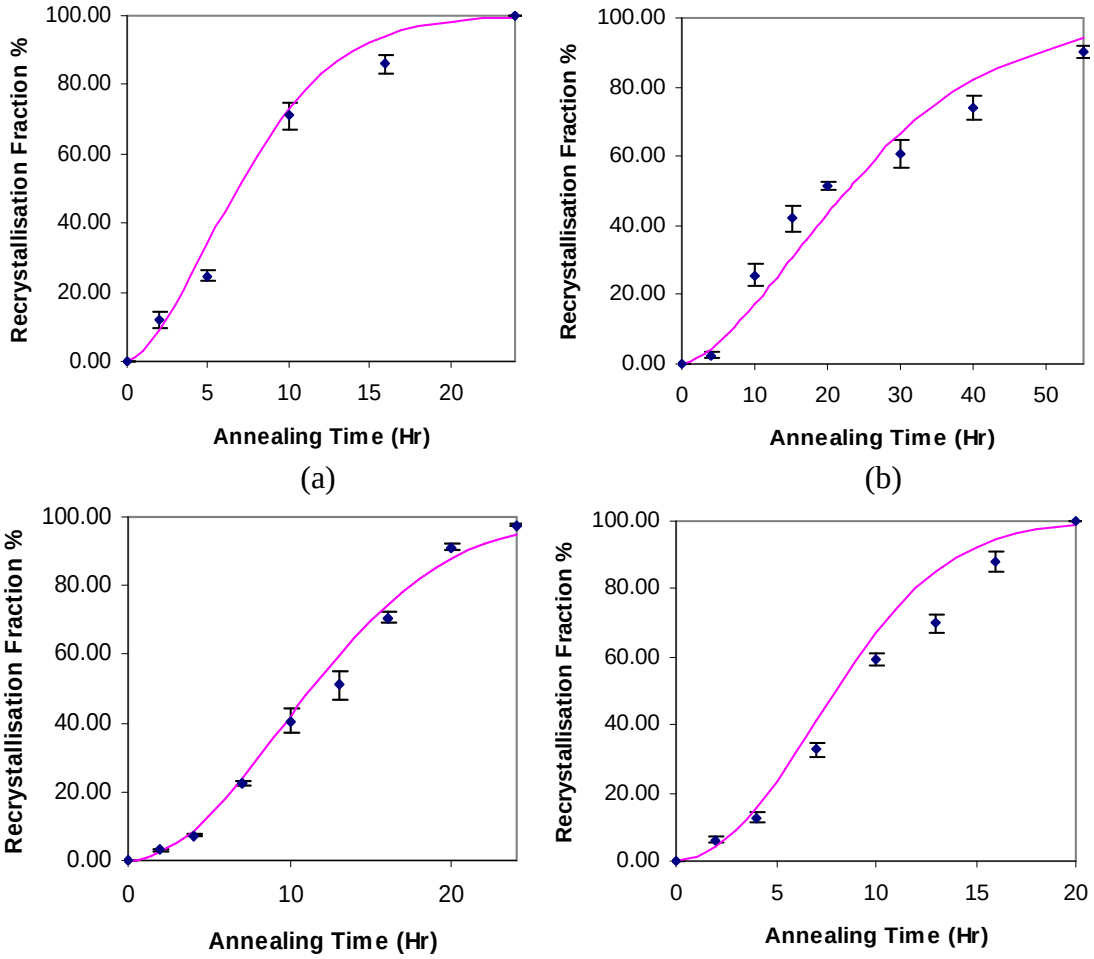

Figure 4.21: Comparison of recrystallisation kinetics obtained from optical microscopy (points) and from JMAK model fitting (line) for HSLA steel for (a) 20% reduction annealed at 560^{o}C, (b) 50% reduction annealed at 500 ^{o}C, (c) 70% reduction annealed at 500^{o}C and (d) 90% reduction annealed at 500^{o}C.

4.4.3 Quantifying Recrystallisation by EBSD

The recrystallised fraction was determined in some partially recrystallised samples using EBSD with the help of VMAP and HKL Channel 5 software. The results were compared with the results from optical microscopy.

An example of a partially recrystallised sample is given in Figure 4.22a, with Figure 4.22b showing the recrystallised grains (green regions) as characterised by the VMAP software. The new (recrystallised) grains were defined as grains bounded by at least 60% high angle grain boundary (HAGB) with a size of at least twice the size of non-HAGB subgrains. The volume fraction of recrystallisation in this sample characterised by EBSD is 16% compared with a 12% recrystallisation fraction measured by optical microscopy.

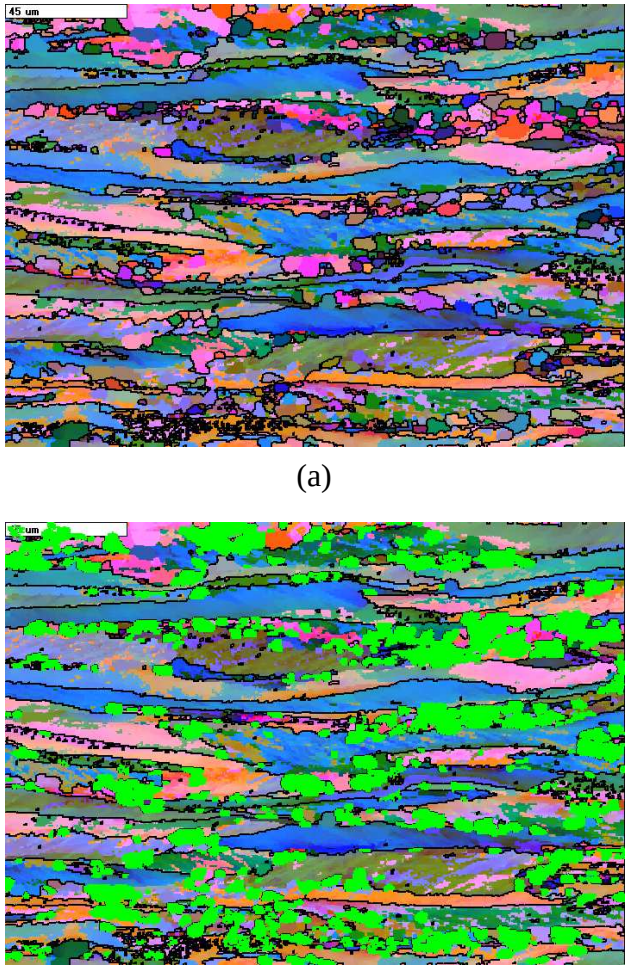

(a)

(b)

Figure 4.22: EBSD micrograph showing 70% cold rolled IF steel annealed at 620^{o}C for 4 hours. (a) raw micrograph, (b) after recrystallisation analysis showing the recrystallised grains as green regions.

Another example of using EBSD to measure the recrystallisation fraction is given in Figure 4.23. This figure shows the microstructure of 50% cold rolled HSLA steel annealed at 500^{o}C for 10 hours. The recrystallisation fraction was calculated by defining the recrystallised grains as in the previous example. The recrystallisation fraction in this sample measured by EBSD is found to be 25%, so giving the same result obtained from optical measurements.

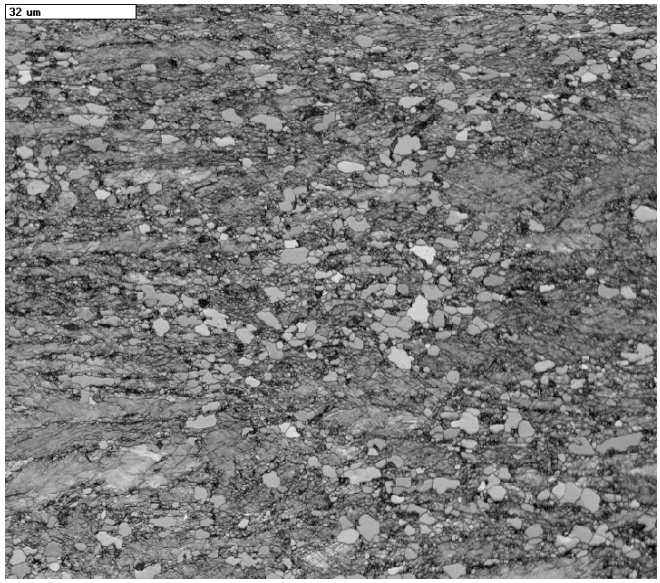

(a)

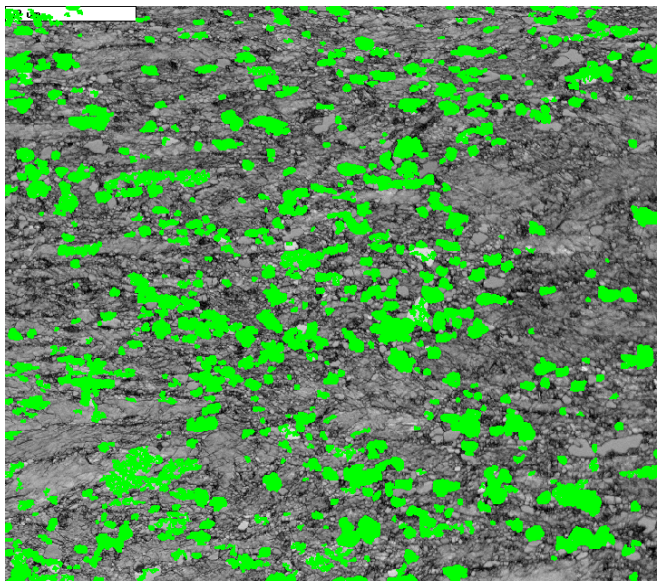

(b)

Figure 4.23: EBSD micrograph showing 50% cold rolled HSLA steel annealed at 500^{o}C for 5 hours. (a) raw micrograph (band contrast), (b) after recrystallisation analysis showing the recrystallised grains as green regions.

4.5 Microstructure and Texture Investigation

The cold rolling and recrystallisation microstructure and texture of IF and HSLA steels have been investigated in this study using the techniques described in Chapter 3. To clarify the possible mechanisms of recrystallisation texture formation, a detailed investigation was carried out. Particular attention was given to the orientation of certain grains, especially those related to the Particle Stimulated Nucleation (PSN) mechanism of recrystallisation.

4.5.1 Cold Rolling Texture

The cold rolling texture for 20%, 50%, 70% and 90% cold rolling reductions of the IF and HSLA steels were measured using EBSD and are shown in Figure 4.24 and Figure 4.25, respectively. The texture for both steels is shown to be largely dependent on the rolling reduction. With increasing rolling reduction, the texture shows gradual intensification of α- and γ-fibre components. However, the intensity of both fibres is weaker in the HSLA steel.

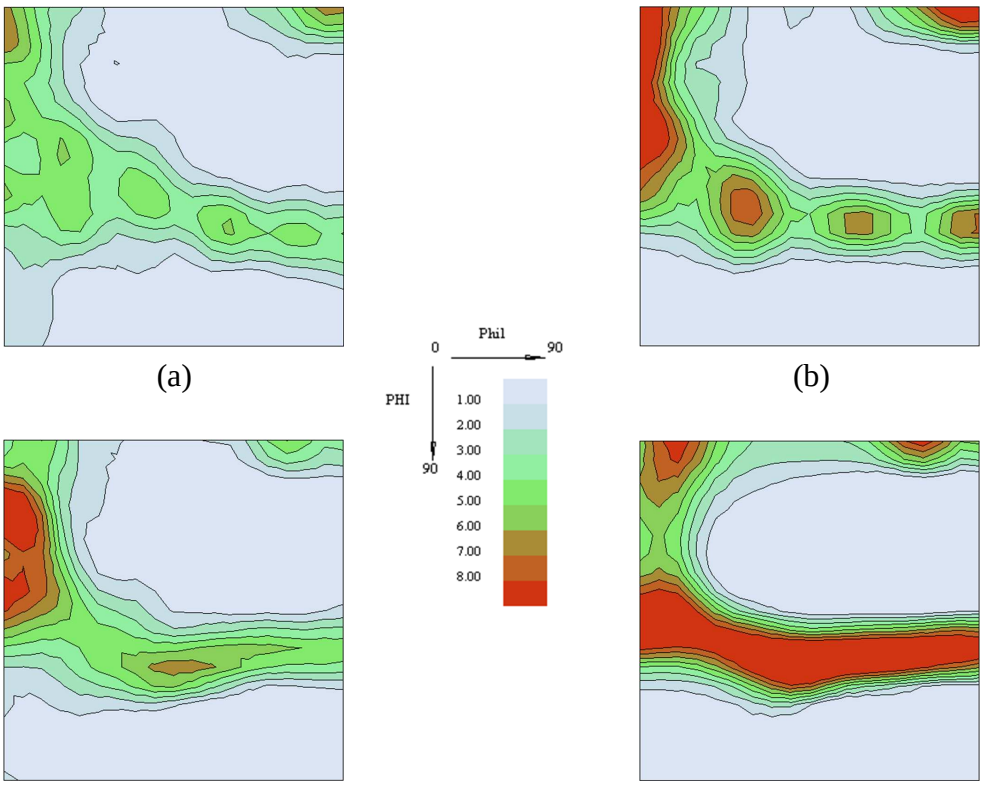

Figure 4.24: Textures of IF steel (ODF φ_2=45^o sections) cold rolled (a) 20%, (b) 50%, (c) 70% and (d) 90%.

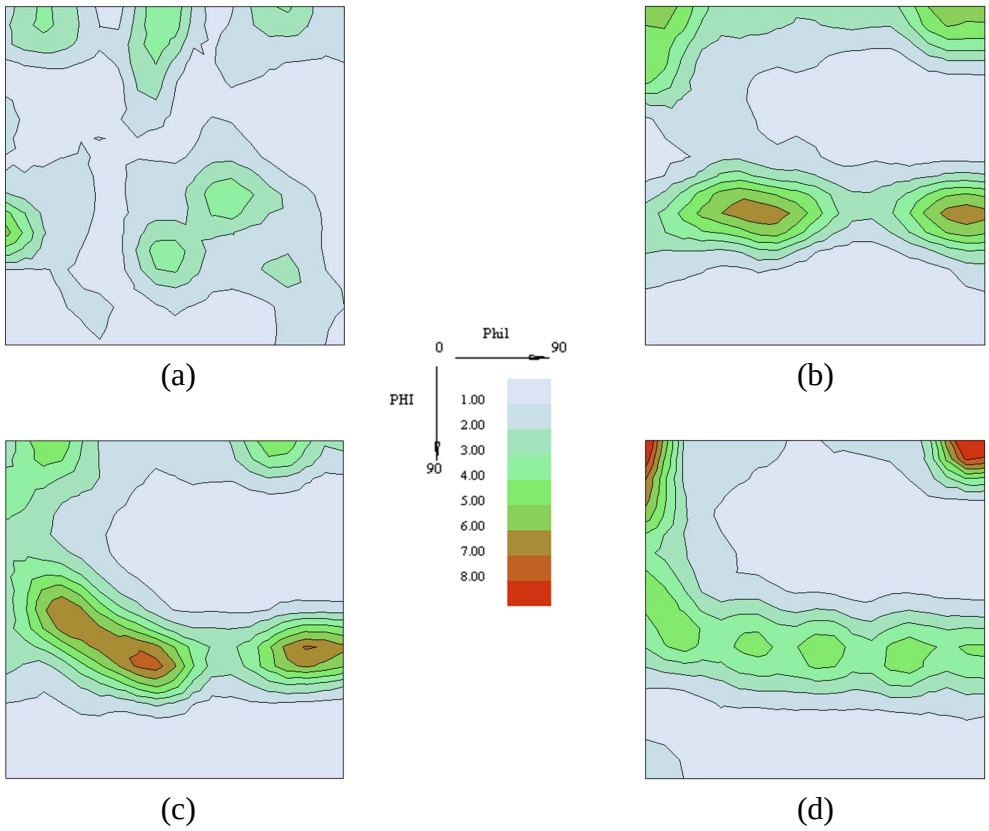

Figure 4.25: Textures of HSLA steel (ODF φ_2=45^o sections) cold rolled (a) 20%, (b) 50%, (c) 70% and (d) 90%.

The orientation density along α- and γ-fibres after several cold rolling reductions can be seen in Figure 4.26 for the IF steel and Figure 4.27 for the HSLA steel. A higher orientation density along the α-fibre in the IF steel compared to the HSLA steel was observed, except for 90% reduction where there is a sharp increase in the (001)[$1\bar{1}0$] texture component in the HSLA steel. A strong peak occurs at (111)[$1\bar{1}0$] is also observed with high reduction (i.e. 90%) in the IF steel. In general, the densities of α-fibre texture components steadily increase with increasing reduction in both steels. On the other hand, the orientation densities along the γ-fibre are quite uniformly distributed. High orientation density along this fibre is observed after 90% reduction in the IF steel compared with the other reductions, where the texture changes are similar. A peak occurring at (111)[$1\bar{2}1$] is observed with 50% reduction. HSLA steel shows a uniform distribution of the texture components along the γ-fibre for 90% reduction whereas the 50% and 70% show high densities of (111)[$1\bar{2}1$] and (111)[$\bar{1}\bar{1}2$] texture components.

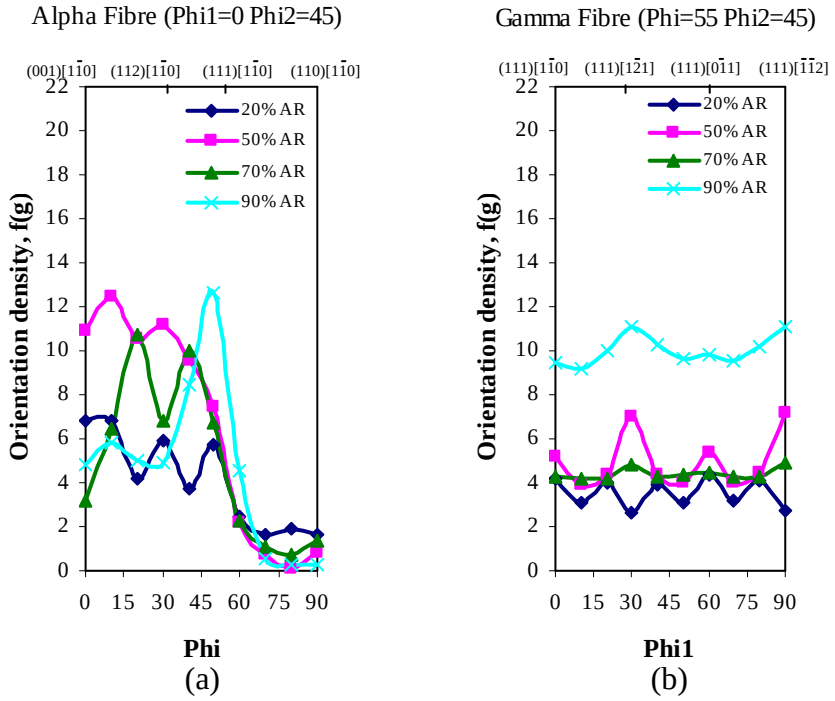

Figure 4.26: Orientation density along (a) α-fibre and (b) γ-fibre, for IF steel after cold rolling reductions of 20%, 50%, 70% and 90%.

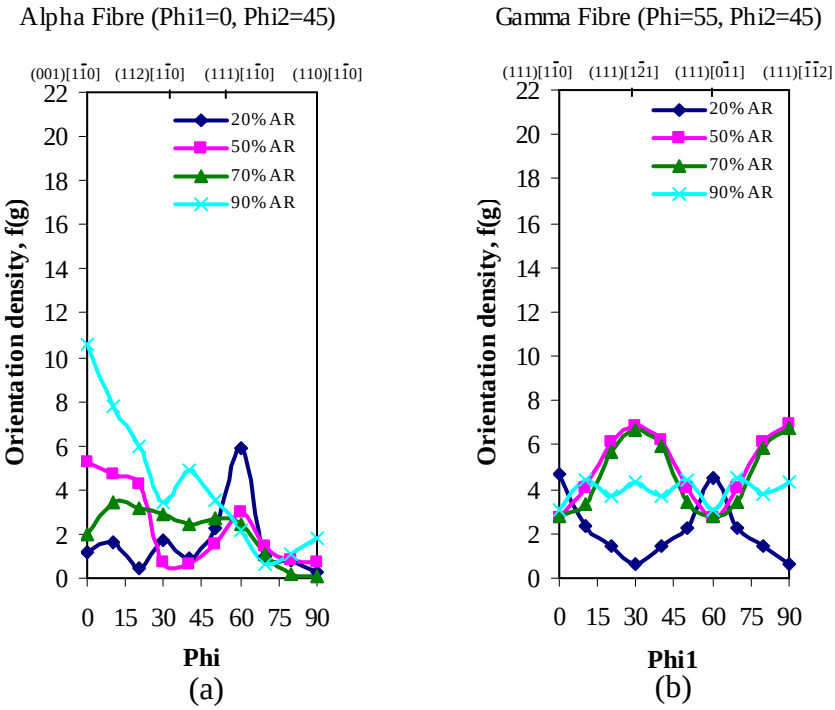

Figure 4.27: Orientation density along (a) α-fibre and (b) γ-fibre, for HSLA steel after cold rolling reductions of 20%, 50%, 70% and 90%.

In order to understand the recrystallisation behaviour, it is important to see how the dislocations are distributed in regions of different texture components. Figure 4.28a shows an EBSD image (band contrast) of 50% reduction HSLA steel with Figure 4.28 b and c showing the orientations of the circled grains showing that their orientations are closed to {hkl}<110> and {111}<uvw> respectively.

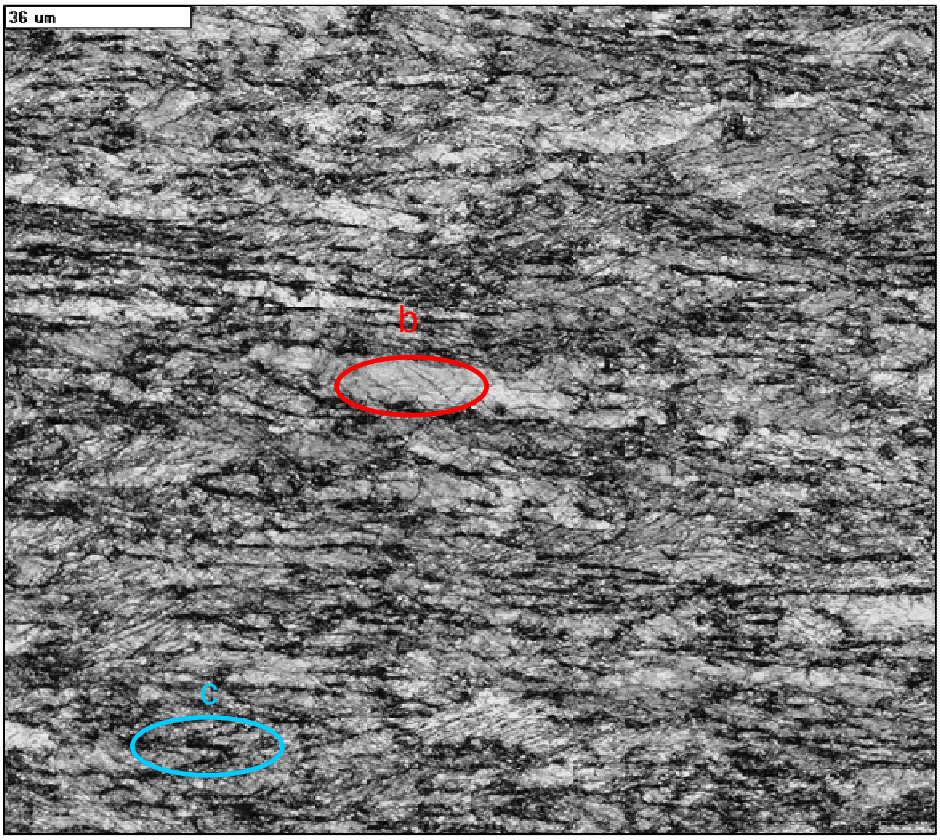

(a)

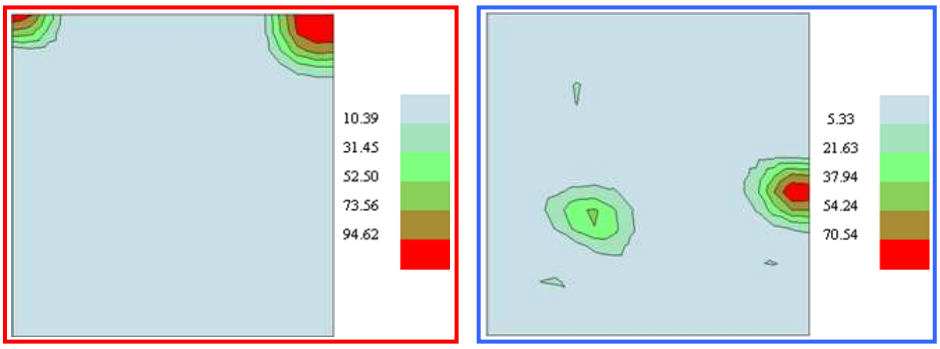

(b) (c)

Figure 4.28: (a) EBSD image (band contrast) of HSLA steel after 50% reduction. The orientation of the two circled regions are given in (b) and (c) as φ_2=45^o section of Euler space.

Figure 4.29 shows the misorientation profiles along RD in α- and γ-fibre grains after 50% reduction (areas circled in Figure 4.28a). The figures show clearly that large misorientations exist in deformed γ-fibre grains which means a higher stored energy and, hence, a higher recrystallisation rate is likely during annealing. Moreover, Figure 4.29a points out the typical properties of α-fibre orientations. The misorientation between neighbouring points of the measurements (i.e. point to point misorientation) is always less than 3^o in these areas, but the misorientations accumulate over longer distances (i.e. point to origin misorientations) to 14^o over a distance of 26μm. On the other hand, much higher misorientations between neighbouring measurement points can be found in γ-fibre deformed grains. However, the misorientations do not seem to accumulate in γ-fibre orientations.

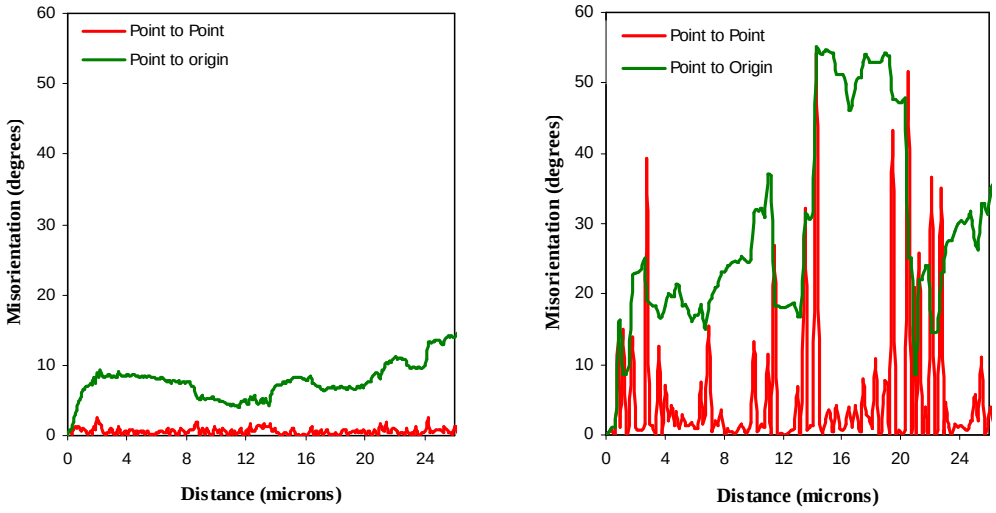

(a) (b)

Figure 4.29: Misorientation profiles of HSLA in (a) α- and (b) γ-fibre deformed grains along RD after 50% reduction. Relative (point to point) and cumulative (point to origin) misorientations are shown.

4.5.2 Investigation of the Deformation Zones by TEM

The effect of pearlitic particles on the development of microstructure and rolling textures in HSLA steel has been investigated in detail by using both EBSD and TEM. The presence of such particles caused large strain inhomogeneities during deformation which create high dislocation density zones (i.e. particle deformation zones) around them. The local deformation and the orientation changes induced around them were investigated using TEM and selected area diffraction patterns, as shown in Figure 4.30. The selected area electron diffraction patterns show the orientation spread within the deformation zone.

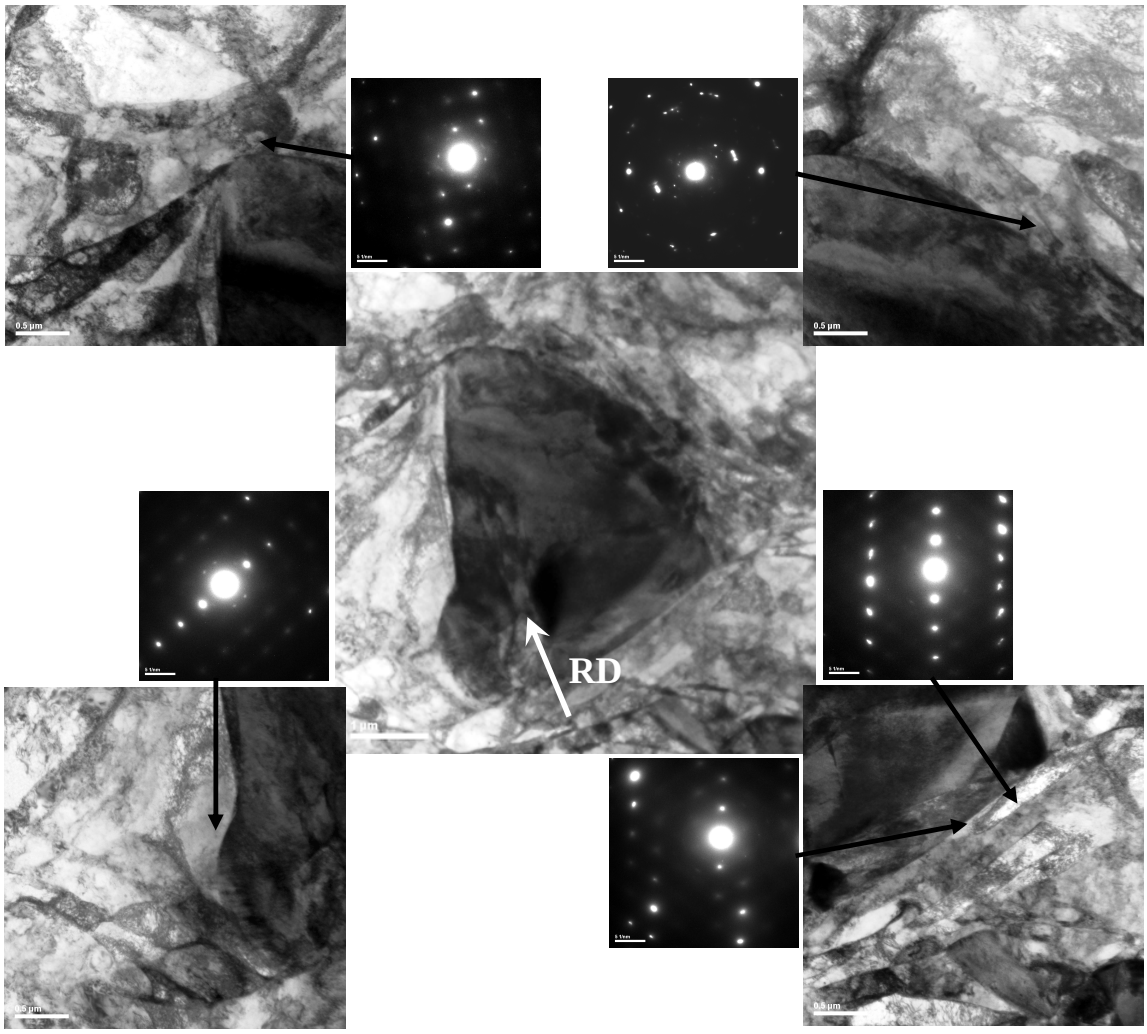

Figure 4.30: Bright field TEM image showing the orientation spread within the deformation zone around a particle cold rolled 50% by using selected area diffraction patterns (the selected areas are magnified).

In addition, the variation of orientation within the deformation zone and the matrix around the same particle is shown in Figure 4.31. [310] selected area electron diffraction patterns obtained in this region showed considerable arcs, especially on the vicinity of the particle (i.e. selected areas a and b in Figure 4.31), and they often contained more than two orientations, indicating the presence of severe local deformation in these areas where the minimum dislocation cell size is found.

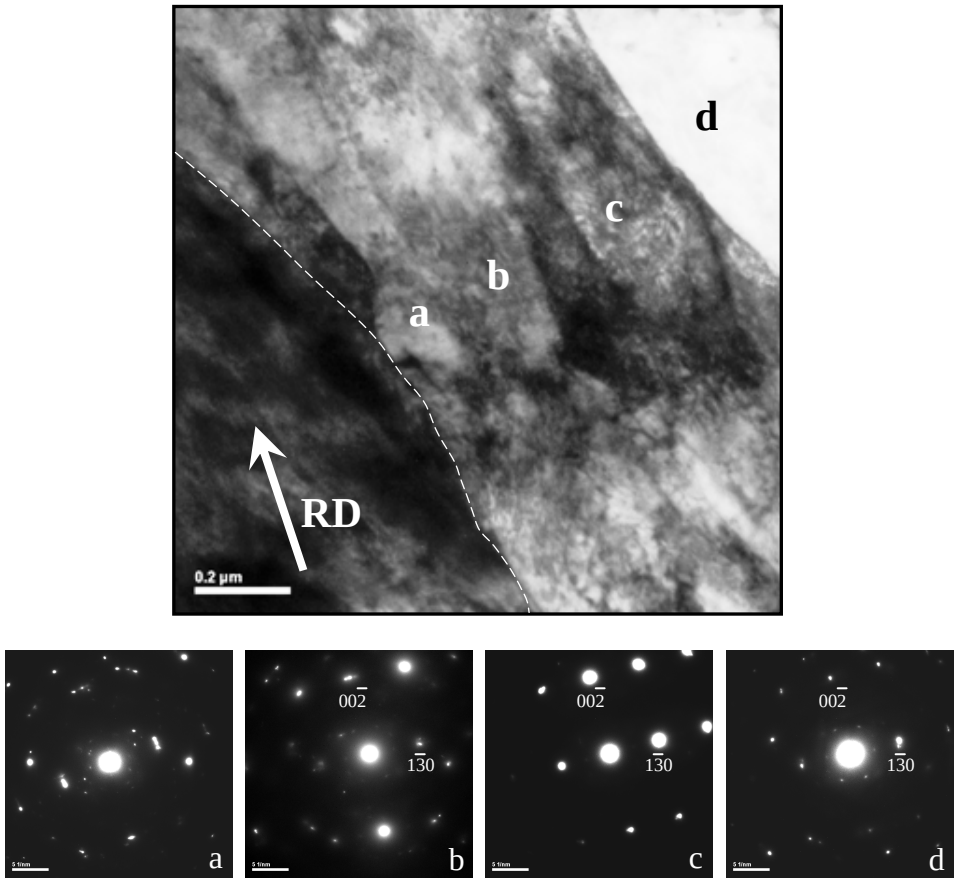

Figure 4.31: The variation of orientation within the deformation zone and in the matrix around a particle in HSLA steel cold rolled 50% (dashed line indicates the particle edge).

4.5.3 Investigation of the Deformation Zones by EBSD

The recent development of high resolution EBSD has enabled the features of the deformation zones near particles to be determined. Figure 4.32 shows the orientation spread within a small volume adjacent to a particle which was measured and represented by 100 pole figures. These pole figures show also rotations with respect to the surrounding matrix about the transverse direction. Figure 4.33 shows clearly these local lattice rotations of the matrix adjacent to a particle which occur to reduce the deformation incompatibilities. The misorientation changes in the vicinity of the particle were also shown in this figure where the maximum rotation was found to be close to the particle-matrix interface. In this example, the observed rotation with respect to the deformed matrix reaches a value of more than 25^{o}. This large misorientation in the vicinity of the particle (i.e. particle deformation zone) indicates high local concentration of stored energy, and can thus indicate favourable nucleation site during annealing.

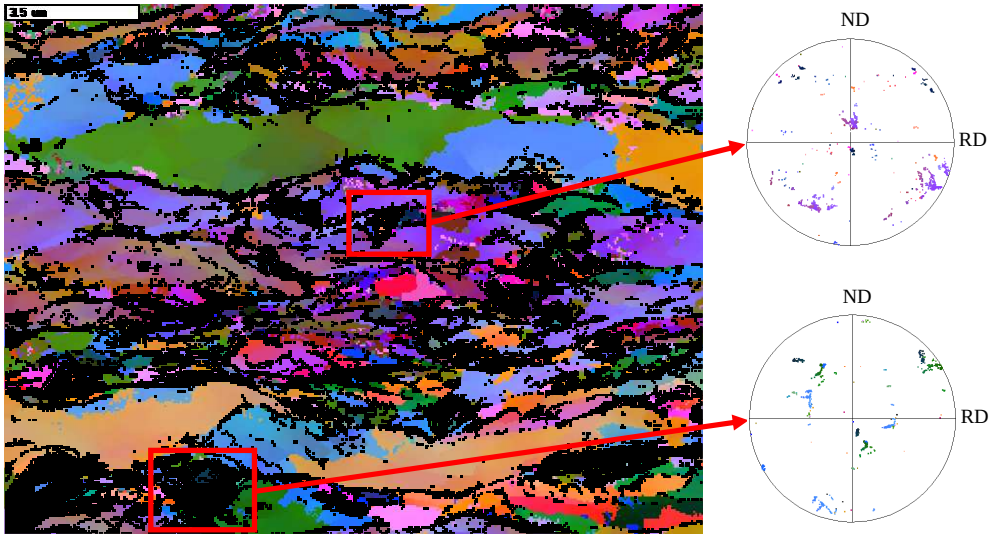

Figure 4.32: EBSD map showing 70% cold rolled HSLA steel with the attached 100 pole figures showing the orientation spread around the selected particles.

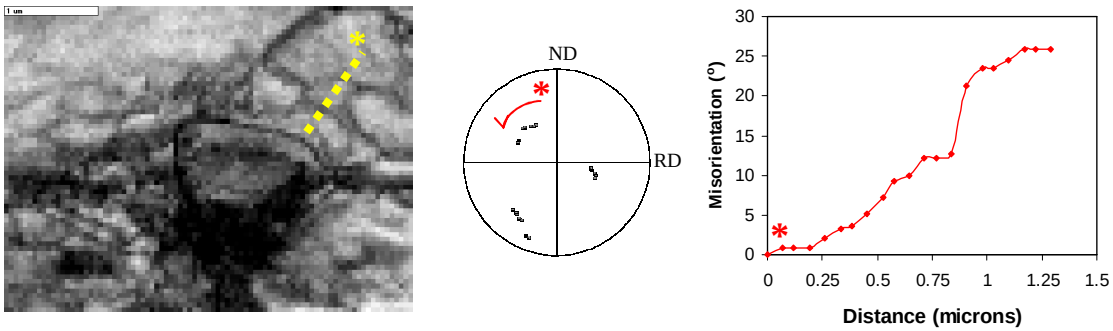

(a) (b) (c)

Figure 4.33: (a) EBSD map (band contrast) of the highly misoriented regions adjacent to the particle, (b) and (c) showing the orientation (using a 100 pole figure) and misorientation changes along the dashed line, respectively.

4.5.4 Microstructure & Texture Evolution During Recrystallisation

In light of the observations reported in Section 4.4, the microstructure and texture evolution of cold rolled IF and HSLA steels during the process of recrystallisation were examined in more details using EBSD. The orientations of certain recrystallised grains, especially those related to the PSN mechanism, are of particular interest in this study and have been investigated in detail.

Figure 4.34 shows the microstructural evolution of the 70% cold rolled IF steel sample annealed at 620^{o}C for different time intervals. Figure 4.34b shows a partially recrystallised microstructure where the recrystallisation fraction is low. In this figure, colonies of recrystallised grains have been observed indicating an oriented nucleation process is taking place. An example of the SIBM mechanism is also shown. This mechanism was rarely found. Figure 4.34c shows that the recrystallisation fraction is increased with increasing annealing time.

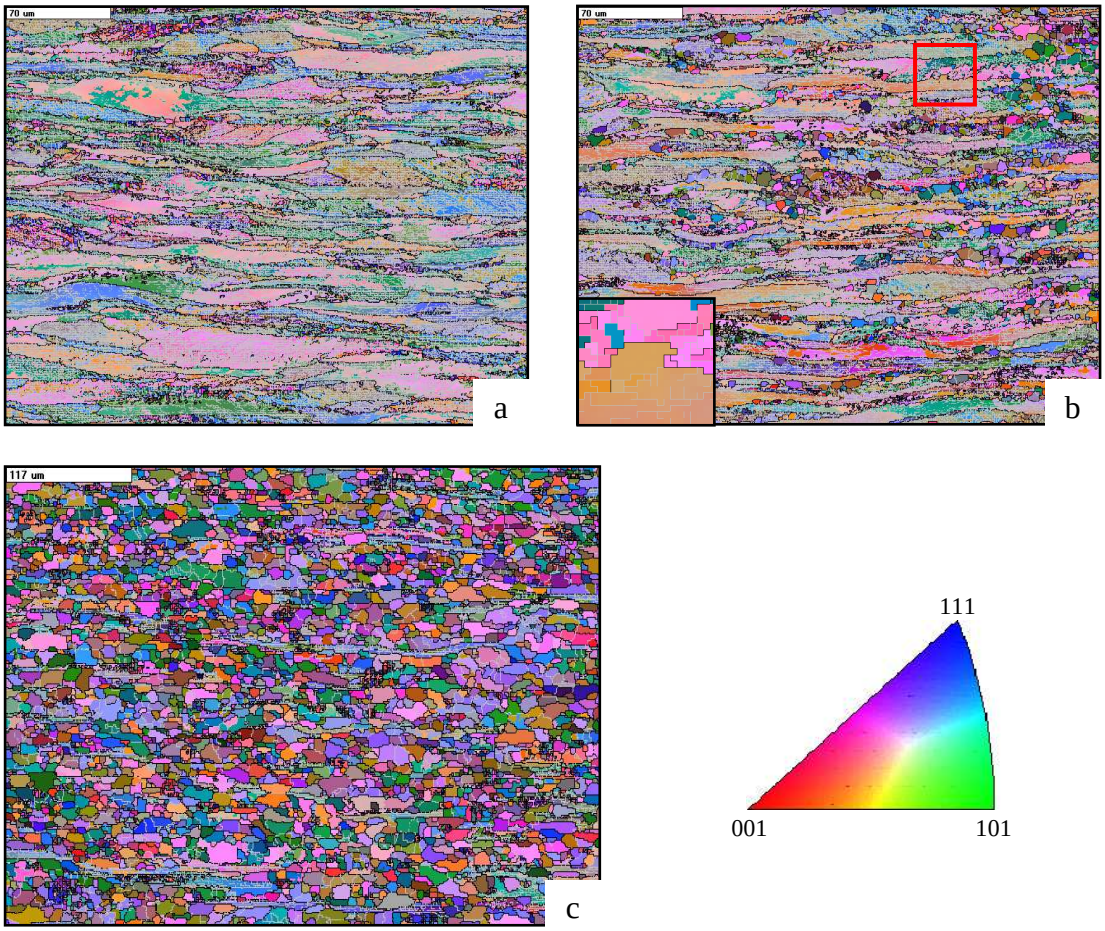

Figure 4.34: (a) EBSD map showing an IF steel sample cold rolled to 70% and (b) and (c) same sample annealed at 620^{o}C for 4 hrs and 24hrs, respectively. The selected area in (b) shows an example of SIBM.

Nucleation of recrystallised grains in HSLA steel occurs mostly in the deformed zones developed around the particles during cold rolling, as can be seen in Figure 4.35-36. In both figures, the "new grains" or nuclei are characterised by a relatively high image quality (high brightness) and are surrounded by high angle grain boundaries. The selected grains in Figure 4.35 which are formed at a row of fragmented particles seem to have grown locally (i.e. within the deformation zone) and then impinged with each other. The orientations of these grains indicate that they are not randomly nucleated. They seem to experience a barrier to further growth after consuming the deformation zone due to the decrease in driving force.

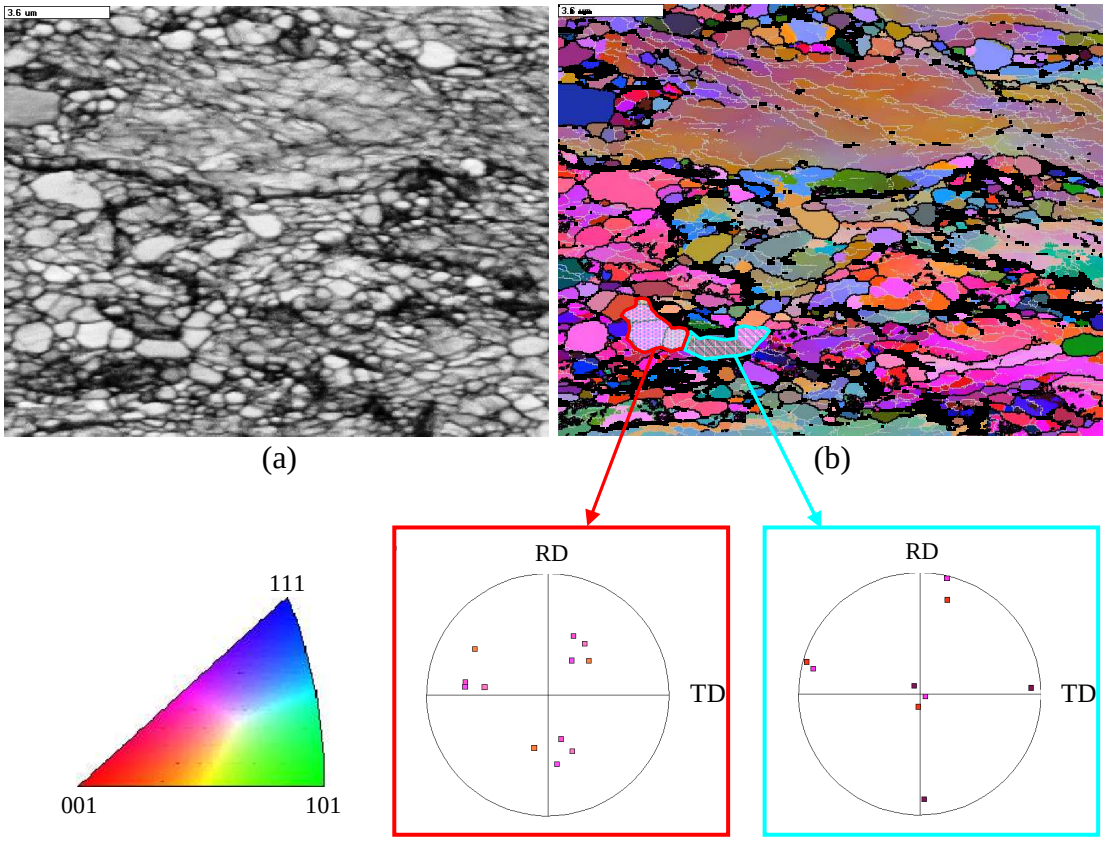

Figure 4.35: EBSD map showing recrystallisation originated, most preferentially, in the deformation zones close to the particles in 70% cold rolled HSLA annealed at 500^{o}C. (a) Band contrast and (b) Euler colour map with the standard 100 pole figures showing the orientation of the selected recrystallised grains.

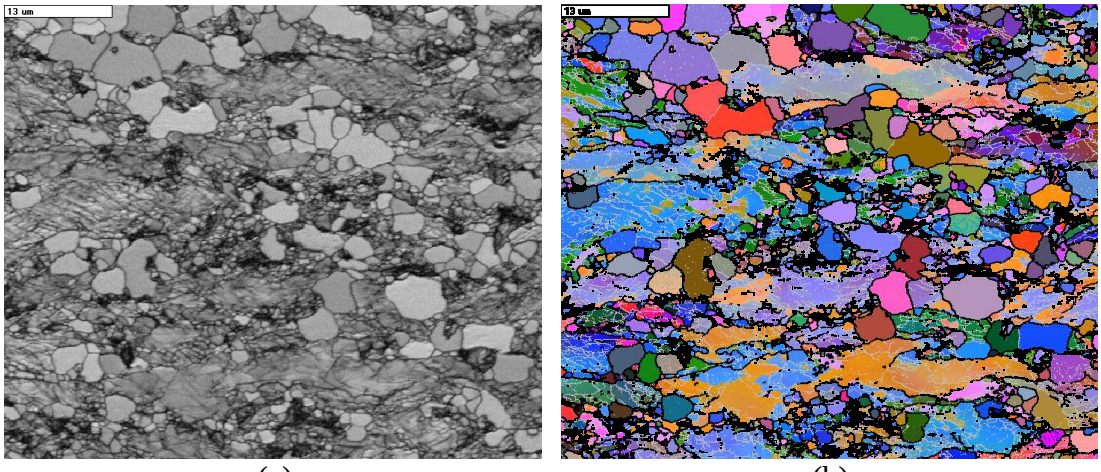

Figure 4.36: EBSD map showing another example of particle stimulated nucleation of recrystallisation in annealed HSLA steel cold rolled to 50%. (a) Band contrast and (b) Euler colour map.

Figure 4.37 shows the effect of the total reduction on the grain size of the fully recrystallised samples of both steels. As expected, the grain size decreases with increasing reduction as a result of the higher stored energy with large reductions and, hence, a higher nucleation rate.

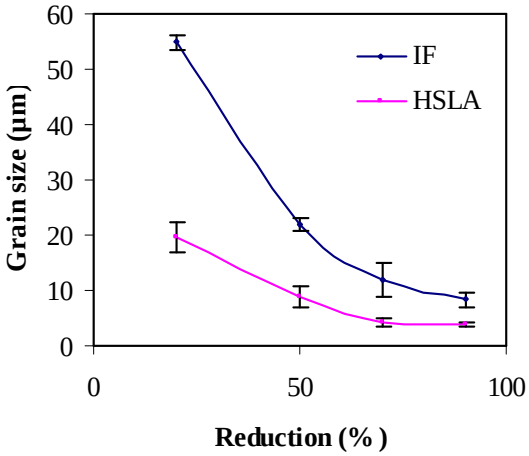

Figure 4.37: Effect of reduction on the grain size of fully annealed samples of the IF and HSLA steels.

For each partially recrystallised sample, data from the unrecrystallised and recrystallised regions were separated and the resulting texture measurements, presented as $\varphi_2=45^o$ sections of Euler space, are shown in Figure 4.38-45. Figure 4.38-41 show IF steel samples with recrystallisation fractions of 17% and 82% with 50% reduction and 12% and 88% with 70% reduction. Figure 4.42-45, on the other hand, show HSLA steel samples with recrystallisation fraction of 24% and 90% with 50% reduction and 16% and 91% with 70% reduction. All EBSD maps attached to these figures show only the recrystallised grains. In the case of IF steel, the early nucleation textures (identified as nucleation texture when the recrystallised volume fraction is about 15%) of both reductions show high γ-fibre intensity, indicating that recrystallisation commences in the as deformed γ-fibre oriented grains. The degree of intensity increases with increasing reductions. On the other hand, the α-fibre intensity increases in the unrecrystallised regions with an increase of the recrystallisation fractions. It increases from $(111)[1\bar{1}0]$, $(223)[1\bar{1}0]$, $(112)[1\bar{1}0]$ to (001)<110>, indicating that the stored energy is of the following order: $E_{110} > E_{111} > E_{112} > E_{100}$ as described by Dillamore *et al.* (1972). The HSLA steel shows, to some extent, similar behaviour to that of the IF steel, although the texture intensity was lower. Despite the dominance of PSN in this steel, the nucleation textures of both reductions show the presence of the cold rolled components of both α- and γ-fibres,

indicating that the PSN nuclei are not randomly oriented even if the orientation spread of the nuclei is high. With increasing recrystallisation fraction, both fibres occur with weaker intensity. The texture of the unrecrystallised regions show that the intensities of both α- and γ-fibres increase with increasing the recrystallisation fraction, with the intensity of α-fibre being slightly higher.

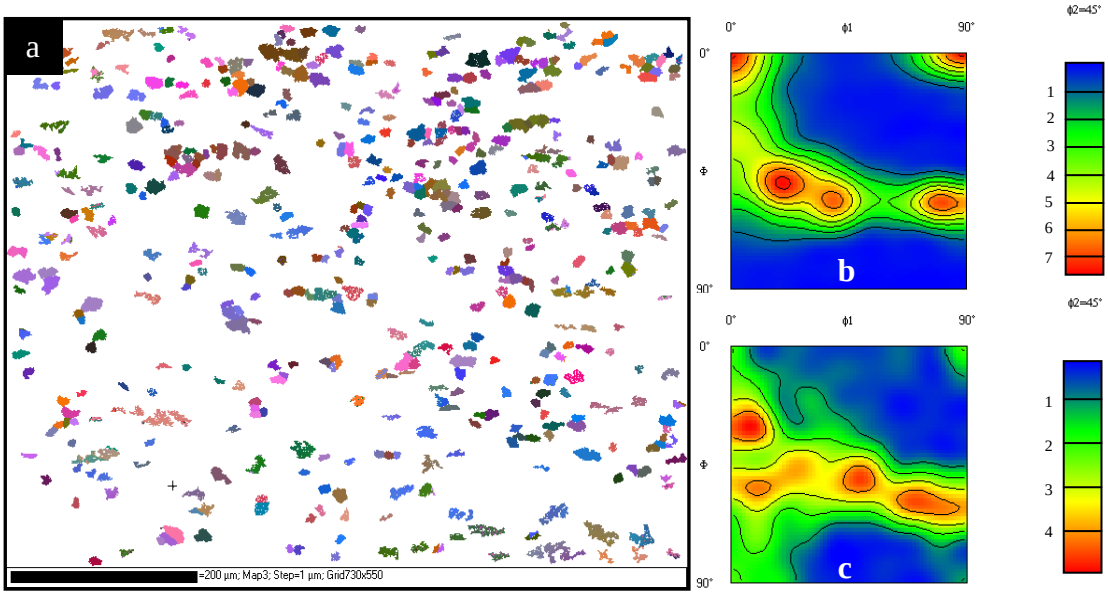

Figure 4.38: (a) EBSD map showing the recrystallised grains of 50% cold rolled IF steel annealed to 17% recrystallisation. (b) Texture of the unrecrystallised region (Max = 7.31). (c) Texture of the recrystallised region (Max = 5.0)

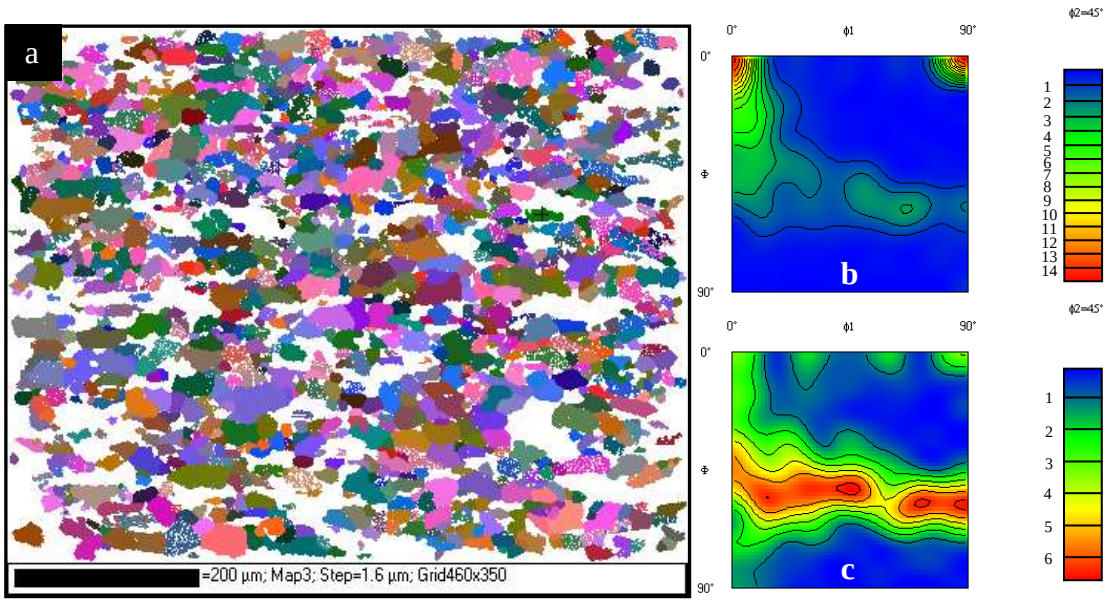

Figure 4.39: (a) EBSD map showing the recrystallised grains of 50% cold rolled IF steel annealed to 82% recrystallisation. (b) Texture of the unrecrystallised region (Max = 14.5). (c) Texture of the recrystallised region (Max = 6.31)

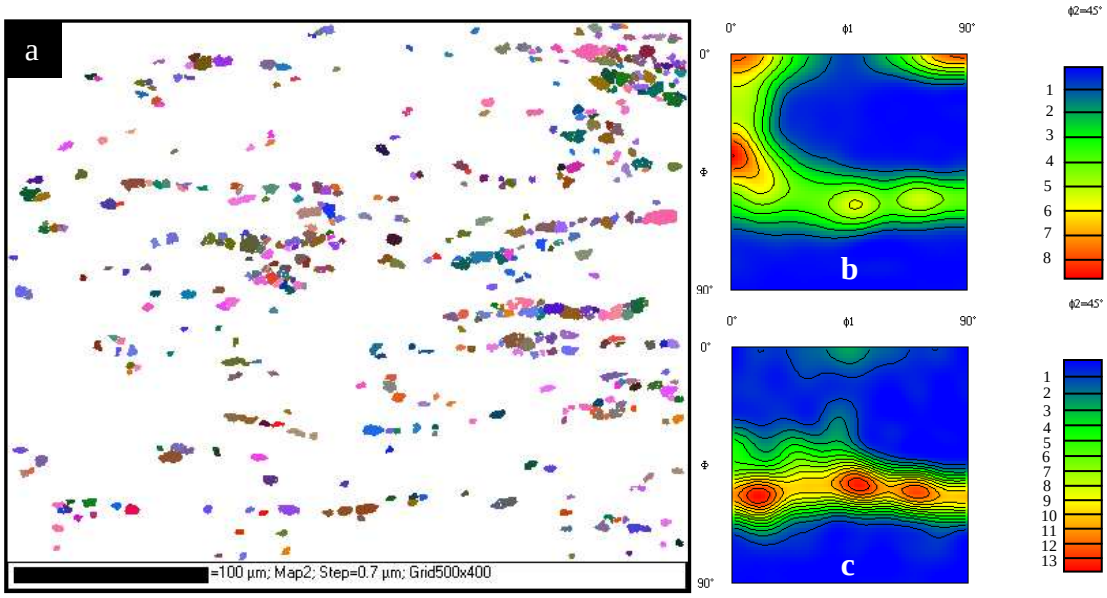

Figure 4.40: (a) EBSD map showing the recrystallised grains of 70% cold rolled IF steel annealed to 12% recrystallisation. (b) Texture of the unrecrystallised region (Max = 8.1). (c) Texture of the recrystallised region (Max = 13.1)

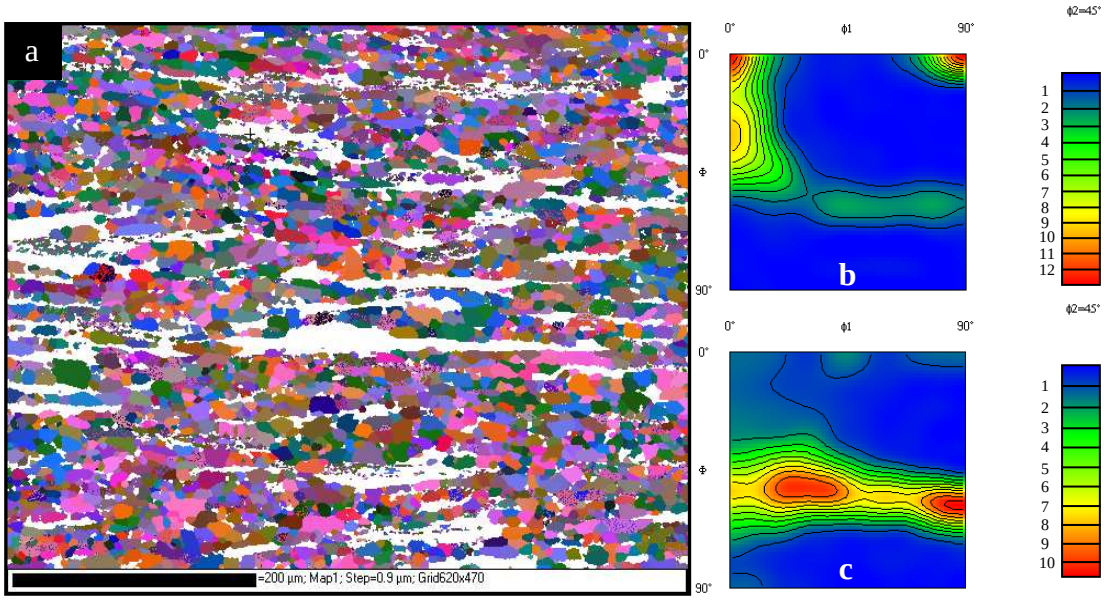

Figure 4.41: (a) EBSD map showing the recrystallised grains of 70% cold rolled IF steel annealed to 88% recrystallisation. (b) Texture of the unrecrystallised region (Max =12.8). (c) Texture of the recrystallised region (Max = 10.8)

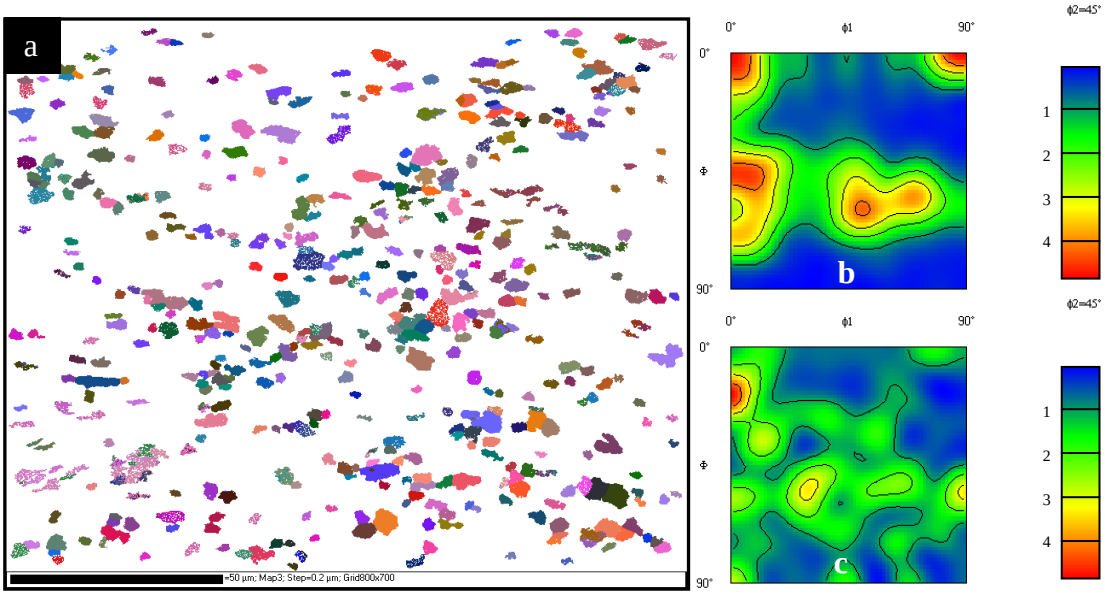

Figure 4.42: (a) EBSD map showing the recrystallised grains of 50% cold rolled HSLA steel annealed to 24% recrystallisation. (b) Texture of the unrecrystallised region (Max = 4.73). (c) Texture of the recrystallised region (Max = 4.71)

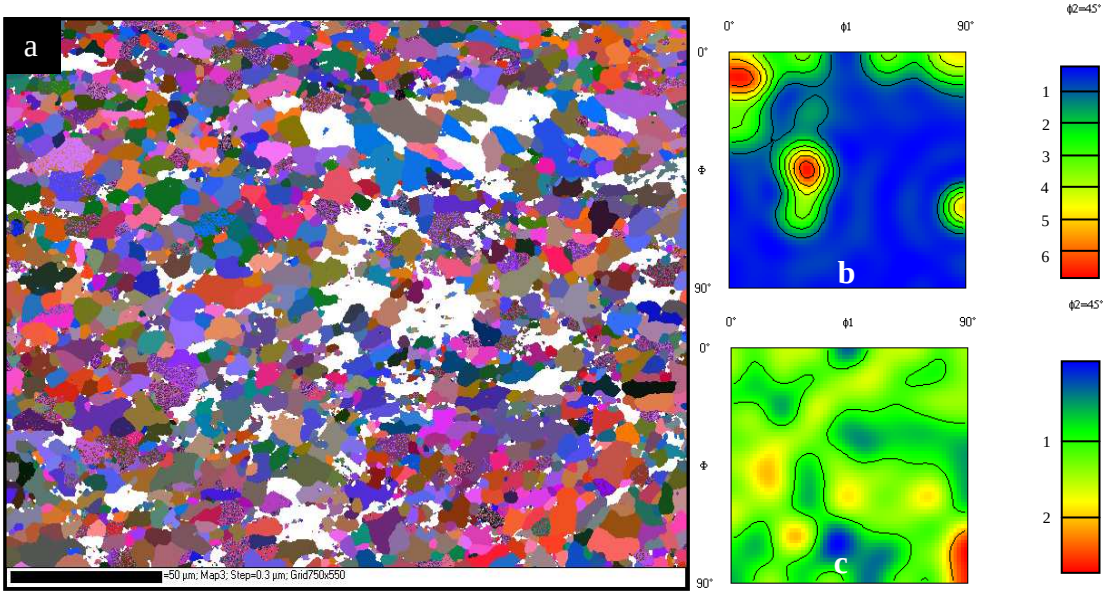

Figure 4.43: (a) EBSD map showing the recrystallised grains of 50% cold rolled HSLA steel annealed to 90% recrystallisation. (b) Texture of the unrecrystallised region (Max = 6.68). (c) Texture of the recrystallised region (Max = 2.55)

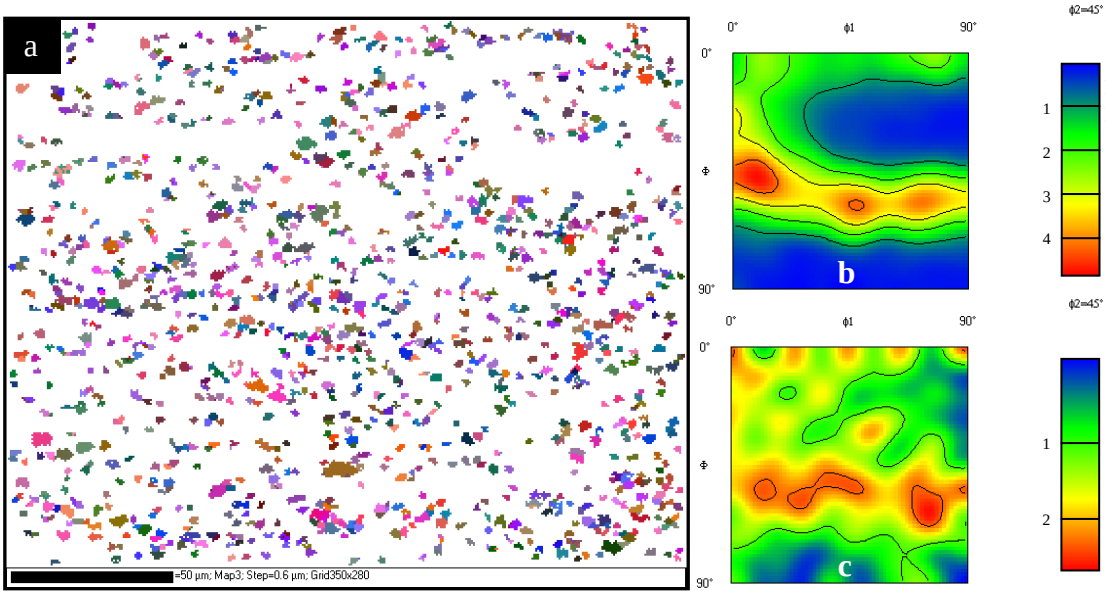

Figure 4.44: (a) EBSD map showing the recrystallised grains of 70% cold rolled HSLA steel annealed to 16% recrystallisation. (b) Texture of the unrecrystallised region (Max = 4.67). (c) Texture of the recrystallised region (Max = 2.32)

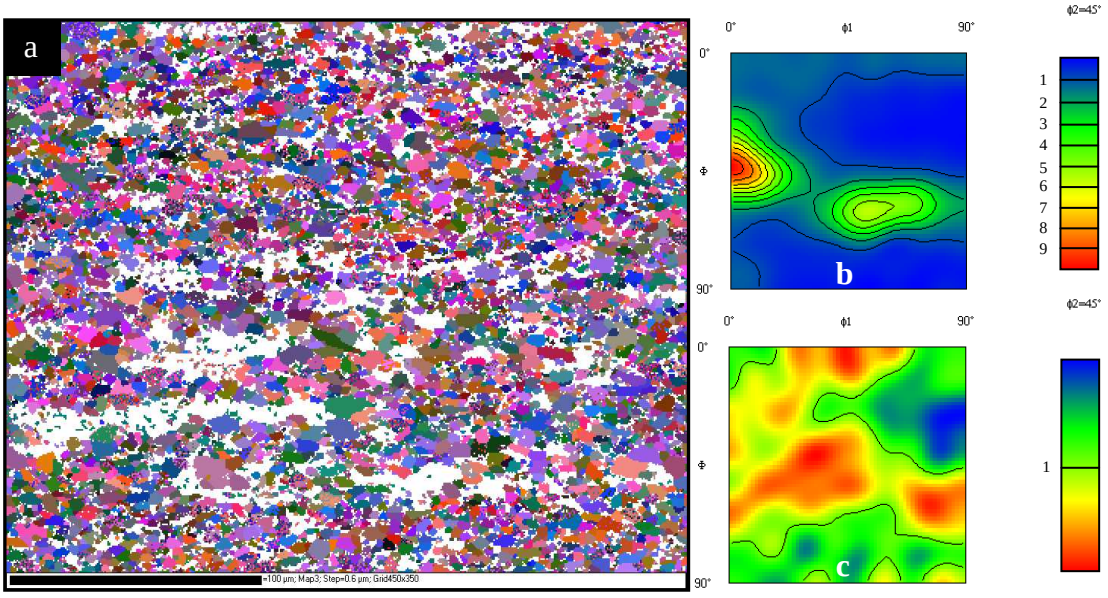

Figure 4.45: (a) EBSD map showing the recrystallised grains of 70% cold rolled HSLA steel annealed to 91% recrystallisation. (b) Texture of the unrecrystallised region (Max = 9.66). (c) Texture of the recrystallised region (Max = 1.98)

4.5.5 Recrystallisation Texture after Fully Annealing

The recrystallisation texture for each of the 20%, 50%, 70% and 90% cold rolling reductions of the IF and HSLA steels after fully annealing were measured and can be seen in Figure 4.46 and Figure 4.47, respectively. The recrystallisation texture for both steels is shown to be largely dependent on the rolling reduction. With increasing rolling reduction, the recrystallisation texture shows a gradual intensification of α- and γ-fibre components. However, the intensity of both fibres is lower in the HSLA steel, as a result of the PSN in this steel.

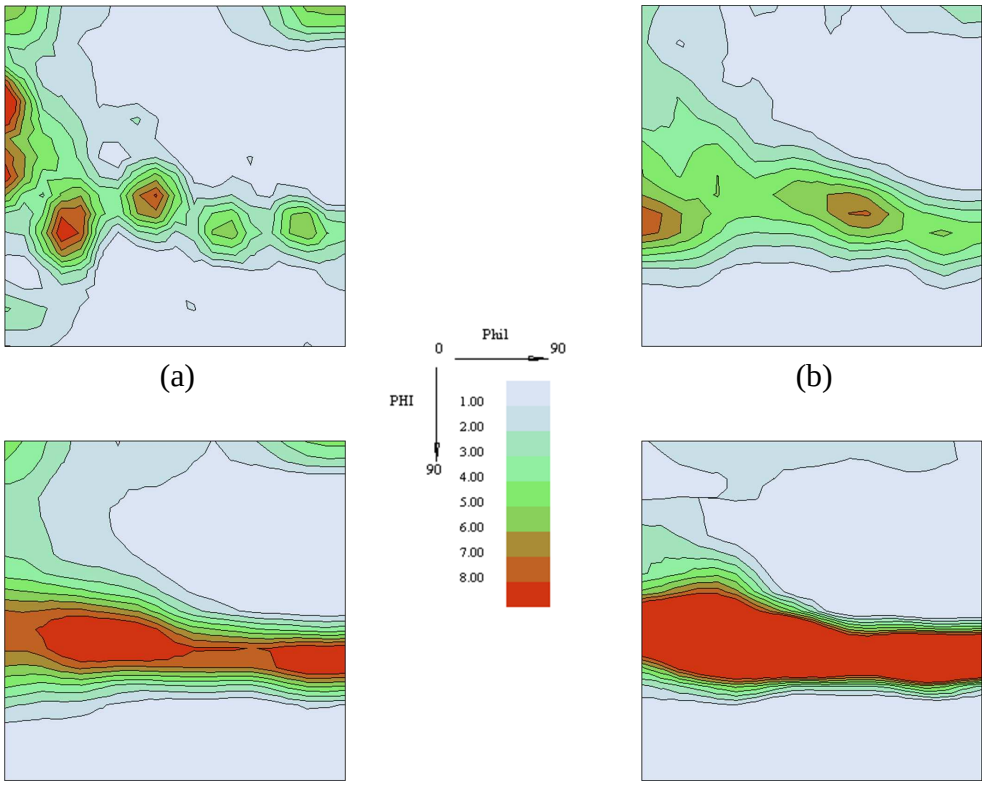

Figure 4.46: Textures of fully annealed IF steel (ODF φ_2=45^o sections) cold rolled (a) 20%, (b) 50%, (c) 70% and (d) 90%.

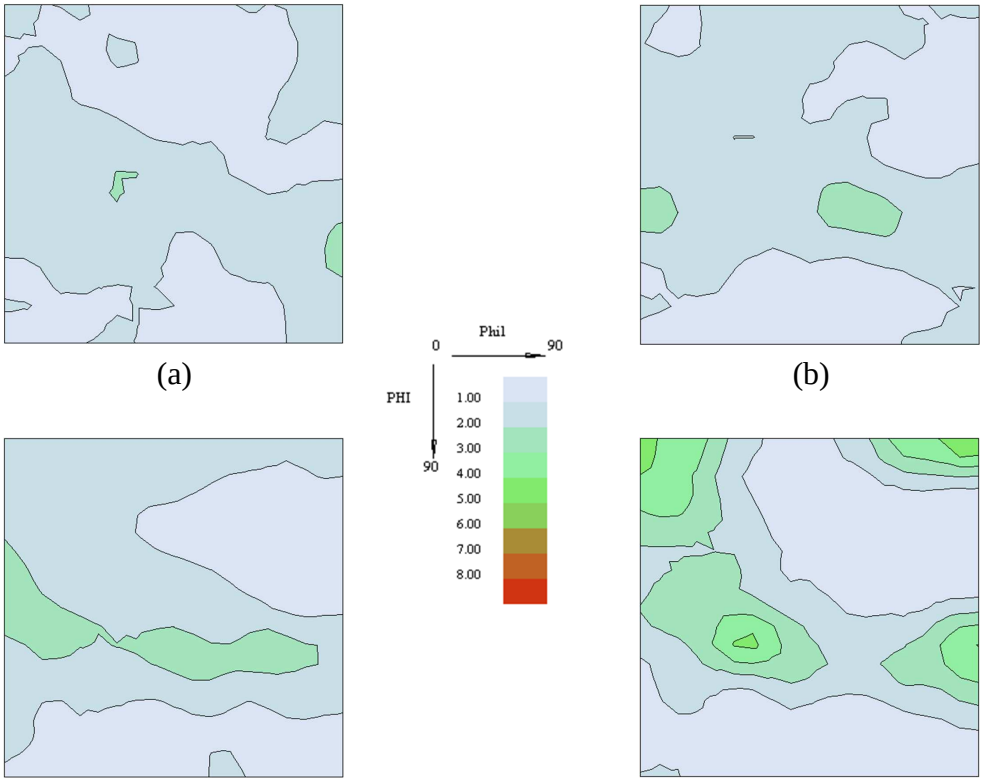

Figure 4.47: Textures of fully annealed HSLA steel (ODF φ_2=45^o sections) cold rolled (a) 20%, (b) 50%, (c) 70% and (d) 90%.

The orientation density along α- and γ-fibres after different cold rolling reductions is shown in Figure 4.48 for the IF steel and Figure 4.49 for the HSLA steel. In general, higher orientation densities along both fibres is observed in the IF steel compared to the HSLA steel. A strong peak occurs at (111)[$1\bar{1}0$] for all reductions in the IF steel, except for the 20% reduction. This peak increases with increasing reduction. The weaker density is observed in (110)[$1\bar{1}0$] for all reductions. On the other hand, low orientation density is observed in the HSLA along the α-fibre with a relatively high peak at (001)[$1\bar{1}0$] for 90% reduction and a low density at (110)[$1\bar{1}0$] for all reductions.

The orientation density along the γ-fibre in the IF steel increases with increasing reduction. It is found to be quite uniformly distributed after 70% reduction. On the other hand, the HSLA steel shows low densities along the γ-fibre, with a slight increase with increasing reduction. Peaks occurring at (111)[$1\bar{2}1$] and (111)[$\bar{1}\bar{1}2$] are observed with 90% reduction.

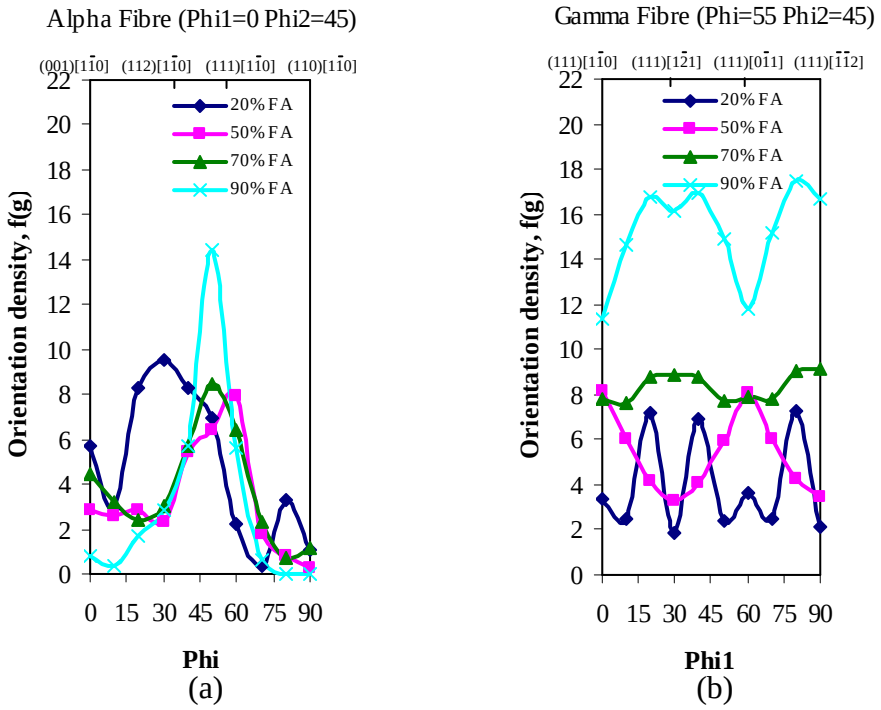

Figure 4.48: Orientation density along (a) α-fibre and (b) γ-fibre, for fully annealed IF steel after cold rolling reductions of 20%, 50%, 70% and 90%.

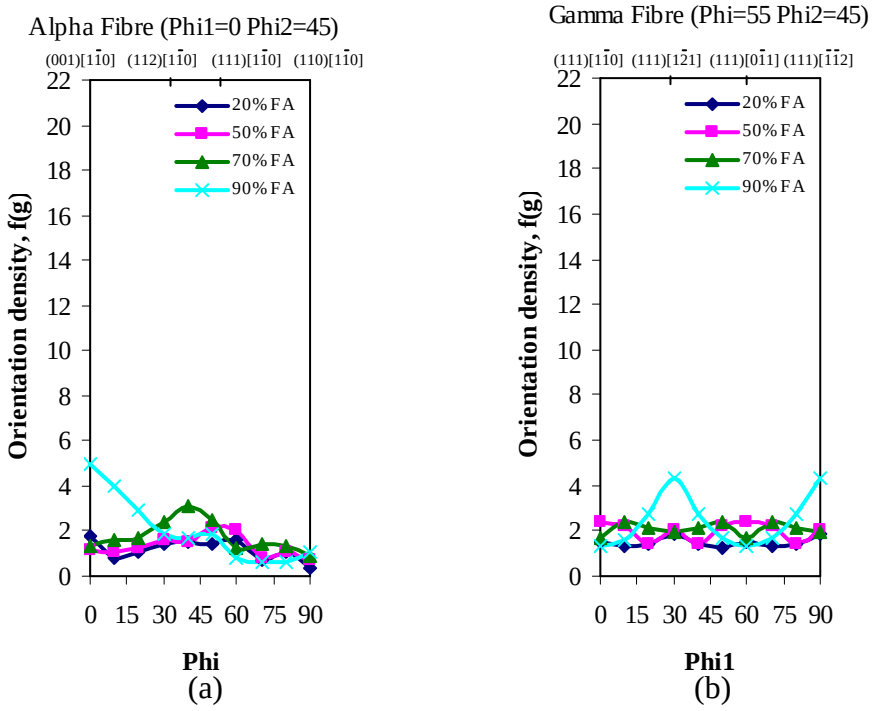

Figure 4.49: Orientation density along (a) α-fibre and (b) γ-fibre, for fully annealed HSLA steel after cold rolling reductions of 20%, 50%, 70% and 90%.

Grain boundary misorientation histograms of the IF and HSLA steels for all the reductions are shown in Figure 4.50 and Figure 4.51, respectively. Each figure shows a comparison between the misorientation distribution of the as-rolled (blue) and the fully-annealed (red) samples for each degree of reduction. A clear development of LAGB's to HAGB's during annealing in all samples can be detected in these misorientation histograms. Moreover, Figure 4.52 shows the maximum orientation intensity for as-rolled and fully annealed samples of both steels. It shows that the maximum intensity increases, in general, with increasing the rolling reduction. It is also observed that the maximum intensity for the as-rolled HSLA steel is much higher than that of the annealed one.

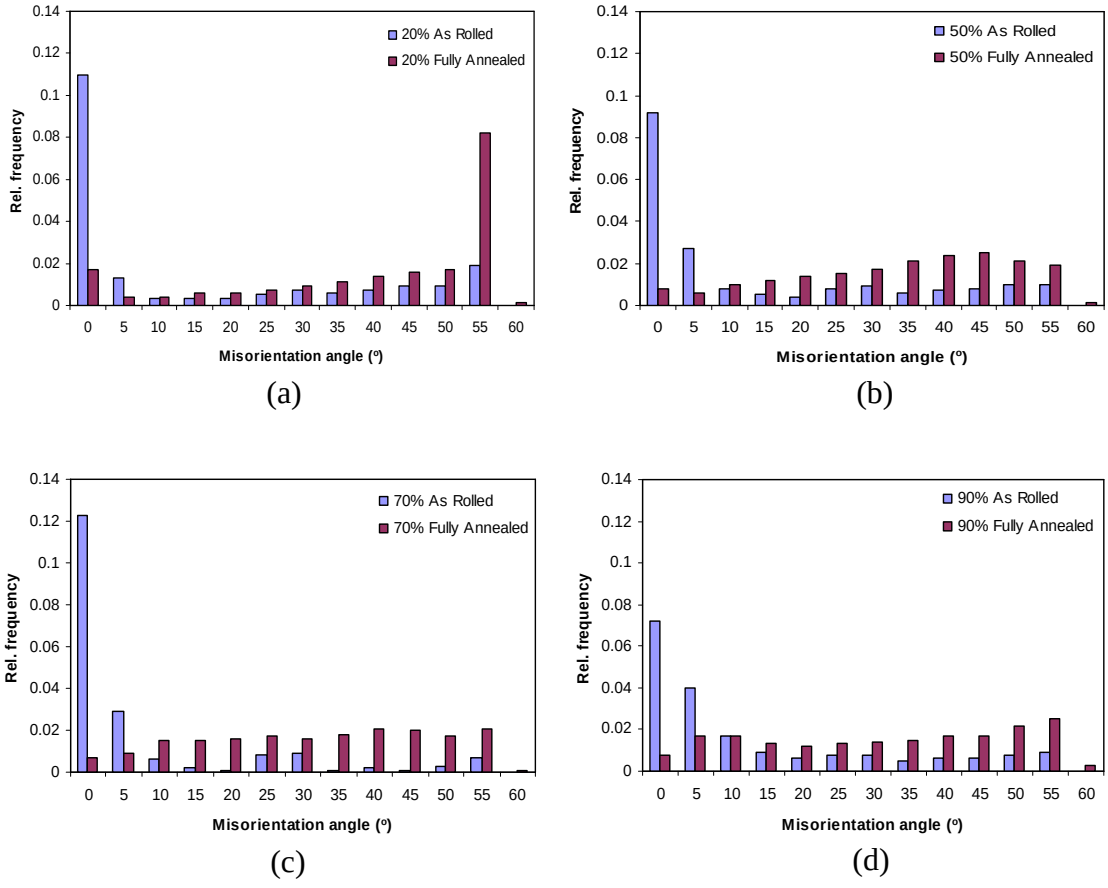

Figure 4.50: Histograms showing comparison between the misorientation angle distribution of the as-rolled and the fully annealed IF steel samples cold rolled to (a) 20%, (b) 50%, (c) 70% and (d) 90% reductions.

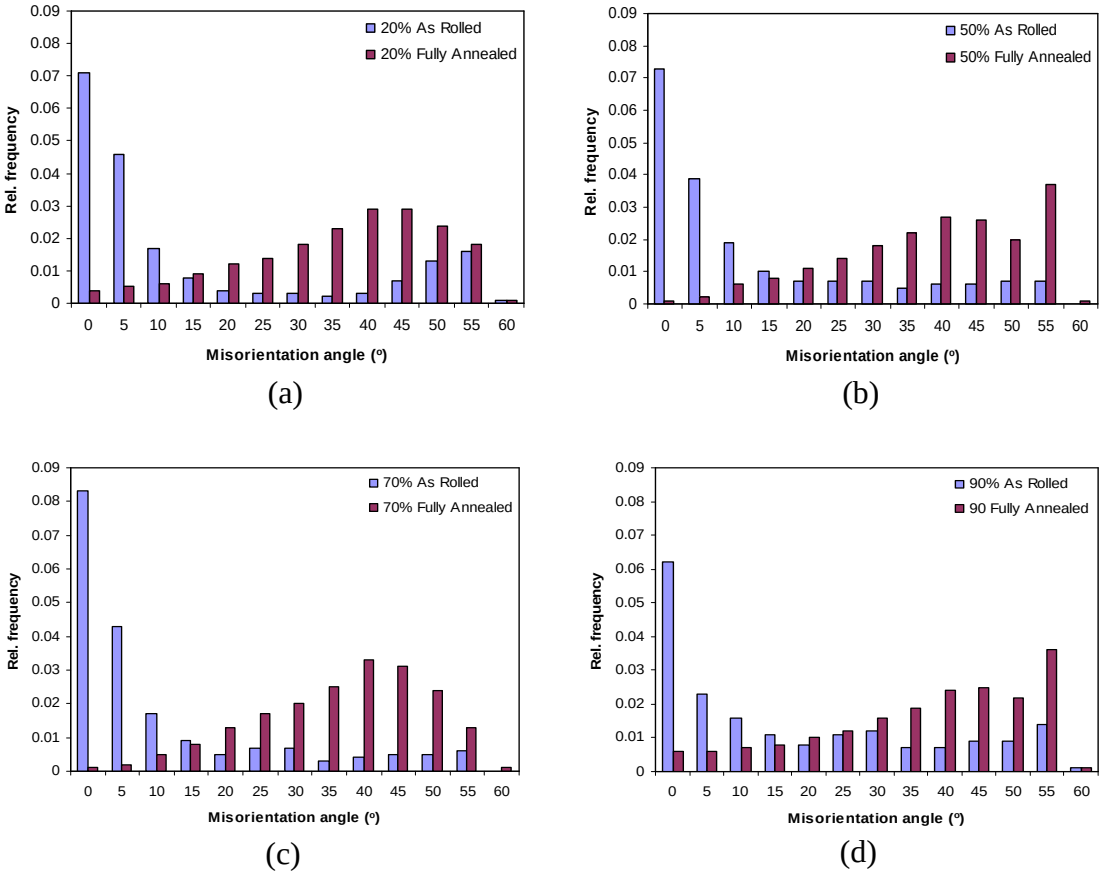

Figure 4.51: Histograms showing comparison between the misorientation angle distribution of the as-rolled and the fully annealed HSLA steel samples cold rolled to (a) 20%, (b) 50%, (c) 70% and (d) 90% reductions.

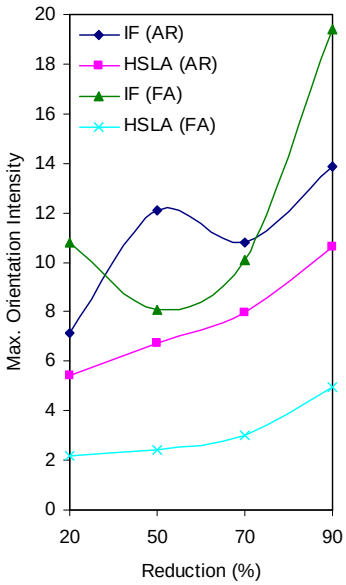

Figure 4.52: Maximum orientation intensity for as-rolled and fully annealed IF and HSLA steels for all reductions.

4.5.6 Texture Measurement by XRD

In order to assess how statistically representative the information obtained from the EBSD data for HSLA steel is, the bulk textures produced by the cold rolling and annealing processes were also evaluated by standard X-ray methods. A comparison between the texture measured by the XRD and EBSD techniques for all reductions for HSLA steel is shown in Figure 4.53-56. These figures show also the fully annealing texture. Texture analysis using XRD are carried out using pole figures measurements and, for the purpose of accuracy, they are represented here as pole figures since the accuracy of the calculated ODF is highly affected by the number of input pole figures, of which are only three in this case.

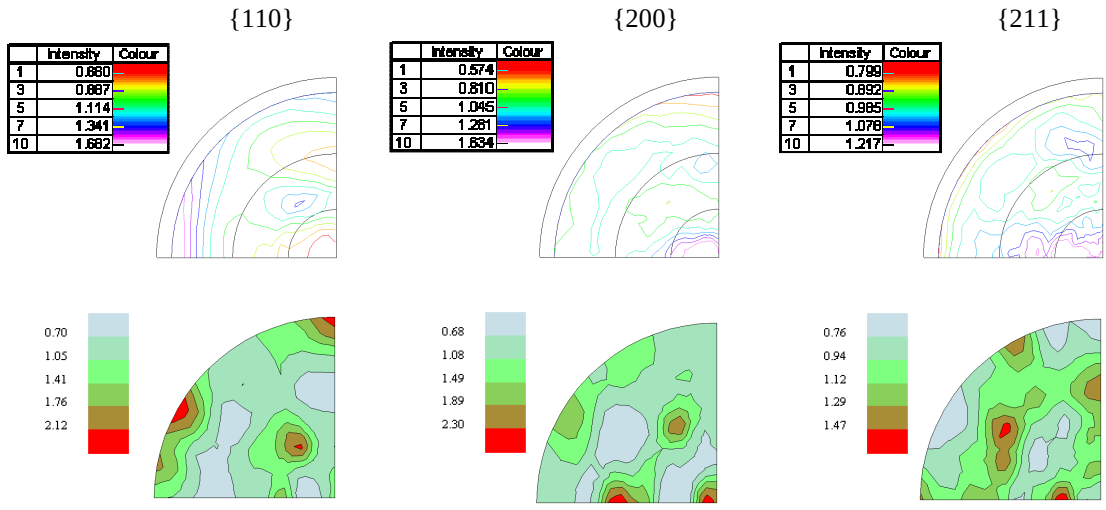

(a)

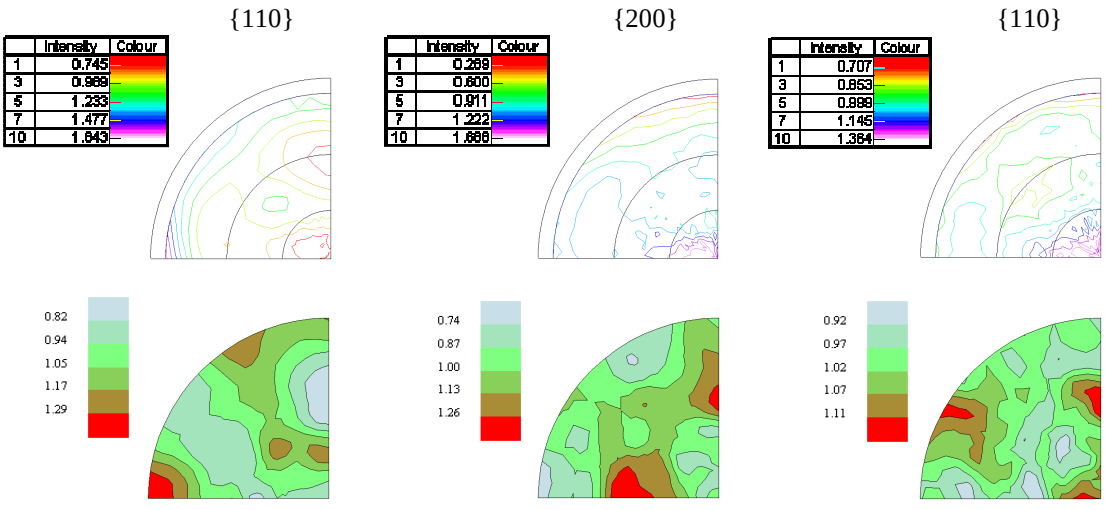

(b)

Figure 4.53: Standard {110}, {200} and {211} pole figures showing the texture measured by EBSD (filled) and XRD (outline only) of (a) 20% reduction HSLA steel and (b) full annealing the same sample.

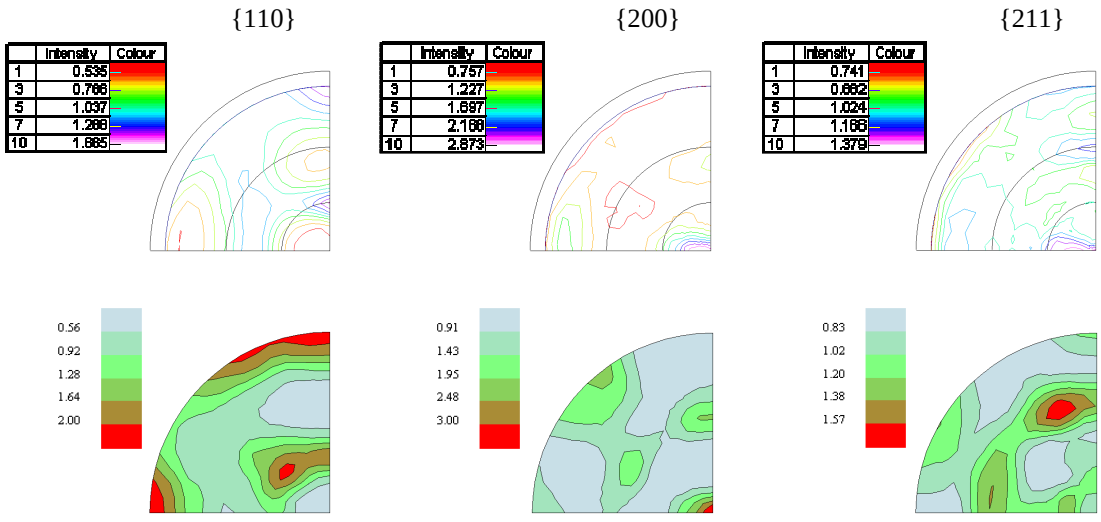

(a)

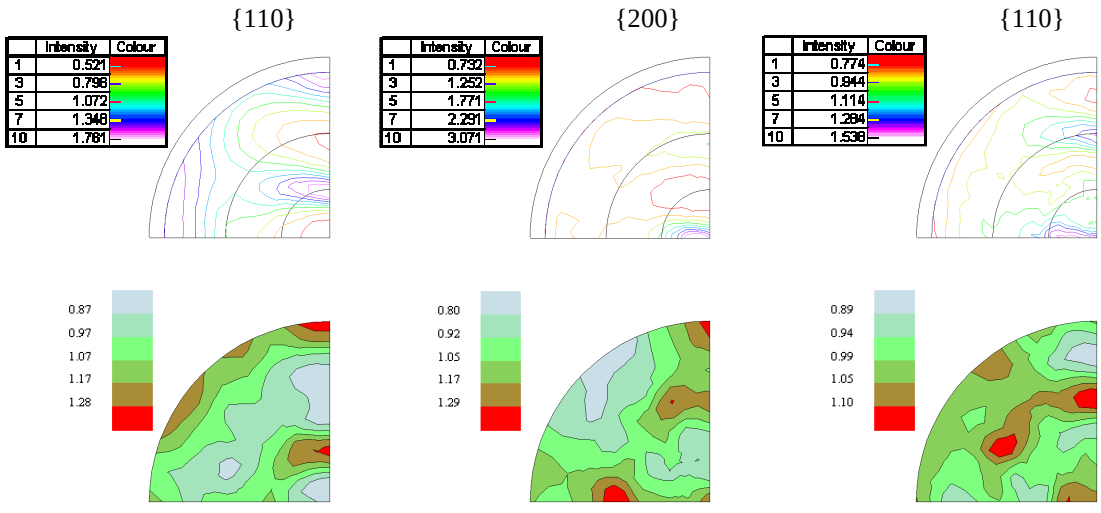

(b)

Figure 4.54: Standard {110}, {200} and {211} pole figures showing the texture measured by EBSD (filled) and XRD (outline only) of (a) 50% reduction HSLA steel and (b) full annealing the same sample.

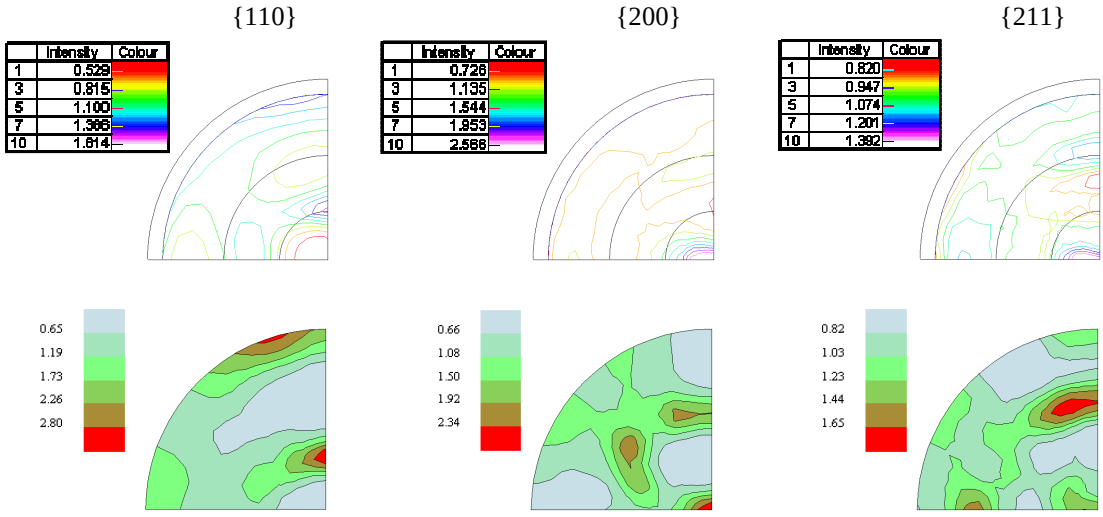

(a)

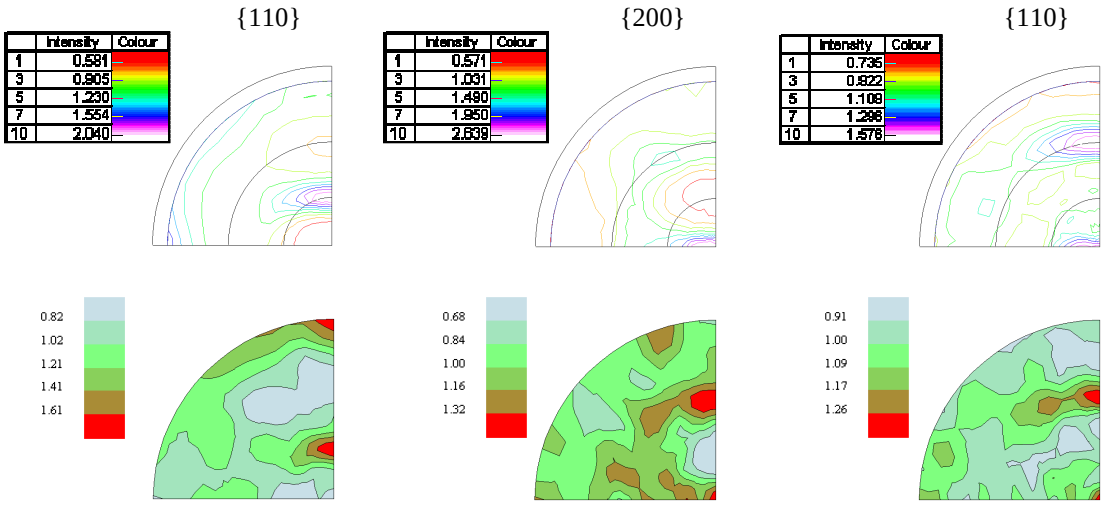

(b)

Figure 4.55: Standard {110}, {200} and {211} pole figures showing the texture measured by EBSD (filled) and XRD (outline only) of (a) 70% reduction HSLA steel and (b) full annealing the same sample.

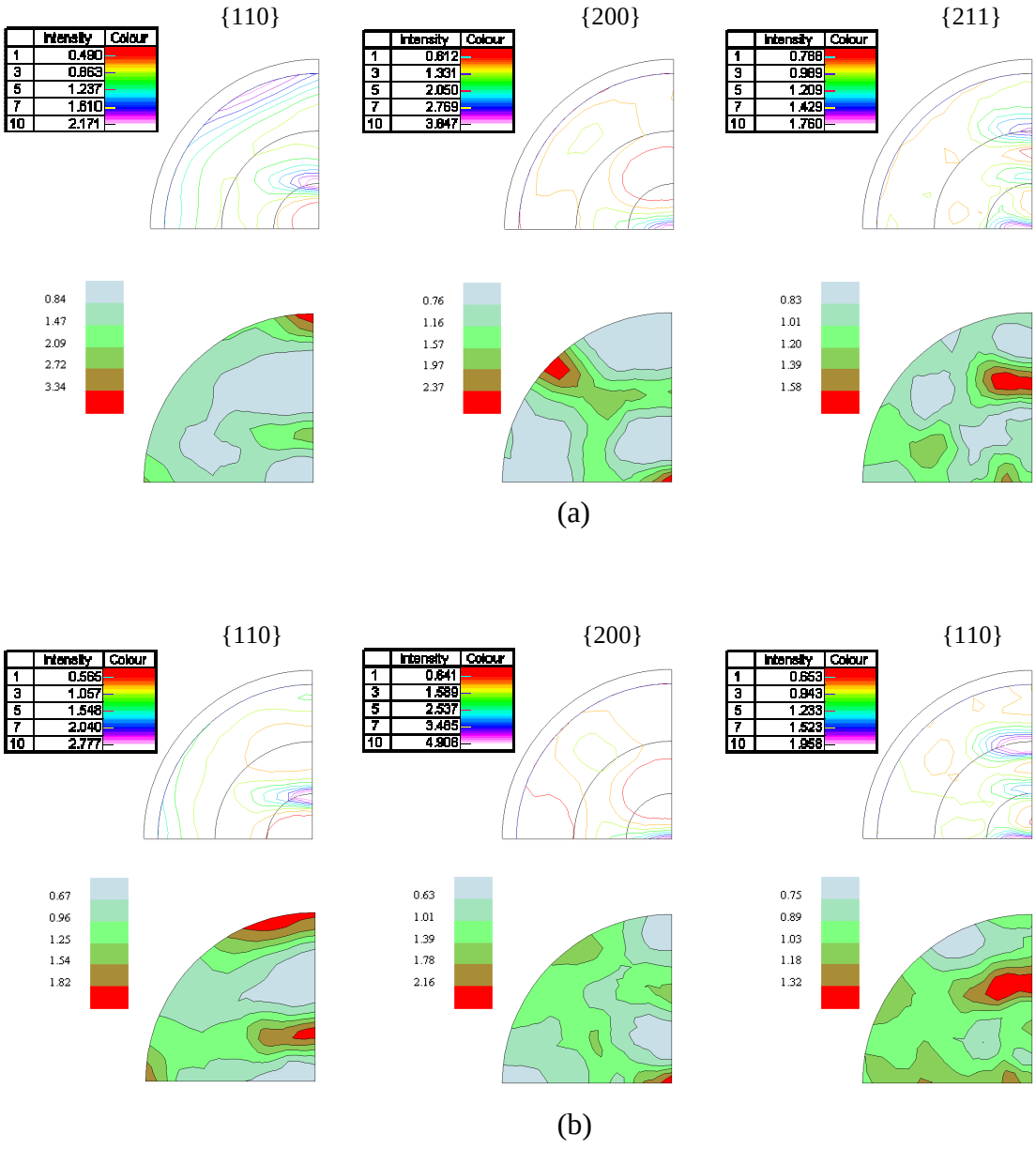

Figure 4.56: Standard {110}, {200} and {211} pole figures showing the texture measured by EBSD (filled) and XRD (outline only) of (a) 90% reduction HSLA steel and (b) full annealing the same sample.

It is important to mention that the difference in basic detection principles of XRD and EBSD must be taken into account when comparing results obtained by these two techniques. The results of both XRD and EBSD measurements for all cases show, in general, similar textures as can also be seen from Figure 4.57 which shows ODFs calculated from XRD pole figure measurements. In this figure, both α- and γ-fibres exist with similar intensity to those of the corresponding EBSD results. This also indicates that the texture is reasonably homogeneous through the sample thickness, since the sampling depth of the two techniques is different. However, some variations- particularly the intensity of certain components in the γ-fibre- can be noticed. It should be borne in mind that these ODFs are generated from only three incomplete pole figures, so at least part of the difference between the EBSD and XRD ODFs is likely to be due to more approximate nature of the XRD-derived results. The differences between the surface and the bulk caused by different preparation methods may also account for some of the variation.

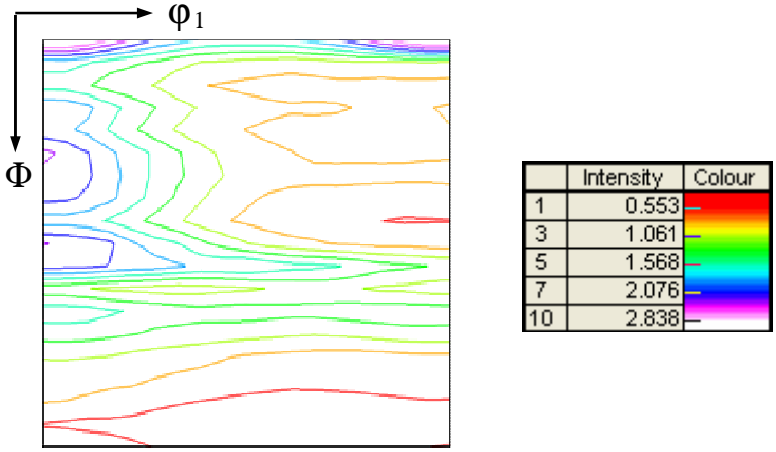

(a)

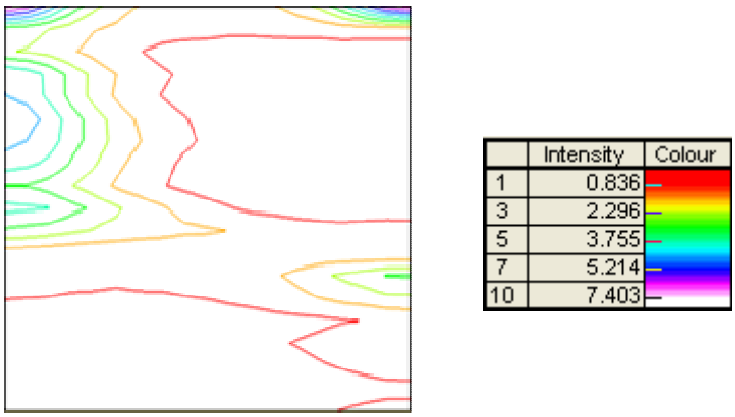

(b)

Figure 4.57: Textures of HSLA steel (ODF φ_2=45° sections, generated from XRD incomplete pole figures) cold rolled (a) 70% and (b) 90%.

4.6 *In-Situ* EBSD Observations

In-Situ SEM-EBSD experiments are a useful tool in understanding texture evolution, as it provides a direct observation of nucleation and growth phenomena during recrystallisation. Three HSLA steel samples with different reductions were used in this *in-situ* experiment. Sample 1 was cold rolled 70% whereas samples 2 and 3 were cold rolled 50%. The samples history, preparation method and operational conditions are detailed in Section 3.5.2.2.

Figure 4.58-60 show sequential EBSD maps of samples 1, 2 and 3 in the as-deformed condition and after holding for various times at elevated temperature. The pearlitic particles, present in this steel, are also shown in each EBSD map. They were identified from the band contrast image of the EBSD map and an in-house image analysis program (described in Section 3.5.1.3) was used to adjust the contrast and changing threshold colour limits of the particles. Then, the image was superimposed on the related coloured map to show the location of these particles as black areas.

It is important to mention that the high temperature used in these *in-situ* experiments and the reduction of time required for data collection have subsequent negative effects on the data produced. In addition, the high magnification EBSD mapping analysis used in these experiments (~ 3000X) makes the control of charging and drifting of the image during EBSD acquisition more difficult.

From the EBSD maps of Figure 4.58-60, it can be seen that the preferred nucleation sites were the pearlitic particles with no evidence of any other nucleation sites. This fact has been clearly recognised in all three samples, where the areas with no particles were the last to recrystallise. The reasons behind this are the low recrystallisation temperature used and the high volume fraction of particles. It has also been found that some of the recrystallised grains appear to grow faster than others. This is the case in all samples, and seems to be through an oriented growth process where a favourable orientation relationship between the recrystallised grains and the neighbouring deformed matrix may exist.

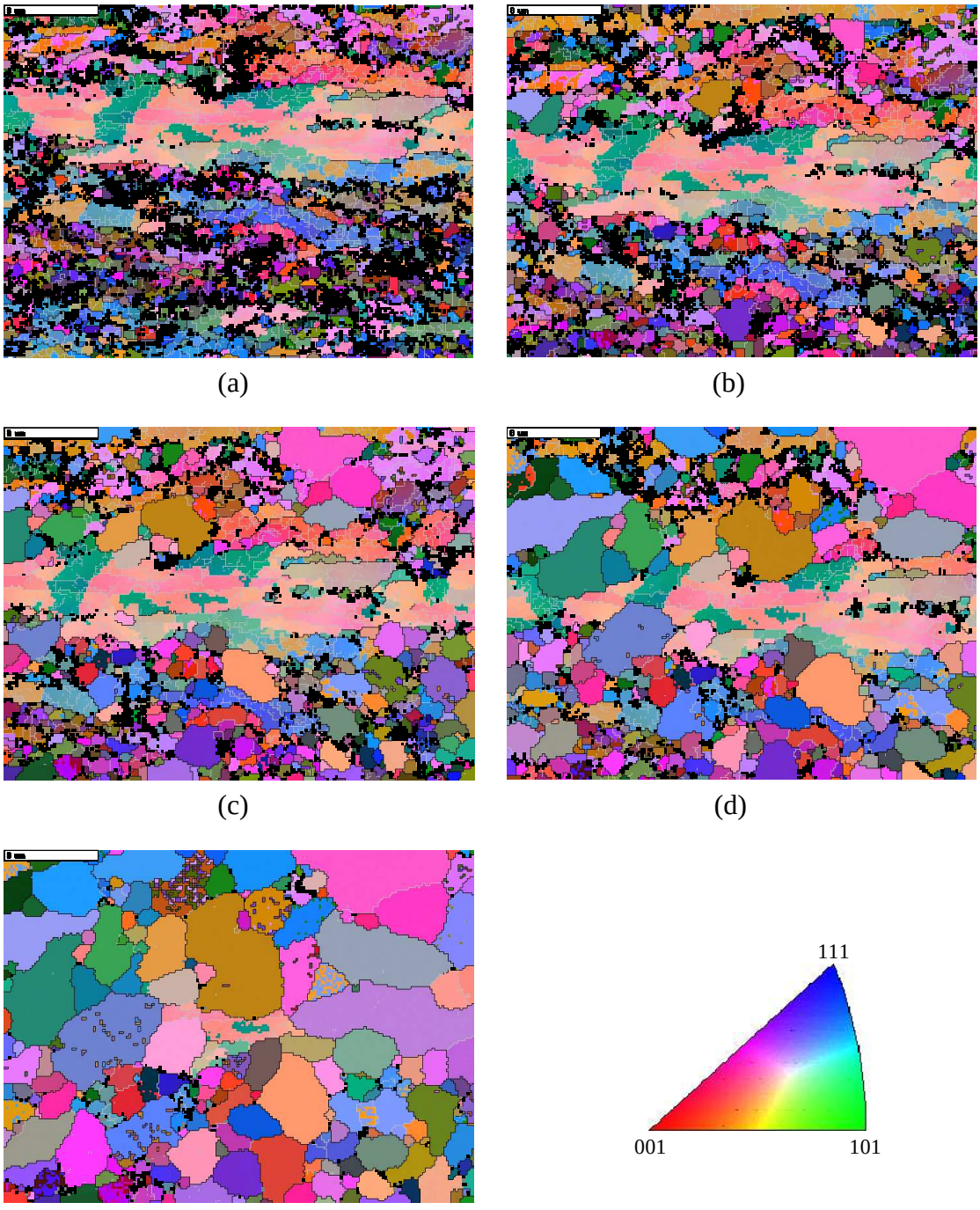

Figure 4.58: EBSD maps showing sequential microstructural evolution of sample 1 (70% reduction). (a) as-rolled condition and (b-e) during annealing at 500-575^{o}C over a total time of 6 hours.

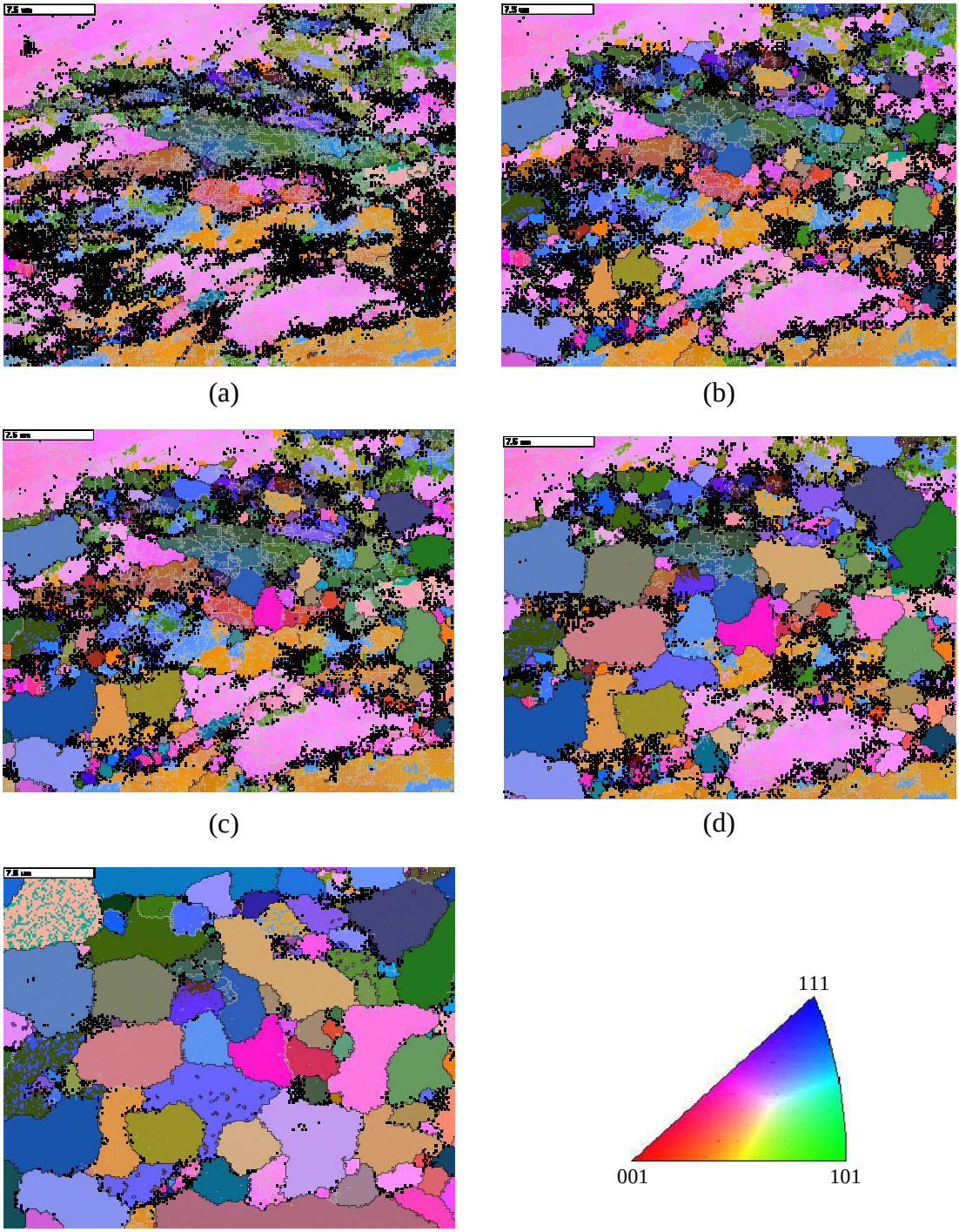

Figure 4.59: EBSD maps showing sequential microstructural evolution of sample 2 (50% reduction). (a) as-rolled condition and (b-e) during annealing at 500-580^{o}C over a total time of 6 hours.

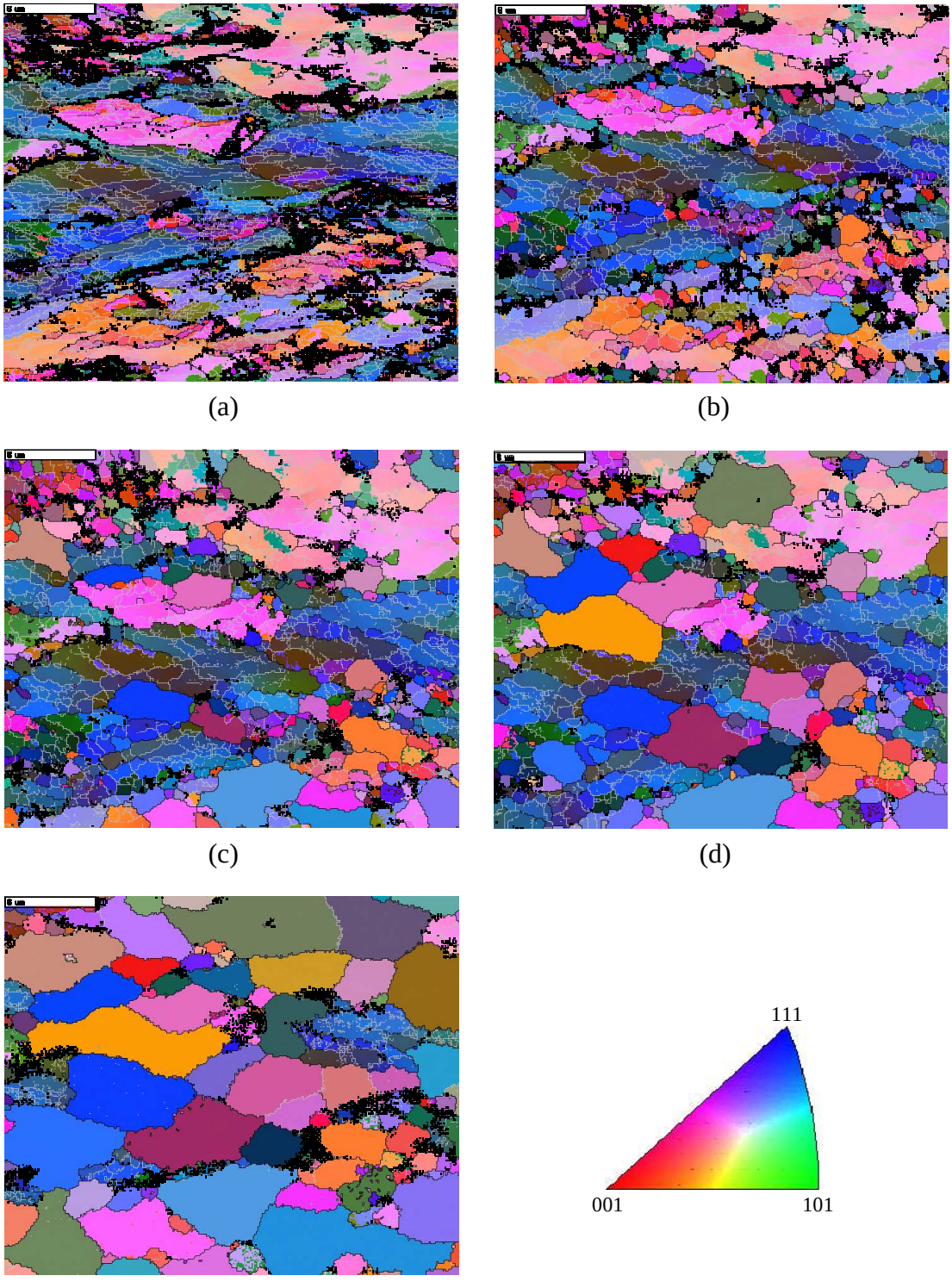

Figure 4.60: EBSD maps showing sequential microstructural evolution of sample 3 (50% reduction). (a) as-rolled condition and (b-e) during annealing at 500-530^{o}C over a total time of 6 hours.

The assumption that the orientations of the recrystallised nuclei already exist in the deformed microstructure seems applicable. Figure 4.61 shows that more than 80% of the orientations of the recrystallised nuclei are already found in the deformed microstructure for all three samples investigated. Those recrystallised nuclei where their orientations do not exist in the deformed microstructure seem to have originated and emerged from the interior of the sample.

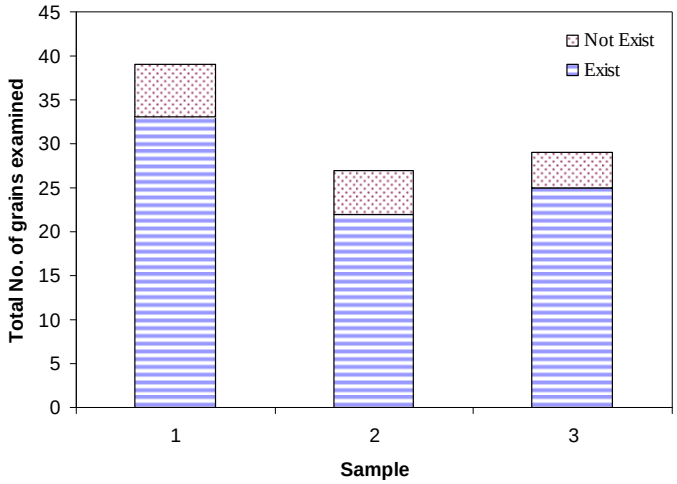

Figure 4.61: The relationship between orientations in the matrix and the recrystallised nuclei for all the samples

Figure 4.62–64(a) show a comparison between the grain boundary misorientation distribution of the as-rolled (blue) and the fully-annealed (red) states of each one of the three samples examined. A clear development of LAGB's to HAGB's during annealing in all samples can be observed in these misorientation histograms. In addition, Figure 4.62-64(b-c) show a comparison between the texture of the same region before and after annealing. Despite the dominance of PSN in this steel, the recrystallisation textures were similar to the rolling textures, with the texture components being α- and γ-fibres, although the texture intensity was lower.

It is important to mention that Figure 4.62-64(b-c) show local texture and may not represent accurately the bulk texture of the sample. This fact can be seen clearly in Figure 4.65. This figure compares the local texture (i.e. as-rolled and fully-annealed textures) of the area examined in sample 3 with the bulk texture of the same sample. The as-rolled textures are, to some extent, similar while the recrystallisation textures are different. A higher intensity of γ-fibre texture components can be observed in the bulk texture compared to the local texture measurement.

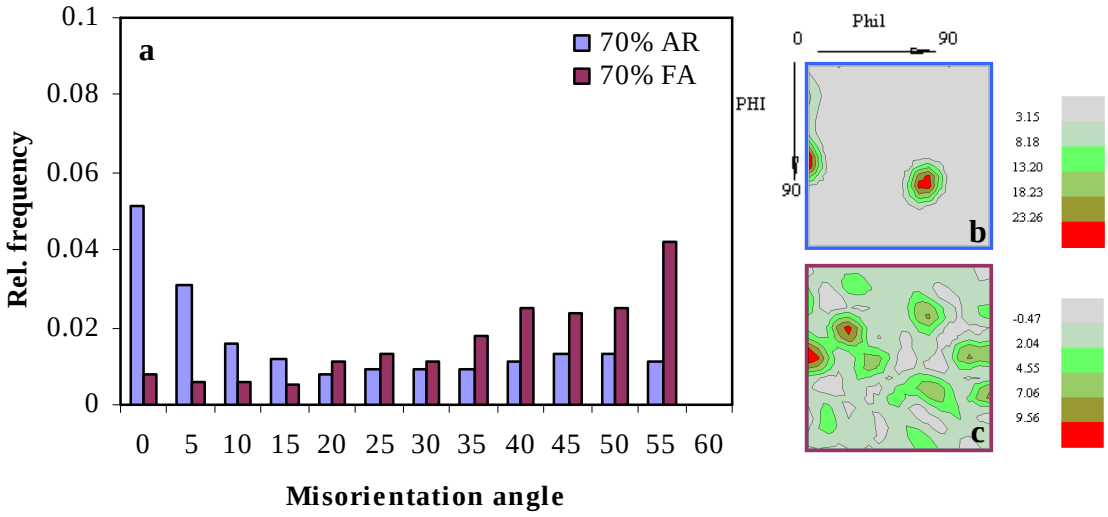

Figure 4.62: (a) Histogram showing comparison between the misorientation angle distribution of the as-rolled (AR) and the fully-annealed (FA) states of sample 1 and (b) and (c) show the AR and the FA textures (ODF φ_2=45^o sections), respectively.

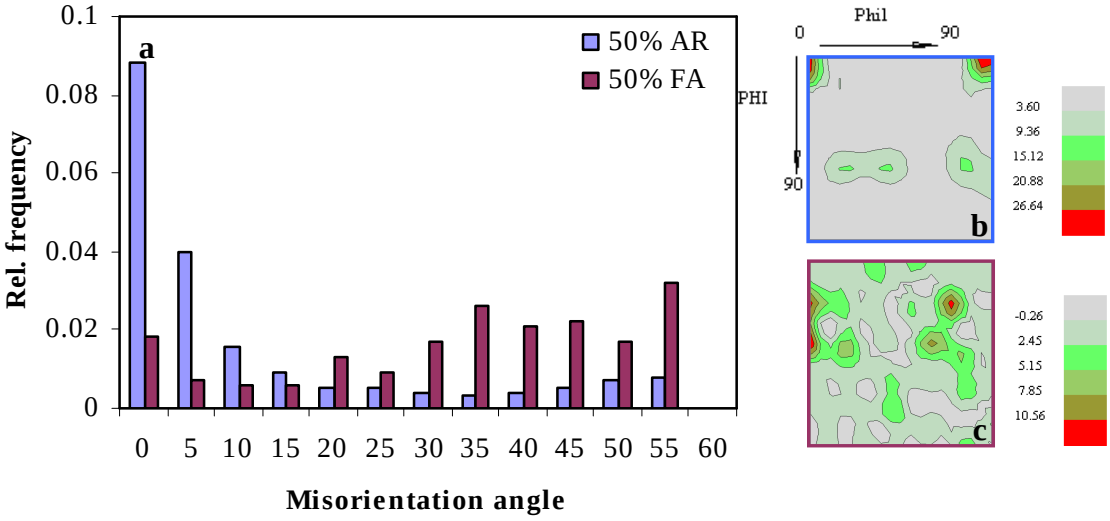

Figure 4.63: (a) Histogram showing comparison between the misorientation angle distribution of the as-rolled (AR) and the fully-annealed (FA) states of sample 2 and (b) and (c) show the AR and the FA textures (ODF φ_2=45^o sections), respectively.

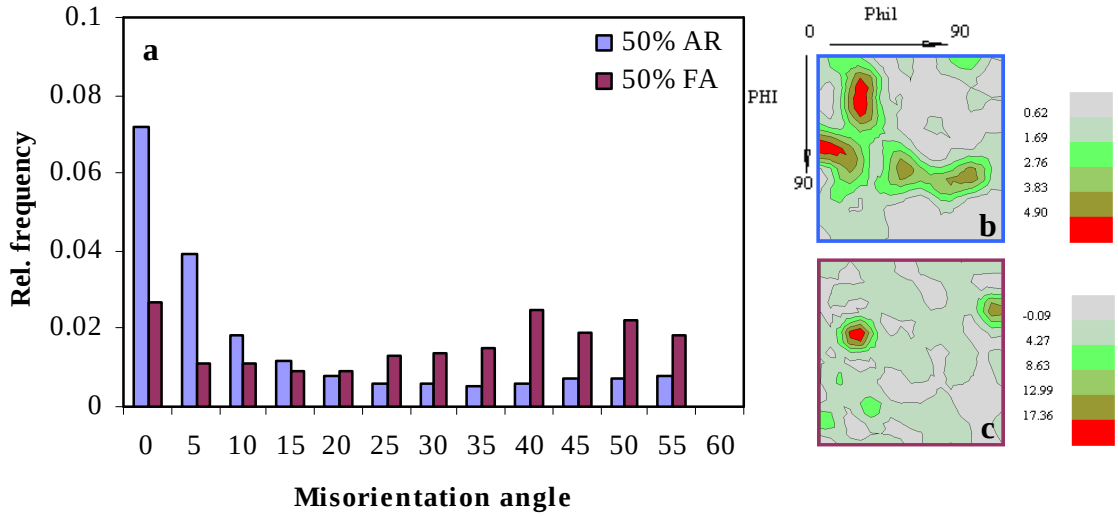

Figure 4.64: (a) Histogram showing comparison between the misorientation angle distribution of the as-rolled (AR) and the fully-annealed (FA) states of sample 3 and (b) and (c) show the AR and the FA textures (ODF φ_2=45^o sections), respectively.

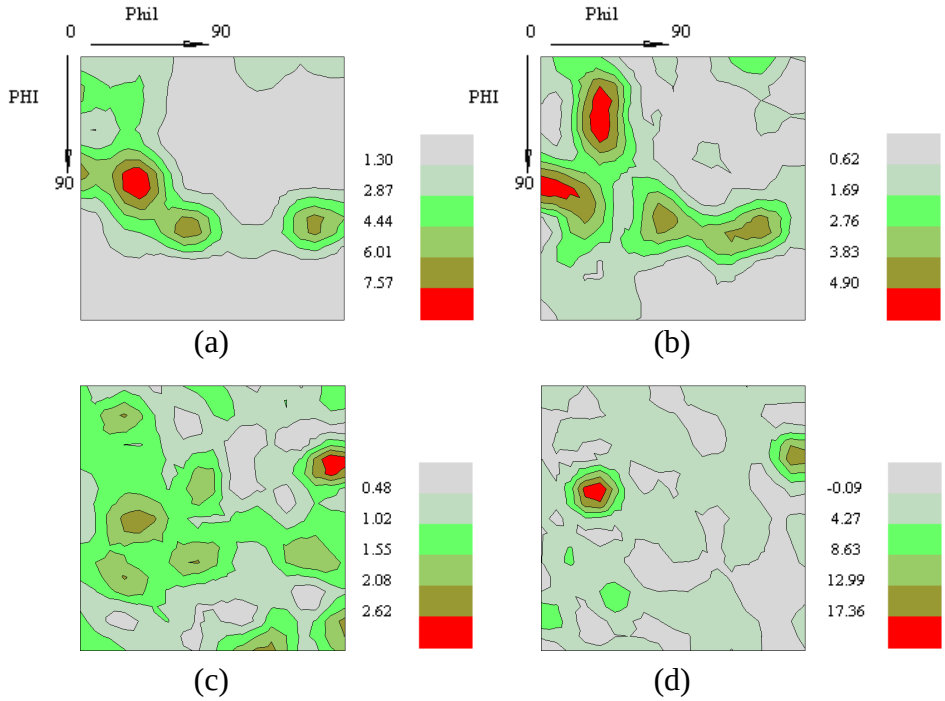

Figure 4.65: Bulk (a and c) and local (b and d) textures (ODF φ_2=45^o sections) of as-rolled (a and b) and fully-annealed (c and d) states of sample 3.

The grain growth of the recrystallised grains seems to be also enhanced by the concurrent dissolution of the particles; many examples of this were observed during the *in-situ* experiments. Figure 4.66 show one example where the "green" grain grew faster than the other two grains (i.e. the orange and purple grains indicated by the arrows). More detail analysis was made into the movement of grain boundaries. Figure 4.67 shows the misorientation between the grains described in the attached EBSD map (a selected area of the map shown in Figure 4.66). Grain f, neighbouring the deformed matrix (i.e. areas d and e), moved more rapidly than grain c as shown in Figure 4.66. However, the misorientation between the deformed matrix and the boundary of grain f, which is about 25^{o}, is almost equal to that of the boundary of grain c. The particles observed in this region may have played a significant role in enhancing the growth of this grain. The same figure shows a high misorientation, with no particle, between grains a and b compared to the misorientation between grains c and b. This possibly explains the faster growth of grain a as a result of the larger misorientation, which can be seen in Figure 4.66.

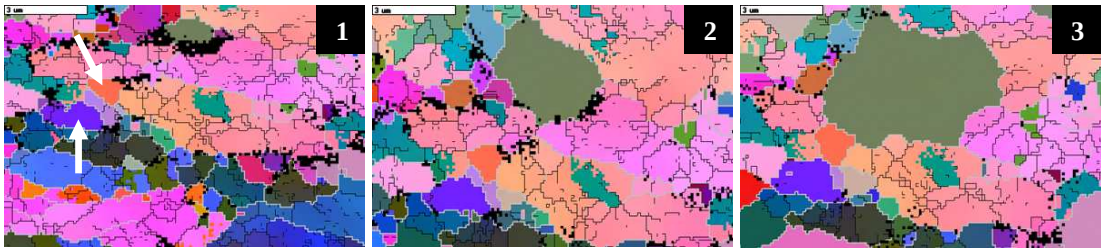

Figure 4.66: EBSD maps (selected area) showing sequential microstructural evolution of sample 3 where the grain growth seems to be enhanced by the dissolution of particles (low angle boundaries are black).

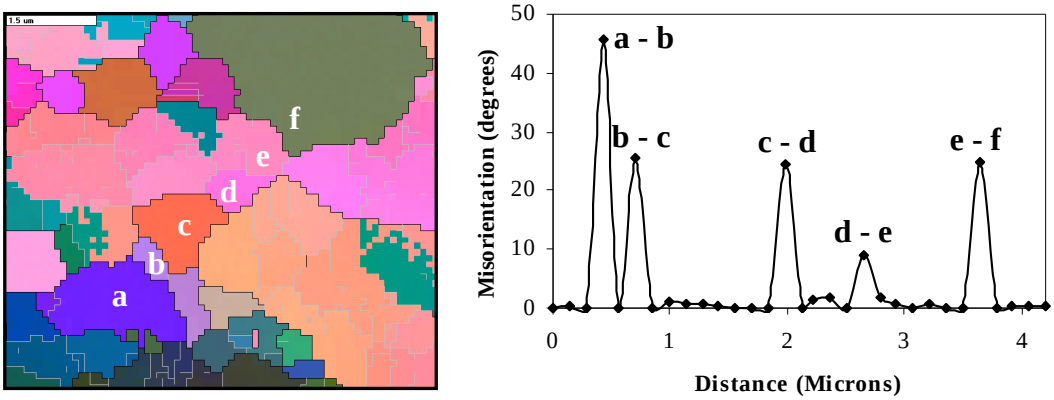

Figure 4.67: Relative misorientation profile (point to point) between the grains described in the attached EBSD map (particles removed).

4.7 Monte-Carlo Modelling

A wide range of recrystallisation and grain growth investigations have been made using two dimensional Monte-Carlo simulations. As this study is focused on the PSN phenomenon, a large particle was introduced into the microstructure in the simulation of recrystallisation. In addition, images of the microstructure at regular time interval during the simulation of grain growth was recorded, with the value of the grain sizes being obtained.

4.7.1 Application to Grain Growth

All of the normal grain growth investigations in this study were simulated on a square domain of 300 x 300 lattice site points with an initial structure of 2000 grains which results in an initial grain diameter of around 8 lattice points. This initial size was obtained by dividing the total domain area by the number of grains, calculating the mean grain diameter from this mean grain area using the relationship:

$$A = D^2 - 2D + 5 \qquad (4.1)$$

where A is the grain area in pixels and D is the grain diameter in pixels. Therefore, a grain of diameter 2 pixels (the diameter has to be an even number) will have a total area of 5 pixels. Examples of this relationship are shown in Figure 4.68 for grains of diameter 2, 4 and 6 pixels.

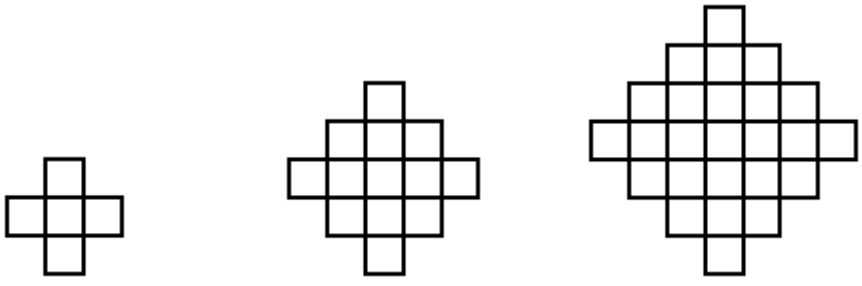

Figure 4.68: Structures showing the total grain area in pixels used in 2-D MCP simulation with a grain diameter of (a) 2, (b) 4 and (c) 6 pixels.

Figure 4.69 shows images of the initial microstructure and that after $1x10^3$ and $1x10^4$ MCS. This simulation was done with a randomly oriented structure where the grain boundary energy and mobility could be considered as being isotropic throughout the system. As a result, uniform normal grain growth is clearly observed in this experiment.

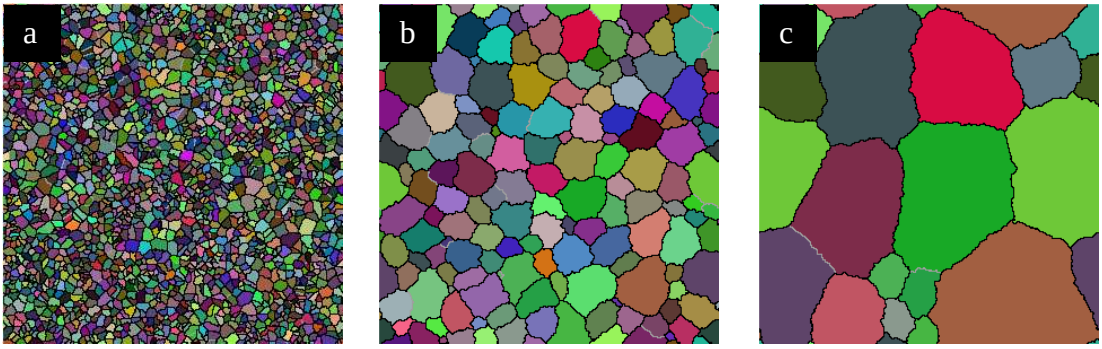

Figure 4.69: The evolution of microstructure from an initial uniform grain size distribution using 2-D MCP simulation. (a) at 0 MCS, (b) $1x10^3$ MCS and (c) $1x10^4$ MCS.

Figure 4.70 shows the evolution of mean grain size with time for the same simulation. A steady decrease in growth rate is observed as the time progress. Moreover, a linear relationship exists between the mean grain size squared and time as can be seen in Figure 4.71. This indicates uniform normal grain growth.

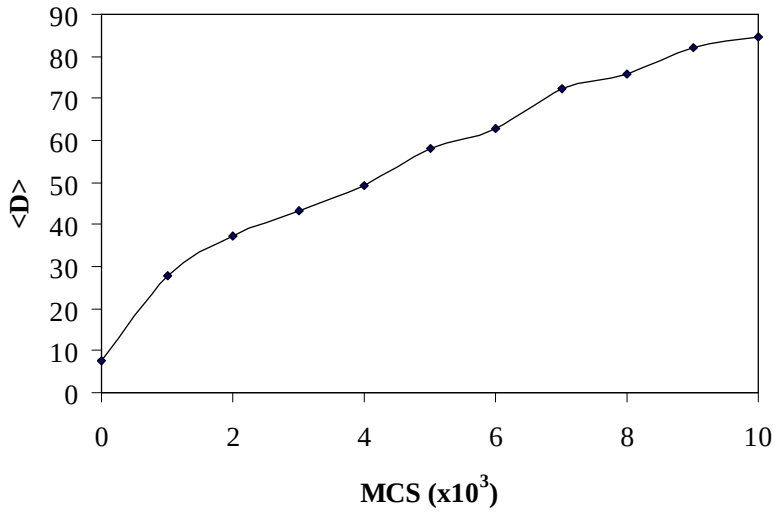

Figure 4.70: Plot of mean grain size with time for the simulation illustrated in Figure 4.69.

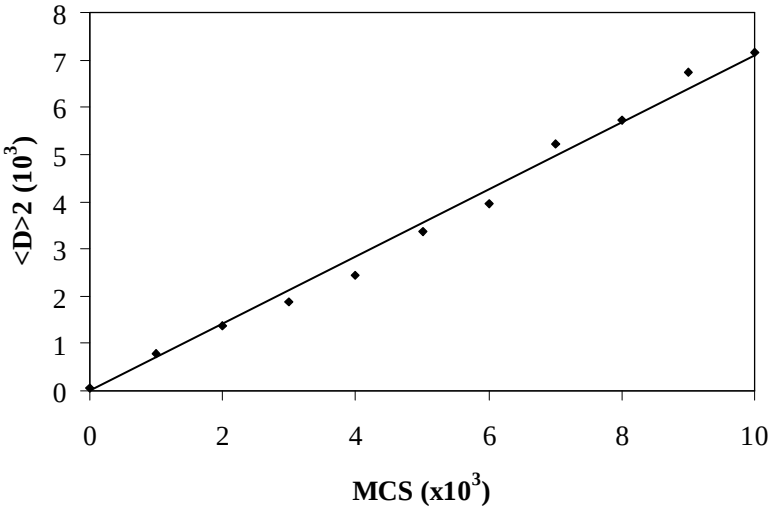

Figure 4.71: Plot of mean grain size squared with time for the simulation illustrated in Figure 4.69

4.7.2 Application to Recrystallisation (Modelling of PSN)

The use of Monte Carlo modelling for simulating the recrystallisation process is more difficult than for the grain growth process (discussed in details in Section 2.5.1). In this study, the focus will be given to the simulation of the PSN mechanism of recrystallisation.

The initial, nucleation, phases of recrystallisation are determined by gradients in orientation and substructural energy. In cell-forming metals such as aluminium the substructural energy is related to cell size and misorientation. While it is difficult to determine, or predict, the distribution of misorientation and stored energy around particles following large deformations, most published work indicates that the gradients in orientation are greatest near the particle surface. However, work using aluminium alloys (Humphreys 1980) has given an indication that PSN may not occur at the regions of highest misorientation close to the particle interface. Humphreys (1979) measured the misorientations as functions of distance from large particles in Al-Si, albeit at relatively small strains, and found that an empirical relationship of the following form fitted the data:

$$\omega(r) \approx \tan (A \exp (-c (r-r_0)/r_0)) \quad r > r_0 \qquad (4.2)$$

where r is radial location (zero at the particle centre), r_0 is the particle radius, c is a constant (3.6 here) and A is the tangent of the maximum misorientation which occurs

at r_0. The value of A was found to be approximately linear with strain, although saturation at larger strains is expected (Humphreys and Ardakani 1994). Humphreys also made the reasonable assumption that dislocation density was linearly related to the gradient of misorientation. With dynamic (and static) recovery, dislocation density can be replaced by inverse subgrain size. Using those functions for misorientations and subgrain size, 2-dimensional Monte Carlo- Potts simulations of PSN were carried out and shown in Figure 4.72. The boundary energies and mobilities followed standard equations given elsewhere (Equations 2.14-15 in Section 2.3.2.7), with a high-angle boundary level of 15º. More description of the computational details of this simulation can be found in Appendix C.

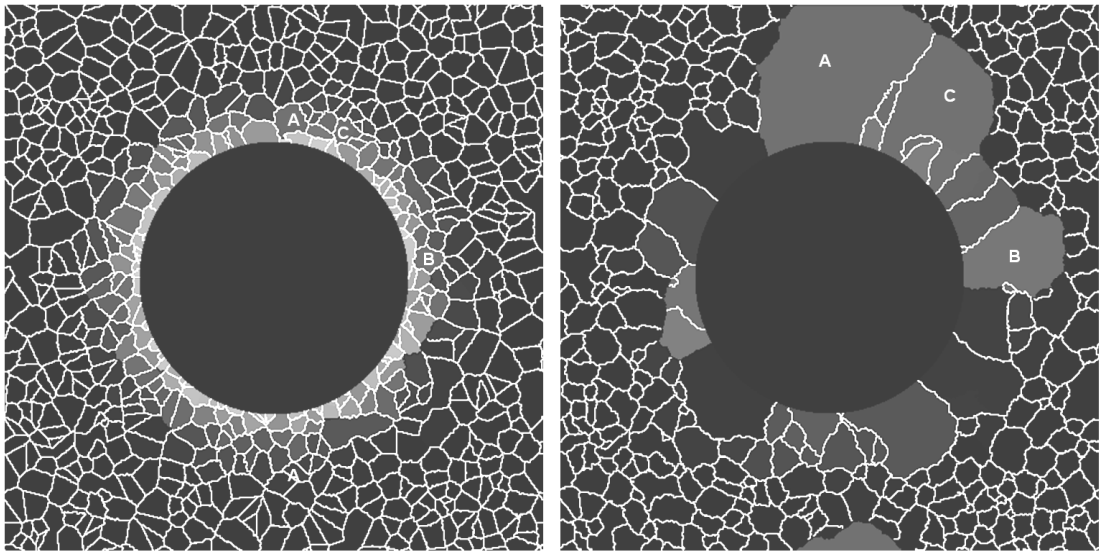

Figure 4.72: Images of MCP domains from a simulation of PSN. The gray scale indicates orientation, with the highly misoriented material at the start of the process (left) showing as lighter shades. After some time (right), all of those grains have vanished, and the nucleation events start from much less misoriented material originating away from the interface. The locations of the three fastest-growing crystallities; A, B and C, are indicated in both images.

In this example, the nucleation of recrystallisation from the deformation zone has been observed. It is also observed that some of the subgrains which eventually became the nucleus were not at the particle/matrix interface. This fact may play a significant role in determining the recrystallisation texture. However, although this simulation shows some similarity to real experiments, it should be regarded as tentative as it has not yet been extended to three dimensions where a larger number of variables need to be considered.

Chapter 5

DISCUSSION

5.1 Introduction

Based upon the results presented in the previous chapter, the following is a discussion of the various effects that different cold rolling reductions, compositions and annealing temperatures can bring about in the annealing behaviour and the texture evolution of the low carbon steels investigated. It takes into account the related published studies. Particular attention is paid to the different features of the deformation zone around large particles in low carbon steels and their influence on the rolling and recrystallisation textures produced.

5.2 Microstructures and Hardness of As-Rolled Material

After cold rolling, the initial grain structures become more elongated along the rolling direction as the reduction level increases, and formed a typical pancake structure (Figure 4.5 and Figure 4.6). The dislocations generated during cold rolling are not distributed uniformly in the different texture component of the microstructure as can be seen in Figure 4.8. The size and misorientation of the cell/subgrain structure are dependent on the grain orientation. Higher dislocation density is observed in the γ-fibre compared with the α-fibre texture components which indicates that γ-fibre regions will have a higher stored energy than α-fibre regions. The hardness increases with increasing rolling reductions as indicated in Figure 4.10. This was expected since a higher dislocation density is created and accumulated during cold rolling which results in the increase of hardness with increasing reduction.

The coarse pearlitic particles present in HSLA steel are formed on the grain boundaries prior to rolling. This initial condition induced complex deformation in the regions near the particles during cold rolling, leading to the disruption of these particles. In addition, the presence of such particles caused large strain inhomogeneities during rolling which create high dislocation zones around them, with steep orientation gradients. The selected area electron diffraction patterns obtained in these zones contain spots from many orientations, and showed considerable arcs rather than simple diffraction spots, especially in the vicinity of the particles (Figure 4.31). This indicates severe local deformation in these areas. The high stresses in the vicinity of particles are known to arise from the accumulation of Orowan loops during the deformation (Ashby 1966).

Since large local strains are found in the vicinity of the particles, which indicate high stored energy, and since large orientation gradients are present in these areas, the nucleation of the recrystallised grains may preferentially occur in these regions (Humphreys 1977).

5.3 Cold Rolling Textures

The cold rolling textures of both steels investigated consists mainly of the α- and γ-fibres texture components which are largely dependent on the rolling reduction. With increasing reduction, the texture shows gradual intensification of both fibres components, with weaker intensity in HSLA steel where particles are present.

Moreover, the strongest texture component, in the case of IF steel, is {112}<110> which rotates about <110>//RD axis toward {223}<110> after 90% reduction. This rotation and other crystallographic rotations occurred in the IF steel during cold rolling seem to follow the two paths given by Inagaki (1987; 1994) which are shown in Figure 5.1. This figure show that both initial orientations rotate to {223}<110> which is identified as the stable end orientation.

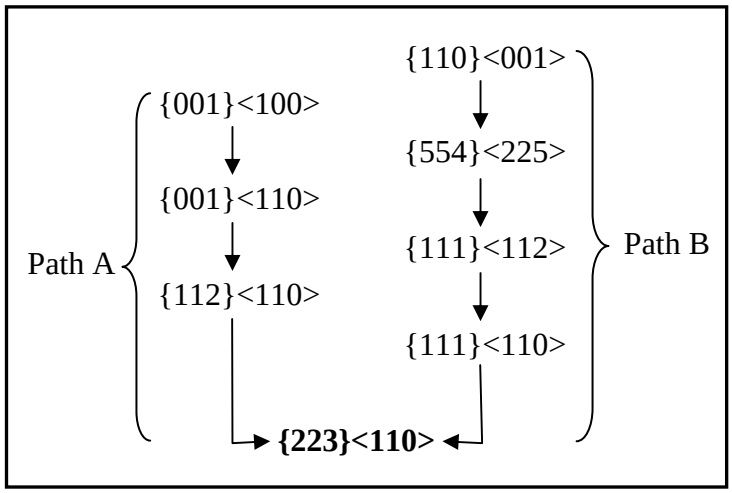

Figure 5.1: Paths of crystal rotation during cold rolling of polycrystalline iron showing the stable end orientation (Inagaki 1987a).

The crystallographic rotation occurs by a consecutive process. In order to reach the stable end orientation of {223}<110>, the orientations are required to pass through {112}<110> and {111}<110> and the other orientations shown. This fact is shown clearly in Figure 4.26a. This Figure shows the orientation density distribution along the α-fibre for IF steel where the maximum density is at {001}<110>, {115}<110>, {112}<110> and {223}<110> for 20%, 50%, 70% and 90% reductions, respectively. This indicates that the crystallographic rotations seem to follow path A, described in Figure 5.1. It is clear that, with increasing reduction, the rotation towards the {223}<110> is observed.

The uniformly distributed orientation density along the γ-fibre in 90% cold rolled IF steel, as given in Figure 4.26b, can be explained by crystallographic rotations following path B. The weak {554}<225> observed in the 20% reduction rotate towards {111}<112> resulting in a strong {111}<112> orientation component after 50% reduction. With higher reductions, the oriented grains having this orientation are rotated to {111}<110> and finally to {223}<110>. A fairly uniform distribution of the γ-fibre components results at the end with an enhancement of the {223}<110> orientation component.

On the other hand, the rolling texture of the HSLA steel was found to be weaker compared to the IF steel. The presence of pearlitic particles in this type of steel plays a significant role in this issue. Since rotation toward the stable end orientations

occurs by dislocation slip, these particles affect dislocation motion and, hence, create highly orientation-spread zones around them. Figure 4.30-31 show this orientation spread within the deformation zone around a particle.

Figure 4.27 shows the orientation density along the α- and γ-fibres after several cold rolling reductions for HSLA steel. This figure shows a peak at {111}<110> for low reduction (i.e. 20%). With increasing reductions, this peak shifted toward {001}<110> and {111}<112> along α- and γ-fibres, respectively. It therefore appears that the rotation paths in this steel differs from that of the IF steel. These differences may have an effect on the recrystallisation behaviour due to the variation in stored energy with different orientation components, although PSN is dominant in this steel.

5.4 Recrystallisation Kinetics

As expected, the recrystallisation rate increased with the degree of cold rolling reduction due to the increase in the stored energy and the number of effective nuclei, as shown Figure 4.14,15 and 17, for both steels investigated. The first two figures show that with constant annealing time (one day in this study) for full recrystallisation for all the reductions, the annealing temperature increases as the reduction decreases. In addition, the recrystallisation rate also increased with higher annealing temperature (Figure 4.16) since recrystallisation is a thermally activated process. Moreover, the effect of the particles in enhancing the recrystallisation is significant, dropping the temperature for recrystallisation by about 100^{o}C.

It is important to mention that the recrystallisation fraction results determined by EBSD, by monitoring the changes of HAGB content during annealing, seem to be consistent with the optical microscopy results. The difference between the two methods did not exceed 5% recrystallisation fraction.

Recrystallisation kinetics are highly influenced by the annealing temperature, where the recrystallisation rate will increase as the annealing temperature increases. Figure 5.2 shows a plot of $\ln(t_{0.5})$ as a function of $1/T$ (Arrhenius plot) in 70% cold rolled IF and HSLA steels annealed at various temperatures. This plot usually generates a straight line with a slope corresponding to the activation energy. In this study, the apparent activation energy is calculated to be 314 and 339 kJ/mol for IF and HSLA steels, respectively. These values are higher than that reported by Glover and Sellars

(1973) of pure ferritic iron of 280 kJ/mol. This fact has previously been attributed to the presence of micro alloying elements such as Ti and Nb (Barnett and Jonas 1999).

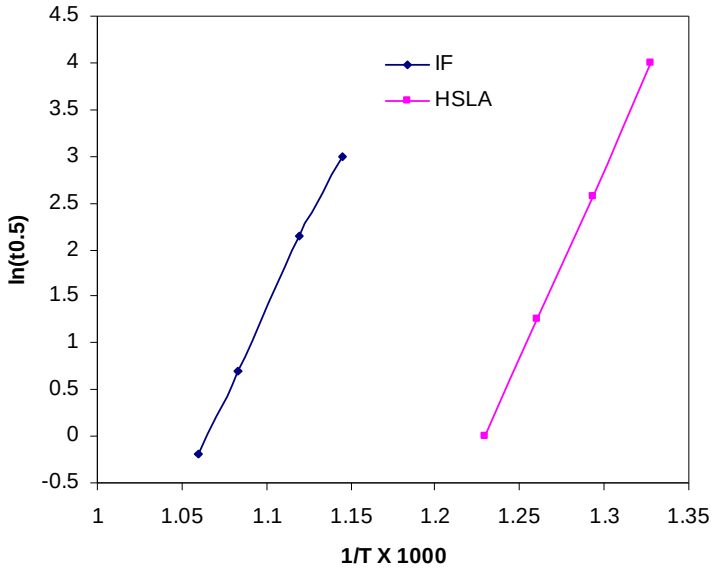

Figure 5.2: Arrhenius plot of the time for 50% recrystallisation for 70% cold rolled IF and HSLA steels.

It is also observed that the hardness decreases with the degree of recrystallisation, as indicated in Figure 4.14-15. This is due to the lower density of dislocations and, hence, the low hardness of the recrystallised grains and recovery in the remaining deformed material. In addition, it is important to mention the greater change in hardness in the fully annealed HSLA steel compare to the as-deformed state. This is associated with the dissolution of the pearlitic particles during annealing. The particle shape also has an effect on the hardness. The more elongated particles, as the reduction increases, give more nucleation sites which reduced the final grain size and, hence, increase the hardness.

5.5 JMAK Modelling

It is assumed in the JMAK model that nuclei are formed at a rate $\dot{N}$ and that grains grow into the deformed material at a linear rate $\dot{G}$. In real recrystallisation processes, the new grains eventually impinge on each other and the rate of recrystallisation then decreases. There are several early experimental investigations of recrystallisation on aluminium (Gordon and Vandermeer 1962), low carbon steel (Rosen *et al.* 1964) and copper (Hansen *et al.* 1981). In these studies, the JMAK exponent *n* is generally observed to be well below the theoretical values. In fact, few experimental data show close agreement with JMAK kinetics (Humphreys and Hatherly 2004). In this

experiment, most of the JMAK plots were approximately linear (Figure 4.18-19), but the *n* values ranged from 1.4 to 2.0. It can, therefore, be concluded that some of the assumptions made in the JMAK analysis do not apply to real recrystallisation processes. In the equation of the JMAK model, there are no parameters relating the microstructure (i.e. grain size) to the recrystallisation process, so the model may be too simple as a quantitative model to fully describe the complex process of recrystallisation in a real material.

5.6 Recrystallisation Textures

5.6.1 General consideration

Recrystallisation textures are usually interpreted in terms of variation in the kinetics of nucleation and/or growth and how such variations may impinge on specific orientations. To address this issue and to understand the recrystallisation behaviour and the type of recrystallisation texture produced, it is important to investigate how the dislocations are distributed among the different texture component during rolling. It was observed that the α- and γ-fibres texture components, in both steels, were the main texture components after cold rolling. In deformed γ-fibre grains, large misorientations exist compare to the deformed α-fibre grains as can be seen in Figure 4.29. This indicates a higher stored energy exists in the γ-fibre grains and, hence, a higher recrystallisation rate during annealing is expected to occur in these grains. This variation in local orientation environment with different texture components will be the basis for understanding and explaining the development of the recrystallisation textures during annealing.

5.6.2 Recrystallisation Texture in IF Steel

Texture development during the recrystallisation of IF steel is shown to be largely dependent on the rolling reduction. The annealing texture is, in general, of the α-fibre components at low reduction (20%) as shown in Figure 4.46a. However, with increasing rolling reduction, the annealing texture shows gradual intensification of the γ-fibre components (Figure 4.46b, c and d).

Figure 4.48 shows the orientation density distribution along the α- and γ-fibres for fully annealed IF steel. Generally, most of the peaks along both fibres for all reductions are at positions different to that of cold rolling textures. For example, the

peaks in the rolling texture for 50% reduction lie at {111}<112> (Figure 4.26b) while those after recrystallisation lie at {111}<110>. Hutchinson and Bate (2003) have explained this interchange by considering conditions where low mobility of grain boundaries may prevent some types of texture change from occurring (i.e. ∑3 twin boundary between $(111)[0\bar{1}1]$ and $(111)[1\bar{1}0]$).

Moreover, Figure 4.48b shows a uniformly distributed orientation density along the γ-fibre in fully annealed IF steel rolled 70%. This uniform and strong γ-fibre plays a significant positive role in determining the planar anisotropy of the sheet properties, particularly in the control of earing in deep drawn parts. Equal amounts of the ideal {111}<112> and {111}<110> orientation components are expected to result in minimal earing. However, this behaviour changed with increasing the rolling reduction where intensification of certain components along the γ-fibre occurred.

This strengthening of γ-fibre, particularly after high reductions, seems to be associated with the recrystallisation mechanisms. The recrystallisation mechanism changes with the degree of reduction. At low reduction (20% in this study), grain boundary nucleation dominates in the recrystallisation process and the boundaries act as nucleation sites by the SIBM process (Humphreys and Hatherly 2004). In this case, the low energy α-fibre orientations (i.e. {001}<110> and/or {112}<110> subgrains) become favoured. This mechanism is changed, with higher reductions, to subgrain growth mechanism in γ-grains since the stored energy in these grains become high (Dillamore *et al.* 1967). In this study, it starts at 50% reduction and continues as the dominant mode for the 70% and 90% reductions. The subgrain growth mechanism favours the nucleation of the γ-fibre orientation components.

There is a close similarity between the orientation spread of the early-formed grains and the texture of the steel at completion of recrystallisation. This fact is clearly seen in Figure 4.38-41 where the texture of recrystallised and unrecrystallised regions of 50% and 70% reductions were measured separately. At the early stage of recrystallisation, the textures of the recrystallised regions in these samples are similar to the final recrystallisation texture shown in Figure 4.46b-c. Moreover, the growing grains consume the deformed γ-fibre matrix first, and only in the latter stages of recrystallisation does the deformed α-fibre disappear (Figure 4.39b and 40b). This behaviour in the evolution of the recrystallisation texture and the depletion of texture in the deformed matrix is in good agreement with the work of Lindh *et al.* (1994).

To address this issue in more detail, Figure 5.3 shows a colour coded map (i.e. α- and γ-fibre and {001}<*uvw*> orientations are highlighted where a spread of 10^{o} was allowed around each fibre). The recrystallised and unrecrystallised regions of 70% cold rolled and partially recrystallised (12%) IF steel sample are also separated. In addition, the recrystallised grains having a grain size of more than 10µm are further separated to represent the size of the later stages of recrystallisation. It is clearly observed in this Figure that in the early stage of recrystallisation, the γ-fibre grains are growing faster than others. This Figure shows also that most of the observed large grains were growing in the deformed γ-fibre grains.

In light of the results and observations discussed above, it can be concluded that the recrystallisation textures of this steel, particularly after high reductions, seem to be controlled by the orientation of the nuclei (oriented nucleation) rather than by growth selection.

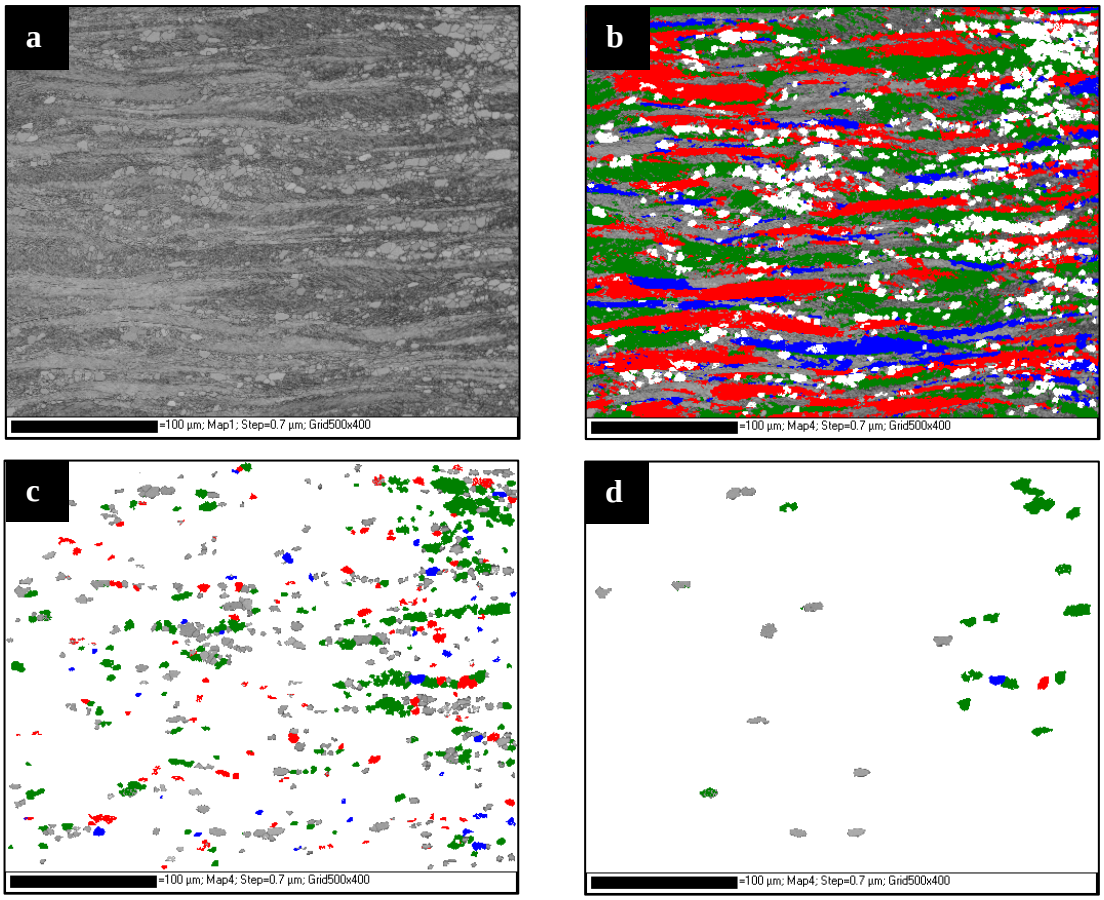

Figure 5.3: EBSD colour coded map showing IF steel sample cold rolled to 70% and partially recrystallised. (a) Band contrast, (b) deformed region, (c) recrystallised region and (d) > 10µm recrystallised grains. (Green, red and blue grains correspond α-fibre, γ-fibre and {001}<*uvw*> orientation. Other orientations are shown in band contrast)

5.6.3 Recrystallisation Texture in HSLA Steel

The pearlitic particles in the HSLA steel have a strong effect on the texture development during recrystallisation, because nucleation of recrystallised grains in this steel occurs preferentially in the deformed zones developed around these particles during cold rolling. No other nucleation sites were observed, as can be seen in Figure 4.23, 35 and 36. Since highly orientation-spread zones were created around these particles, the orientations of the recrystallised grains nucleated in these regions are expected to be weak.

The recrystallisation textures for this steel can be seen in Figure 4.47. This Figure shows that with increasing the rolling reduction, gradual intensification of both the α- and γ-fibres are observed. This behaviour differs from that of the IF steel where only the γ-fibre becomes significant with increasing reduction. In addition, the orientation density distribution along both fibres for fully annealed HSLA, shown in Figure 4.49, show low densities along both fibres compared to IF steel, with slight increase with increasing reduction. This existence of both fibres, even with low densities, in this type of steel where PSN is the preferential nucleation mechanism leads to questions about the detailed mechanism of PSN and its effect on the recrystallisation textures produced.

Figure 4.42c shows the texture of the recrystallised grains at the early stage of annealing and the α- and γ-fibres are clearly shown. It can be seen that the peaks along both fibres for the recrystallised grains are at positions different to that of cold rolling textures (Figure 4.42b). The peaks in the rolling texture lie at {111}<110>, {223}<110> and {001}<110> while those after recrystallisation lie at {111}<112> and {115}<110>. This rotation of the recrystallised grains from the deformed matrix can also be seen in the high magnification maps shown in Figure 5.4, where the peaks after recrystallisation are at orientation different to that of the cold rolling texture.

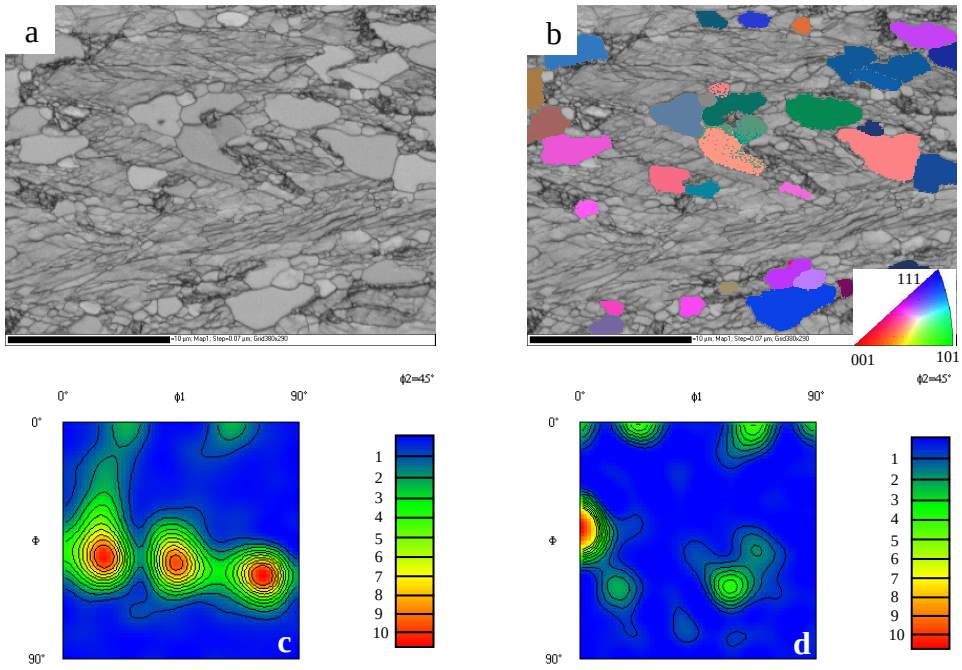

Figure 5.4: EBSD map showing partially recrystallised HSLA steel rolled 50% and annealed at 500°C. (a) Band contrast, (b) Euler colour of the recrystallised grains, (c) and (d) show the textures of deformed and recrystallised grains, respectively.

To address this issue in more detail, Figure 5.5 shows a recrystallised grain nucleated within a deformation zone of a particle located in γ-fibre deformed matrix. The new grain also has a γ-fibre texture component shifted from the deformed matrix orientation, as shown in the attached pole figure. In addition, Figure 5.6 shows the orientations of the recrystallised grains (i.e. grains 1 and 2) and the orientation of the surrounding matrix. It seems to be that, since the present particles have complex forms (discussed in Section 2.3.2.5), no systematic orientation change was found within the deformation zones around them during rolling and subsequently with the recrystallised grains after annealing. Generally, these figures (i.e. Figure 5.4-6), in addition to that shown in Figure 4.35, show that the orientations of PSN nuclei are not random, although the orientation spread is high. It seems that the location of the nucleation events within the deformation zones around the particles plays a significant role in this issue. The formation of nuclei seems to occur within the deformation zones in regions away from the particle surface (i.e. the centre of the zone) where the orientations were perturbed by a critical amount to give high mobility boundaries. This might account for the general weakening of texture, rather than the generation of new specific orientations, when significant PSN occurs.

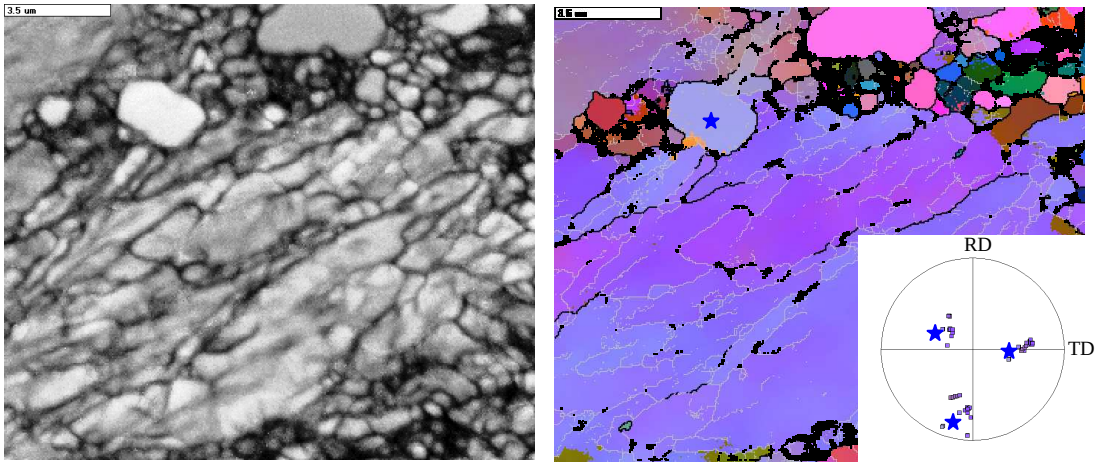

(a) (b)

Figure 5.5: EBSD map showing partially recrystallised HSLA steel rolled 50% and annealed at 500^{o}C. (a) Band contrast and (b) Euler colour map with the standard {100} pole figure showing the orientation of the selected grain. (Star and square correspond to recrystallised grains and surrounding deformed matrix)

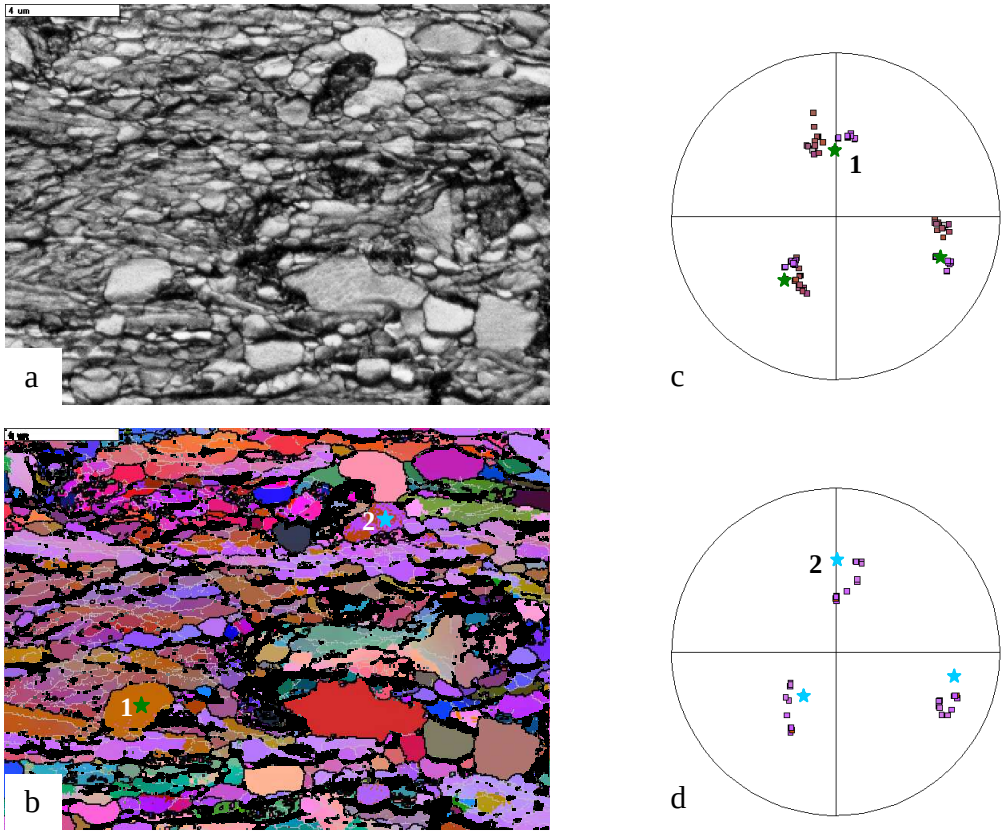

Figure 5.6: EBSD map showing partially recrystallised HSLA steel rolled 70% and annealed at 500^{o}C. (a) Band contrast, (b) Euler colour map, (c) and (d) standard {100} pole figures showing the orientations of selected grains in (b); grains 1 and 2, respectively (Star and square correspond to recrystallised grains and surrounding deformed matrix, respectively).

It is likely that particles situated in regions where high strains and high strain gradients occur, such as at the boundaries of γ-fibre grains, may provide more favoured nucleation sites than other particles. The nucleation rate, as well as the growth rate, of these "new" grains is higher than those nucleated around particles located in the boundaries of α-fibre grains. Similar stored energy differences were observed in IF steel and there is some evidence of this effect in HSLA steel. The textures of the unrecrystallised regions of Figure 4.43c and 45c show high intensity of the α-fibre. This behaviour was expected as the stored energy is low in α-fibre orientation grains compared to γ-fibre orientation grains. The growth rate of these nuclei will be higher in these regions of higher stored energy.

5.7 *In-Situ* EBSD Observations

Direct observation of nucleation and growth phenomena clarifies many issues of the recrystallisation mechanisms. The *in-situ* experiments performed in this study have shown that most of the orientations of the recrystallised nuclei are present in the deformed structure. Those recrystallised nuclei whose orientations do not exist in the deformed microstructure seem to have originated and emerged from the interior of the sample. In addition, the difficulty in obtaining a high quality EBSD image in the deformation zone around the particles plays a significant role in this issue.

The recrystallisation microstructures and textures of all the three samples examined in these *in-situ* experiments show similar behaviour to that observed using conventional examination after heating and cooling. However, slight variation in the recrystallisation textures in these experiments compared to the bulk texture has been observed (Figure 4.65), probably as a result of the free surface effect and the small areas examined. Figure 5.7 shows an EBSD map of sample 1 with a partially recrystallised microstructure (separated and shown in (b)). The texture of the recrystallised region was measured and is shown in (c), and the recrystallised grains with size less than 4μm were further separated and their texture was also measured as shown in (d). This separation may provide a better representation of the texture in the early stages of recrystallisation prior to any "selective" grain growth. Despite the dominance of PSN in this steel, Figure 5.7(d) shows clearly that the orientations of the nuclei are not random. When comparing the recrystallisation texture to the rolling texture of the same sample shown in Figure 4.62, a slight rotation of the recrystallised grains from the deformed matrix within the α- and γ-fibres can be

observed. This rotation has been observed elsewhere in this study (see Section 5.6.3) and it indicates that the recrystallisation may originate at regions within the deformation zone away from the particle/matrix interface. This behaviour is in good agreement with the work of Humphreys (1977), as nucleation can originate at any pre-existing subgrains within the deformation zone. The growth of the large grains (> 4µm) seems to be enhanced by the existence of high misorientation with respect to the surrounding matrix as well as the concurrent dissolution of the particles during annealing.

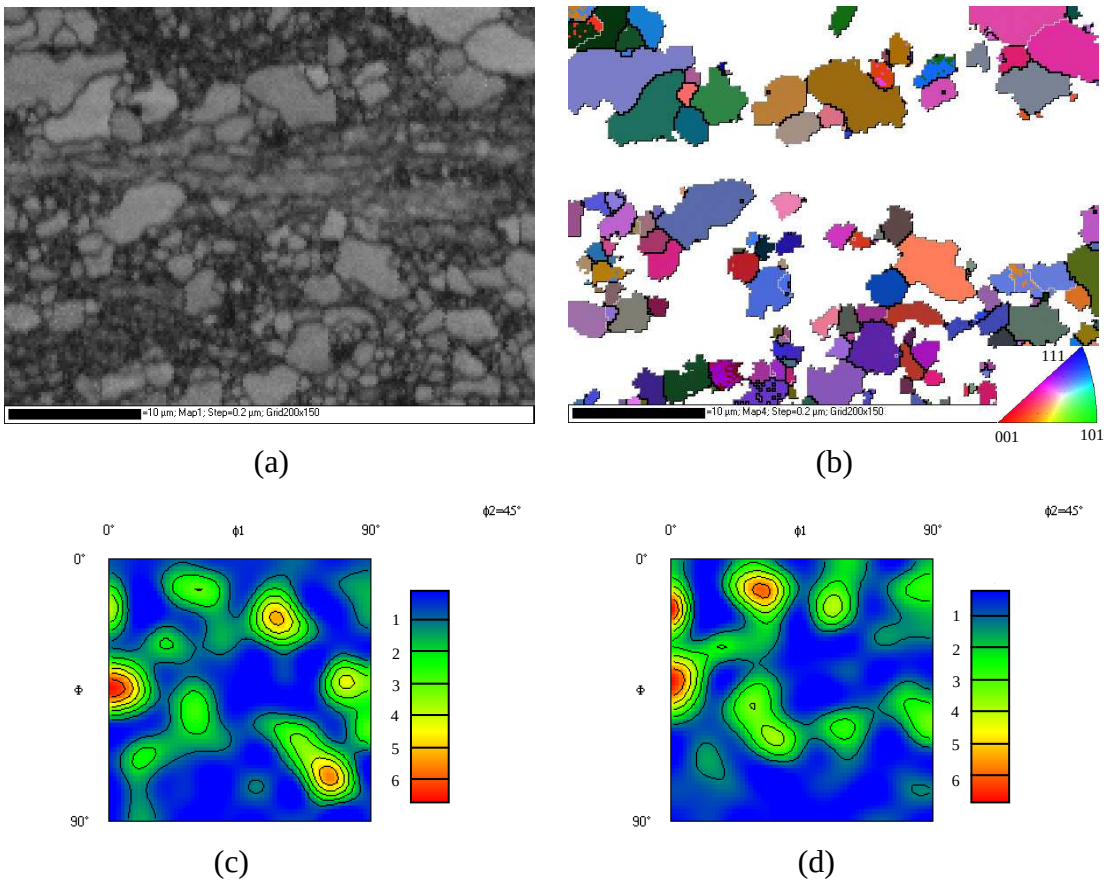

Figure 5.7: (a) EBSD map (band contrast) of sample 1 showing partially recrystallised microstructure, (b) Euler colour of the recrystallised grains, (c) texture of the recrystallised grains and (d) textures of the recrystallised grains with size less than 4µm.

The three *in-situ* annealing experiments of the HSLA steel enable the same area to be examined at different stages of the annealing. This allowed the growth direction of the recrystallised grains to be observed and, hence, the angle and axis of misorienations of only the moving (i.e. growing) interface between the recrystallised

grain and the surrounding deformed matrix to be determined as can be seen in Figure 5.8-9. As expected, the small misorientation angles (less than 10^o) as well as the large misorientation angles (greater than 60^o) are rarely observed as shown in Figure 5.8. A peak value of about 30^o was observed in all samples, with no particular rotation axis.

There is a slight difference in rotation angle distribution between the three samples. More scattered data were recognised with the low reduction samples, particularly sample 2. The lower rotation angles of the highly deformed sample 1 suggest that the nucleation originated within the deformation zones far from the particle/matrix interface. This is in agreement with the texture measurement of the unrecrystallised and recrystallised regions shown in Figure 4.44 where both textures are, to some extent, similar. Figure 5.9 show that no strong evidence of the 27^o misorientation around a <110> axis, as this was reported to be an example of oriented growth (e.g. Ibe and Lücke 1968). However, it should be noted that the number of measurements is too limited to be conclusive.

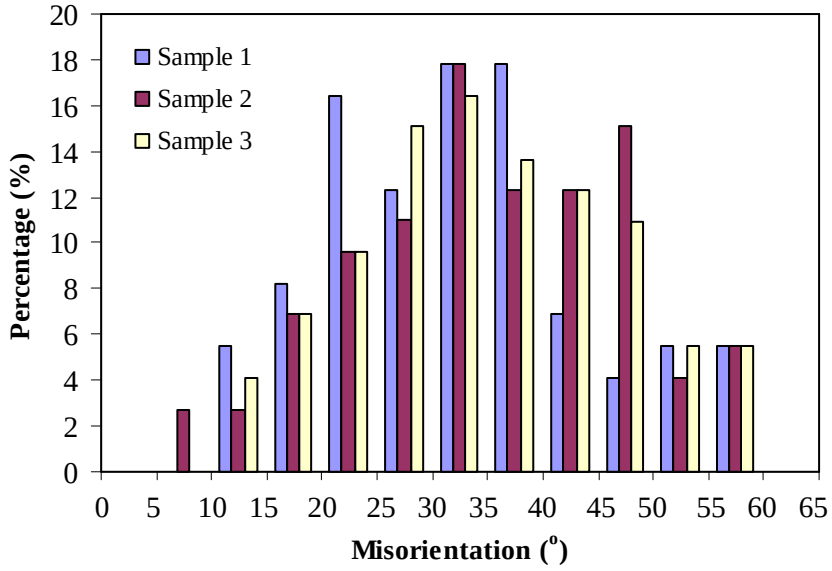

Figure 5.8: The distribution of rotation angles between the growing boundary of the recrystallised grains and the surrounding deformed matrix for all *in-situ* samples.

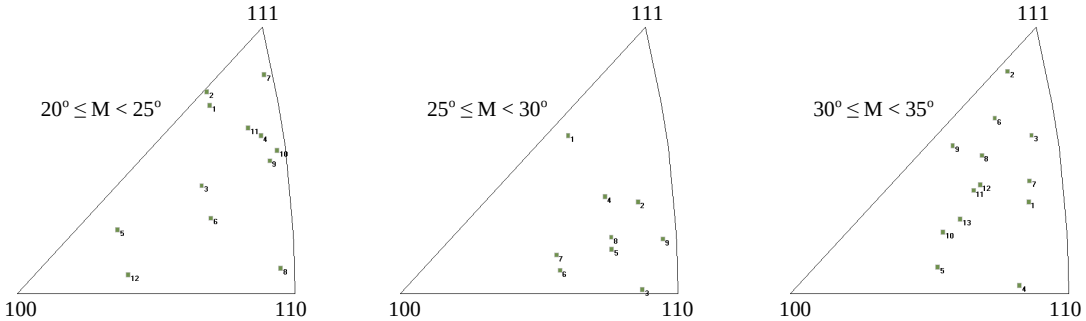

(a)

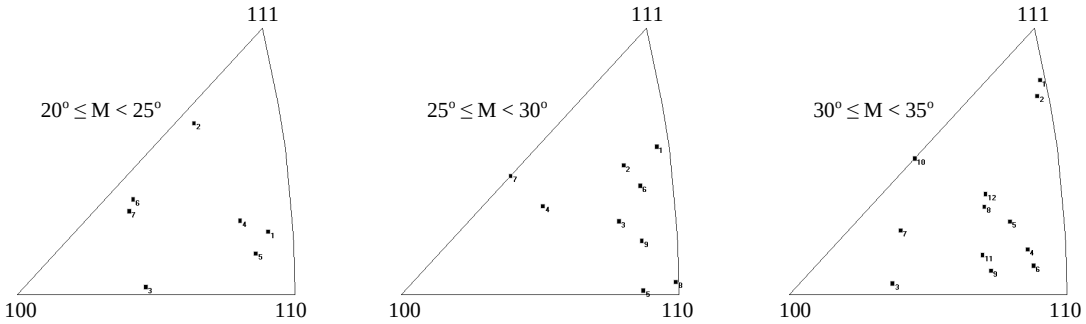

(b)

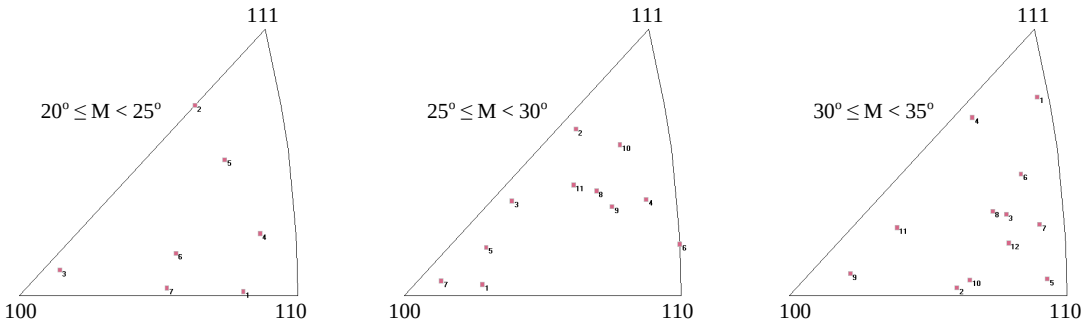

(c)

Figure 5.9: Axis and angles (M) of misorientations between the growing boundary of the recrystallised grains and the surrounding matrix in (a) sample 1, (b) sample 2 and (c) sample 3.

5.8 Monte-Carlo Modelling

The use of Monte-Carlo modelling for simulating the recrystallisation and grain growth processes help to improve understanding of the complex phenomena associated with them. In addition to the grain growth simulation, the results of the effect of PSN on the recrystallisation texture, the main focus of this study, obtained from the TEM, EBSD and *In-situ* EBSD experiments were utilised and a simple model for simulation of the PSN mechanism of recrystallisation was developed.

Figure 4.72 shows this model where an approximate representation of the deformation zone around the particle is shown. The small subgrains, with a large orientation gradient introduced close to the particle made the nucleation of recrystallisation start from this zone. This simulation shows also that the nucleation of recrystallisation can occur in regions away from the particle/matrix interface where high mobility boundaries exist. The radial gradient of dislocation density (or subgrain size) derived from Equation 4.2 has actually a maximum away from the particle interface, at about 0.3 r_0. However, other forms of orientation and size distribution also gave nucleation away from the highest misorientation material and the precise form of distribution may not be too important. In addition to the issues of misorientation and size gradients, larger subgrains have some advantage because of reduced boundary curvature pressure.

In reality, of course, the microstructures around particles are much more complicated than modelled here, but the hypothesis that PSN will often give orientations which are only different from those of the deformed material by a minimal amount- sufficient to give high boundary mobility, typically of the order of 15º- is potentially true and this may account for the general weakening of texture, rather than the oriented growth of specific orientations, when significant PSN occurs.

Chapter 6

CONCLUSIONS

Two low carbon steels with different compositions and initial microstructures were investigated in this study. The effects of the initial microstructures, cold rolling reductions and annealing temperatures on the annealing behaviour and texture evolution have been determined. Particular attention was paid to deformation zones around large particles and its influence on the rolling and recrystallisation textures produced. The following conclusions may be explicitly or implicitly inferred from this study.

1. After cold rolling, the textures of both steels investigated consist mainly of the α- and γ-fibres texture components. The development of these are largely dependent on the rolling reduction. With increasing reduction, the textures show gradual intensification of both fibres, with weaker intensities in the HSLA steel where pearlitic particles are present. These particles, in addition, affect the rotation paths towards the stable end orientation during cold rolling, with IF steel exhibiting a strong {223}<110> component and HSLA exhibiting a strong {001}<110>.

2. In both steels, a higher dislocation density after cold rolling is observed in γ-fibre material compared with α-fibre texture components, indicating that γ-fibre regions have a higher stored energy. The selected area electron diffraction patterns obtained in the deformation zone near the particles in HSLA steel have shown that high dislocation density and large lattice misorientations occur in the vicinity of particles during deformation.

3. Annealing temperature has a great effect on the recrystallisation kinetics of both steels. Reduction also has an effect on the kinetics: the higher the reduction, the

shorter the full recrystallisation time. In addition, the presence of particles can significantly reduce the temperature needed for recrystallisation, as they enhance the recrystallisation and act as nucleation sites by the Particle Stimulated Nucleation (PSN) mechanism. The recrystallisation kinetics data for all the different reductions in both steels were found to fit the JMAK relation reasonably well, with *n*-values ranging from 1.4 to 2.0. These low *n*-values can be related to failure of the simple assumptions made in the basic JMAK model. The apparent activation energy is calculated to be 314 and 339 kJ/mol for IF and HSLA steels, respectively. They are higher than that for pure ferritic iron (i.e. 280kJ/mol) as a result of the micro-alloying elements present in the steels investigated.

4. Determining the recrystallisation fraction by monitoring the changes of HAGB content during annealing using EBSD mapping is shown to be a rapid and reliable method, giving results which are consistent with results from optical microscopy. The difference between the two methods did not exceed 5% recrystallised fraction.

5. Texture development during the recrystallisation of IF steel is shown to be largely dependent on the rolling reduction. It can be concluded that the annealing texture is mainly α-fibre at low reduction (20%) as a result of grain boundary nucleation by SIBM. However, with increasing rolling reduction, the nucleation mechanism changed to subgrain growth in γ-fibre grains since the stored energy in these grains become high and, hence, the annealing texture show gradual intensification of γ-fibre components. An interchange of the orientation density peaks along both fibres for all reductions has been observed between the rolling textures and the fully annealed textures.

6. The pearlite particles in the HSLA steel have a strong influence on texture development during recrystallisation since nucleation occurs preferentially in the deformed zones developed around these particles during cold rolling. The orientations of PSN nuclei were found to be none random, although the orientation spread is high. The formation of the nucleus seems to occur within the deformation zones in regions away from the particle surface leading to recrystallisation textures similar to that of the rolling textures (i.e. both α- and γ-fibre exist) and, although the texture intensity was lower, to recrystallisation textures in IF steel.

7. The PSN nuclei seem to experience a barrier to further growth after consuming the deformation zone due to the decrease in driving force. The growth of certain grains seems to be enhanced by the high misorientation with respect to the surrounding matrix as well as the concurrent dissolution of the particles during annealing.

8. The application of *in-situ* annealing combined with EBSD mapping to the study of recrystallisation microstructures and textures of HSLA steel was found to be useful. New input to the understanding of recrystallisation phenomena was generated from such experiments. More than 80% of the orientations of the recrystallised nuclei are already found in the deformed microstructure, with the remainder probably originating, and emerging from, the interior of the sample or to be related to the difficulty in obtaining high quality EBSD image in the deformation zone around the particles. The recrystallisation microstructures and textures from these *in-situ* experiments show similar behaviour to that observed using conventional examination of heated and cooled samples. There is no strong evidence of particular misorientation axes or angles from the moving interface between recrystallised grains and the surrounding deformed matrix.

9. Monte Carlo modelling was used to simulate the PSN mechanism of recrystallisation. This was to show, in general, the feasibility of using these mesoscale simulations to capture the microstructure changes associated with PSN mechanism. The simulation was able to capture the nucleation of recrystallisation occuring within the deformation zone close to the particles, in agreement with the results observed experimentally. It shows also that the nucleation can occur in regions away from the particle/matrix interface where high mobility boundaries exist which may account for the general weakening of texture, rather than the oriented growth of specific orientations, when significant PSN occurs.

Chapter 7

FURTHER WORK

Based on the investigations carried out in this study, certain areas where further work could be useful can be identified. These are as follows:

- The application of in-situ annealing, combined with EBSD mapping, to the study of recrystallisation texture as used in the present work is influenced by the presence of the free surface. Other techniques, such as synchrotron x-ray beam techniques, are potentially useful in this situation due to their greater depth of penetration. However, these methods are still at an early stage of development.
- Although in this work it was possible to model the PSN mechanism of recrystallisation, and give a reasonable prediction to the overall phenomenon, further development of the current model is necessary to investigate the effect of the non-uniform microstructure in three-dimensions on the recrystallisation kinetics. The detailed nature of the deformation microstructure around particles needs to measured, and possibly modelled, and there are many uncertainties in the values needed for the annealing model, for example the energy and mobility of boundaries as functions of misorientation and boundary character. Such a detailed study would require considerable time and effort.
- The current study has focused on large second phase particles and shows their strong influence on the rolling and recrystallisation textures. Since most industrial alloys also contain small particles, it would be useful to investigate their effect on textures in steel as well. As well as effects on deformation microstruture, small particles can have large effects on boundary mobility which may be anisotropic.

References

Aaronson, H. I. (1962), The Proeutectoid Ferrite and the Proeutectoid Cementite Reactions, in *Decomposition of Austenite by Diffusional Processes*, Zackay, V. F. and Aaronson, H. I. (ed.), *Interscience*, New York, 1962, 387-548.

Aaronson, H. I. (1993), Atomic Mechanisms of Diffusional Nucleation and Growth and Comparisons with Their Counterparts in Shear Transformations, *Metall. Trans.*, 24A, 241-76.

Aaronson, H. I. and Domian, H. A. (1996), Partition of Alloying Elements between Austenite and Proeutectoid Ferrite and Bainite, *Transactions AIME*, Vol. 236, 781-796.

Aaronson, H. I., Laird, C. and Kinsman, K. R. (1970), Mechansims of Diffusional Growth of Precipitate Crystals, in *Phase Transformations*, ASM, 313-96.

Aaronson, H. I., Reynolds, W. T. and Purdy, G. R. (2004), Coupled Solute Drag Effects Formation in Fe-C-X Systems, *Metall. and Mater. Trans*., Vol. 35A, 1187-1210.

Abe, M. (1992), Formable Steel, in *Constitution and Proprties of Steel, Materials Science and Technology*, Cahn, R. W., Haasen, P. and Kramer, E. J. (eds), Vol. 7, Chapter 7, VCH, New York, 288-333

Akbari, G. H., Sellars C. M. and Whitman J. A. (1997), Microstructural Development During Warm Rolling of an IF Steel, *Acta Mater*., Vol. 45, 5047-5058.

Anderson, M. P., Srolovitz, D. J., Grest, G. S. and Sahni, P. S. (1984), Computer Simulation of Grain Growth. I. Kinetcs, *Acta Metall.* Vol. 32 (5), 783.

Armstrong, R. W. (1983), The Yield and Flow Stress Dependence on Polycrystalline Grain Size, Yield, Flow and Fracture of Polycrystals, Baker, T. N., (ed.), *Applied Science Publishers*, London, 1-31.

Ashby, M. F. (1966), Work Hardening of Dispersion Hardened Crystals, *Phil. Mag*., Vol. 14, 1157-1178.

Ashby, M. F. (1970), The Deformation of Plastically Non-Homogeneous Crystals. *Phil. Mag*., Vol. 21, 399-424.

Avrami, M. (1939), Kinetics of Phase Change. I. General Theory, *J. Chem. Phys*., Vol. 7, 1103-1112.

Bailey, J. E. (1960), Electron Microscope Observations on the annealing Processes Occurring in Cold-Worked Silver, *Phil. Mag*., Vol. 5, 833-842.

Bain, E. C. (1939), Function of alloying Elements in Steel, First edition, *ASM*, Cleveland, Ohio, 8-12.

Barbaro, F. J., Krauklis, P. and Easterling, K. (1989), Formation of Acicular Ferrite at Particles in Steel, *Mater. Sci. and Tech*., Vol. 5, 1057-1077.

Barnett, M. R. and Jonas, J. J. (1999), Distinctive Aspects of the Physical Metallurgy of Warm Rolling, *ISIJ Int*., Vol. 39, 856-873.

Bate, P. S. (1990), TEXTAN: Program for Texture Determination and Analysis, IRC, Birmingham.

Beck, P. A. (1949), The Formation of Recrystallization Nuclei, *J. of Appl. Phys*., Vol. 20(6), 633-634.

Beck, P. A. (1954), Annealing of Cold-worked Metals, *Adv. Phys*., Vol. 3, 245-324.

Beck, P. A. and Sperry, P.R. (1950), Strain Induced Boundary Migration in High Purity Aluminium, *J. Appl. Phys*., Vol. 21, 150-152.

Bhadeshia, H. K. D. H. (1981), A Rationalisation of Shear Transformations in Steels, *Acta Metall*., Vol. 29, 1117-1130.

Bunge, H. I. (1965), The General Description on Texture, *Z. Metallkd*, Vol. 56, 872-874.

Burke, J. E. and Turnbull, D. (1952), Recrystallization and Grain Growth, *Prog. Metal Phys.*, Vol. 3, 220-292.

Cahn, R. W. (1949), Recrystallization of Single Crystals after Plastic Bending, *J. of the Inst. of Metals*, Vol. 76(2):121-143.

Cahn, R. W. (1950), A New Theory of Recrystallization Nuclei, *Proceedings of The Physics Society*, Vol. 63(364), 323-336.

Callister, W. D. Jr., (2001), Fundamentals of Materials Science and Engineering, *John Wiley & Sons*, New York.

HKL Technology, (2001), HKL Channel 5 User's Manual. *HKL Technology*, Danbury, CT, USA.

Chen, L. Q. and Yang, W. (1996), Continuum Field Approach to Modelling Microstructural Evolution, *JOM*, Vol. 48, 13-18.

Cizek, P., Wynne, B. P., Davies, C. H. J., Muddle, B.C., and Hodgson, P. D. (2002), Effect of Composition and Austenite Deformation on the Transformation Characteristics of Low-Carbon and Ultralow-Carbon Microalloyed Steels, *Metall. Mater. Trans*., Vol. 33A, 1331-1349.

Cohen, M. and Hansen, S. S. (1979), Microstructural Control in Microalloyed Steels, in MiCon78:Optimisation of Processing, Properties, and Service Performance Through Microstructural Control, *ASTM STP 672*, Abrams, H., Maniar,G. N., Nail, D. A. and Solomon, H. D. (eds.), 34-52.

Cottrell A. H. (1953), In: Theory of Dislocations. Chalmers, B. (ed.), *Progress in Metal Physics*. Vol. 4, 251-255.

Cottrell, A. H., (1964), The Mechanical Properties of Matter, *John Wiley and Sons Inc*., New York.

Courtney, T. H. (1990), Mechanical Behavior of Materials, *McGraw Hill*, 173-184.

Dieter, G. (1986), Mechanical Metallurgy, *McGraw Hill*, 203-207.

Dillamore, I. L., Morris, P.L., Smith, C.J.E. and Hutchinson, W.B. (1972), Transition Bands and Recrystallization in Metals, *Proc. R. Soc. Lond*., Vol. 329A, 405-420.

Dillamore, I. L., Roberts, J.G. and Busch, A.C. (1979), Occurrence of Shear Bands in Heavily Rolled Cubic Metals, *Met. Sci*., Vol. 13, 73-79.

Dillamore, I. L., Smith, C. J. E. and Watson, T. W. (1967), Oriented Nucleation in the Formation of Annealing Textures in Iron, *Metal Science Journal*, Vol. 1, 49-54.

Doherty, R. D. (1996), in: Diffusive Phase Transformations in Physical Metallurgy, Cahn, R. W., Haasen, P. (eds.), 4th ed., *Elsevier*, Amsterdam, 1369.

Doherty, R. D., Gottstein, G., Hirsch, J. R., Huttchinson, W. B., Lucke, K., Nes, E. and Wilbrandt, P. J. (1988), in: Panel Discussion on Recrystallization Texture, Kallend, J. S. and Gottstein, G. (eds.), *ICOTOM 8*, TMS, Warrendale, PA, 369.

Doherty, R. D., Hughes, D. A., Humphreys, F. J., Jonas, J. J., Juul Jensen, D., Kassner, M. E., King, W. E., McNelley, T. R., McQueen, H. J. and Rollett, A. D. (1997), Current Issues in Recrystallization: a review, *Mater. Sci. Eng*. Vol. 238A, 219-274.

Dubé, C. A. (1984), Ph. D. Thesis, *Carnegie Institute of Technology*, Pittsburgh, PA.

Dubé, C. A., Aaronson, H. I. and Mehl, R. F. (1958), The Formation of Proeutectoid Ferrite in Carbon Steels, *Reviewed Metallurgia*, Vol. 55, 201.

Dunn, C. G. and Walter, J. L. (1966), Recrystallization, Grain Growth and. Textures, *ASM*, Metals Park, OH, 461

Farrar, R. A. and Harrison, P. L. (1987), Acicular Ferrite in Carbon –Manganese Weld Metals: an Overview, *J. of Mater. Sci*., Vol. 22, 3812-3820.

Fernández, A. I., Uranga, P., López, B. and Rodriguez-Ibabe, J. M. (2003), Dynamic Recrystallization behaviour covering a wide austenite grain size range in Nb and Nb-Ti microalloyed steels, *Mater. Sci. and Eng*., Vol. 361A, 367-376.

Fletcher, E. E. (1979), High-Strength, Low –Alloy Steels: Status, Selection and Physical Metallurgy, *Battelle Press*, 111-134.

Fukuda, M. (1967) The Effect of Carbon Content Against r Value-Cold Reductions Relations in Steel Sheets, *J. Iron Steel Inst. Japan*, 53(4): 559-561.

Gil Sevillano, J., van Houtte, P. and Aernoudt, E. (1980), Large Strain Work Hardening and Textures, *Prog. Mater. Science*, Vol. 25, 69-134.

Ginzburg, V. B. (1989), Steel-Rolling Technology: Theory and Practice, *Marcel Dekker*, Inc., 107-123.

Gladman, T. (1997), The Physical Metallurgy of Microalloyed Steel, *The Institute of Materials*, Cambridge, UK.

Gladman, T., Dulieu, D. and McIvor, I. (1977), Structure Property Relationships in High-Strength Microalloyed Steels, *Microalloying `75*, (Washington, D.C. October1-3, 1975), Union Carbide Corp. New York, 32-58.

Glover, G., Sellars, C. M. (1973), Recovery and Recrystallisation during High Temperature Deformation of α-iron, *Metall. Trans.*, Vol. 4, 765-775.

Gordon, P. and Vandermeer, R.A. (1962), Mechanism of Boundary Migration in Recrystallization, *Trans. Metall. Soc. A.I.M.E.* Vol. 224, 917-928.

Gourgues, A. F., Flower, H. M. and Lindley, D. C. (2000), Electron Backscattering Diffraction Study of Acicular Ferrite, Bainite, and Martensite Steel Microstructures, *Mater. Sci. and Tech.*, Vol. 16, 26-40.

Hansen, N. (1975), Accelerated and Delayed Recrystallization in Dispersion Hardened alloys, *Mem. Sci. Rev. Met*. Vol. 72, 189-203.

Hansen, N., Leffers, T. and Kjems, J.K. (1981), Recrystallization Kinetics in Copper Investigated by In Situ Texture Measurements by Neutron Diffraction, *Acta Metall*. Vol. 29, 1523-1533.

Haratani, T., Hutchinson, W. B., Dillamore, I. L. and Bate, P. S. (1984), Contribution of Shear Banding to Origin of Goss Texture in Silicon Iron, *Metal Sci*. Vol. 18, 57-65.

Heslop, J. and Petch, N. J. (1956), The Stress to Move a Free Dislocation in Alpha Iron, *Phil. Mag.*, Vol. 1(9), 866-873.

Held, J. F. (1965), Mechanical Working and Steel Processing IV, Paper 3, *The Metall. Soc. of AIME*, New York, 1965.

Higginson, R. L., Aindow, M. and Bate, P. S. (1997), The Effect of Finely Dispersed Particles on Primary Recrystallisation Textures in Al-Mn-Si Alloys, *Mater. Sci. and Eng*., Vol. 225A, 9-21.

Hillert, M. (1965), On the Theory of Normal and Abnormal Grain Growth, *Acta Metall*., Vol. 13, 227-238.

Hillert, M. (1988), Inhibition of Grain Growth by Second-Phase Particles, *Acta Metall*., Vol. 36, 3177.

Honeycombe, R. W. K. (1976), Transformation from Austenite in Alloy Steels, *Metall. Trans*., Vol. 7A, 915-936.

Hoogendorn, T. M. and Spanraft, M. J. (1977). Quantifying the Effect of Microalloying Elements on Structures during Processing. In *Micro Alloying.* Vol. 75, 75-85. New York: Union Carbide.

Hosford, W. F. (2005), Mechanical Behavior of Materials, *Cambridge University Press*, 425.

Hu, H. (1962), Direct Observations on the Annealing of Si-Fe Crystals in the Electron Microscope, *Trans. Metall. Soc. A.I.M.E*. Vol. 224(1), 75-84.

Hu, H. (1963), Annealing of Silicon-Iron Single Crystals, in *Recovery and Recrystallization of Metals*, Himmel (eds.), *Interscience*, 311-362.

Hudd, R. C. (1987), Some Aspects of the Annealing of Low Carbon Strip Steel, *Metals and Materials*, Vol. 3(2), 71-76.

Humphreys, F. J. (1977), The Nucleation of Rectsrallization at Second Phase Particles in Deformed Aluminium, *Acta Metall*. Vol. 25(11), 1323-1344.

Humphreys, F. J. (1979), Local Lattice Rotations at Second Phase Particles in Deformed Metals, *Acta Metall*. Vol. 27(12), 1801-1814.

Humphreys, F. J. (1980), Nucleation of Recrystallization in Metals and alloys with Large Particles, in *Recrystallization and Grain Growth in Multi-Phase and Particle*

Containing Materials, Hansen, N., Jones, A. R. and Leffers, T. (eds), RisØ Nat. Lab, Denmark, 35-44.

Humphreys, F. J. (1985), in Dislocations and Properties of Real Materials, M. Loretto (ed.), *Inst. Metals*, London, 175-204.

Humphreys, F. J. (1992), A Network Model for Recovery and Recrystallisation, *Scripta Metall. Mater*., Vol. 27(11), 1557-1562.

Humphreys, F. J. (1997), A Unified Theory of Recovery, Recrystallization and Grain Growth, Based on the Stability and Growth of Cellular Microstructures-I. The Basic Model, *Acta Mater*. Vol. 45(10), 4231-4240.

Humphreys, F. J. (1999), Quantitative Metallography by Electron Backscattered Diffraction. *J. Microsc.* Vol. 195(3), 170-185.

Humphreys, F. J. (2000), Modelling Microstructural Evolution During Annealing, Modelling Simul. *Mater. Sci. Eng*., Vol. 8(6), 893-910.

Humphreys, F. J. (2004), Nucleation in Recrystallization, in *Recrystallization and Grain Growth*, ReX & GG2, France, 107-116.

Humphreys, F. J. (2006), Orientation Mapping and Quantitative Metallography by EBSD, *Manchester Materials Science Centre*, UK.

Humphreys, F. J. and Ardakani, M. G. (1994), The Deformation of Particle-Containing Aluminium Single Crystals, *Acta Metall*. Vol. 42(3), 749-761.

Humphreys, F. J. and Hatherly, M. (2004), Recrystallization and Related Annealing Phenomena. Second edition. *Elsevier Ltd*., Oxford, UK.

Humphreys, F. J., Miller, W.S. and Djazeb, R. (1990), Microstructural Development During Thermo-mechanical Processing of Partculate Metal Matrix Composites, *Mats. Sci. and Tech*. Vol. 6, 1157-1166.

Hutchinson W. B. (1994), Practical Aspects of Texture Control in Low Carbon Steels, *Mater. Sci. Forum*, Vol. 157-162, 1917-1928

Hutchinson, W. B. (1984), Development and Control of Annealing Textures in Low-Carbon Steels, *Int. Met. Rev.*, 1984, Vol. 29(1), 25–42.

Hutchinson, W. B. (1999), Deformation Microstructures and Textures in Steels. *Phil. Trans. Royal Society*. Vol. 357, 1471-1485.

Hutchinson, W. B. and Bate, P. (2003), Mechanisms of Texture Development in Deep-Drawable Steels, *Int. Forum Prop. Appl. IF Steels*, Japan, 337-346.

Hutchinson, W. B. and Ushioda, K. (1984), Texture Development in Continuous Annealing, *Scand. J. Met*, Vol. 13, 269.

Hutchinson, W. B., Artymowicz, D. (2001), Mechanisms and Modelling of Microstructure/Texture Evolution in Interstitial-Free Steel Sheets, *ISIJ Int.*, Vol. 41(6), 533-541.

Hutchinson, W. B., Nilsson, K. I. and Hirsch, J. (1990), Annealing Textures in Ultra-low Carbon Steels, in *Metallurgy of Vacuum-Degassed Steels Products*; Indiana; USA, 109-125.

Hutchinson, W.B. (1989), Recrystallisation Textures in Iron Resulting from Nucleation at Grain Boundaries, *Acta Metall*. Vol. 37(4), 1047-1056.

Ibe, G. and Lücke, K. (1968), Orientation Relationships in the Recrystallization of Single Crystals of Iron-Silicon Alloy with 3% Silicon, *Archiv für das Eisenhüttenwesen*, Vol. 39(9), 693-703.

Inagaki, H. (1987a), Stable End Orientations in the Rolling Textures of the Polycrystalline Iron, *Z. Metallkde*., Vol. 78(6), 431-439.

Inagaki, H. (1987b), Cracking of Cementite Particles and Its Influence on the Development of the Rolling Texture in Low Carbon Steels, *Z. Metallkde*., Vol. 78(9), 630-638.

Inagaki, H. (1991), Effect of Coarse Cementite Particles on the Deveopment of Recrystallization Textures in High-Purity Iron, *Z. Metallkde*., Vol. 82(2), 99-107.

Inagaki, H. (1994), Fundamental Aspect of Texture Formation in Low Carbon Steel, *ISIJ Int.* Vol. 34(4), 313-321.

Inokuti. Y. and Doherty, R.D. (1978), Transmission Kossel Study of the Structure of Compresses Iron and Its Recrystallization Behaviour, *Acta Metall*. Vol. 26(1), 61-80.

Johnson, W. A. and Mehl, R. F. (1939),Reaction Kinetics in Processes of Nucleation and Growth, *Trans AIME*, Vol. 135, 416-458.

Kolmogorov, A.N. (1937), A Statistical Theory for the Recrystallization of Metals, *Izv. Akad. Nauk. USSR-Ser-Matemat*. Vol. 1(3), 355-359.

Kozasu, I. (1992), Processing – Thermomechanical Controlled Processing, in *Constitution and Properties of Steels*, Pickering, F. B. (ed.), Vol. 7, *Mater. Sci. and Tech*., Germany, 183-217.

Krauss, G, Wilshynsky, D. O. and Matlock, D. K. (1991), Processing and Properties of Interstitial-Free Steels, in *Interstitial-Free Sheet Steel: Processing, Fabrication and Properties*, Collins, L. E. and Barager, D. L. (eds.), *CIM*, Ottawa, 1-14.

Krauss, G. (2005), Steels: Processing, Structure, and Performance, *ASM Int*., Metals Park, OH, USA.

Kreisler A. and Doherty R. D. (1987), Structure of Well Defined Deformation Bands and Formation of Recrystallization Nuclei in Aluminium. *Metal Science*. Vol. 12, 551-560

Kuhlmann-Wilsdorf, D. (1984), Theory of Workhardening 1934-1984, *Metall. Trans*., Vol. 16A, 2091-2108.

Kurdjumov, G. and Sachs, G. (1930), About the Mechanism of Steel Hardening, *Z. Phys*. Vol. 64, 325-343.

Langford, G. and Cohen, M. (1969), Strain Hardening of Iron by Severe Plastic Deformation, *Trans. ASM*, Vol. 62, 623-638

Lankford, W. T., Bauscher, J. A. and Snyder, S. C. (1950), New Criteria for Predicting the Press Performance of Deep Drawing Sheets. *Trans. ASM*, Vol. 42, 1197-1205.

Leffers, T. (1981), Microstructures and Mechanisms of Polycrystal Deformation at Low Temperature, in *Deformation of Polycrystals: Mechanisms and Microstructures*, Proc. 2nd Int. Risø Symp. Hansen *et al.* (eds.), Denmark, 55-71.

Leslie, W. C. (1972), Iron and its Dilute Substitutional Solid Solutions, *Metall. Trans.*, Vol. 3(1), 5-26.

Leslie, W. C., Michalak, J.T. and Aul. F.W. (1963), The Annealing of Cold-Worked Iron, in *Iron and its Dilute Solid Solutions*. Spencer, C. W. and Werner, F. E. (eds.). *Interscience*, New York, 119-212.

Li, J.C.M. (1962), Possibility of Subgrain Rotation during Recrystallization, *J. Appl. Phys*. Vol. 33(10), 2958-2965.

Lindh, E., Hutchinson, B. and Bate, P. (1994), Texture Evolution During Recrystallization of Ultra-Low Carbon Steel. *Mater. Sci. Forum*, Vol. 157-162, 997-1002.

Liu, J., Mato, M. and Doherty, R. D. (1989), Shear Banding in Rolled Dispersion Hardened $AlMg_2Si$ Alloys. *Scripta Mater*., Vol. 23(10), 1811-1816.

Llewellyn D. T. and Hudd R. C. (1998), Steels: Metallurgy and Applications, 3rd Edition, *Reed Educational and Professional Publishing*, 151.

Martin, J. W., Doherty, R. D. and Cantor, B. (1997), Stability of Microstructure in Metallic Systems, 2nd ed., *Cambridge University Press*, Cambridge.

Massalski, T. B. (1970), Massive Transformations, in Phase Transformations, *ASM*, 433-86.

Matrosov, Y. (1984), Mechanisms of the effect of vanadium, niobium, and titanium doping on the structure and properties of low-pearlite steels, *Metal Science and Heat Treatment*, Vol. 26(11), 798-807.

McQueen, H. J. and Jonas, J.J. (1975), Recovery and Recrystallization During High Temperature Deformation, in *Treatise on Materials Science & Technology*. 6th edition. Arsenault. *Academic Press*, N.York, 393-493.

Mecozzi, M. G., Sietsma, J. and Van Der Zwaag, S. (2006), Analysis of $\gamma \rightarrow \alpha$ transformation in a Nb Micro-Alloyed C-Mn Steel by Phase Field Modelling. *Acta Mater.*, Vol. 54(5), 1431-1440.

Mehl, R.F. (1948), Recrystallization. in *Metals Handbook*, ASM (ed.), *ASM*, Ohio, 259-263.

Meyers, M. and Chawla, K. (1984), Mechanical Metallurgy, Principles and Applications, *Prentice-Hall Inc*., 402-437.

Michalak, J. J. (1965), The Influence of Temperature on the Development of Long-Range Internal Stress During the Plastic Deformation of High-Purity Iron, *Acta Metall.*, Vol. 13(3), 213-222.

Miodownik, M.A. (2002), A Review of Microstructural Computer Models Used to Simulate Grain Growth and Recrystallisation in Aluminium Alloys, *J. Light Metals*, Vol. 2(3), 125-135.

Miodownik, M.A., Cerezo, A. and Martin, J. W. (1999), Mesoscale Simulations of Particle Pinning, *Phil. Mag*., Vol. 79A, 203-222.

Nabarro, F. R. N. (1947), Dislocations in a Simple Cubic Lattice, *Proc. Phys. Soc*., Vol. 59(2), 256-272.

Nes, E., Ryum, N. and Hunderi, O. (1985), On the Zener Drag. *Acta Metallurgica*, Vol. 33, 11-22.

Novikov, V. (1996), Grain Growth and Control of Microstructure and Texture in Polycrystalline Materials, *CRC Press*, Boca Raton, FL.

Orowan, E. (1948), Discussion in Symposium on Internal Stresses in Metals and Alloys, *Institute of Metals*, London, 451-488.

Peierls, R. E. (1940), The Size of a Dislocation, *Proc. Phys. Soc*., Vol. 52, 34-37.

Pickering, F. B. (1977), HSLA Steels - A Decade of Progress, in *Microalloying 75*, Union Carbide Corporation, New York, 9-30.

Pickering, F. B. (1978), Physical Metallurgy and the Design of the Steels, *Applied Science Publishers*, London, 1-88.

Porter, J. and Humphreys, F. J. (1979), Nucleation of Recrystallization at Second-Phase Particles in Deformed Copper Alloys, *Metal Sci*. Vol. 13(2), 83-88.

Raabe, D. (1998), Discrete Mesoscale Simulation of Recrystallization Microstructure and Texture Using a Stochastic Cellular Automation Approach, *Mater. Sci. Forum*, Vol. 273-275, 169-174.

Raabe, D. and Hantcherli, L. (2005), 2D Cellular Automation Simulation of the Recrystallization Texture of an IF Sheet Steel Under Consideration of Zener Pinning, *Comp. Mater. Sci.*, Vol. 34(4), 299–313.

Radhakrishnan, B. and Sarma, G. (2004), The Effect of Coarse Non-Deformable Particles on the Deformation and Static Recrystallization of Aluminium Alloys, *Phil. Mag.*, Vol. 84(22), 2341-2366.

Randle, V and Engler, O. (2000), Introduction to texture analysis, macrotexture, microtexture and orientation mapping, *Gordon and Breach Science Publishers*, UK.

Rangel, R. P., Siciliano, J. F., Sandim, H. R., Plaut, R. L. and Padilha, A. (2005), Nucleation and growth during recrystallization, *Materials Research*, Vol. 8(3), 225-238.

Ray, R. K. and Jonas, J. J. (1990), Transformation textures in steels, *Int. Mater. Rev*., Vol. 35, 1-36.

Ray, R. K., Hutchinson, W.B. and Duggan, B.J. (1975), A Study of the Nucleation of Recrystallization using HVEM, *Acta Metall*. Vol. 23(7), 831-840.

Ray, R. K., Jonas, J. J. and Hook, R. E. (1994), Cold Rolling and Annealing Textures in Low and Extra Low Carbon Steels, *Int'l Mater. Rev*., Vol. 39(4), 129-172.

Ray, R. K., Jonas, J. J., Butron-Guillen, P. and Savoie, J. (1994), Transformation Textures in Steels, *ISIJ Int*, Vol. 34, 927-942.

Read, W. T. (1953), Dislocations in Crystals. *McGraw Hill*.

Read, W. T. and Shockley, W. (1950), Dislocation Models of Crystal Grain Boundaries, *Phys. Rev*., Vol. 78(3), 275-289.

Reed-Hill, R. E., and Abbaschian, R. (1994), Physical Metallurgy Principles. 3rd edition. *PWS Publishing Company*, Boston, USA.

Repas, P. E. (1988), Metallurgical Fundamentals for HSLA Steels, in *Microalloyed HSLA Steels*, ASM International, 3-14.

Reynold, W. T. Jr. , Enomoto, M. and Aaronson H. I. (1988), The Proeutectoid Ferrite Reaction, in *Phase Transformations in Ferrous Alloys*, Marder, A. R. and Glodstein, J. I. (eds), *TMS-AIME*, Warrendale, PA, 155-200.

Ricks, R. A., Howell P. R. and Barritte G. S. (1982), The Nature of Acicular Ferrite in HSLA Steel Weld Metals, *J. of Mater. Sci*., Vol. 17(3), 732-740.

Roberts, W. L. (1978), Cold Rolling of Steel, *Marcel Dekker*, New. York, Chap. 12.

Rollet A. D. (1997), Overview of Modeling and Simulation of Recrystallization, *Progress Mater. Sci*., Vol. 42, 79-99.

Rosen, A., Burton, M.S. and Smith, G.V. (1964), Recrystallization of High-Purity Iron, *Trans. AIME*. Vol. 230, 205-215.

Satoh, S., Obara, T. and Tsunoyama, K. (1986), Effect of Precipitate Dispersion on the Recrystallization Texture of Niobium-Added Extra-Low Carbon Cold-Rolled Steel Sheet, *Trans. Iron Steel Inst. Jpn.*, Vol. 26 (8), 737–744.

Schläfer, D. and Bunge, H.-J. (1974), The Development of Rolling Texture in Iron Determined by Neutron-Diffraction, *Texture*, Vol. 1, 157-171.

Schulz, L. G. (1949), A Direct Method of Determining Preferred Orientation of a Flat Reflection Sample Using a Geiger Counter X-ray Spectrometer, *J. Appl. Phys.*, Vol. 20(11), 1030-1033.

Schwartz, A. J., Kumar, M. and Adams, B. L. (2000), (eds) Electron Backscatter Diffraction in Materials Science, *Kluwer Academic/Plenum Publishers*, New York.

Smallman, R. E. and Bishop, R. J. (1999), Modern Physical Metallurgy and Materials Engineering, 6th ed. *Butterworth-Heinmann*, Oxford, Chap. 7, 233-234.

Smith, C. S. (1948), Introduction to Grains, Phases, and Interfaces – an Interpretation of Microstructures, *Trans. AIME*, Vol. 175, 15-51

Spanos, G., Reynolds, W. T. Jr., and Vandermeer, R. A. (1991), The Role of Ledges in the Proeutectoid Ferrite and Proeutectoid Cementite Reactions in Steel, *Metall. Trans.*, Vol. 22A, 1367-1380.

Spur, G and Stöferle, T. (1987), (eds.), Handbook of Manufacturing Technology, Vol. 4/2, *Wärmebehandeln*, Carl Hanser, Munich.

Subramanian, S. V., Prikryl, M., Gaulin, B. D., Clifford, D. D., Benincasa, S. and O'Reilly, I. (1994), Effect of Precipitate Size and Dispersion on Lankford Values of Titanium Stabilized Intersititial-free Steels, *ISIJ Int.*, Vol. 34(1), 61-69.

Talef, E. M., Syn, C. K., Lesuer, D. R. and Sherby, O. D. (1996), Pearlite in Ultrahigh Carbon Steels: Heat Treatments and Mechanical Properties, *Metall. and Mater. Trans*., Vol. 27A, 111-118.

Taylor, G. I. and Elam, C. F. (1926), The Distortion of Iron Crystals, *Proc. Roy. Soc. A*, Vol. 112(761), 337-361

Thelning, K. E. (1984), Steel and Its Heat Treatment, 2nd ed., *Butterworths*, London.

Thompson, S. W., Colvin, D. J., and Krauss, G. (1990), Continuous Cooling Transformations and Microstructures in Low-Carbon HSLA Plate Steel, *Metall. Trans*., Vol. 21A, 1493-1507.

Totten, G. E. (2006), (ed.) Steel Heat Treatment: Metallurgy and Technologies, *CRC Press*.

Tsunoyama, K. (1998), Metallurgy of Ultra-Low-C Interstitial-Free Sheet Steel for Automobile Applications, *Physica Status Solidi*, Vol. 167(2), 427-433.

Verhoeven, J. D. and Gibson, E. D. (1998), The Divorced Eutectoid Transformation in Steel, *Metall. and Mater. Trans*., Vol. 29A, 1181-89.

Verlinden, B., Driver, J., Samajdar, I. and Doherty, R. D. (2007), Thermo-Mechanical Processing of Metallic Materials, Pergamon Materials Series, Cahn, R. W. (ed.), *Elsevier*, Amsterdam.

Walter, J.L. and Koch, E.F. (1963), Substructures and Recrystallization of Deformed (100)[001]-Oriented Crystals of High-Purity Silicon-Iron, *Acta Metall*. Vol. 11(8), 923-938.

Weaire, D. and Kermode, J. P. (1983), Computer Simulation of A Two-Dimensional Soap Froth-I. Method and Motivation, *Phil. Mag. B*, Vol. 48(3), 245-259.

Wilson, E. A. (1994), The γ to α Transformation in Low Carbon Irons, *ISIJ Int*., Vol. 34 (8), 615-630.

Wu, K. M.(2006), Three-Dimensional Analysis of Acicular Ferrite in a Low-Carbon Steel Containing Titanium, *Scripta Materialia*, Vol. 54(4), 569-574.

Wu, K. M., Inagawa, Y. and Enomoto, M. (2004), Three-Dimensional Morphology of Ferrite Formed in Association with Inclusions in Low-Carbon Steel, *Mater. Char*., Vol. 52 (2), 121-127.

Young, J. (1926), The Crystal Structure of Meteoric Iron as Determined by X-Ray Analysis, *Proc Roy Soc Lond*, Vol. 112A, 630-641.

Zhang, S. and Wu, C. (1992), Ferrous Materials, *Metallurgical Industry Press*, Beijing.

Appendices

Appendix A Texture

The cold rolling and annealing textures in low carbon steels are often represented using φ_2=45^o section of Euler space. Table A-1 shows the important orientations as well as their corresponding Euler angles. The attached figure shows their location in the Euler space.

Table A-1: Important texture orientations present in low carbon steels and their corresponding Euler angles. (The locations are shown in the attached φ_2=45^o section of Euler space) (Ray *et al.* 1994)

Component	Texture Orientation		Euler angles		
	(*hkl*)	[*uvw*]	φ_1	Φ	φ_2
H	0 0 1	1 -1 0	0	0	45
J	1 1 4	1 -1 0	0	19.5	
I	1 1 2	1 -1 0	0	35.3	
E	1 1 1	1 -1 0	0	54.7	
F	1 1 1	1 -2 1	30	57.7	
E’	1 1 1	0 -1 1	60	54.7	
F’	1 1 1	-1 -1 2	90	54.7	
C	0 0 1	0 -1 0	45	0	
L	1 1 0	1 -1 0	0	90	
G	1 1 0	0 0 1	90	90	

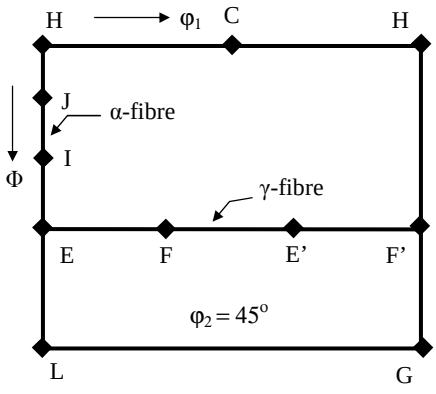

The relationship between Euler angles and Miller indices can be defined in the following equations.

$$h = \sin\Phi \sin\varphi \quad \text{(A-1)}$$

$$k = \sin\Phi \sin\varphi_1 \quad \text{(A-2)}$$

$$l = \cos\Phi \quad \text{(A-3)}$$

$$u = \cos\varphi_1 \cos\varphi_2 - \sin\varphi_1 \sin\varphi_2 \cos\Phi \quad \text{(A-4)}$$

$$v = -\cos\varphi_1 \sin\varphi_2 - \sin\varphi_1 \cos\varphi_2 \cos\Phi \quad \text{(A-5)}$$

$$w = \sin\varphi_1 \sin\Phi \quad \text{(A-6)}$$

$$\tan\Phi \cos\varphi_2 = \frac{k}{l} \tag{A-7}$$

$$\tan\varphi_2 = \frac{h}{k} \tag{A-8}$$

$$\cos\Phi \tan\varphi_1 = \frac{lw}{ku - hv} \tag{A-9}$$

Appendix B Microstructures and Measurements

The microstructural evolution during the annealing process examined by optical microscopy for all reductions are shown in Figure B-1-3 for the IF steel and Figure B-4-6 for HSLA steel. Moreover, the recrystallisation fraction and macrohardness measurements data during the annealing process for the various reductions are given in Table B-1-6 for IF and Table B-7-11 for HSLA steels, respectively.

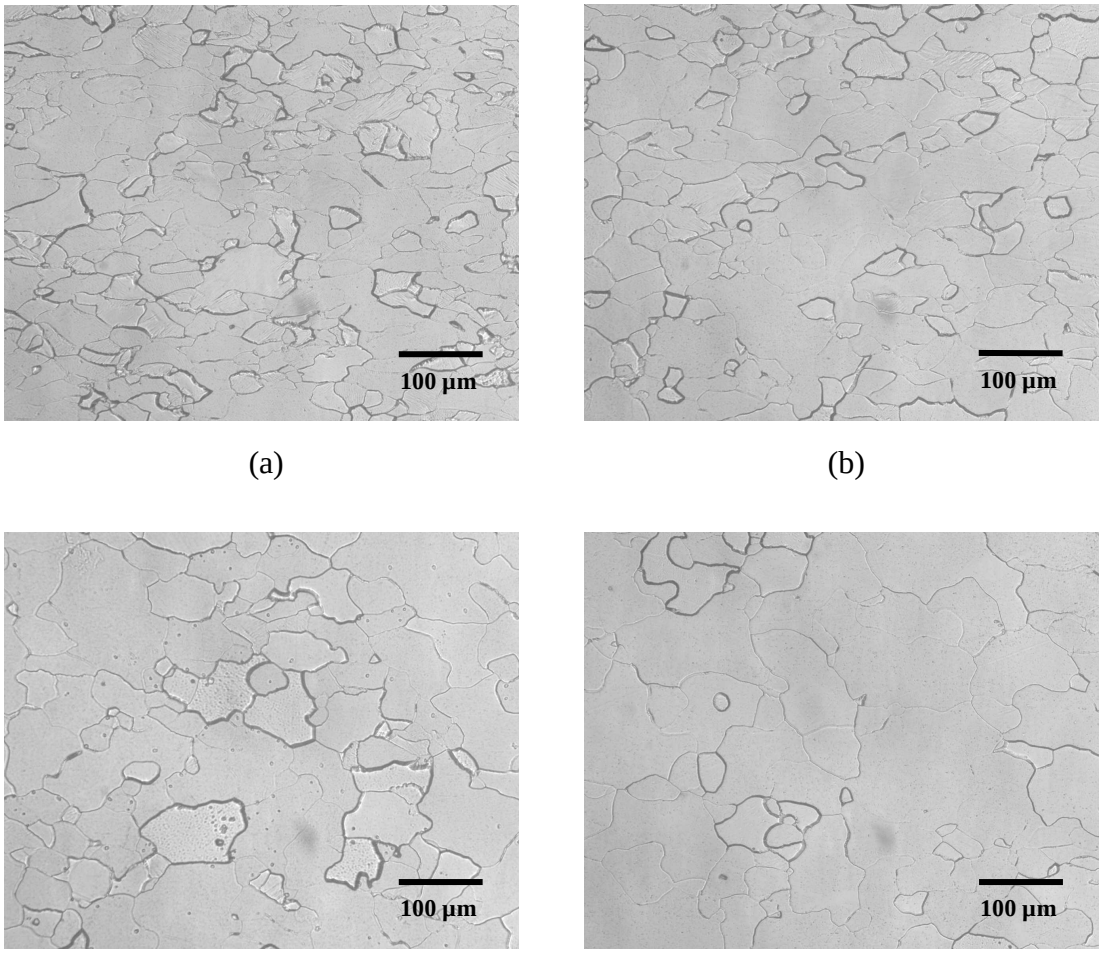

(a) (b)

(c) (d)

Figure B-1: Optical micrographs of IF steel samples cold rolled to 20% and annealed at 690^{o} for (a) 2, (b) 8, (c) 15 and (d) 24 hrs.

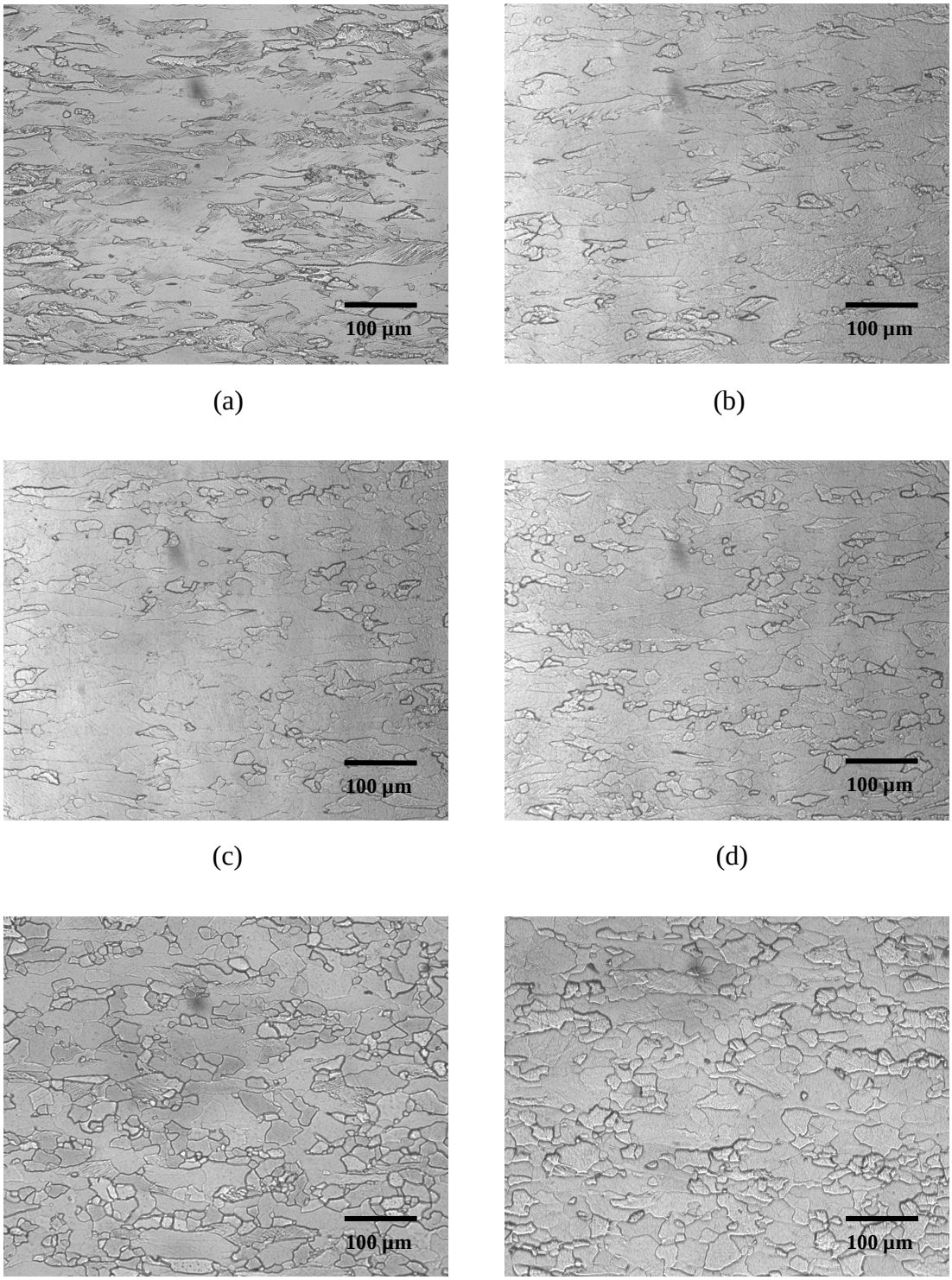

(a) (b)

(c) (d)

(e) (f)

Figure B-2: Optical micrographs of IF steel samples cold rolled to 50% and annealed at 640^{o} for (a) 4, (b) 6, (c) 10, (d) 12, (e) 17 and (f) 24hrs.

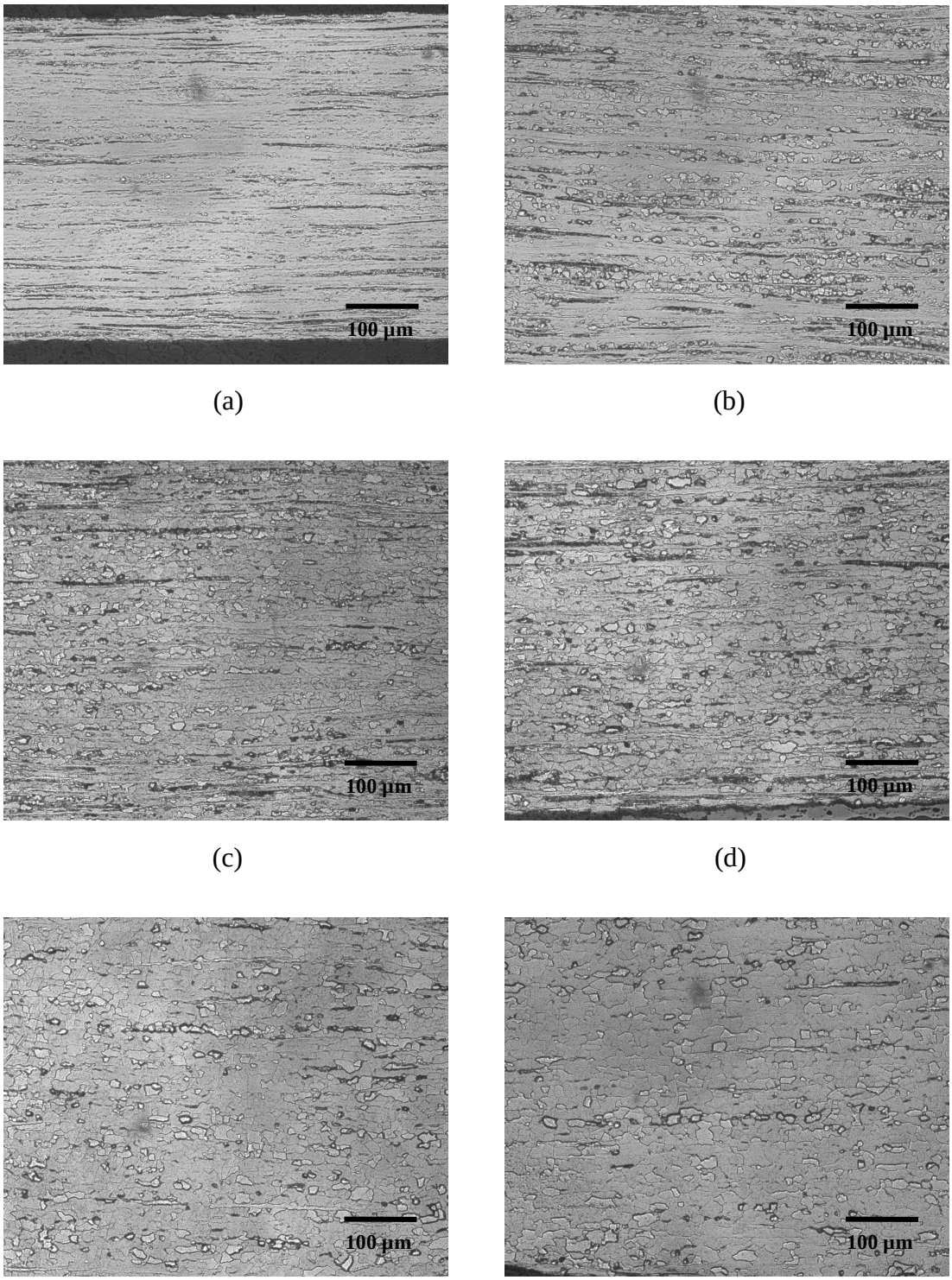

(a) (b)

(c) (d)

(e) (f)

Figure B-3: Optical micrographs of IF steel samples cold rolled to 90% and annealed at 620^{o} for (a) 2, (b) 5, (c) 8, (d) 10, (e) 15 and (f) 24hrs.

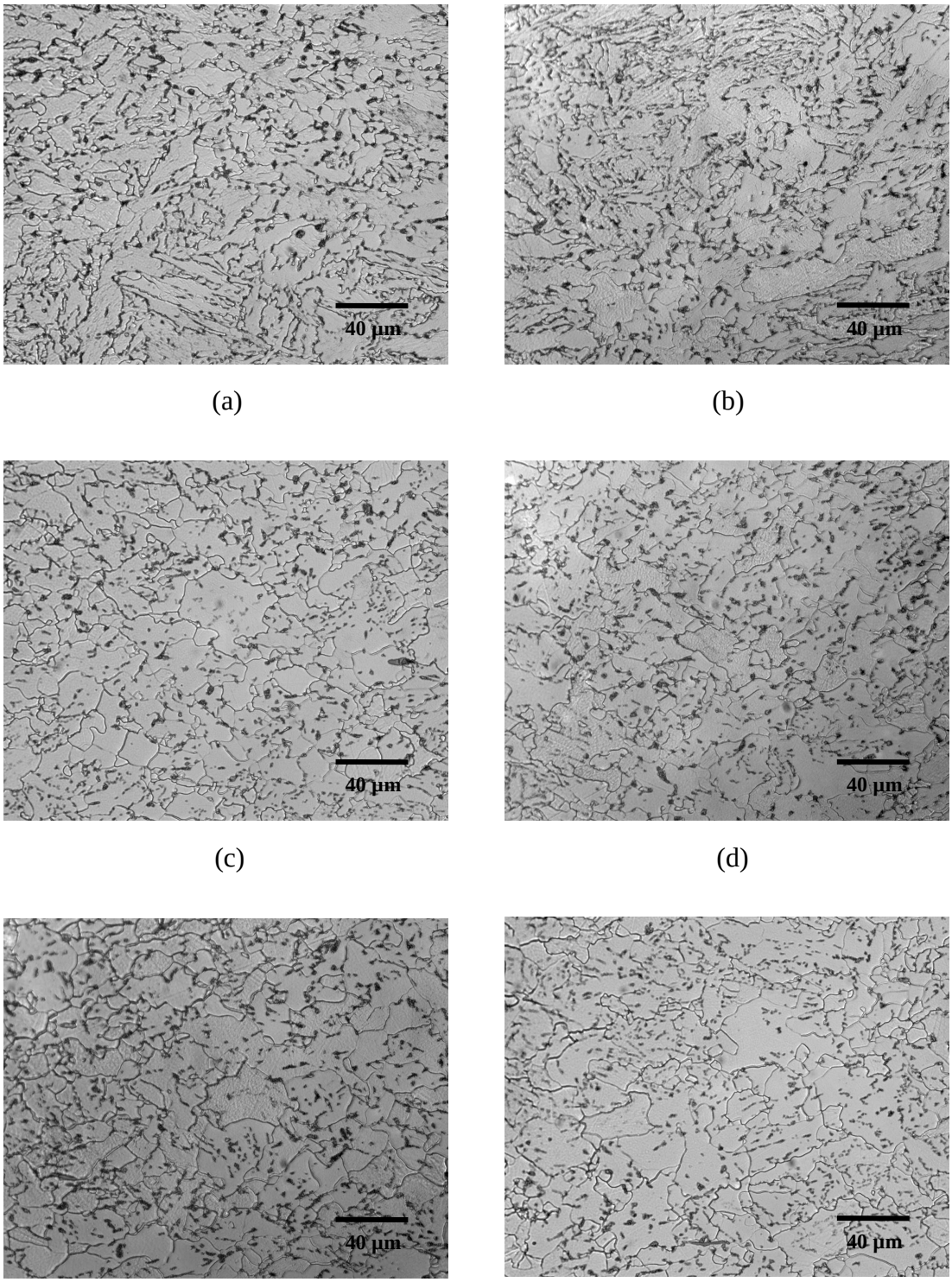

(a) (b)

(c) (d)

(e) (f)

Figure B-4: Optical micrographs of HSLA steel samples cold rolled to 20% and annealed at 560^{o} for (a) 2, (b) 5, (c) 10, (d) 16, (e) 24 and (f) 30hrs.

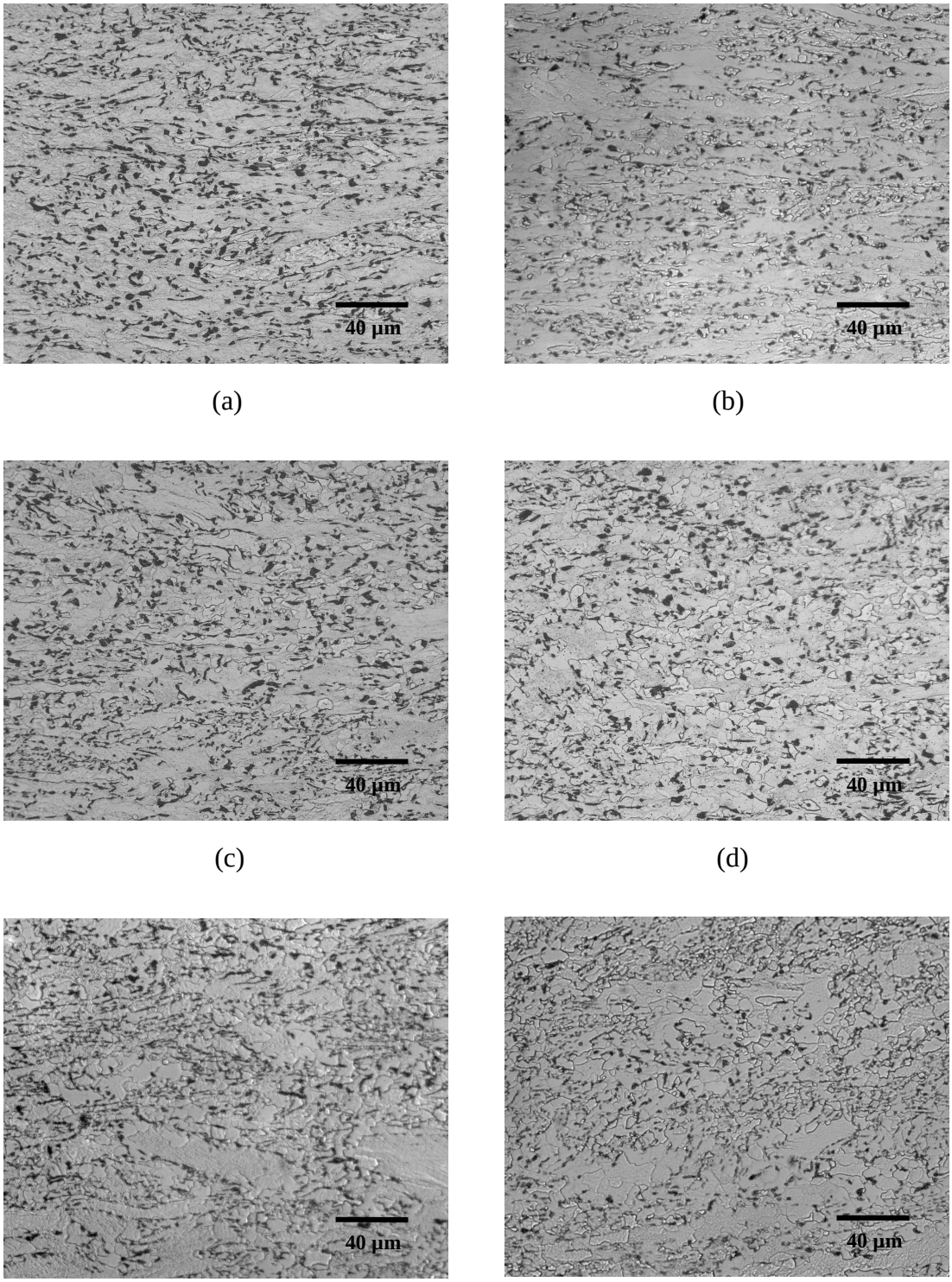

Figure B-5: Optical micrographs of HSLA steel samples cold rolled to 50% and annealed at 500^{o} for (a) 4, (b) 10, (c) 15, (d) 20, (e) 40 and (f) 55hrs.

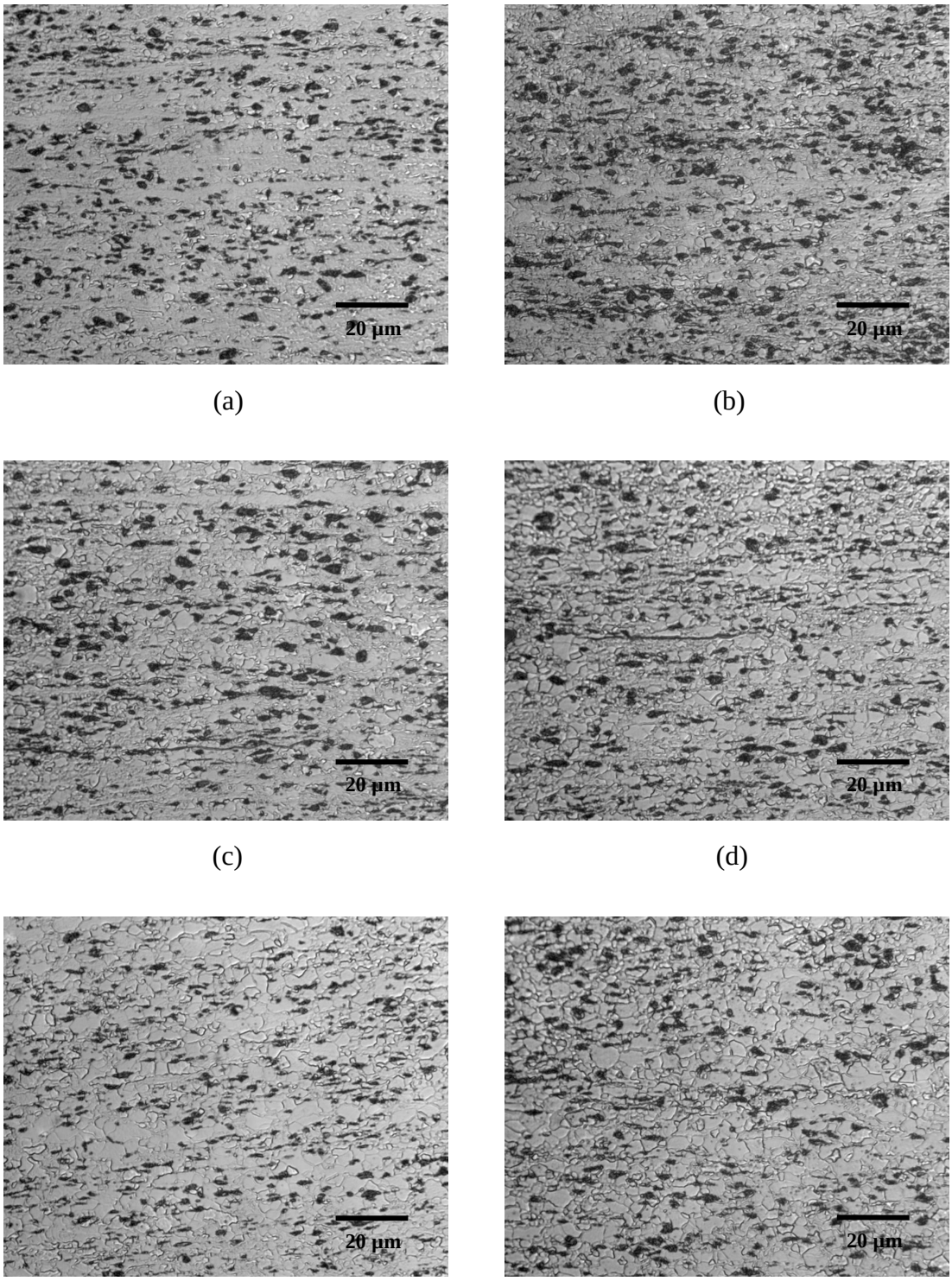

(a) (b)

(c) (d)

(e) (f)

Figure B-6: Optical micrographs of HSLA steel samples cold rolled to 90% and annealed at 500^{o} for (a) 4, (b) 7, (c) 10, (d) 13, (e) 16 and (f) 20hrs.

Table B-1: Recrystallised fraction and macrohardness measurements for IF steel cold rolled to 20% and annealed at 690°C for different annealing times.

Time (Hr)	Rex. Fraction Readings (%)			Rex. (Avg)	Rex. (Stdev)	Hardness Readings			Hardness (Avg)	Hardness (Stdev)
	1	2	3			1	2	3		
0	0	0	0	0	0	129	130	127	128.7	1.5
1	11	15	16	14.0	2.6	118	117	117	117.3	0.6
2	14	18	17	16.3	2.1	118	120	117	118.3	1.5
3	26	24	21	23.7	2.5	114	117	113	114.7	2.1
4	26	31	29	28.7	2.5	113	112	113	112.7	0.6
5	39	42	41	40.7	1.5	108	110	107	108.3	1.5
6	55	53	53	53.7	1.2	108	107	103	106.0	2.6
8	52	56	54	54.0	2.0	105	104	99.3	102.8	3.0
10	68	72	73	71.0	2.6	99.3	97.1	97.1	97.8	1.3
12	83	79	85	82.3	3.1	88.9	92.9	91.7	91.2	2.1
15	95	94	92	93.7	1.5	85.1	82.6	82.6	83.4	1.4
17	100	100	100	100.0	0.0	82.6	80.2	85.1	82.6	2.5
24	100	100	100	100.0	0.0	85.1	84.1	82.6	83.9	1.3

Table B-2: Recrystallised fraction and macrohardness measurements for IF steel cold rolled to 50% and annealed at 640°C for different annealing times.

Time (Hr)	Rex. Fraction Readings (%)			Rex. (Avg)	Rex. (Stdev)	Hardness Readings			Hardness (Avg)	Hardness (Stdev)
	1	2	3			1	2	3		
0	0	0	0	0	0	159	156	157	157.3	1.5
1	0.8	3.3	1.1	1.7	1.4	151	146	145	147.3	3.2
2	1.1	1.4	3.8	2.1	1.5	148	145	146	146.3	1.5
3	6.1	4.3	4.7	5.0	0.9	140	140	142	140.7	1.2
4	10	10.7	7	9.2	2.0	139	143	143	141.7	2.3
5	18	16.1	12.8	15.6	2.6	132	132	133	132.5	0.5
6	18.2	15.1	13.4	15.6	2.4	132	134	132	132.7	1.2
8	24.2	21.7	27.7	24.5	3.0	125	123	125	124.3	1.2
10	31.1	29	25.3	28.5	2.9	128	120	128	125.3	4.6
12	45.5	47	44.6	45.7	1.2	118	118	116	117.3	1.2
17	84	82.1	80.7	82.3	1.7	84.1	84.4	85.9	84.8	1.0
24	94.7	92.6	92.3	93.2	1.3	87.5	86.5	84.4	86.1	1.6

Table B-3: Recrystallised fraction and macrohardness measurements for IF steel cold rolled to 50% and annealed at 620°C for different annealing times.

Time (Hr)	Rex. Fraction Readings (%)			Rex. (Avg)	Rex. (Stdev)	Hardness Readings			Hardness (Avg)	Hardness (Stdev)
	1	2	3			1	2	3		
0	**0**	**0**	**0**	0	0	**159**	**156**	**157**	157.3	1.5
1	0.4	0.4	0.6	0.5	0.1	153	155	153	153.7	1.2
2	0.6	0.8	0.9	0.8	0.2	153	156	153	154.0	1.7
4	1.2	1.8	2.1	1.7	0.5	153	154	153	153.3	0.6
6	2.8	3.7	3.1	3.2	0.5	151	148	145	148.0	3.0
17	26	31	30	29.0	2.6	120	114	117	117.0	3.0
24	34	27	29	30.0	3.6	123	120	124	122.3	2.1

Table B-4: Recrystallised fraction and macrohardness measurements for IF steel cold rolled to 70% and annealed at 620°C for different annealing times.

Time (Hr)	Rex. Fraction Readings (%)			Rex. (Avg)	Rex. (Stdev)	Hardness Readings			Hardness (Avg)	Hardness (Stdev)
	1	2	3			1	2	3		
0	0	0	0	0	0	175	174	179	176.0	2.6
1	0.6	1	0.3	0.6	0.4	159	161	154	158.0	3.6
2	1	1.6	2	1.5	0.5	158	160	161	159.7	1.5
3	8	5	6	6.3	1.5	149	143	147	146.3	3.1
4	15	9	11	11.7	3.1	142	142	143	142.3	0.6
5	19	25	18	20.7	3.8	137	139	142	139.3	2.5
6	26	33	35	31.3	4.7	131	131	137	133.0	3.5
8	41	42	36	39.7	3.2	135	132	137	134.7	2.5
10	57	64	61	60.7	3.5	114	117	116	115.7	1.5
12	63	65	68	65.3	2.5	112	115	111	112.7	2.1
15	77	74	80	77.0	3.0	91.1	98	95.9	95.0	3.5
17	82	79	83	81.3	2.1	81.6	81.9	78.4	80.6	1.9
24	87	85	92	88.0	3.6	82.4	82.6	85.1	83.4	1.5

Table B-5: Recrystallised fraction and macrohardness measurements for IF steel cold rolled to 90% and annealed at 620°C for different annealing times.

Time (Hr)	Rex. Fraction Readings (%)			Rex. (Avg)	Rex. (Stdev)
	1	2	3		
0	0	0	0	0	0
1	1.1	0.5	0.6	0.7	0.3
2	3.2	1.6	1.5	2.1	1.0
3	9.2	10.3	15	11.5	3.1
4	34.3	31.8	28.6	31.6	2.9
5	45.9	42.3	48.3	45.5	3.0
6	42.7	49.7	40.2	44.2	4.9
8	61.3	63.5	69.8	64.9	4.4
10	71.1	69.4	75	71.8	2.9
12	85.7	83.6	79.8	83.0	3.0
15	87.1	91.8	94.8	91.2	3.9
17	96.3	96.8	92.5	95.2	2.4
24	95.6	92.8	90.5	93.0	2.6

Table B-6: Recrystallised fraction and macrohardness measurements for HSLA steel cold rolled to 20% and annealed at 560°C for different annealing times.

Time (Hr)	Rex. Fraction Readings (%)			Rex. (Avg)	Rex. (Stdev)	Hardness Readings			Hardness (Avg)	Hardness (Stdev)
	1	2	3			1	2	3		
0	0	0	0	0	0	230	227	233	230.0	3.0
2	10	11	15	12.0	2.6	195	189	192	192.0	3.0
5	26	25	23	24.7	1.5	171	172	177	173.3	3.2
10	67	75	71	71.0	4.0	134	137	137	136.0	1.7
16	84	85	89	86.0	2.6	129	134	130	131.0	2.6
24	100	100	100	100.0	0.0	123	122	122	122.3	0.6
30	100	100	100	100.0	0.0	117	122	123	120.7	3.2

Table B-7: Recrystallised fraction and macrohardness measurements for HSLA steel cold rolled to 20% and annealed at 500°C for different annealing times.

Time (Hr)	Rex. Fraction Readings (%)			Rex. (Avg)	Rex. (Stdev)	Hardness Readings			Hardness (Avg)	Hardness (Stdev)
	1	2	3			1	2	3		
0	0	0	0	0	0	230	227	233	230.0	3.0
7	0	0	0	0.0	0.0	203	205	203	203.7	1.2
15	1.8	1.3	2.2	1.8	0.5	198	198	201	199.0	1.7
24	4.1	4.6	4.5	4.4	0.3	200	194	198	197.3	3.1
40	4.3	5.5	5.1	5.0	0.6	197	197	196	196.7	0.6
55	13	15	13	13.7	1.2	191	191	189	190.3	1.2

Table B-8: Recrystallised fraction and macrohardness measurements for HSLA steel cold rolled to 50% and annealed at 500°C for different annealing times.

Time (Hr)	Rex. Fraction Readings (%)			Rex. (Avg)	Rex. (Stdev)	Hardness Readings			Hardness (Avg)	Hardness (Stdev)
	1	2	3			1	2	3		
0	**0**	**0**	**0**	0	0	**258**	**262**	**264**	261.3	3.1
4	2.1	2.5	3.3	2.6	0.6	235	238	238	237.0	1.7
10	22	27	28	25.7	3.2	220	215	217	217.3	2.5
15	41	39	46	42.0	3.6	196	198	198	197.3	1.2
20	52	50	52	51.3	1.2	178	187	182	182.3	4.5
30	65	58	59	60.7	3.8	169	167	174	170.0	3.6
40	70	77	75	74.0	3.6	164	160	165	163.0	2.6
55	93	90	90	91.0	1.7	153	147	149	149.7	3.1

Table B-9: Recrystallised fraction and macrohardness measurements for HSLA steel cold rolled to 70% and annealed at 500°C for different annealing times.

Time (Hr)	Rex. Fraction Readings (%)			Rex. (Avg)	Rex. (Stdev)	Hardness Readings			Hardness (Avg)	Hardness (Stdev)
	1	2	3			1	2	3		
0	0	0	0	0	0.0	278	278	282	279.3	2.3
2	2.3	3.1	3.4	2.9	0.6	267	262	262	263.7	2.9
4	6.8	7.6	7.1	7.2	0.4	252	246	248	248.7	3.1
7	23	22	22	22.3	0.6	233	224	224	227.0	5.2
10	38	39	45	40.7	3.8	215	213	213	213.7	1.2
13	51	47	55	51.0	4.0	205	204	209	206.0	2.6
16	69	72	71	70.7	1.5	187	187	186	186.7	0.6
20	92	90	92	91.3	1.2	180	179	179	179.3	0.6
24	98	97	98	97.7	0.6	179	179	176	178.0	1.7

Table B-10: Recrystallised fraction and macrohardness measurements for HSLA steel cold rolled to 90% and annealed at 500°C for different annealing times

Time (Hr)	Rex. Fraction Readings (%)			Rex. (Avg)	Rex. (Stdev)	Hardness Readings			Hardness (Avg)	Hardness (Stdev)
	1	2	3			1	2	3		
0	0	0	0	0	0.0	321	321	321	321.0	0.0
2	5.3	6.5	6.7	6.2	0.8	260	256	261	259.0	2.6
4	11	13.8	13.5	12.8	1.5	241	237	236	238.0	2.6
7	35	31	32	32.7	2.1	221	225	221	222.3	2.3
10	61	59	58	59.3	1.5	203	206	209	206.0	3.0
13	73	69	68	70.0	2.6	195	192	193	193.3	1.5
16	91	88	85	88.0	3.0	189	193	187	189.7	3.1
20	100	100	100	100.0	0.0	186	181	182	183.0	2.6
24	100	100	100	100.0	0.0	175	185	185	181.7	5.8

Appendix C Monte-Carlo Modelling

The Monte-Carlo model uses a discretised representation of microstructure in the form of a lattice, in which each lattice point is assigned a number, S_i, which represents the local grain orientation (or spin). A grain will therefore comprise of one or more lattice sites of the same orientation while those lattice sites adjacent to sites with different orientations are considered as being separated by a grain boundary as shown in Figure C-1.

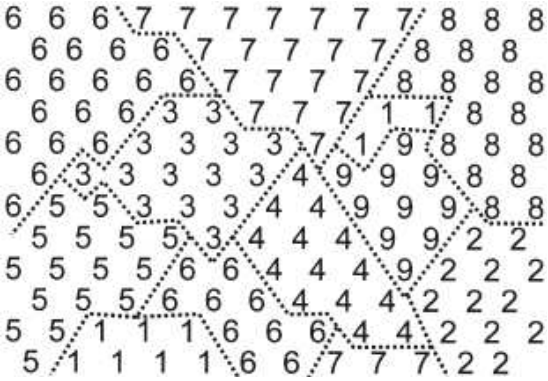

Figure C-1: Sample microstructure on a triangular lattice where the numbers indicate the orientation and the dotted lines represent grain boundaries.

The grain boundary energy may therefore be considered as number pairs where the like number pairs are considered to have zero energy (i.e. grain interior) while those unlike pairs to have the same high energy value. Summing bulk and surface energy contribution, the total energy of the system is calculated using the Potts Hamiltonian:

$$H = \sum_{i=1}^{N} \left\{ \sum_{j=1}^{n} \frac{\gamma(s_i s_j)}{2} + F(s_i) \right\} \qquad \text{(C-1)}$$

where γ is the free energy of a unit of grain boundary that depends on the misorientation between S_i and S_j in the units of Boltzmann constant k, F is the volumetric energy of a site of orientation S_i in units of k. the inner summation is taken over the neighbourhood of site i consisting of n sites and the outer summation is taken over all the lattice sites, N.

The evolution of the structure is modelled by selecting a site at random, and reorienting it to one of the adjacent grain orientations. The change in total system

energy, ΔE, for the new state is computed, and the reorientation is implemented with transition probability, p, such that

$$P(\Delta E) = \begin{cases} 1 & \text{if } \Delta E \leq 0 \\ \exp(-\Delta E/kT) & \text{if } \Delta E > 0 \end{cases} \qquad \text{(C-2)}$$

where T is the simulation temperature. It is important to note that T is not the physical temperature. In the simulation, this temperature governs the degree of disorder in the lattice. Most of the simulations of recrystallisation have been performed at zero temperature. The unit of time in the simulation is the Monte Carlo Step (MCS) which represents N reorientation attempts.